UNIVERSITY OF SOUTHAMPTON

FACULTY OF ENGINEERING and PHYSICAL SCIENCES

School of Electronics & Computer Science

Helium Ion Beam Lithography

by

Xiaoqing Shi

Thesis for the degree of Doctor of Philosophy

February 2018

UNIVERSITY OF SOUTHAMPTON

ABSTRACT

FACULTY OF PHYSICAL SCIENCES & ENGINEERING
SCHOOL OF ELECTRONICS & COMPUTER SCIENCE

Doctor of Philosophy

HELIUM ION BEAM LITHOGRAPHY

by Xiaoqing Shi

As nanoelectronic device design pushes towards ever smaller feature sizes, there is an increasing need for new lithographic patterning techniques and resists. Helium ion beam lithography (HIBL), an emerging technique that uses a high-intensity, sub-nanometer focused beam of helium ions generated in the helium ion microscope (HIM) to expose resist, promises to drive nano-patterning beyond the capabilities of conventional electron beam lithography (EBL). In this work, an investigation on HIBL in direct comparison with EBL using both conventional EBL resist PMMA and a novel fullerene-based molecular resist is described. Analysis of large area exposures reveals a sensitivity of 2 μC/cm^2 on PMMA and 40 μC/cm^2 on fullerene derivative resist with 30-keV helium ion beam, which are 60 times and 500 times higher than those with an electron beam for the same resists respectively. This improved resist sensitivity in HIBL demonstrates the potential for faster pattern definition and therefore high throughput. The proximity effect, caused by the backscattered primary particles and known to limit the performance of EBL, was then quantitatively studied using a "doughnut" method on 20-nm-thick PMMA resist on silicon with 30 keV HIBL and EBL. The lithographic results were fitted to the proximity function and the backscattered electrons/ions range were found out to be ~3.26 μm and ~0.067 μm, revealing a 60 times proximity effect reduction in HIBL compared to EBL. This suggests that the negligible proximity effect in HIBL enables high-density pattern definition, whilst avoiding the inadvertent exposure of surrounding material. Finally, to demonstrate the benefit of the smaller spot size and the reduced proximity effect in HIBL, line dose optimisation was carried out with high-resolution single-pixel line arrays on both resists. Linewidth of ~11.7 nm was achieved in 20-nm PMMA with pitches down to 30 nm. In 10-nm fullerene resist, line widths of 7.2 nm were achieved in sparse line arrays. The fabrication of 8.5 nm half-pitched lines with good feature separation and 6 nm half-pitched lines with inferior but still resolvable separation is also shown in this resist. Thus, sub-10 nm patterning with high resist sensitivity and small proximity effect is demonstrated using HIBL with standard processing conditions, establishing its potential as an alternative to EBL for rapid prototyping of beyond CMOS devices.

Contents

Declaration of Authorship

I, *XIAOQING SHI*, declare that this thesis entitled *HELIUM ION BEAM LITHOGRAPHY* and the work presented in the thesis are both my own, and have been generated by me as the result of my own original research. I confirm that:

- This work was done wholly or mainly while in candidature for a research degree at this University;
- Where any part of this thesis has previously been submitted for a degree or any other qualification at this University or any other institution, this has been clearly stated;
- Where I have consulted the published work of others, this is always clearly attributed;
- Where I have quoted from the work of others, the source is always given. With the exception of such quotations, this thesis is entirely my own work;
- I have acknowledged all main sources of help;
- Where the thesis is based on work done by myself jointly with others, I have made clear exactly what was done by others and what I have contributed myself;
- Either none of this work has been published before submission, or parts of this work have been published as: Articles listed in the following “List of Publications and Conferences”.

Signed: ……

Date: ……30/11/2017……

List of Publications and Conferences

Journal Articles

1. Shi, X., Prewett, P., Huq, E., Bagnall, D.M., Robinson, A.P. and Boden, S.A., 2016. Helium ion beam lithography on fullerene molecular resists for sub-10nm patterning. *Microelectronic Engineering*, *155*, pp.74-78. https://doi.org/10.1016/j.mee.2016.02.045

2. Boden, S. and Shi, X., 2017. Helium ion beam lithography for sub-10nm pattern definition. *SPIE Newsroom*. https://doi:10.1117/2.1201702.006839

3. Shi, X., Prewett, P., Huq, E., Bagnall, D.M. and Boden, S.A., A quantitative comparison between helium ion and electron beam lithography on PMMA resist, *Nanotechnology*, in preparation.

4. Shi, X., Yang, D., Huq, E., Boden, S.A., Bagnall, D.M., Lada, T.A., Robinson, A.P. and Prewett, P., Solvent effects in a fullerene resist for helium ion beam lithography, *Microelectronic Engineering*, in preparation.

Book Chapter

Shi, X. and Boden, S.A., 2016. Scanning helium ion beam lithography. In: Robinson, A.P. and Lawson, R. A. ed. Materials and Processes for Next Generation Lithography, Volume 11. Elsevier, pp. 563-594

International Conferences

1. Shi, X., Prewett, P., Huq, E., Bagnall, D.M. and Boden, S.A., "A quantitative comparison between helium ion and electron beam lithography on PMMA resist", 42nd international conference on micro and nano engineering, September 19-23, Vienna, Austria (2016)

2. Shi, X., Prewett, P., Huq, E., Bagnall, D.M. and Boden, S.A., "Proximity effect quantification and dose optimisation for high resolution helium on beam lithography", 41st international conference on micro and nano engineering, September 21-24, The Hague, The Netherlands (2015)

3. Shi, X., Prewett, P., Huq, E., Bagnall, D.M., Robinson, A.P. and Boden, S.A., "Helium ion beam lithography on fullerene molecular resist for sub-10 nm patterning", 41st international conference on micro and nano engineering, September 21-24, The Hague, The Netherlands (2015)

Competitions

1. Shi, X. “Fabrication at the nanoscale: using a focused helium ion beam to make the electronic devices of the future”, Three Minute Thesis (3MT), March 23rd, University of Southampton, UK (2016)

2. Shi, X. “Helium ion beams for rapid prototyping of future nanoelectronic devices”, STEM for Britain, March 13th, Westminster Parliament, London, UK (2017)

Other Presentations

1. Single Nanometer Manufacturing (SNM) Workshop (Barcelona, Spain, July 2014)
2. SNM Workshop (Sankt Florian am Inn, Austria, July 2015)
3. SNM Workshop (Bayreuth, Germany, May 2016)
4. PicoFIB Workshop (Sheffield, UK, January 2017)

Acknowledgements

First and foremost, I wish to express my sincere gratitude to my supervisor Dr. Stuart Boden for his guidance and support throughout my PhD. I hold great respect for his rigorous research attitude and his systematic and meticulous scientific approach has always being a source of motivation for me. I am deeply inspired by his knowledge, patience, and perseverance. Stuart guided me into research: he spared no efforts in training me on multiple pieces of equipment, demonstrating various analysis packages; whilst giving me great space to develop and grow. Stuart always encourage and support me to reach my full potential. I sincerely appreciate all his contribution of time, ideas and supervision, which made my PhD an extremely positive experience. I could not have asked for a better supervisor and mentor.

The research leading to the results in this work has received funding from the European Union Seventh Framework Programme FP7/2007-2013 Single Nanometer Manufacturing (SNM) project (grant agreement No. 318804) through the collaboration with Prof. Philip Prewett and Prof. Ejaz Huq from Oxford Scientific Consultants Ltd. I always enjoy our stimulating discussions during meetings. I am very grateful that I was given opportunities and generous financial support to attend various project workshops and conferences over the last four years, where I learned a tremendous amount from my project partners and significantly broadened my horizon. The fullerene related studies presented in this thesis would not have been possible without the novel molecular resists developed and provided by the group of Dr. Alex Robinson at the University of Birmingham and the Irresistible Materials Ltd. I greatly appreciate their collaboration, ideas and advices. I thank Dr. Dongxu Yang for preparing various fullerene resist solutions and sharing his expert knowledge with me during his research visits, and I enjoyed working with him immensely.

I would like to thank my viva examiners: Prof. Martin Charlton and Dr. Yoshishige Tsuchiya for their insightful comments and suggestions, but also for the hard questions which incentivised me to widen my research from various perspectives. My thanks also go to my personal tutor Prof. Darren Bagnall, who initially provided me with the opportunity to join his research team as intern during my undergraduate study where I discovered my research interest in nanoelectronics, and brought me in to this PhD project with confidence.

I would like to express my appreciation to staff and technicians at Southampton Nanofabrication Centre, whose hard work to ensure the smooth running of the facilities allowed me to have conducted my experiments successfully. I thank my fellow Nano Research Group and cleanroom colleagues for giving me a friendly and professional working environment, especially Dr. Kian Kiang, for his time and valuable advices. I also thank my group secretary Laila and staff from ECS postgraduate research

office for your love and care. All my friends, whom I met in UK during studying and working, you are my greatest treasure and thank you for the inspiration and support. Thank you Xiaoye for giving me your love and encouragement all these years and treat me like family.

Lastly, I would like to give special thanks to my family for giving me their love and encouragement in all my pursuits. Words cannot express how grateful I am for their sacrifices that they've made to allow me the best possible opportunities in life. For my grandparents who bring me up with a love of science and engineering and a spirit of striving for the best. Most of all for my loving, supportive and patient husband Chen who is always there for me, supporting me for everything. Thank you.

List of Abbreviations

AFM	Atomic force microscopy
BEs	Backscattered electrons
BIV	Best imaging voltage
CARC	Critical aspect ratio of collapse
CD	Critical dimension
DI	Deionised
E-beam	Electron beam
EBL	Electron beam lithography
ECP	Exposure control program
ET	Everhart Thornley
EUV	Extreme ultraviolet
EUVL	Extreme ultraviolet lithography
FIB	Focused ion beam
FOV	Field of view
GFIS	Gas field ion source
HF	Hydrofluoric acid
HIBL	Helium ion beam lithography
HIM	Helium ion microscope
HP	Half-pitch
HSQ	Hydrogen silsesquioxane
ICs	Integrated circuits
IPA	Isopropyl alcohol
LER	Line-edge roughness
MIBK	Methyl isobutyl ketone
M_n	Molecular weight
MOSFET	Metal-oxide-semiconductor field-effect transistor
NIL	Nanoimprint lithography
ON	Ohnishi number
OSC	Oxford Scientific Consultants Ltd.
PEC	Proximity effect correction
pH	Power of hydrogen
PHS	polyhydroxystyrene

PMMA	Polymethyl methacrylate
PSF	Point spread function
RP	Ring parameter
rpm	Revolutions per minute
SEs	Secondary electrons
SNC	Southampton Nanofabrication Centre
SNM	Single nanometer manufacturing for beyond CMOS devices
SNR	Signal-to-noise ratio
SPL	Scanning probe lithography
SRIM	The Stopping and Range of Ions in Matter
TEM	Transmission electron microscopy
UI	User interface

CHAPTER 1

INTRODUCTION

1.1 Single Nanometer Manufacturing

In the last 40 years, the dimensions of electronic devices on silicon chip have become smaller and smaller, which agrees with Moore's Law. The scaling of solid-state devices has the property of reducing cost whilst improving performance and power. This has resulted in an exponential increase in the number of transistors per chip. The minimum dimensions of the metal-oxide-semiconductor field-effect transistor (MOSFET) used in the latest commercial integrated circuits (ICs) has reached the 10 nm node [1]. IBM is currently working on the 7 nm process node using the extreme ultraviolet lithography (EUVL) on SiGe test chips [2]. This is a breakthrough into the sub-10 nm era, however, due to the difficulty in controlling the device current and the significant influence of quantum mechanical effects such as electron tunnelling, MOSFETs are predicted to be no longer feasible for scales much smaller than 10 nm. Additionally, fabrication of the increasingly-dense nanoscale devices using conventional lithographic techniques will become challenging and problematic. Both facts suggest that new devices are demanded for next-generation nanomanufacturing and this can only be realised with new nanolithographic approaches.

"Single Nanometer Manufacturing for Beyond CMOS Devices" (SNM) is an EU funded research integrated project (Grant Agreement No: 318804), connecting 15 strong teams (Table 1.1) across industry and academia to investigate and develop novel technologies for single nanometer manufacturing, with the aim of reaching the theoretical limit of future nanoelectronic and nanomechanical systems [3].

Participant Organisation Name	Name in short	Country
Technische Universität Ilmenau (Project Co-operator)	TUIL	Germany
EV Group E. Thallner GmbH	EVG	Austria
IMEC	IMEC	Belgium

Mikrosistemi Ltd.	μS	Bulgaria
Universität Bayreuth	UBT	Germany
Technische Universiteit Delft	TUD	Netherlands
Spanish National Research Council	CSIC	Spain
IBM Research GmbH	IBM	Switzerland
École Polytechnique Fédérale de Lausanne	EPFL	Switzerland
SwissLitho AG	SL	Switzerland
Oxford Instruments Nanotechnology Tools Ltd.	OINT	UK
Imperial College London	IMPERIAL	UK
The Open University	OU	UK
Oxford Scientific Consultants Ltd.	OSC	UK
VSL Dutch Metrology Institute	VSL	Netherlands

Table 1.1: List of all participants in the SNM project.

Pushing the limits of nanomanufacturing down to the single nanometer scale and opening new horizons for beyond CMOS technology with novel, cost-effective nanolithographic technologies are the project objectives [4]. The main focus of this project is combining high resolution scanning probe lithography (SPL) and nanoimprint lithography (NIL), but other high-resolution patterning techniques are also being explored such as helium ion beam lithography (HIBL), the subject of this thesis. The applications into novel ultra-low power electronics, quantum devices (quantum dots) and manipulation of individual electrons (single electron devices) are also being explored.

This PhD is partly funded by OSC, one of the participants in the SNM project, for the investigation into using the ultra-high-resolution helium ion microscope (HIM) for the resist based sub-10 nm nanolithographic applications.

1.2 Structure of Report

In Chapter 2, the helium ion beam system used for the resist-based lithographic technique and the unique helium ion-solid interactions are described. A review of the literature on lithography with a focus on resist patterning using a focused helium ion beam is then presented. Also introduced in this chapter is a new class of molecular C_{60}-based resist which was adopted in this PhD.

Methodology developed for the systematic investigation of helium ion beam lithography (HIBL) is presented in Chapter 3. This includes working procedures for sample preparation, pattern generation, resist exposure using HIBL and electron beam lithography (EBL) and development processes. In addition, techniques of the key measurement and characterisation tools deployed in this PhD are described.

In Chapter 4, PMMA, a conventional E-beam resist, was used in the HIBL investigation. Experiments on resist sensitivity and resist resolution are described. The effects of varying the thickness of the resist and applying different pre-exposure bake are also discussed.

This is followed, in Chapter 5, by a direct and quantitative investigation of comparing the resist sensitivity and proximity effect in 20-nm PMMA using HIBL and EBL at 30 keV. This is followed by the demonstration of high-resolution HIBL patterning of dense line arrays.

Chapter 6 explores the use of a novel molecular fullerene derivative resist for high resolution and high density patterning using HIBL, before conclusions are drawn and areas for future work are highlighted in Chapter 7.

CHAPTER 2

REVIEW OF LITERATURE*

2.1 Lithography

Lithography is a process where an arbitrary pattern can be accurately and repeatedly produced in a specialised layer of material on a substrate by inducing a chemical modification. Typically, that pattern is then transferred to another functional layer through a traditional etching or lift-off process [5]. Lithography facilitates the drive for ever-decreasing dimensions of semiconductor devices and is therefore a keystone of the nanotechnology revolution.

Resist-based charged particle beam lithography is the most prevalent approach, where resist materials that are sensitive to energetic photons or particles are exposed, and it consists of the following steps (Figure 2.1). First, a radiation sensitive material (the "resist") is applied as a thin film to a substrate before exposure to the energetic electron/ion beam. Secondly, the resist is exposed with desired patterns either through a pre-designed mask or directly traced out by a focused beam. Upon irradiation, the inelastic collisions excite secondary electrons (SEs) in the resist. This ionisation process is accompanied by physical/chemical modifications that cause a solubility change of the resist material in a developer. Finally, the features are formed after resist is removed during the development process and are ready for the subsequent pattern transfer.

Resists are categorised into two types: Positive tone resists go through scission of polymeric chains on exposure and become more soluble in the developer. An example of a high-resolution positive tone resist is polymethyl methacrylate (PMMA), which is composed of long chain polymers that will break into smaller fragments upon exposure and become more soluble [6]. Negative tone resists, on the other hand, become less soluble due to cross-linking reactions, where smaller molecules combine into larger ones, leading to a decrease in solubility [7]. Hydrogen silsesquioxane (HSQ) is a good example of a high-resolution negative tone resist.

---

* Part of this chapter was published in the book "Materials and Processes for Next Generation Lithography" (2016), by X. Shi and S. Boden.

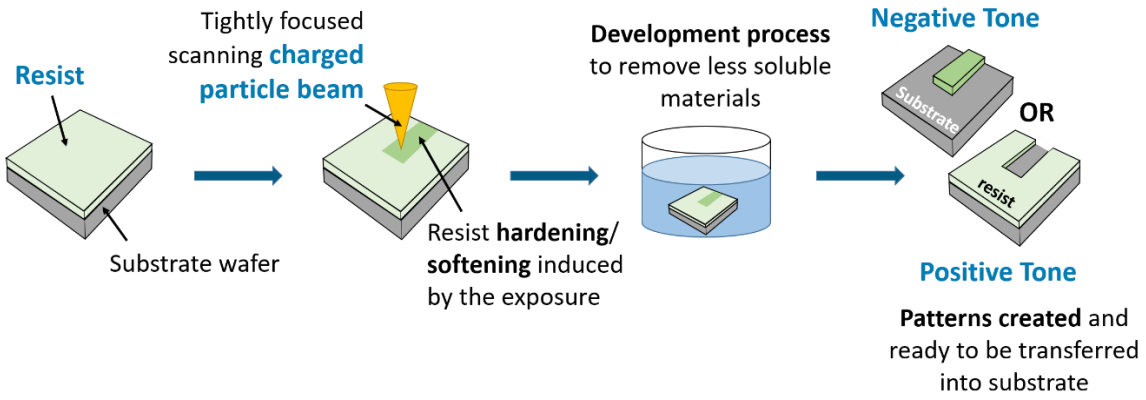

Figure 2.1: Key processing steps of resist-based lithography: coating of resist material, exposure of resist using a charged particle beam and finally forming structures in negative and positive tone resists during the development process.

Several chemical and mechanical properties make resist materials appropriate for a given set of lithographic processes. Resolution specifies the reproducibility of the printing of minimum sized features under conditions of reasonable variation. The contrast of a resist is related to the rate of changes in solubility of the material, i.e. polymer chain scission/cross-linking, upon exposure. Resists with higher contrast are generally capable of being patterned with smaller features than those with lower contrast. A dose response curve of a hypothetical positive tone resist is plotted in Figure 2.2, where the remaining thickness of resist after the development process normalized to the original resist thickness is plotted against the exposure dose in a logarithmic scale. It can be observed that at low doses, the resulting resist thicknesses remain relatively unchanged with an increase of exposure dose. However, when the dose increases further from below to above the threshold value, a nonlinear and abrupt transition happens and causes rapid change in the resulting resist layer thickness. The resist contrast, γ, is determined from the slope of the linear portion of the dose response curve, and a steeper edge gives a greater γ, hence a higher contrast value. Typical contrast values for resists range from 2, found in conventional resists such as PMMA, to as high as 15 for modern chemically amplified resists [8].

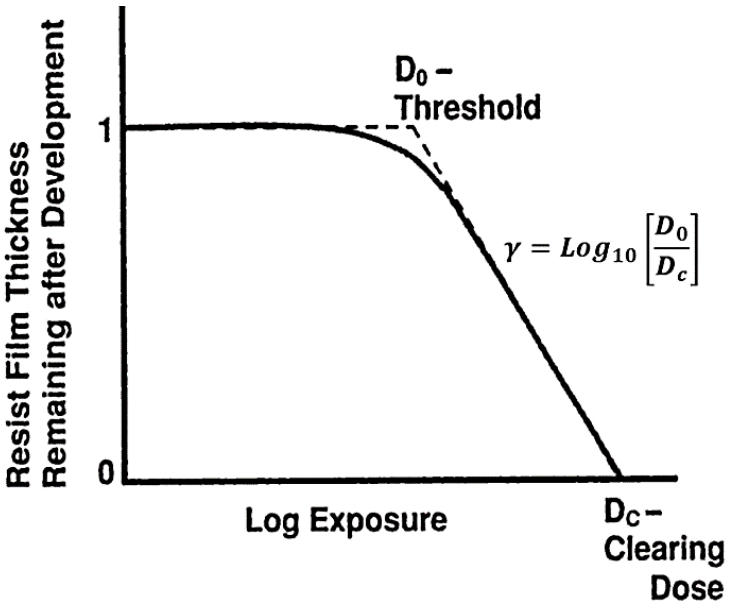

Figure 2.2: Characteristic curve of a hypothetical positive tone resist, where the slope of the transition curve is the value of the resist contrast [5].

Other important factors in lithography are sensitivity and throughput. Sensitivity indicates the required exposure dose to produce desired chemical reactions in the resist for pattern definition. For positive-tone resist, it is often defined as the dose required to completely clear the resist material, whilst for negative-tone resist, it is the dose required to form 50% of final fully-exposed thickness. Beam species, landing energy, resist thickness and development processes are known to have a substantial impact on the sensitivity of a resist. Throughput is a measure of the number of features patterned per second and indicates the speed of the lithographic technique. A high resist sensitivity means less exposure time is required, which allows faster beam writing, hence leading to a higher throughput and higher writing efficiency.

After the exposure, a developer is used to remove either the (exposed) fragments from the positive tone resist or the (unexposed) non-crosslinked molecules from the negative tone resist. This is done by immersing the sample in the developer solution. Longer polymers are less mobile and more resistant to the developer, and hence, they take longer to dissolve [9], [10]. The process can be accelerated by using a developer of a higher concentration, but this can degrade the resolution. In addition to the strength of the developer, the temperature and the duration of the development are also contributing factors that could affect the development results. Due to the inseparable relationship between the exposure and development, when a pattern shows underdevelopment, it could be due to underexposure; likewise, if a pattern appears to be overdeveloped, it could be overexposed. From the step of resist spinning to the final development process, various steps involve complex chemical and physical reactions. Hence, there are many parameters that can affect the final result (see Table 2.1),

and understanding impacts of these parameters is very important when carrying out lithography experiments.

Parameter	Process impact
Exposure energy	Resolution, sensitivity, proximity
Exposure dose	Pattern quality
Pattern density	Proximity, pattern quality
Resist material	Sensitivity, resolution, contrast
Resist thickness	Sensitivity, resolution, pattern quality
Developer	Sensitivity, resolution, development window
Development temperature	Sensitivity, resolution, exposure window
Development time	Sensitivity, resolution, exposure window

Table 2.1: Some key aspects of lithography and their impacts on the lithographic outcomes [8].

Many lithographic approaches are currently implemented in industry as well as in research, and they can be categorised into parallel and serial lithography. Parallel lithography uses suitable masks and projects an image of the mask onto the resist layer to form desired patterns. Serial lithography is a direct write technique that exposes resist point-by-point using a beam of charged particles or a probe. Optical lithography is the most common top-down parallel patterning method that allows for cost-efficient, high-volume fabrication of microelectronic and nanoelectronic devices. It is used daily for mass production of ICs, which, at the time of writing, are being shipped with feature sizes corresponding to the 10 nm technology node [11]. However, alternative lithography methods can be more favourable for low-volume fabrication where the requirement for a photomask is a disadvantage. For example, electron beam lithography (EBL) is a common direct-write method that uses a focused electron beam (e-beam) to expose resist. EBL at energies of 30 keV and above is well established for sub-20 nm nanofabrication and a minimum feature size of below 10 nm has been demonstrated [12], [13].

The high-resolution masks and templates fabricated by EBL have enabled high-volume nanoscale patterning technologies including optical and NIL. Furthermore, EBL is used for rapid prototyping of new device designs. However, at high energies (such as 30 keV and above), EBL suffers from long-range proximity effects, a phenomenon that the developed patterns are wider than the scanned patterns, mainly due to the backscattered electrons (BEs) generated when the primary electrons interact with the resist and substrate. This effect significantly limits its performance. Although the proximity effect has been demonstrated to be greatly reduced to ~200 nm range when adopting low beam energies (15-nm half-pitch (HP) structures were achieved on 15-nm thick HSQ at 2 keV [14]), the resolution of low-energy EBL is compromised compared to that of high-energy EBL due to increased electron scattering and larger spot size. Moreover, patterning thick resists proves to be

difficult at this energy level. The finite penetration depth of low-energy electrons limits the thickness of the resist and hinder the subsequent pattern transfer; forward scattering also reduces resolution as the resist thickness increases [15].

Proximity effect correction (PEC) in EBL was developed to enhance lithographic accuracy and resolution via (i) exposure dose modulations, (ii) modifications of the pattern geometry (shape bias) or (iii) combining both methods [16]–[19]. Commercial software that corrects the proximity effect was made available with EBL tools, however, these packages are optimised for high throughput of highly hierarchical design topologies consisting mainly of a relatively low-density arrangement of rectangular-shaped features and can be costly [20].

Another method is the lesser known, but highly versatile focused ion beam (FIB) lithography. In EBL, electron beam generates low-energy SEs to activate the physical/chemical reactions in the resist materials. FIB lithography adopts the same principle, but more SEs are generated, hence, the process is more efficient and therefore potentially faster. In FIB lithography, proximity effects are negligible due to the very low number of ions that are backscattered.

In theory, densely packed patterns with a resolution comparable to the FIB probe size are achievable. For heavy ions such as gallium generated from a liquid metal ion source, the large beam spot size of 5 nm makes it difficult to reach comparable lithographic resolution to EBL. Other constraints are sputtering effect, substrate damage and contamination produced by the ion impact [21]. Both factors have inhibited large-scale applications of heavy ion beam lithography in resist patterning.

For light ions such as helium, ~200 nm resolution was demonstrated using a gas field ion source (GFIS) over 20 years ago [22]; however, deficiencies in column technology halted its progress. Recently, developments in light ion sources and columns have made sub-nanometer spot sizes possible, whilst limiting sample damage [23]. With the shorter range, weaker forward scattering and smaller lateral diffusion of the yielded SEs, FIB lithography can now reach resolutions comparable to the best demonstrated by well-established EBL [24].

Compared to parallel lithography approaches including conventional optical lithography, FIB lithography has two main advantages. First, its mask-less approach offers good flexibility in writing arbitrary patterns, similar to EBL. For single-item or low volume runs, it is a relatively low cost and high efficiency option. In parallel techniques, the masks must be fabricated first to transmit radiation accurately, which can be time consuming and expensive. Second, due to the short wavelength, the ultimate resolution in ion beam lithography is defined and limited by the diameter of the focused beam, rather than the wavelength of the exposing irradiation and diffraction that limit techniques such as optical lithography.

Nonetheless, there are also disadvantages that limit ion beam lithographic applications. Due to the nature of serial write, the throughput is lower than that for a parallel technique, hence, it is not as economically favourable for large area, or high-volume, fabrication. However, this has minimal effects on applications such as rapid prototyping for nanoscale devices where wafer-scale mass production is not required. The area on a sample surface that can be exposed without stage movements tends to be smaller for FIB lithography than EBL; however, this can be conquered by good alignment techniques that enable the stitching of write fields to produce the complete pattern. Key parameters, such as resolution, throughput and cost of the instrument for several common nanolithographic techniques are presented in Table 2.2. Some generic issues are often associated with the resist-based lithography techniques. The throughput is often limited by the brightness of the source, and the source needs to be of high monochromaticity to achieve a high resolution. Furthermore, high stability of the system is essential to ensure the linearity of the delivered dose during the exposure time. In terms of optical lithography, photon sources need to be of shorter wavelength to meet demands for higher resolution.

Technique	Photolithography	EBL (Direct-write)	FIB lithography	NIL
Resolution	a few tens of nanometers to a few microns	< 5 nm	~20 nm with a minimal lateral dimension of 5 nm	6 – 40 nm
Throughput [a]	very high, 60-80 wafers/hr	Very low, 1 chip/8 hrs	Very low	High, > 5 wafers/hr
Instrument Cost [b]	$ 10^7	$ 10^6	$ 10^6	$ 10^5
Applications	Commercial production and advanced electronics	Masks and IC production, rapid prototyping, R&D	Rapid prototyping, R&D	Bio-sensors, nanowires, bio-electronics

[a] Highly dependent on feature size for many techniques. Here we quote approximate numbers for features at the technique resolution.
[b] Approximate cost for basic state-of-the-art instrument, where available. This does not include the usage costs such as masks which can be significant and even dominant in a manufacturing mode.

Table 2.2: The comparison of the major nanolithography techniques. All numbers quoted are approximate and highly configuration/application dependent. [8], [25]

The helium ion microscope, introduced by Carl Zeiss SMT, Inc. in 2006, based on GFIS technology, is a new entry into the field of FIB lithography [23], [26]. It produces a sub-nanometer ion beam probe, which can be used for high-resolution, high pattern-density nanolithography, as well as for imaging. Reported state-of-the-art helium ion beam lithography performance is comparable to the

best EBL achievements [27], but with a one to two orders of magnitude higher sensitivity. Being the workhorse of nanoscale lithography, EBL has benefited from not only the high brightness of the Schottky source of electrons, but also decades of incremental innovation and engineering of apparatus around the source. HIBL techniques are, on the other hand, in their infancy but showing great potential. The success of the HIM in lithography encourages extensions of this technology to produce beams of other ion species. For example, sub-20-nm-pitch features have been demonstrated with neon ion beam lithography [28], [29].

In the following sections, the working principles of the helium ion beam system as well as the unique properties of the ion-solid interactions in HIBL will be described. Analysis of the key features that enable high-resolution nanofabrication will also be presented.

2.2 Helium Ion Beam System

2.2.1 Helium Ion Microscope

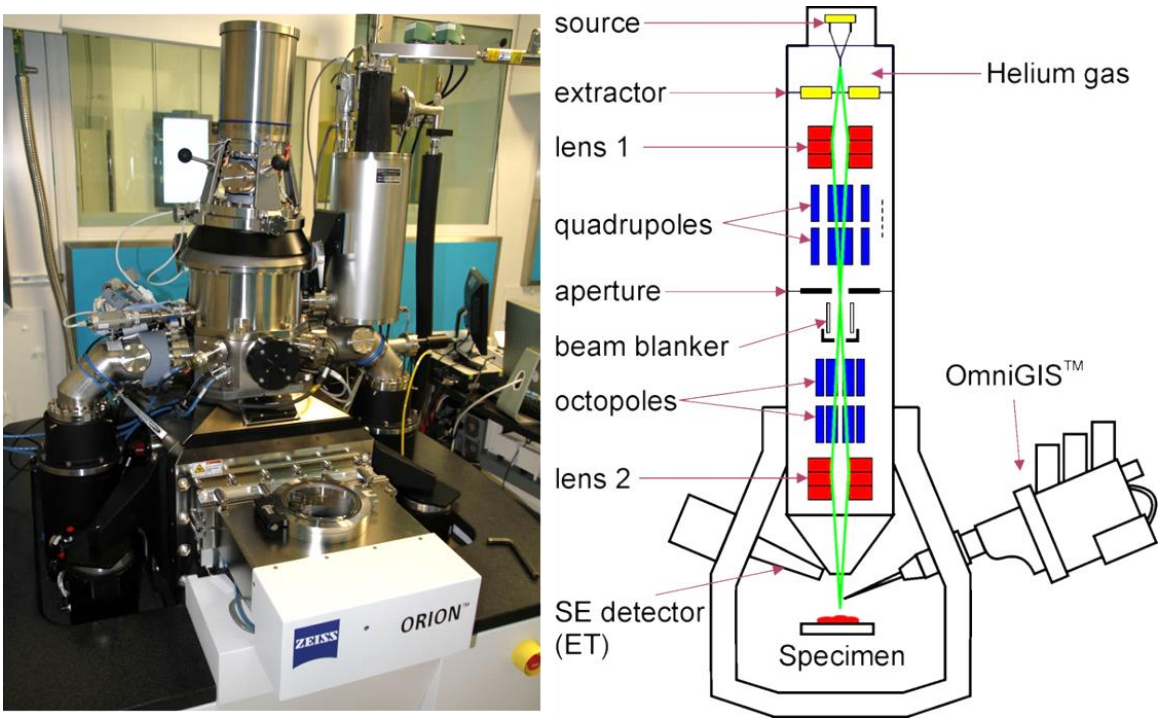

Figure 2.3: (a) Helium ion microscope (Orion™ Plus, Carl Zeiss) at SNC; (b) Schematic of a helium ion beam system, showing the ion source, column, optics, and sample chamber. [30]

A focused helium ion beam system consists of three main components: a source, a column and a sample chamber (Figure 2.3). The ion source is a tungsten electrode at a high voltage relative to ground. Helium gas is ionised by the strong field near the tip of the source. The helium ions (He^+)

are accelerated down the column that contains various electrostatic optics, deflectors, and apertures used to focus and steer the ion beam onto a sample in the chamber. An aperture is a disk with a central orifice that only allows the centre of the beam to pass through, and the focusing lenses produce electric fields whose lines of force drive the outermost particles toward the centre and converges the beam. A blanker is included to steer the beam into a fixture called Faraday cup. This not only prevents the beam from exiting the column, but also measures the beam current. To avoid interference from other gas particles in the generation/manipulation of the helium ion beam, the source and the column operate under high vacuums ranging from 10^{-9} to 10^{-10} Torr. The sample chamber is also maintained at high vacuum of typically ~10^{-7} Torr and it houses a gas injection system, a flood gun and several particle detectors to collect emitted SEs and backscattered ions from the sample surface.

The primary detector used in HIM for imaging for this PhD is the Everhart Thornley (ET) Secondary Electron Detector, which is also the standard detector used in SEMs. It consists of a positively-biased collection grid which attracts SEs, emitted from the sample surface as a result of excitation by the He^+ beam, onto a scintillator. The electrons cause photons to be emitted by the scintillator, which then travel down a light pipe and into a photomultiplier. This produces and amplifies an electrical current by photocathode emission and cascading electron-multiplication, which becomes the video signal feed to the scan and acquisition system. The ET detector produces electric signals with magnitudes proportional to the number of detected particles from the point where the beam is dwelling on the sample. These signals at each point are converted to digital brightness values based on a relative grey scale, varying from black (000) to white (255). The brightness values are stored one point after another; hence, the image is formed pixel-by-pixel. The stored image is displayed on a computer screen based on both their location and brightness information. Due to the size difference between the actual specimen and a screen, a high magnification with factors in the order of 1,000,000 can be achieved. The octopole deflector coils in the column controls and directs the beam to either follow a raster-style scan over an area on the sample surface, or in a defined pattern for other purposes including lithography.

2.2.2 The Gas Field Ion Source

The ultimate probe size of an EBL system is around 1 nm and it is limited by diffraction and chromatic aberration. In comparison, the helium ion beam system has a smaller, sub-nanometer probe size, enabled by the extremely bright GFIS [23], [26]. GFIS technology has been investigated and developed over many years for imaging applications [31]. However, it is only recently that a stable ion source with a high brightness, small virtual source size and small energy spread has been realised, enabling the focused helium ion beam technique [32], [33].

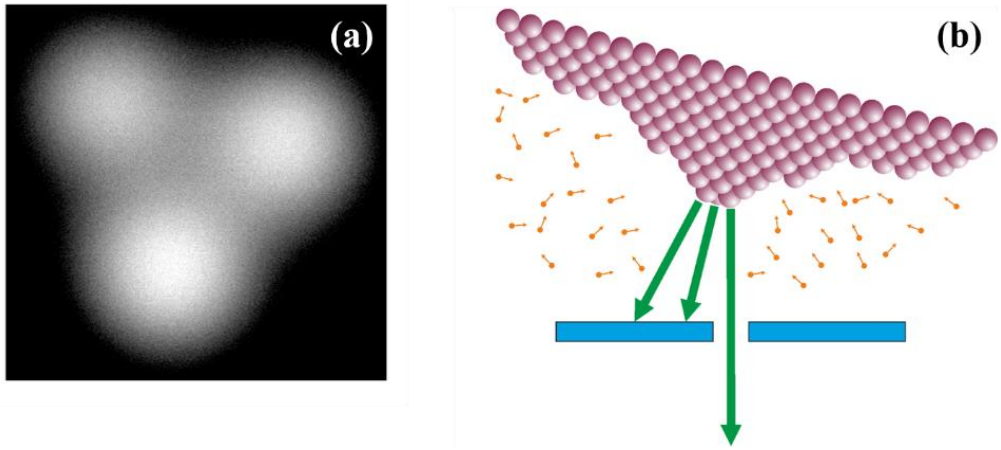

Figure 2.4: (a) Image of the trimer containing three atoms at the top of the pyramid of a tungsten pin where ionisation occurs, and three beams of helium ions are generated; (b) GIFS emitter tip region. Neutral helium atoms (orange) are ionised at the emitter forming three beams of helium ions (green). They are accelerated away from the tip and one of them is aligned to the axis of the column and focused on the sample in the chamber. [30]

The GFIS is based on a needle-shaped tungsten electrode called the emitter. The emitter has an atomically sharp tip (Figure 2.4a) and it is kept in a vacuum chamber under cryogenic conditions. When a high voltage (typically ~30 keV) is applied to the source, an electric field is created between the emitter and an adjacent grounded electrode. A very large electric field is concentrated at the individual atoms of the emitter tip. The helium gas is released close to the emitter tip at a pressure of ~5×10^{-6} Torr. Electrons from the helium atoms that drift into the ionisation zones surrounding the tungsten atoms will escape due to a quantum-mechanical tunnelling effect, producing positive ions by field ionisation. These are repelled from the source, pass through the extractor plate and are accelerated down the column in a continuous beam of helium ions. The success of the helium GFIS is attributed to the very high electric field strength that is required to ionise the helium gas atoms into ions. The value is 4.4 V/Å which is considerately greater than that of other noble or common gases such as Ne at 3.45 4V/Å, Ar at 1.9 4V/Å and H_2 at 1.88. [28] Under normal operating conditions, the apex of the ion source will reach exactly 4.4 V/Å, which only permits the ionisation of helium at the apex. This high electric field strength prevents most other gas atoms from reaching the emitter surface, since they would be field ionised and accelerated away at a lower field strength.

For a GFIS, there are normally only three atoms at the very tip of the source emitter, hence, the source is also called a trimer. Three ion beams are produced by these atoms, only one of which is aligned to the column optics and used to probe the specimen (see Figure 2.4b). The resulting beam is extremely narrow due to the atomic scale source and is ideal as a high-resolution probe. Most of the helium gas is ionised at one of the three atoms that form the trimer, resulting in sufficient beam

current for lithographic applications. Typically, a beam current of 0.1–10 pA can be generated under standard operating conditions.

Virtual source size (estimated)	≤ 0.25 nm
Angular intensity (measured)	0.5-1 μAsr^{-1}
Brightness (calculated)	~1 × 10^{9} Acm^{-2}sr^{-1}
Energy spread (measured)	<1 eV
Beam convergence angle	<1 mrad

Table 2.3: Typical parameters for the source of the helium ion beam system [34], [35].

Some critical source parameters in a GFIS based helium ion beam system are listed in Table 2.3. Virtual source size is the dimension of the smallest circular spot that the particle beam emitted from the source would form, if it were projected back into the interior of the source. The virtual source size is estimated to be 0.25 nm in diameter [26]. The source brightness is calculated to be roughly 30 times better than a Schottky electron source in an EBL system [23]. The very small energy spread of < 1 eV of the GFIS limits the detrimental effects of chromatic aberration on probe size.

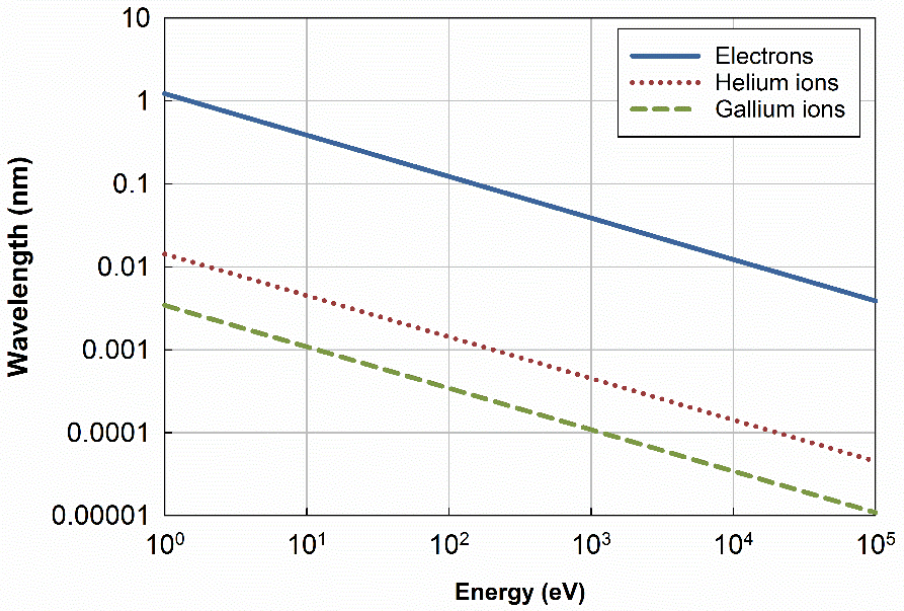

Figure 2.5: Comparison of the wavelength of particles as a function of their energy, revealing a two orders of magnitude difference between helium ions and electrons. [30]

Another contributing factor to the smaller probe size generated in HIBL is the use of heavier He^+ ions compared to the electrons (by three orders of magnitude). The higher mass gives the moving helium ions a momentum that is ~300 times larger than for an electron beam, and hence a de Broglie wavelength that is ~300 times smaller (see Figure 2.5). The shorter the wavelength, the less diffracted the He^+ ion beam will become while passing through the focusing aperture in the column. Hence, smaller apertures (less than 10-µm diameter) can be used in the helium ion beam system enabling a smaller probe size compared to EBL.

To maximise the performance of the source, the system is operated at the best imaging voltage (BIV) at around 30 keV for the helium ion beam system. BIV is defined as the voltage that allows the maximum emission current from the three atoms of the trimer.

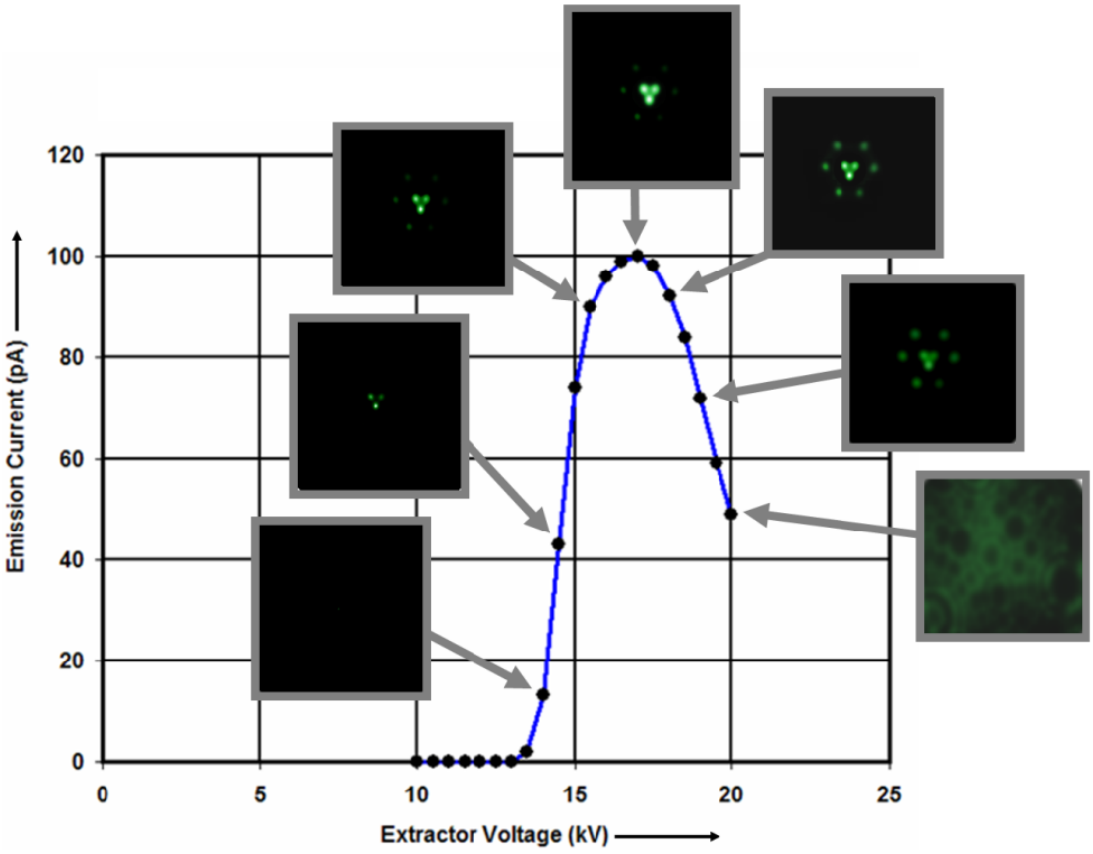

Figure 2.6: The curve of emission of current against the extractor voltage reveals at best imaging voltage the emission is the highest; Insets show the brightness of the trimer under various voltages. [36]

The emission current is plotted against the extractor voltage in Figure 2.6, revealing that the current peaks at a specific voltage i.e. BIV. The corresponding trimers captured at different voltages are shown in the insets along the curve. It can be observed that at BIV, the trimer is the brightest whilst

surrounding atoms are dim. This means that most of helium atoms are ionised by the three atoms, leading to a sharp but powerful beam. Below BIV, the probability of helium ionisation is low and results in a small overall current and an unstable signal. Above BIV, the trimer becomes dimmer, this is because the surrounding atoms gain sufficient electric field and become capable of ionizing the helium atoms. Since only the He^+ ions generated at the trimer contributes to the beam current, the more helium atoms are ionised at non-trimer atoms, the smaller the emission current.

In summary, the shorter wavelength of the imaging helium ion beam along with the ultra-high-brightness GFIS, with a small energy spread makes the helium ion beam system well-suited for producing a high-quality beam that can be focused down to a sub-nanometer probe on the surface of a sample.

2.3 Ion-Solid Interaction

2.3.1 Interaction Volume

Having a small beam spot size is the first step in achieving sub-nanometer resolution imaging and patterning. Another key element is the unique interaction of the primary energetic He^+ ions with the target at and just below the surface. When a particle beam dwells on a sample surface, a chain of reactions happens, not only at the initial point of impact from the incident beam, but also quite widely and deeply into the material (see Figure 2.7). The incident particles lose energy in two ways as they travel through the sample: (1), nuclear stopping via momentum transfer to the target atom nuclei and (2), electronic stopping via interaction with the target electrons [37]. Nuclear stopping depends on the ion velocity as well as the charges of two colliding atoms, whereas electronic stopping is determined mainly by the charge state of the ion and its velocity.

For high-energy ions (in the keV to MeV range), electronic excitation and ionisation occur during electronic stopping [38] and this dominates at the start of the ion track. Energy loss through nuclear interactions dominates near the end of the ion track, creating backscattered ions. They are ions reflected in the general direction from which they came and this effect is called backscattering. These backscattered ions also lose energy in the same ways as the primary ones, forming a collision cascade. In the first 10 to 100 nanometers from the surface, energetic He^+ ions mainly lose their energy through inelastic collisions where electronic stopping dominates. SEs are generated during this process and they are the most abundant and useful particles generated during the beam sample interaction. The number of yielded SEs at a dwelling point is linked to the composition of the material, but mainly depends on the incident angle. On the contrary, the amount of backscattered beam particles is mostly decided by the material composition. There is a general trend for backscattering

yield to rise with the atomic number of the targeted material, but it exhibits non-monotonic oscillation with several local peaks at various materials [39], [40].

Compared to electrons at the same energy, 30-keV He^+ ions lose about 50 to 100 times more energy traversing a thin resist layer [41]. Abundant low-energy SEs—with energies typically below 20 eV—are created, which have short mean free paths of the order of a few nanometers [42], [43]. These are localised close to the beam path and cause insignificant lateral straggle at the surface. As He^+ ions penetrate through the target, nuclear stopping becomes dominant, creating recoils and causing greater lateral straggle far below the target surface.

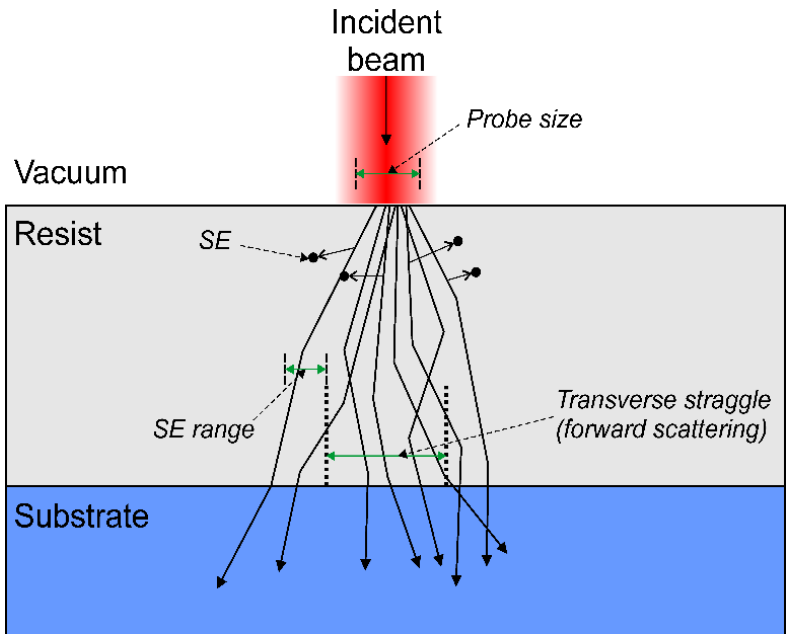

Figure 2.7: Schematic of the interactions of primary energetic He+ ion beam with a resist layer on silicon substrate, showing the production of secondary electrons, which is the main driver for the resist exposure. Three factors limiting the lithographic resolution are the spot size of the beam, ion scattering, and secondary electron emission.

The finite volume excited and affected within the sample by the primary beam is called the interaction volume. Its shape and size are usually determined by factors such as charged particle species, the angle and landing energy of the incident beam, and the sample material composition (mass and density). The interaction volume provides strong indications of the subsequent generation of SEs and hence ultimately determines the performance of a lithographic technique. A smaller interaction volume results in SEs generated from a small area localised around the incident beam and allows for higher resolution.

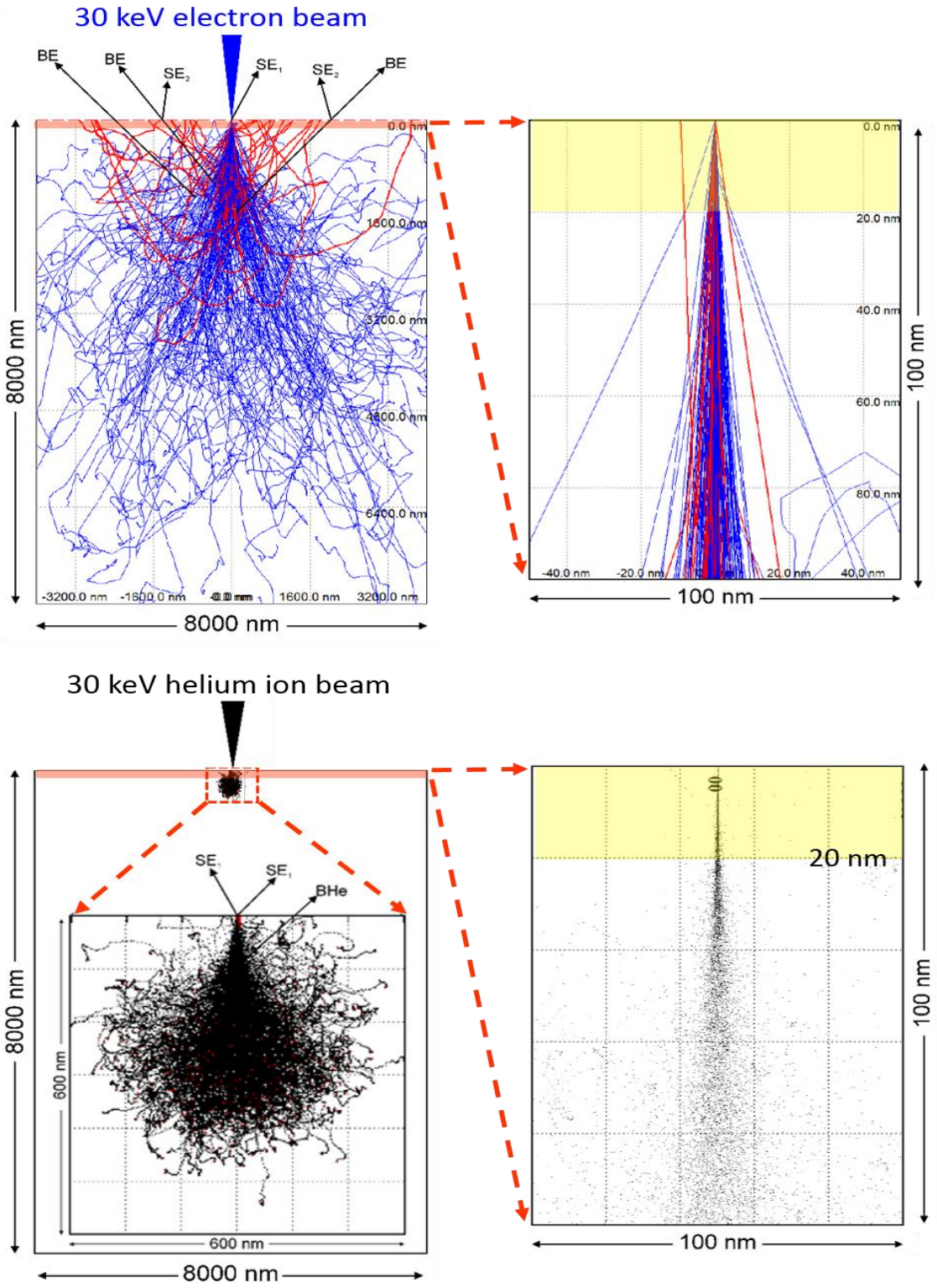

Figure 2.8: Comparison of a 30-keV electron beam (modelled by the Monte Carlo program CASINO 2.48; top) and a 30-keV helium ion beam (modelled by SRIM 2008.04; bottom) into an infinitely thick silicon substrate. The fundamental difference in the size and depth of the interaction volumes for the two beams are demonstrated. BEs are shown in red. The interactions happening in the top 100 nm layer from the initial interfaces are zoomed in and presented on the right for both beams. [30]

A good way of visualizing the interaction volume is by modelling the trajectories of charged particles in the sample. Figure 2.8 illustrates a comparison of modelled trajectories of incident and BEs and ions using Monte Carlo simulations (CASINO for EBL and The Stopping and Range of Ions in Matter software package (SRIM) for HIBL). The SE_1 SEs are excited directly by the primary beam, and SE_2 by scattered ions/electrons exiting the surface. For both simulations, the particle beams have an energy of 30 keV and expose an infinitely thick silicon sample at an incident angle normal to the surface. A much smaller interaction volume is evident in the helium ion beam case (Figure 2.8 top left) compared to the e-beam simulation (Figure 2.8 bottom left). On entering the sample, helium ions are lighter than most sample nuclei, whilst much heavier than electrons, leading to weak deflection from their original direction and a low number of ion recoil events. Therefore, the ion trajectories tend not to alter significantly— helium ions stay collimated whilst penetrating deeply into the sample before starting to disperse. The low ion backscattering fraction from the substrate back into resist layer is especially favourable in lithography, leading to a reduced proximity effect compared to EBL [44], and facilitating high density patterning.

Although the estimated smallest spot size can be controlled down to 1 nm in EBL systems, the lateral straggle of the electrons near the surface is significantly wider, due to a large yield of high energy BEs just below the sample surface. They excite further SE_2 and this cascade of electron production over a large volume limits the resolution of EBL. In the lithographic context, additional resist material will be exposed which degrades the pattern fidelity. This relatively large interaction volume limits the resolution in EBL regardless of the probe size. The electron/ion trajectories in the top 100 nm from the initial interface in the silicon sample are zoomed in and illustrated in Figure 2.8 (right). The beam broadening at a depth of 20 nm is only 1 nm for the helium ion beam, compared to 5 nm for the electron beam (measured at the bottom edge of the highlighted area in both graphs).

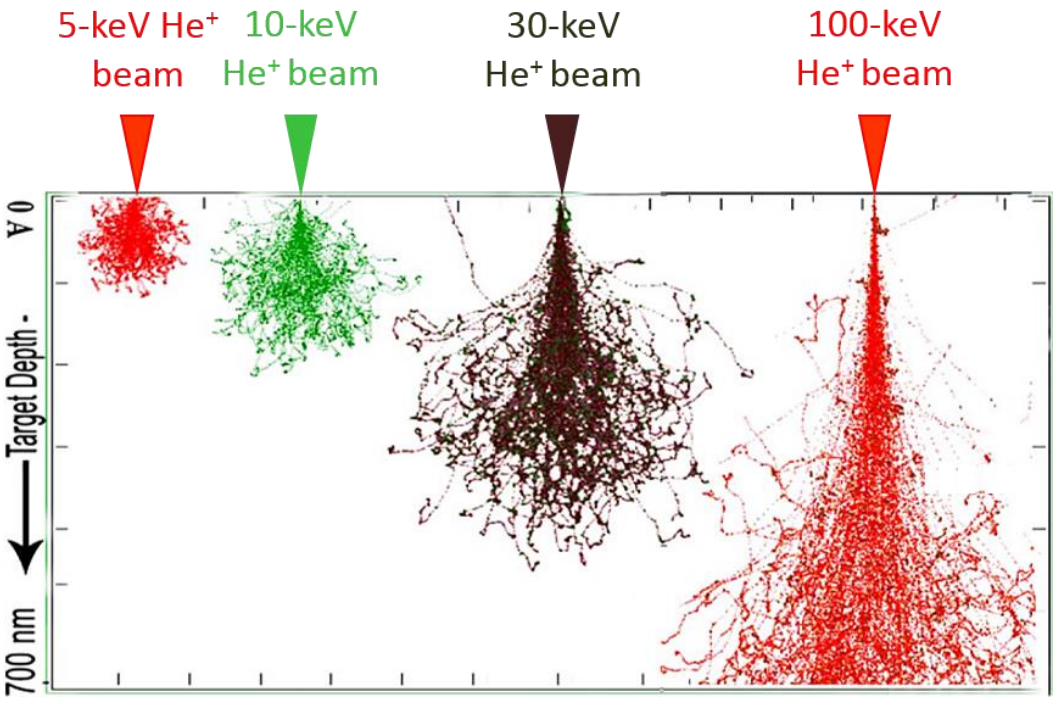

Figure 2.9: Monte Carlo simulations of helium ion beam trajectories at beam energies of 5, 10, 30, and 100 keV in a 700-nm thick bulk silicon. It illustrates that the penetration depth increases as the beam energy increases from left to right, however, a smaller interaction radius is achieved. [45]

Figure 2.9 illustrates the trajectories of helium ion beam at energies of 5, 10, 30 and 100 keV in bulk silicon simulated in the Monte Carlo software. It reveals differences in the resulting interaction volumes under different beam energies. As beam energy increases (from left to right), the beam becomes more directional and collimated along the path in the sample and the ion range increases. The trajectory of the 30-keV helium ion beam This suggests that a smaller interaction radius at the sample surface can be achieved at a high beam energy. Currently, the typical operating voltage for a helium ion source is around 30 keV, but advances in source technology may further improve the resolution by increasing the operating energy.

2.3.2 Secondary Electrons Characteristics

Low-energy SEs are often considered as the most important drivers of the local chemical conversion of resist molecules in lithographic applications. In principle, ion beam lithography follows the same mechanism as EBL, since both primary particles generate low-energy SEs in the resist. All SEs along the He^+ trajectory are relevant if they have sufficient energy for bond-breaking or cross-linking reactions. A He^+ beam generates a much higher SE yield compared to an electron beam. Due to its larger mass, the He^+ ion can transfer only a small fraction of its energy to an electron on collision. This allows the helium ion to excite more electrons before its energy dissipates. On average 2 to 8 SEs are generated by each He^+, substantially higher than the 0.5 to 1.25 per incident electron in EBL

[23], [36]. For imaging, the large SE yield enhances the signal-to-noise ratio (SNR) and forms information rich images. It has been shown that different materials generate considerably different numbers of SEs on exposure to He^+ [23], this property allows superb material contrast when imaging different materials using the HIM. More importantly, the large number of SEs makes reactions such as bond-breaking or cross-linking more efficient, resulting in higher resist sensitivities [46].

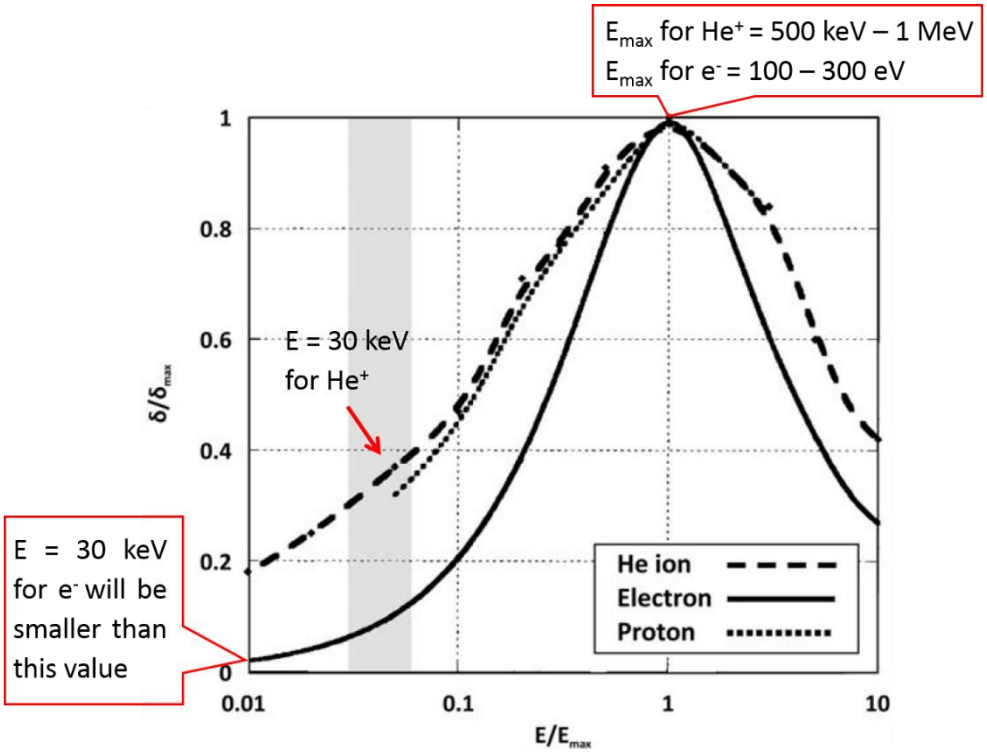

Figure 2.10: Universal yield curves for secondary electrons produced by primary beams of electrons, helium ions and protons. Normalized SE yield is plotted as a function of normalized incident beam energy. The grey area marks the E/E_{max} region for a 30-keV helium ion beam [42].

Ramachandra et al. described a Monte Carlo simulation technique–Ion Induced SE or "IONiSE" – for modelling SE production by ions. Figure 2.10 shows the normalized SE yield as a function of normalized beam energy for electrons, He^+ ions, and protons. The SE yield from the incident helium ions reaches a maximum when the beam energy is between 500 keV and 1 MeV (E_{max} for helium ions), whereas the SE yield from energetic electrons reaches a maximum at a very low beam energy between 100 and 300 eV (E_{max} for electrons) [42]. A beam energy of 30 keV (E for both helium ions and electrons) is widely used in both EBL and HIBL. This gives the helium ion beam an E/E_{max} value of 0.03–0.06 (30 keV/1 MeV to 30 keV/500 keV) which is an equivalent 30 to 40 % of the maximum SE yield (δ/δ_{max} = 0.3–0.4), indicated by the grey box on Figure 2.10. In contrast, the E/E_{max} value for electrons at 30 keV is at 100 to 300 (30 keV/300 eV to 30 keV/100 eV)—far off the right-hand

side of the chart—which results in a much smaller percentage of the maximum SE yield. This suggests that with further helium ion source developments, a higher operating voltage will further enhance the SE yield.

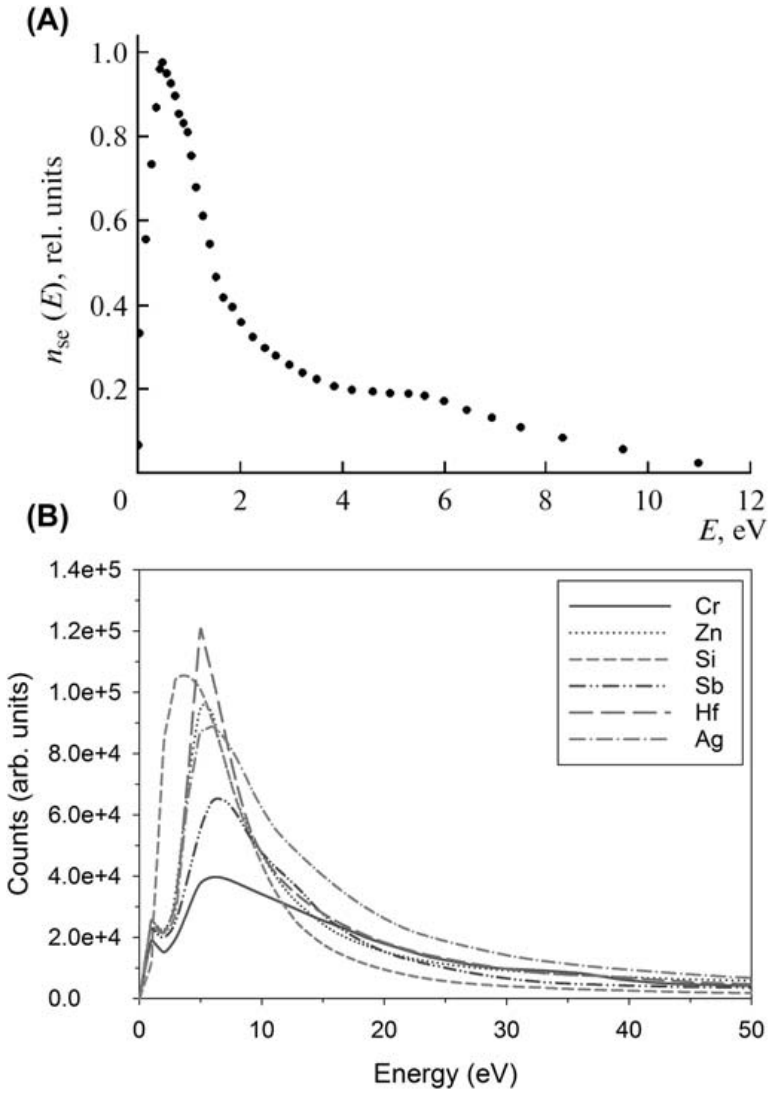

Figure 2.11: (a) Energy distribution of secondary electrons obtained for the Au film upon excitation by a 35-keV helium ion beam, revealing the main fraction of secondary electrons has energy of 2 eV or less; (b) Comparison of energy distribution of SE emitted from various element due to impacts of a 1-keV electron beam [47], [48].

Knowing that more SEs are generated by the helium ion beam than the electron beam, an understanding of the energy profiles of the SEs becomes important. Petrov et al. studied the energy distribution of SEs obtained from a gold sample exposed to 35-keV helium ions. The majority of SEs excited by He^+ ions have an energy of 2 eV or less, and over half of the generated SEs have energies less than 3 eV. Furthermore, the energy distribution peaks at ~1 eV and there are almost no SEs with

energies above 20 eV as shown in Figure 2.11 [42], [43]. It is worth noting that the mean free path of low-energy SEs in most materials is below ten nanometers, meaning only SEs created within a few nanometers from the top surface of a sample can escape [42] and be collected by the ET detector. Hence, these SEs only carry information regarding the surface of the sample, making HIM imaging extremely high surface sensitivity.

In contrast, for e-beam irradiation at a beam energy of 1 keV, there are a large number of SEs at energies ranging from a few eVs to the full primary beam energy and the energy distribution of SEs peaks in the range of 5 to 15 eV as shown in Figure 2.11b. SEs with higher energies travel further than those that have a lower energy, and SEs of more than 100-eV energy are known to have a very long range in resists and cause modifications in a relatively large region around the impact site [49]. This effect contributes greatly towards the proximity effect in EBL and limits pattern fidelity and resolution. The low-energy SEs excited by the helium ion beam makes HIBL favourable for creating ultra-dense patterns due to the consequently reduced proximity effect.

2.3.3 Ion Induced Defects and Sample Damage

Compared to electrons, ions have a much higher momentum and hence can cause greater damage than electrons of the same energy. However, He^+ ions are much lighter than Ga^+ ions, which are used in most FIB systems for material modification. Thus, He^+ ions make weaker ion impacts in the sample and introduce less surface contamination. The primary energetic He^+ ions penetrate deep into the sample due to low ion backscattering and the majority become embedded in the substrate.

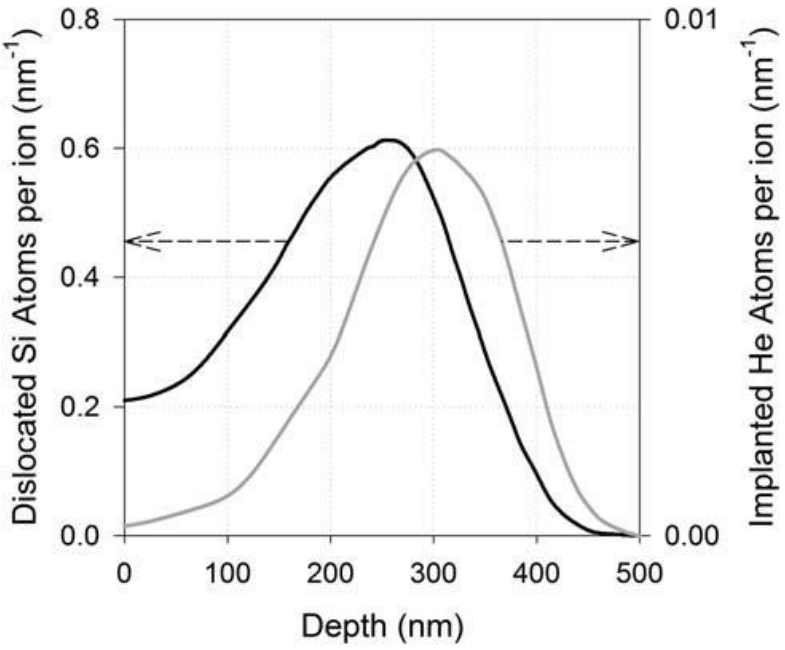

Figure 2.12: The statistical depth distributions of both implanted ions and lattice dislocations from a simulated helium ion beam of 30-keV energy incident on a silicon substrate, based on 1000 ions [50].

The typical penetration depth for 30-keV He^+ ions has been modelled and was found to be on the scale of hundreds of nanometers (see Figure 2.12), whilst common resist thicknesses for high-resolution patterning are of the order of tens of nanometers. When exposure dose is high, a large amount of He^+ ions will accumulate under the target surface. An ion-induced damage zone can be formed, which can subsequently alter the material properties, causing surface swelling, amorphisation and bubble formation [50], [51]. Obviously, this must be avoided when using the ion beam for lithography, and so it is important to understand over what dose range substantial subsurface modification can occur.

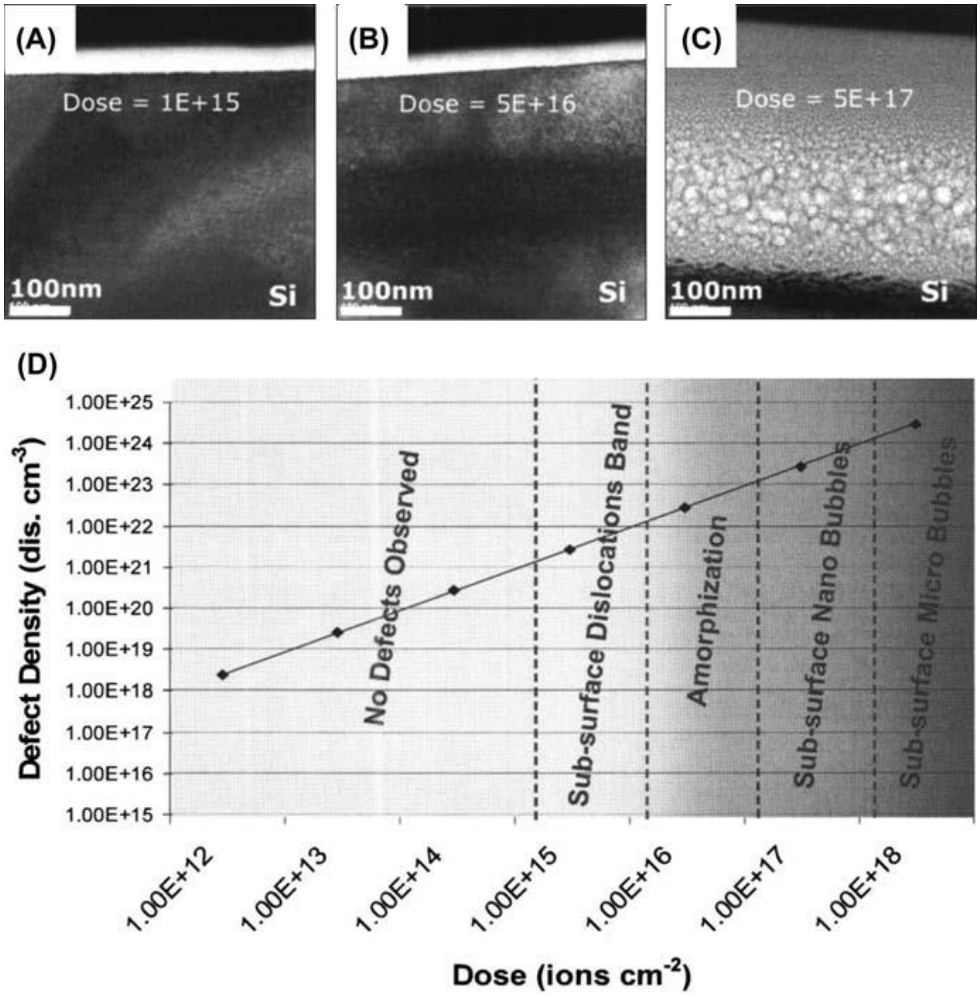

Figure 2.13: Transmission electron microscope images of silicon samples with increasing dose: (a) No defects were detected at a dose of 1 × 10^{15} ions/cm^2; (b) A complete amorphisation occurred in the implant depth of Si with a distinct dislocation band formed close to the ion stopping range at a dose of 5 × 10^{16} ions/cm^2; (c) Nanobubbles were observed in the amorphous Si layer at a dose of 5 × 10^{17} ions/cm^2; (d) Volumetric defect density graph derived from SRIM simulations highlighting the defect density regimes observed in experiments and simulations performed on silicon and copper substrates [50].

The type and degree of damage caused usually depends on the sample, landing energy, and the dose of the ions. Livengood et al. conducted a comparison study of experimental damage volumes with Monte Carlo simulations using the SRIM software package. Figure 2.13a–c show representative transmission electron microscopy (TEM) micrographs of silicon samples after exposure to a 32-keV He^+ ion beam at various doses. No damage was observed apart from some minor modifications at a depth of 30–40 nm from the surface with a dose of 1 × 10^{15} ions/cm^2. A distinct dislocation band was detected 150 to 310 nm beneath the surface when the dose was increased to 5 × 10^{16} ions/cm^2. At a high dose of 5 × 10^{17} ions/cm^2, the silicon becomes completely amorphous and nanobubbles are formed within this region. The diameter of the bubbles ranges from < 1 nm to 30 nm, and the diameter distribution of the nanobubbles follows the He^+ ion distribution in Si. Figure 2.13d shows the

relationship between the damage regimes and the applied ion dose, which is valid for both semiconductor materials such as silicon and metals such as copper [50]. Higher exposure dose causes greater physical damage to the sample. Five dose regions were identified based on the defect levels, suggesting that damage can be controlled as long as a relatively small exposure dose (less than 1×10^{15} ions/cm^2) is applied. Typically, the exposure dose for HIBL is ~10 μC/cm^2, which corresponds to ~6.25×10^{14} ions/cm^2 in Figure 2.13d. Since the corresponding defect density at this dose is below the threshold of any detectable damage by TEM and SEM, the physical damage appears to be limited. The predicted defect density for this dose from Figure 2.13d (~10^{20} cm^{-3}) is similar to that generated during a typical boron implantation [52], which is a routinely used process in semiconductor device fabrication. Annealing is employed to remove damage in this case, so it is likely that the same approach could be used to remove lattice damage following HIBL, although further investigation is required.

2.4 Resist Exposure in Helium Ion Beam Lithography

Breakthroughs into sub-10 nm pattern definition were made in the field of HIBL with the development and commercial release of the HIM based on GFIS technology. In addition to its application in the field of high-resolution imaging, HIM is also an emerging nanofabrication technique that has found many applications in the sub-10 nm regime for ultra-high-resolution and high-density patterning. This has been made possible by the extremely bright source and the unique ion–solid interactions as described in the previous section. HIBL is a promising alternative to well-established EBL, with sensitivity enhancement, higher resolution and reduced proximity effect. However, it follows similar process steps to those in conventional EBL.

Apart from the native raster-scan generator in the HIM, a compatible external pattern generator is often employed to steer and blank the beam in order to form complex patterns during the exposure. A pattern file can be imported, and the beam will trace along the pattern in a serial writing style. Dose variation can be achieved by means of changing beam current, the dwell time, and the pixel spacing of the beam.

Several groups have made breakthroughs into the sub-10 nm patterning regime, using HIBL on the high-resolution HSQ and PMMA resists [27], [53], [54]. The best results achieved in terms of feature size are comparable to the best results in EBL but with a sensitivity improvement of one to two orders of magnitude at the same beam energy. These studies also reveal that HIBL exhibits a lower proximity effect and makes pattern density irrelevant to pattern definition. More recently, a study demonstrated sub-10-nm-pitched dense patterns fabricated with a combination of HIBL and NIL [55]. Another study used HIBL as an alternative approach to EBL for pre-screening extreme ultraviolet

(EUV) resists, resulting in sub-20 nm patterns [56]. The next section will describe the work carried out in this nascent field to date, before evaluating the potential of HIBL as a nanopatterning technique.

2.4.1 Sensitivity

Sensitivity indicates the dose required to produce the chemical reactions in the resist for pattern definition. For positive tone resists, such as PMMA, it is usually defined as the dose that leads to a full clearance of resist; for negative tone resist, such as HSQ, it is often defined as the dose necessary to achieve 50% of the film's original thickness after development.

The sensitivity can be determined from plots of normalized resist thickness vs. applied dose (so called 'dose–response curves'). Likewise, the contrast can also be calculated from the slope of the falling (positive tone) or rising (negative tone) part of the response curve. Figure 2.14 shows dose–response curves for ~70-nm-thick PMMA and HSQ resist layers on silicon substrates obtained after exposure to 30-keV HIBL and EBL. PMMA behaves as a positive tone resist for low dose ranges, and exhibits negative tone behaviour when it is exposed to high doses for both beams (Figure 2.14a) [57], [58]. A reduced layer thickness is observed in the negative tone region and the trend of decreasing thickness continues with increasing dose. This may be caused by shrinkage of the resist under heavy bombardment by energetic particles. A sensitivity enhancement of the HIBL compared to EBL is confirmed in the PMMA experiments with a gain of ~70 in the positive tone region and a gain of ~116 in the negative tone region. The contrast values are 3.7 and 4.7 for positive and negative region respectively. The HSQ sensitivity values (extracted from Figure 2.14b) are 31 and 137 $\mu C/cm^2$ in HIBL and EBL respectively, whilst the contrast values, obtained from the tangent at half-height on the dose response curve, are approximately equal for the two different beams at around 2.1. The results show that He^+ ion exposure is ~4.4 times more effective than electron beam, in exposing HSQ at the same beam energy.

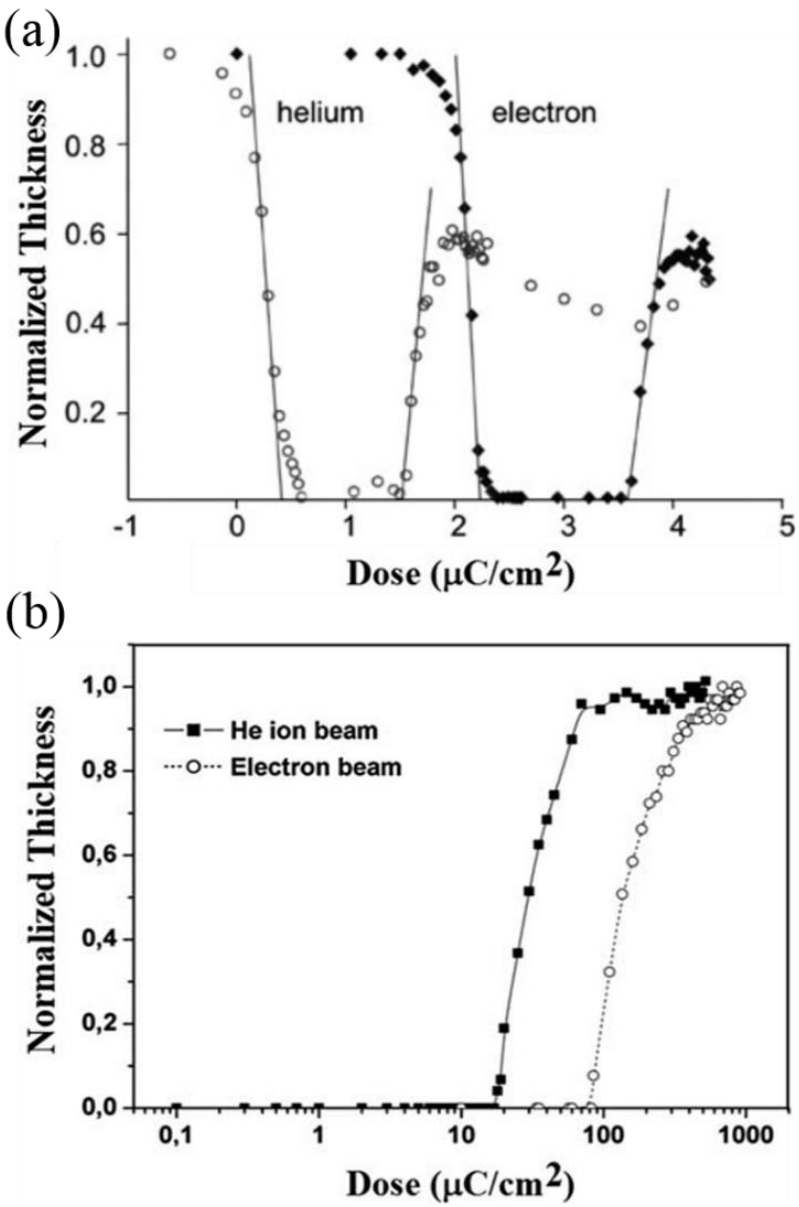

Figure 2.14: Dose response curves of 70 nm (a) PMMA [5] and (b) HSQ [53] on silicon substrate using He+ and e-beam exposures at 30 keV, revealing two orders and one order of magnitude sensitivity enhancement in HIBL compared to EBL, respectively (The electron dose data are scaled down from the measured 100-keV data by a factor of 100/30).

For both resists, HIBL exposure is substantially more efficient than EBL without compromising the resolution, which means that much lower doses are required in HIBL, while a good contrast is obtainable in the formed patterns. This effect is due to a significantly larger low-energy SE yield from the energetic He^+ ions compared to an electron beam of the same energy, which is in agreement with the modelling results from the previous section.

2.4.2 Proximity Effect

The proximity effect is defined as the unintentional exposure of resist surrounding the impact site of the primary incident beam. It is caused by backscattered primary particles and is a common issue in EBL [59]. Simulation results presented in the previous section suggest that the low yield of backscattered helium ions and the subsequent limited generation of SEs by backscattered ions leads to a smaller proximity effect in HIBL compared to EBL. To verify this experimentally, two approaches have been adopted.

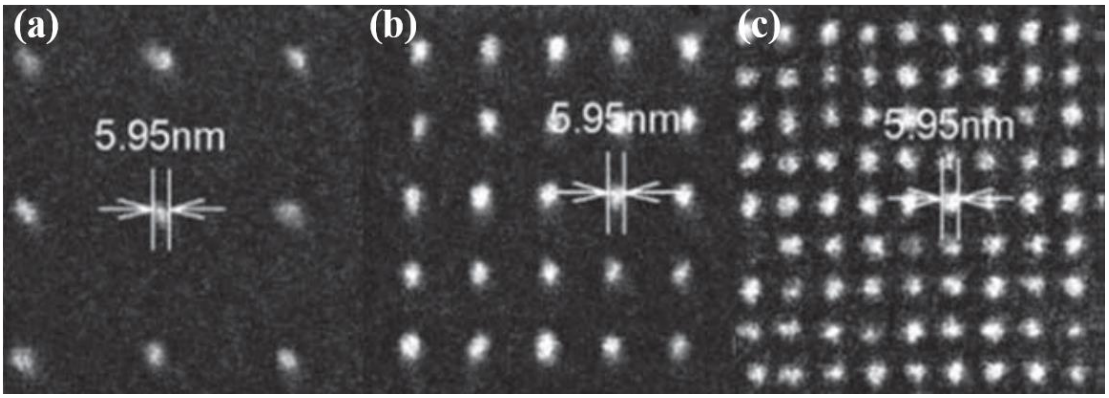

Figure 2.15: SEM images of nanodot arrays with pitches of (a) 48 nm; (b) 24 nm and (c) 14 nm fabricated by a 30-keV helium ion beam on a 5-nm-thick HSQ film on silicon and the average size of the dots for all pitches were measure to be of 6 ±1 nm [53].

The first method is a qualitative approach, which compares individual patterns at different densities. If dimensions and shapes of a specific pattern remain identical regardless of the density, the conclusion is that proximity effect is negligible. Figure 2.15 illustrates sets of nanodots patterned by HIBL at a fixed dose on a 5-nm-thick HSQ resist on silicon from experiments by Sidorkin et al. [53]. The pitches of the dot arrays are 48 nm, 24 nm and 14 nm, respectively. An identical dot size of 6 ±1 nm was achieved for all pitches down to 14 nm. Similar results were achieved in the experiments conducted to fabricate single-pixel line arrays at a fixed dose with pitches from 100 to 15 nm (see Figure 2.16). The line width was found to be 6.5 nm in all pitches down to 15 nm [54]. These results consistently show that the pattern definition does not depend on the pitch, indicating a negligibly small proximity effect in HIBL down to 14-nm-pitch patterning. Very few He^+ ions are backscattered, and the low-energy SEs generated tend not travel far in the resist, leading to very fine features. Beam broadening is also minimised by using a resist layer with a thickness of only 5 nm, however, this ultrathin resist can be impractical when the patterns need to be transferred into a subsequent layer by etching or lift-off.

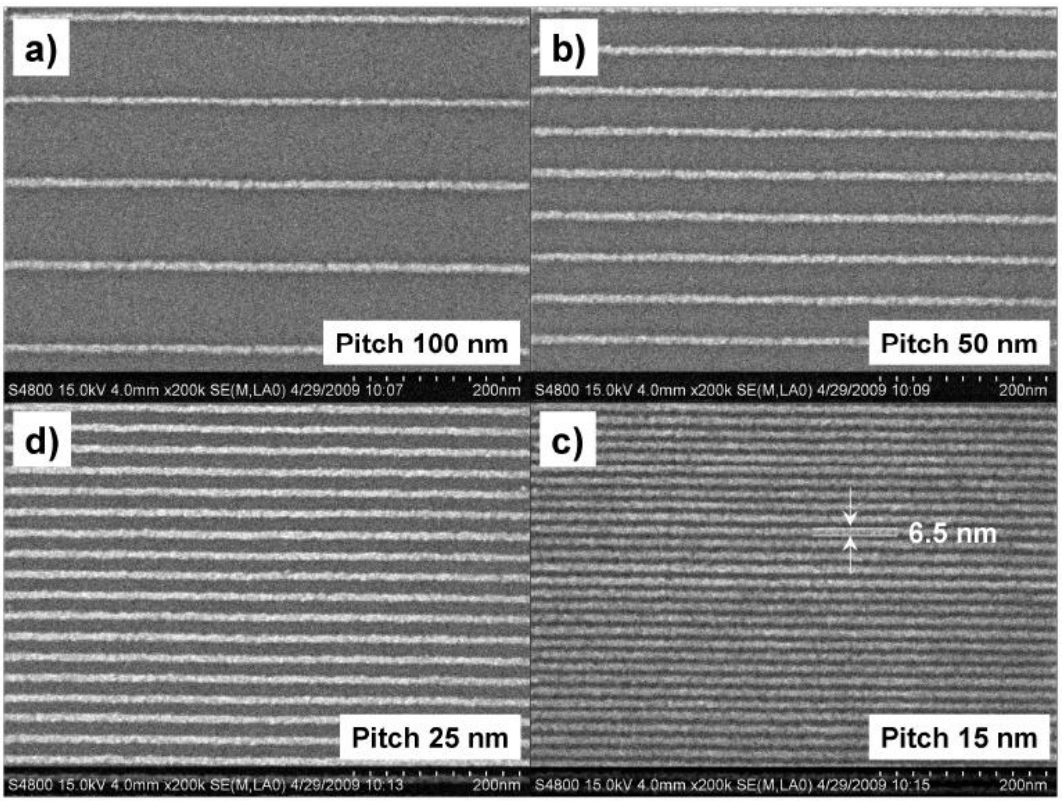

Figure 2.16: SEM images of line arrays with pitches of (a) 100 nm; (b) 50 nm; (c) 25 nm and (d) 15 nm fabricated by a 30-keV helium ion beam on a 5-nm-thick HSQ film on silicon and the average line width for all pitches were measured to be 6.5 ± 1 nm. [54]

Another way of analysing the proximity effect in HIBL is a quantitative approach where experimental results are fitted to the proximity function for determination of the proximity parameters. In EBL, the proximity effect is often analysed using a two-Gaussian approximation function [60] in Equation 2.1:

$$f(r) = \frac{1}{\pi(1+\eta)}\left[\frac{1}{\alpha^2}\, e^{-\left(\frac{r}{\alpha}\right)^2} + \frac{\eta}{\beta^2}\, e^{-\left(\frac{r}{\beta}\right)^2}\right] \qquad (2.1)$$

The proximity parameters α and β represent the range of forward scattered electrons and BEs, respectively, and η is the ratio of energy deposited by the backscattering to the forward scattering component. This formula describes the absorbed dose at a distance r from the primary incident beam due to effects of both forward scattering of the incident focused electron beam in resist and the backscattering of electrons from the substrate. In EBL, α is typically 10–50 nm and β is typically 1–10 μm at a beam energy of 20 – 30 keV [61]–[63].

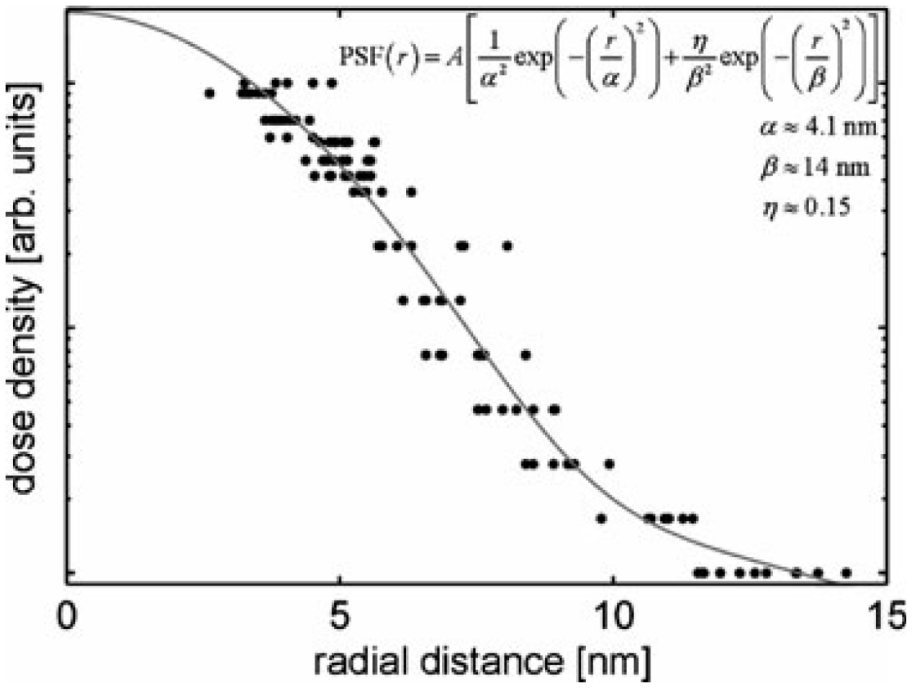

Figure 2.17: Lithographically estimated point-spread function of focused He+ ion beam exposure on 31-nm-thick HSQ resist layer [27].

A finite point-spread function (PSF) of energetic particles causes overlapping exposure dose tails of neighbouring features and when the sum is sufficiently high, unwanted regions between the closely spaced features will be exposed during the lithography process. This process degrades the resolution as well as the pattern density. Winston et al. carried out arrays of point exposures across a large dose range to determine the PSF describing the lithographic behaviour of HIBL. Figure 2.17 presents the results from a 31-nm-thick HSQ resist exposed using 30-keV He^+ beam. It is a semi-logarithmic plot of dose density (proportional to the reciprocal of beam dwell time, e.g., the smaller the dose density, the longer the dwell time, and the higher the delivered dose) versus the measured radius of the fabricated pillar structures. For HIBL, the model parameters obtained are $\alpha \approx 4$ nm and $\beta \approx 14$ nm. Care must be taken when comparing PSF results as they are affected by many parameters including the resist, the exposure tool/process, the pattern development process and metrology. However, the HIBL PSF results indicate a slightly reduced forward scattering range and a much-reduced backscattering range compared to EBL. The forward scattering range matches the simulated helium ion scattering behaviour where the beam broadening is around 2.5 to 3 nm at 30-nm depth in silicon [64]. The backscattering range is in agreement with modelling results from Ramachandra et al [42].

In summary, both approaches to analysing proximity effect suggest that it is significantly smaller in HIBL compared to EBL at 30 keV. This advantage enables HIBL to achieve high-resolution and high-density patterning without applying complex and costly PEC.

2.4.3 High Resolution Patterning

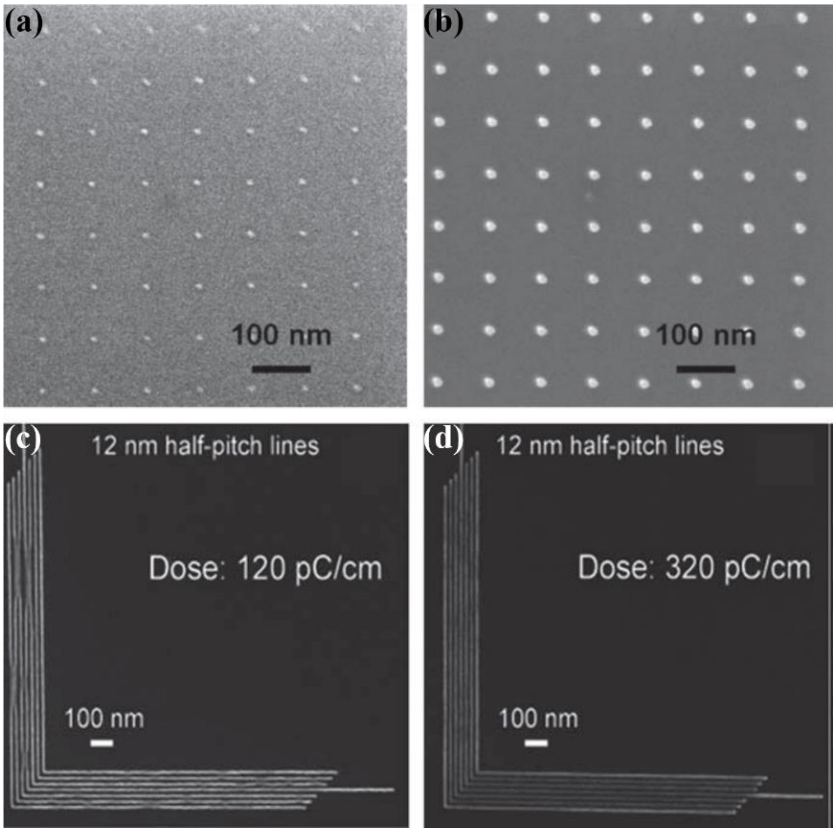

Figure 2.18: SEM images of dot arrays written in (a) 5-nm and (b) 55-nm-thick HSQ layers at 98-nm pitch using HIBL. The averaged dot diameters are (a) 6 ± 1 nm and (b) 14 ± 1 nm [53]; SEM images of 12 nm hp nested L shapes patterned in HSQ layer by HIBL at doses of (c) 120 pC/cm and (d) 320 pC/cm illustrating a broad dose window in HIBL [55].

Higher resolution feature definition with HIBL, at sub-10 nm scales, has been demonstrated by several groups using HSQ resist. One study looked at the effect of HSQ resist thickness on ultimate feature size limits. Sparsely placed dot arrays were patterned in HSQ resists with identical helium ion beam exposures and subsequent development processes, the only variance being the resist thickness (Figure 2.18a and b) [53]. The results reveal that the average size of dots for the 55-nm-thick HSQ (Figure 2.18a) is 14 nm, which is more than twice the average size of 6 nm achieved on the 5-nm-thick HSQ (Figure 2.18b). The thicker the resist, the more scattering the beam will undergo and therefore the broader the exposed feature will be. This result shows that the resist layer thickness is an important parameter in high-resolution lithography and suggests that a thin resist with thickness less than or equal to the escape depth of the SEs may enhance the lithographic results in the sub-nanometer regime.

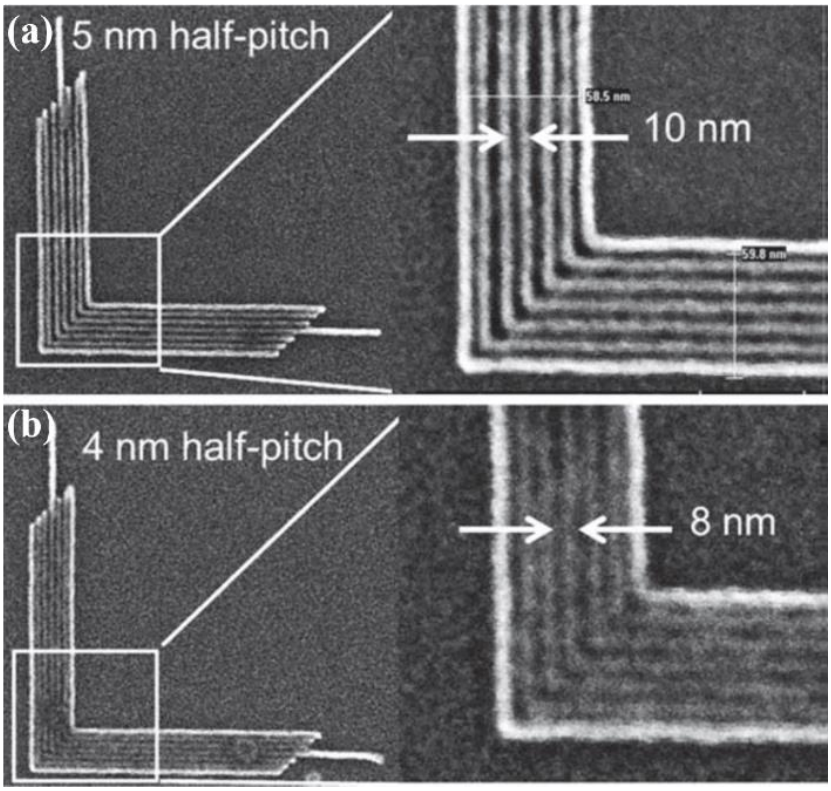

Figure 2.19: SEM images of (a) 5-nm and (b) 4-nm HP nested L's formed by HIBL in an HSQ layer. Both features were clearly resolved demonstrating high resolution patterning capabilities [55].

Results from a different study on HIBL with HSQ by Li et al. are presented in Figure 2.18c and d and demonstrate the wide dose window for HIBL high-resolution patterning: 12 nm hp nested L shapes were patterned in 12-nm-thick HSQ on silicon using line doses of 120 and 320 pC/cm [55]. Both doses resulted in well-defined line features with similar qualities. This relatively large process window increases the reproducibility of the high-resolution patterns. This study also included fabrication of clearly resolved 5 nm hp lines with no resist residuals between features and resolvable 4-nm hp lines with clear contrast but resist residues (Figure 2.19). The optimal line doses were 110 and 90 pC/cm, respectively. This line dose is an order of magnitude lower than the dose required for HSQ in EBL for the fabrication of similar features [65]. These findings on sensitivity and resolution are consistent with the results obtained from the high-resolution investigations by Winston et al. and Sidorkin et al [27], [54]. Moreover, the 4 nm hp lines provided, for the first time, experimental evidence of HIBL exceeding the highest reported EBL resolution to date, which is a 4.5-nm hp [12].

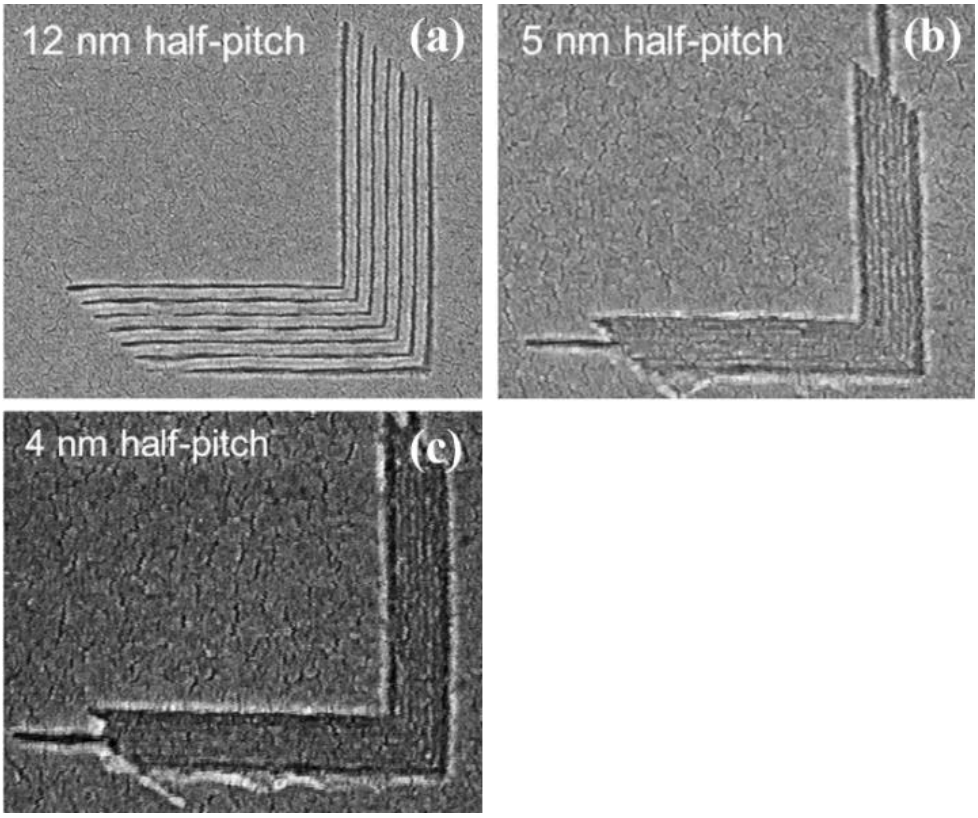

Figure 2.20: SEM images of nanoimprinted nested L's from a HIBL written master to create depressions in a layer of imprint resist. The half-pitches are (a) 12 nm, (b) 5 nm and (c) 4 nm and features were resolved for all pitches. [55]

Li et al. went on to demonstrate successful transfer of the nested L structures produced by HIBL in HSQ to a UV resist layer via a nanoimprint process as shown in Figure 2.20. This approach is particularly attractive because it takes advantage of the high-resolution capabilities of HIBL to produce sub-10-nm features in resist whilst avoiding the potential issue of subsurface damage and defects induced by the energetic He^+ ion beam. Furthermore, it may be possible to re-use the HIBL-formed nanoimprint master stamps to reproduce patterns many times over at low cost, paving the way toward higher throughput and mass production [55].

2.4.4 Evaluation of EUV Resists

Another promising application of HIBL is in the evaluation of resists for EUVL, where a pattern is projected onto the resist using EUV light via a patterned mask. Due to its parallel nature, the high throughput technique is being developed as a promising next-generation lithography candidate. For the introduction of EUVL, development of high-performance EUV resists is of key importance and involves characterising resist, for instance their sensitivity, resolution and pattern uniformity. Currently, EBL is often used to prescreen EUV resists [66] partly due to its flexible direct-write

approach, which means that no mask is required for complex arbitrary patterns. However, due to its pronounced proximity effect, PEC is often required for high-density pattern definition. As an alternative to EBL, HIBL has a clear advantage of having a greatly reduced proximity effect.

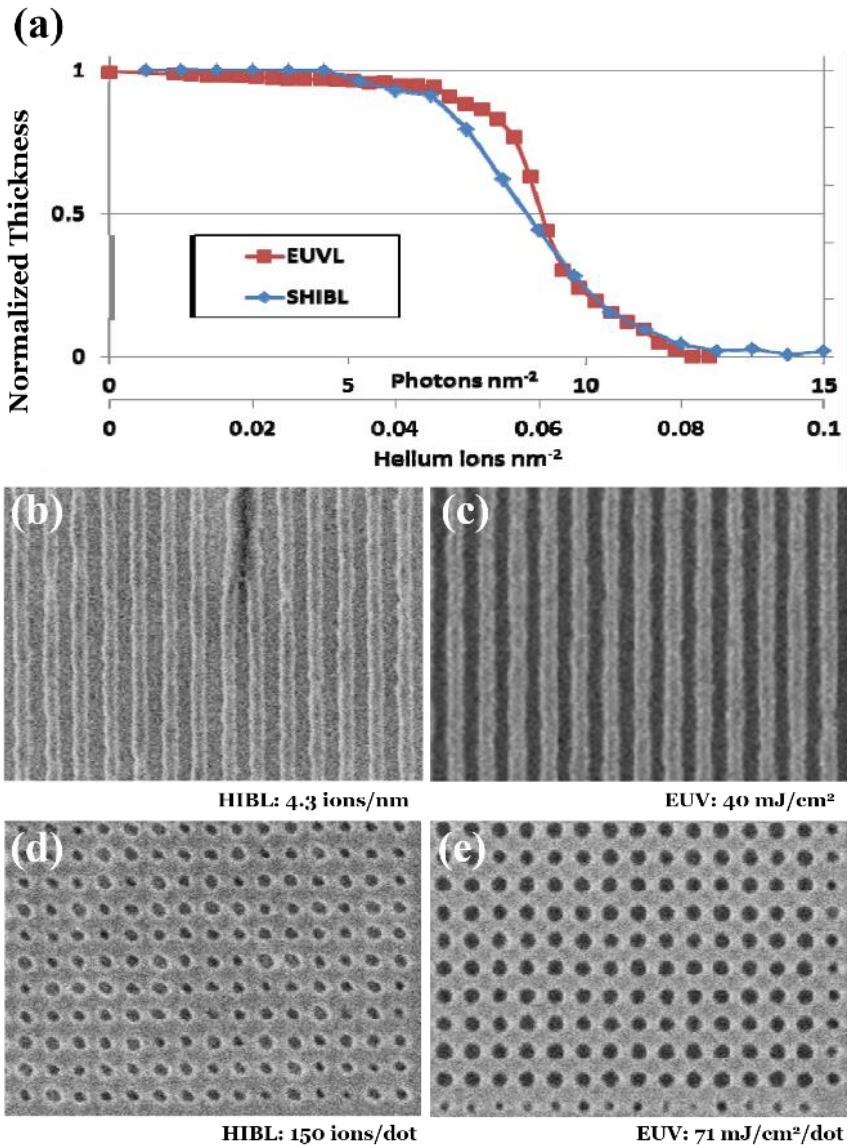

Figure 2.21: (a) Dose response curve for EUV CAR A exposed to 92 eV EUV and 30-keV He ions. The dose-to-clear of EUVL is 12.8 photons/nm^2 (18 mJ/cm^2), the contrast is 3. The dose-to-clear of the resist in HIBL is 0.085 ions/nm^2 (1.36 µC/cm^2, 41 mJ/cm2), the contrast is 2. (b) – (e) SEM images of lines-and-spaces at 40-nm pitch in EUV resist (a) type A exposed with HIBL at; (d) type B exposed with EUV at 5.3 times the dose of 13.5 mJ/cm^2. SEM images of arrays of contact holes at 40-nm pitch in EUV resist (c) type A exposed with HIBL at 150 ions per contact hole dose; (d) type B exposed with EUV at 5.3 times the dose of 13.5 mJ/cm^2. [56]

Maas et al. used 30-keV HIBL to expose chemically amplified EUV resist for sensitivity and resolution characterisation for the application of EUV resist prescreening. Dose–response curves of

chemically amplified EUV resist using 30-keV HIBL and 92-eV EUVL showed highly similar shapes and close contrast values, but with a large difference in the sensitivities as shown in Figure 2.21. Here, the authors have used the quantity of incident energy received in the resist for pattern definition as the dose. The full clearance of the positive tone resist was reached at a dose of 0.085 ions/nm^2 in HIBL and 12.8 photons/nm^2 in EUV, suggesting that a single 30-keV helium ion is as effective as 150 EUV photons. This is mainly because energetic helium ions excite more SEs during inelastic collisions along the trajectory before all energy is dissipated, whilst each EUV photon excites far fewer SE along its path. Arrays of 40-nm-pitched circular holes and lines patterned in HIBL and EUVL were shown to be comparable in resolution, indicating that HIBL could find use as a rapid characterisation and prescreening tool for EUV resists.

2.5 Fullerene Molecular Resist

HIBL has shown great promise for prototyping and fabrication of "beyond CMOS" devices which are defined by innovative new architectures, operating principles, heterogeneous materials, and—most importantly for lithography—scaling to sub–10 nm feature sizes [67]. However, there is another vitally important key to the success of this writing technique, which relies on the performance of the resist material to enable the high-resolution definition of patterns and successful pattern transfer.

HSQ is a popular inorganic negative tone EBL resist for its high resolution and excellent etch resistance [12], [68]. However, its poor reproducibility, for instance the achievable feature size in HSQ is a function of the time between exposure and development, is highly disadvantageous in direct write lithography processes [69]. The effects of delay are exacerbated in a complex manner by patterning conditions, humidity, film thickness, underlayer choice and other factors, making HSQ unsuitable for complex patterning tasks. PMMA is a widely used high-resolution organic resist. Feature sizes of 20 nm can routinely be achieved using EBL with high reproducibility [70]. However, due to its long-chain polymeric composition, PMMA struggles to perform in the sub-10 nm regime and suffers from very low etch durability, making subsequent pattern transfer problematic [71] .

As a result, the development of a suitable HBIL resist that can potentially outperform the current resist options to fully realise HIBL's potential for the single nanometer beyond CMOS regime, becomes pressingly essential. Such a resist should be compatible with standard processing requirements, such as deposition via spin-coating. It should also exhibit reasonable stability and reproducibility with wide environmental tolerance during and after patterning, together with high-resolution capability, high sensitivity and good etch durability. The development of such a resist faces a significant number of challenges, as detailed below.

The maximum aspect ratio (resist film thickness/feature width) is often limited by the critical aspect ratio of collapse (CARC), beyond which extensive pattern collapse will occur in the resist. This is due to unbalanced capillary forces during the drying stage of typical photoresist wet development. Conventionally, a maximum aspect ratio of between 3:1 and 4:1 is achievable. However, this is known to decrease, owing to increased capillary forces as the pitch is reduced [72], falling below 2:1 at a pitch of 60 nm [73]. Furthermore, as the required resist film thickness decreases below 100 nm, interfacial effects become dominant in the film and its elastic modulus decreases drastically from the bulk value [74], which has led to a further reduction in the CARC towards 1:1 [75]. This has forced the adoption of resist films with sub 20-nm thicknesses to address the highest resolutions.

Meanwhile, line edge roughness (LER), defined as the deviation of a real feature from the idealised shape, strongly affects device performance and becomes increasingly detrimental at small feature sizes. LER will tend to increase as the pitch decreases due to material stochastics (e.g. formulation variation), imaging stochastics (e.g. shot noise) [76] and aerial image quality [77]. It has also been shown that, as film thickness is reduced, the LER will tend to increase. This is due both to a reduction in the averaging effect of the film thickness on sidewall roughness and an increase in the importance of the resist-substrate interface area (resist footing) [78], but also due to material stochastics in the film [79]. Therefore, whilst it is necessary to reduce film thickness to avoid pattern collapse and enable ultrahigh-resolution patterning, it is also essential to be mindful of line edge roughness failure modes. Simulations indicate that so-called molecular resist films (utilising small molecule materials rather than polymeric components) are more resistant to LER effects in thin films [80]. However, the task of pattern transfer from such thin materials into semiconductor substrates using traditional plasma etching techniques remains challenging.

In order to enable such etch transfer, it is necessary to provide a resist with an exceptionally high etch durability under typical etchant process gases. One of two empirical models are typically used to predict the etch durability of photoresist materials. The Ohnishi number (*ON*) [81] is given by Equation 2.2:

$$ON = \frac{N}{N_C - N_O} \qquad (2.2)$$

where N is the total number of atoms in a resist molecule, N_C is the number of carbon atoms, and N_O is the number of oxygen atoms. In this model, a low number indicates a high etch durability, i.e. the etch durability of the resist improves when the proportion of carbon increases and the proportion of oxygen decreases. Typically, resist polymers range from a value of 2–3 for the most durable, such as novolac or polyhydroxystyrene (PHS) based resists, to 6–8 for the least durable such as PMMA. The

second model, known as the ring parameter (RP) [82], addresses the experimental observation that aromatic polymers are typically more etch resistant, and is given by Equation 2.3:

$$RP = \frac{M_{ring}}{M_{tot}} \qquad (2.3)$$

where M_{ring} is the mass of carbon in ring structures, and M_{tot} is the total mass of the resist molecule. In this case, a higher value indicates better etch durability, i.e. the more carbon atoms in ring structures, the better etching performance of the resist. PMMA has an *RP* of 0, compared with 0.6 for PHS. A number of more complicated models can be used to examine the details of particular molecular structures [83], but the Ohnishi and Ring models are sufficient to guide general resist design for high etch durability.

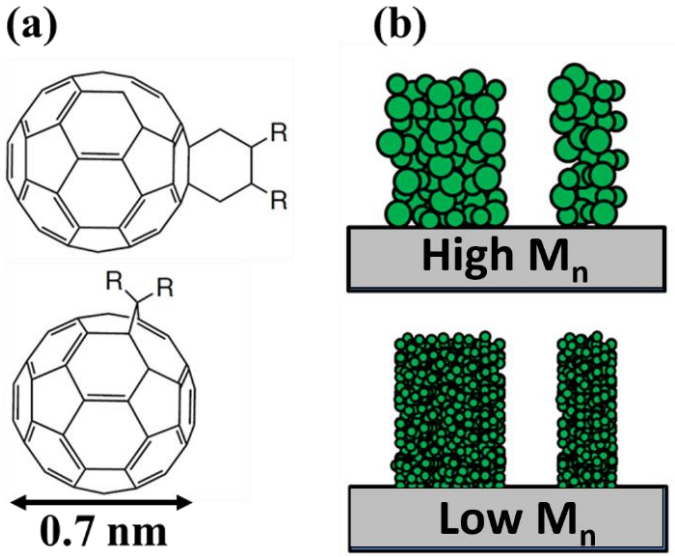

Figure 2.22: (a) Molecular diagram of generic fullerene resists, R represents the attached side chains to the carbon ball; (b) Schematic shows the comparison between patterns formed from a high molecular weight resist and that from a low molecular weight resist after development. [30]

Recent developments in novel molecular resists, such as molecular glasses [84], [85] and fullerene derivatives [86] have attracted great interest in the EBL community due to their small molecular size and therefore high resolution patterning potential. With all the considerations above taken into account, the monoadduct methanofullerene derivative resist stands out as a promising candidate for HIBL patterning. The photopolymerisation of fullerene C_{60} was first demonstrated by Rao et al. and its behaviour as an e-beam resist was described by Tada et al. [87], [88]. The exposure mechanism

for fullerene derivatives is thought to involve fragmentation of the fullerene cage when exposed to the high energy charged particles and the subsequent cross-linking of the remaining material fragments to form an insoluble deposit [89]. With a small molecular size, down to ~0.7 nm, and a molecular weight (M_n) of ~1000 (C_{60} plus the side chains) [88], fullerene resists offer great potential to improve lithographic resolution with a reduced LER (see Figure 2.22).

More recent work has described the development of a new class of negative tone fullerene-based molecular resists. The highest resolutions achieved on chemically amplified fullerene resists using EBL are isolated features with a line width of 13.6 nm as well as 20-nm lines on a 15 nm hp [90], [91], at a sensitivity of <50 μC/cm^2. Higher resolutions have been demonstrated in non-chemically amplified fullerene resists. However, their relatively low sensitivity in EBL, typically at around 200-20,000 μC/cm^2, which is two to four orders of magnitude less than required for commercial resists, limits their applications [92], [93]. HIBL, however, offers high resolution and low proximity effect in sub-20 nm fabrication. High exposure sensitivity (2 orders of magnitude better than that in EBL) has been demonstrated from the previous study on PMMA. Hence, it is believed better performance can be achieved by a combination of HIBL and the molecular resists.

In terms of etching performance, it is self-apparent that the nature of the fullerene molecule itself, with its 60 carbon atoms in a three-dimensional cage or ring structure, gives the maximum possible RP and the minimum possible ON, hence, both indicating that the resist has excellent etching resistance. Non-chemically amplified fullerene derivative resists exhibit an etch durability double that of SAL601 (a high durability commercial resist) and almost eight times than that of silicon in plasma etching [94]. This increased material selectivity is desirable for subsequent pattern transfer in the sub-10 nm regime.

With the properties of high resolution, reduced LER and a high etch resistance, the fullerene derivatives appear to be feasible resist candidates for next-generation lithography. However, fullerene is not easily spin coated due to the extremely low solubility in all solvents. This can be addressed through the derivatisation of the fullerene molecule to enhance the solubility in appropriate spin coating solvents [95]. In Chapter 4 of this report, a detailed study into HIBL with a fullerene-derivative molecular resist is presented, with a focus on resist sensitivity and high resolution, high density patterning.

CHAPTER 3

METHODOLOGY

Most of the experiments and measurements were carried out in the class 100/1000 cleanroom of the Southampton Nanofabrication Centre for this PhD. In this chapter, the methodology developed and adopted for investigating the technique of HIBL is described.

3.1 Sample Cleaning and Resist Spinning

Consistent and standardised sample preparation is vital for achieving high resolution and repeatable lithographic results. In this section, treatments on silicon samples and resists are described and these procedures were followed throughout the HIBL experiments.

Single-side polished 6-inch N type <100> Si wafers with a resistivity of 1-10 Ω/cm in a thickness of 525 μm were obtained. Due to the nature of only being used as the supporting substrate, the parameters such as doping, orientation and thickness are not critical, but these were kept identical in all experiments for consistency. The wafer is initially diced into size of 20 × 20 mm silicon chips for all the samples used in this PhD. Three short grooves, illustrated in Figure 3.1, are made at the backside of each chip by a diamond scriber. This practise prepares for the further cleaving step after the resist spinning and introduces significantly less particulate contamination on the sample surface. Patterning normally takes place near the cleaved edges that were in the centre of the 2 cm by 2 cm chip after the cleaving. The reason for not having 1 cm by 1 cm silicon chips for resist spinning is to avoid the significant resist thickness variation from the centre to the edges, an effect that is more evident in small samples.

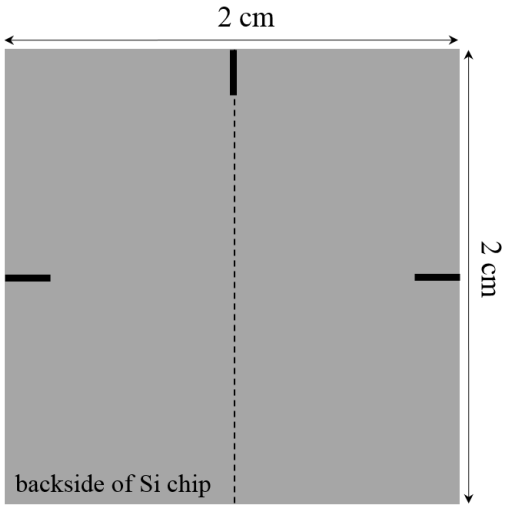

Figure 3.1: Illustration of the backside of a diced silicon substrate of 2 cm by 2 cm in size. The three short black grooves demonstrate where the diamond scribe marks for cleaving (along the dotted line first) after the spinning of the resist.

Semiconductor grade chemicals were used in the cleaning procedures. The silicon chip is rinsed thoroughly in flowing deionised (DI) water and then dipped into a non-metal contaminated, weak 20:1 aqueous solution of hydrofluoric acid (HF) for 2 minutes for the removal of the native silicon dioxide on the surface. Finally, the sample is rinsed in flowing DI water for ~ 1 minute until the power of hydrogen (pH) value is 7 (which is neutral) before being blown dry with nitrogen.

The chips are then immediately transferred to the yellow room, a designated area for photo and EBL processes, for the resist coating. The glass sheet, where the samples are placed on top of, inside the hotplate (Sawatec) is first wiped thoroughly by a clean cloth dampened with isopropyl alcohol (IPA). This is to remove any resist residues from previous processes and to avoid cross contamination. The lid of the machine is left open, and then set to reach and stabilise at the temperature required for the pre-exposure baking process depending on the resists used.

The EMS 6000 Photo Resist Spinner is used to spin layers of resist onto silicon chips. It is controllable through a touch screen interface, and the recipe is fully programmable in terms of spin speed (200-8500 revolutions per minute, rpm), acceleration (1-9999 rpm/s) and duration (1-999 s) for each step (up to 10 steps). Due to its small dimensions, the chip is firstly secured on the sticky side of a 3-inch one-sided piece of sticky tape. The tape is then placed on the chuck in the spinner and held securely by a vacuum. The chip is usually spun without resist being dispensed to check the grip as well as the setting of the recipe. A small amount of resist (~0.1 ml) is then dispensed onto the middle of the sample using a disposable pipette with a bulb sucker. The lid of the spinner is closed before the spin sequence is initiated. Once the rotation has completed, the sample is removed from the spinner, and moved onto the hotplate for the pre-exposure bake.

The lid of the hotplate is closed and remains shut during the bake to allow any released solvent fumes to be extracted safely by the exhaust of the machine. The duration of the baking varies depending on the resist, and when the process is completed, the sample is removed from the hotplate and allowed to cool down to room temperature. Along the scratches made at the backside of Si chip (as shown in Figure 3.1), the sample was cleaved into four 1 cm by 1 cm pieces. On each chip, a 2-mm long groove is gently made by the diamond scriber on the front surface. It is placed in the middle across a fresh cleaved edge, which serves as a location marker during the navigation and provides fine features to be focused on for the final adjusting of the beam before carrying out the patterning. The sample is ready to be mounted onto the sample holder after being blown by nitrogen to remove any dust particles.

3.2 Exposure in the HIM

The helium ion microscope (Orion^{TM} Plus, Zeiss) is operated through the graphical controls implemented in the ALIS System UI (user interface) software provided by Zeiss (Figure 3.2a). This covers both commonly-used operational functions, such as choosing the aperture size, setting the acceleration voltage of the beam, and adjusting the contrast/brightness of the images; it also covers less commonly-used functions for maintenance purposes, such as closing/opening of the pressure valves, purging/pumping down any section of the microscope and carrying out the source build. The most frequently used functions are also accessible via a manual control panel, generally referred to as the knob panel (shown in Figure 3.2b) as shortcuts.

Firstly, the vacuum pressures in the gun (~2×10^{-9} Torr), column (~2.5×10^{-8} Torr) and chamber (~3.5×10^{-7} Torr), and the temperature of the gun (~75 K) are checked to be in the normal ranges. The sample of interest, either the unpatterned resist sample or the patterned sample, is loaded into the HIM along with a calibration sample, which has carbon substrate covered with fine metal tin balls on top (tin-on-carbon). It is conductive and generates an abundance of SEs when bombarded by helium ions, forming information rich images; it also exhibits high contrast difference between the metal and the carbon. Both factors make it easy to optimise the beam whilst imaging. The HIM is equipped with an Evactron (XEI Scientific) plasma cleaner, which provides an optional cleaning procedure for the sample. It removes organic contamination which minimises the chance of hydrocarbon build-up during imaging/nanofabrication processes [96]. The plasma is generated remotely from the sample at a power of 10 W using the O_2 content of the ambient air in the sample chamber, and regulated to 0.5 Torr during the cleaning procedure [97], [98]. Plasma cleaning facilitates higher resolution to be achieved; however, it can cause fine-scale damage to organic materials, such as graphene polymers or biological samples, so the cleaning procedure is not recommended for these samples. [99]

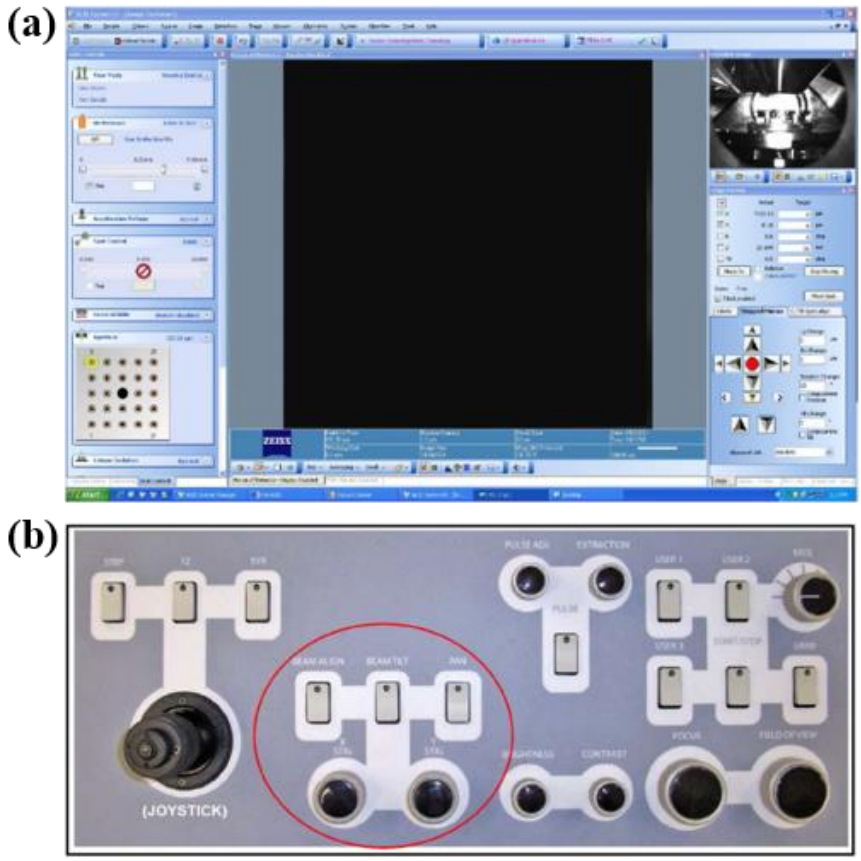

Figure 3.2: (a) Screenshot of the ALIS System UI; (b) HIM knob panel. The buttons and knobs circled in red are used for the alignment adjustments.

Once the sample loading is complete, the stage is moved so that the tin-on-carbon is directly underneath the beam. The presence of the trimer is then checked in the source viewing mode, a high brightness trimer is shown in Figure 3.3a. The operating voltage is then adjusted to the BIV, an optimum operating voltage when the source is the brightest and generates the highest current. The beam current can reach 7-9 pA in the setting of 20-μm aperture, 5×10^{-6} helium pressure, spot control of 4. This is important since it provides sufficient current and high SNR for a wide spectrum of applications in high/low resolution (using any size of the aperture). For each formed trimer the average life span is about a week, and its condition dictates the maximum accelerating voltage (normally between 29 – 33 keV) and beam current. With the trimer aging, both factors deteriorate, and one or more atoms can detach from the source, leaving a dimer or a monomer instead. The source becomes less stable, although the beam current can be higher than that from a trimer. When BIV has dropped below 30 keV, the beam current is smaller than 5 pA, or the trimer has disappeared, a new trimer or a source need to be formed prior to the imaging and nanofabrication processes.

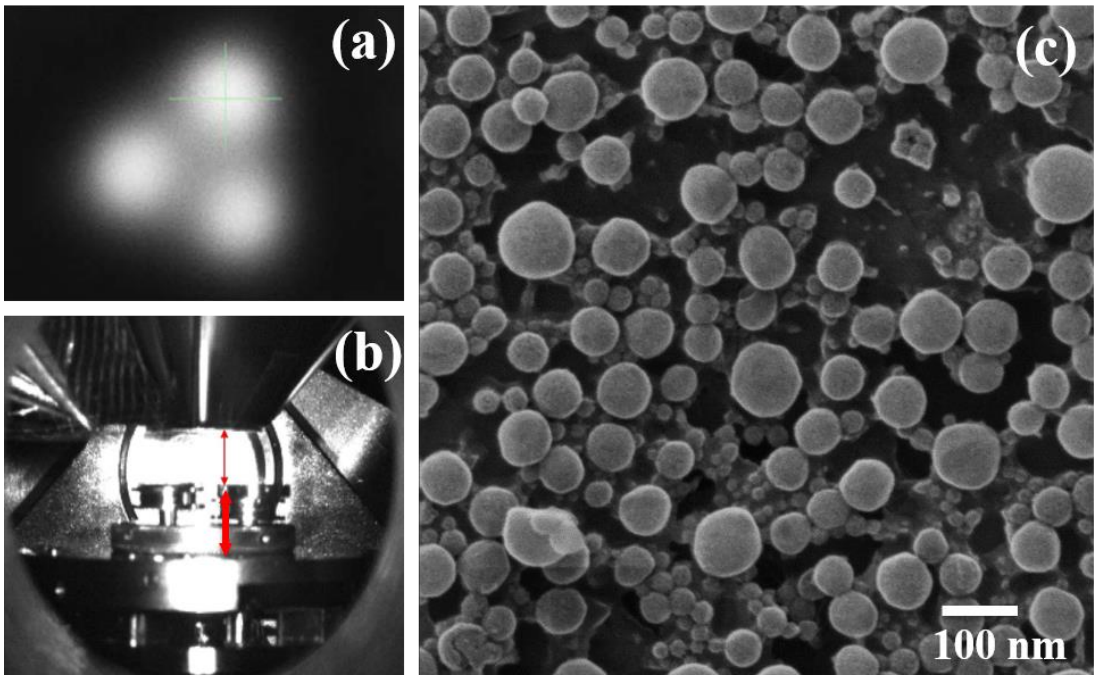

Figure 3.3: (a) Image of the trimer in source viewing mode in UI; (b) Chamber scope of the HIM sample chamber with the working distance marked in red; (c) A high resolution HIM image of tin-on-C sample at BIV.

The loaded sample and part of the column of the HIM are shown in Figure 3.3b, which is an image captured by the chamber scope of the HIM. The maximum height of a sample to be loaded into HIM is 20 mm so that it fits through the loading hatch. The working distance, illustrated by the red arrow, is the distance between the top of the sample surface and the bottom of the pole piece. It can be adjusted by the combination of changing the focus and adjusting the stage vertically. The working distance set between 6 to 8 mm was found to provide the highest resolution.

HIM has a beam energy typically ranging from 10 to 35 keV, and produces a beam current of 0.1 to 10 pA, and raster scans the beam across a sample, exciting the emission of SEs. The aperture and the spot control in the column determine the proportion of the beam that passes through onto the sample, and this value can be measured by the Faraday cup on the sample holder. A bigger aperture results in a larger field of view (FOV) and is useful during the initial navigation around the sample. Images produced also exhibit a greater SNR as the current is increased, however, for a long dwell time at high magnification, the higher beam current can lead to material removal and feature shrinkage [100]. When the sample is not a good conductor, the locally accumulated positively-charged helium ions can cause charging effects, which may alter the generated SE signal and result in a darker image. Using a smaller aperture increases the resolution and the depth of field, however, the compromise is that the SNR decreases.

The helium pressure is set to be around 5×10^{-6} Torr for normal operation. It can be increased to achieve a higher current, however, this practise tends to reduce the lifespan of a trimer. The spot control is usually set between 3.5 and 7 depending on the required beam current (the smaller the current, the higher the spot control value): a beam current of 0.2-0.6 pA is suitable for high resolution imaging/lithography whilst surface modification and damage are also minimal and limited; a beam current of 1 pA or above is often used for lithography (large area), milling and deposition. The grid voltage of the ET detector is set to the maximum of 500 V, this positive bias attracts SEs from the sample to form images. Various adjustments are then performed to align the beam to the selected beam limiting aperture at the centre of the column, where beam tilt, align and stigmation are tuned via the X and Y knobs on the knob panel shown in Figure 3.2. A few iterations are carried out until no further improvements can be observed. This procedure helps to minimise the beam spot size and hence enhance the resolution. The image should appear sharp when in focus and without any movements, distortions or stretches when zoomed in/out.

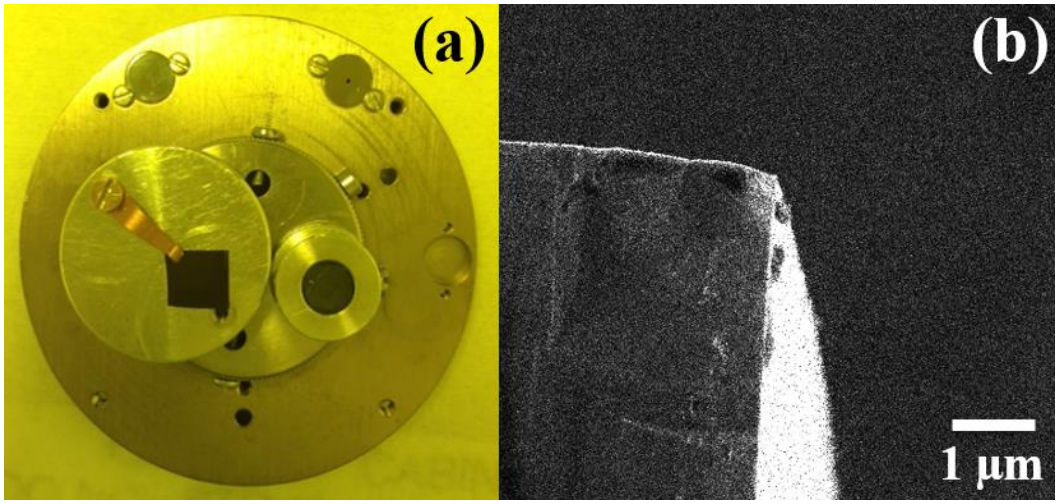

Figure 3.4: (a) HIM sample holder loaded with 8mm×8mm PMMA resist sample piece and the tin-on-carbon calibration sample; (b) HIM imaging of the top right corner of the sample with a FOV of 7.5 µm.

With the completion of the previous steps, the beam is adjusted to its optimum. The contrast, brightness and image intensity are finely tuned to enhance the overall image quality. An image is taken with a standard condition (exposure beam energy of ~30 keV), FOV of 900 nm, 10-µm aperture, 0.5 pA current, 5×10^{-6} Torr helium pressure), see Figure 3.3c, where features of 10 nm or below are well resolved. The textures are captured from the tin balls in front as well as the carbon in the background, suggesting a good depth of view. The image is compared qualitatively with images taken previously to minimise any instrumental uncertainties.

Both samples were kept at similar heights and angles initially when fixed to the sample holder before loading into the HIM (Figure 3.4a), hence only a few adjustments need to be carried out after switching the sample. The sample of interest is then ready to be moved underneath the beam. During the navigation, the dwell time is normally set to be small at around 2-3 µs with large FOV, resulting a minimum dose delivery and modification on the sample. Any dust particles nearby or the edge of the pattern that is not critical can be used for the final beam optimisation. If there are no features to focus on locally, the spot mode can be switched on for around 5-7 s, the helium ion beam can locally remove material from the surface and form a small hole next to the features of interest. This effect is a combination of sputtering and thermal evaporation [101], since it introduces a large amount of ions, this procedure is not recommended to be carried out too close to the feature. The final beam focusing can be performed by focusing on the edge of the small hole drilled by the helium ion beam. A SE image can then be captured with a specified FOV, resolution, contrast and brightness, etc. The quality of the image can be further improved by increasing the dwell time or applying line averaging to reduce the noise. Dwelling at the same location for a long duration at a high magnification can cause large accumulation of ions, which can modify and damage the sample permanently, hence this should be avoided.

If it is a resist sample to be patterned, extra care is taken to avoid any beam scanning in the centre of the sample, which can cause undesired exposure. An edge of the sample is first located and normally traced until a top corner (e.g. shown in Figure 3.4b) and then the scratch (scribed halfway on the top edge of the sample) is reached. Final optimisation and focusing of the beam is performed at the end of the scratch before the beam is blanked for the exposure. When multiple patterns are required to be exposed, the stage is stepped across 1.5-2 times the overall length of the pattern writing field between each exposure to avoid any overlapping, e.g. patterns of 50 µm in size will be 25 to 50 µm away from the adjacent pattern; but at the same time the patterns are placed relatively close to each other and this provides convenience in navigating amongst the patterns during characterisation. Each pattern is exposed twice so that the consistency and repeatability of the results can be verified at a later stage.

Thus far, the general procedures of exposing resists using a HIM have been outlined and these were followed in all the experiments relating to HIM during this PhD detailed in the following chapters. The hardware and software of the pattern generator which are vital for lithography will be described in the following section.

3.3 Pattern Generator Systems

The helium ion beam is designed to follow a raster scan style within a specified FOV on a sample surface. Meanwhile, the beam can also be navigated and switched on/off to trace a certain pattern within a specified field and this is achieved by the pattern generator. The ALIS System UI is equipped with an internal pattern generator unit, which recognises either a user defined rectangle or any imported bitmaps prepared by image processing software such as CorelDRAW. The dimensions and location of the pattern can be defined along with the pixel spacing, dwell time of the beam at each pixel and the number of repeats. However, neither the beam current nor the dwell time is adjustable between different elements within a same pattern, meaning a fixed dose is applied throughout a pattern. This limits the application of the internal pattern generator, and hence it is less useful for complex patterning.

Figure 3.5: The external pattern generator of HIM system: XENOS Pattern Writer XeDraw2.

A XENOS Pattern Writer XeDraw 2 unit serves as an external pattern generator to the HIM system (see Figure 3.5). This nanolithography tool controls the beam, and offers good flexibility in generating arbitrary patterns as well as the exposure of the pattern. It is implemented by the Exposure Control Programme (ECP) software, offering a writing field of 50,000 by 50,000 addressable pixels. The internal clock speed is 1000 kHz which defines the writing speed of the beam to be 100 ns when using the unit. Unlike the internal pattern generator, ECP allows different dwell times and pixel spacing to be applied for each element in one pattern, hence, dose variation is achievable.

Two ECP files need coding to generate the arbitrary patterns transferrable to the sample by the external pattern generator. A pattern file (.pat) determines the overall writing field of the pattern. It consists of lines of code that define the locations and shapes of each element by coordinates. For each element, a user defined name is given, and the increment, i.e. how closely the two adjacent exposure spots are positioned, and the dwell time, i.e. how long the beam stays at each pixel, are set to meet the required dose. The pixel spacing is mutually decided by the field size and the increment. The number of addressable points is fixed and with a given field, the distance between two adjacent points can then be determined. The increment ($I \geq 1$) in the .pat file then controls the beam to expose at every I point of the pattern, so the overall pixel spacing is I times the distance between two addressable points. A control file (.ctl) communicates with the pattern generator for exposing the patterns. It calls each element in the .pat file and determines the overall location of the pattern file on the sample. The control file also sets the order for the elements to be exposed. Sometimes this ordering is critical to the success of the pattern formation, for instance, in the case of the milling of nanoribbons on membranes [102].

To start the patterning the beam is blanked, and the imaging mode remains switched off throughout the process. The beam control is switched from the ALIS System UI to the external pattern generator. ECP software is started with both .pat and .ctl files opened. The stage is moved in micrometre steps along the horizontal plane, and a map is drawn to record and keep track of each exposure locations, which is useful in this non-imaging scenario as well as the imaging of the sample after the development process. All patterns exposed in this PhD have dimensions of 5 - 50 μm, which fit well within the FOV. Furthermore, the corresponding minimum pixel spacing is 0.1 – 1 nm, ranging from below to above the theoretical beam spot size of 0.35 nm, allowing for both high and low-resolution exposures. However, it is worth noting that the HIM is not a dedicated lithographic tool and there is error associated with stage movements, hence, field stitching is not recommended without manually correcting for stitching errors.

ECP has been used throughout the HIBL experiments during this PhD, and the coding language has been grasped for creating the patterns as well as the commands in the software. For each chapter, the graphical illustrations of the pattern used are presented and examples of the ECP coding to generate various exposure patterns can be found in Appendix 8.1.

3.4 Exposure in the EBL System

For a comparison study between HIBL and EBL, a high-resolution scanning electron microscope from the NVision 40 FIB-SEM (Zeiss) equipped with Elphy Quantum (Raith) lithography system was used to expose resists, see Figure 3.6. The SEM features a Schottky field emission Gemini source

that achieves edge resolution down to 1.1 nm at 20 keV and 2.5 nm at 1 keV, and it operates at beam energies ranging from 0.1 to 30 keV. The instrument is equipped with a range of imaging detectors, including an Everhart-Thornley SE detector, in-lens SE and one backscattered electron detector. It is operated in a very similar way as a HIM via SmartSEM UI. Before starting the machine, the system vacuum levels are checked to be within the operating range: electron gun vacuum $\leq 5 \times 10^{-9}$ mBar and system/chamber vacuum $\leq 2 \times 10^{-6}$ mBar. The sample loading chamber is then purged with the column chamber valve (the airlock) closed.

Figure 3.6: The NVision 40 FIB-SEM (Zeiss) at SNC.

The resist sample to be patterned by EBL is mounted onto a holder that has a Faraday cup, which is used to measure the beam current which is essential in calculating the dose for the exposure. A 1 cm × 1 cm calibration sample, Chessy, comprising over 1 million gold squares on silicon which form a four-fold chequerboard pattern in an area of 5 mm square, with smallest chequerboard being 10 µm by 10 µm, is also loaded for the calibration of the SEM magnification in the range between ×20 and ×50k. Once the sample holder is securely positioned inside the chamber, it is manually fed through to the bottom of the column after the specimen chamber is pumped down.

The position of the holder can be controlled by the joystick or from the stage navigation tab of the software to adjust x, y, z, rotation and tilt based on the live camera feed from the two chamberscopes that monitor the position of the stage and the pole piece of the gun. The working distance is normally set between 7 mm and 10 mm. After the chamber vacuum is stabilised at ~2×10^{-6} mBar, the EHT is turned on and the beam energy is set to be 30 keV for resist exposure. The FIB lock is disabled to allow for a bigger FOV, resulting in quicker navigation. The tilt correction is disabled to avoid any imaging/patterning distortion.

The stage is moved so that the Faraday cup is directly underneath the electron beam. The spot mode is turned on to allow the full focused beam into the current monitor for an accurate reading. Under 30 keV, the following table, concluded from a range of experiments, serves as a general guide to what currents can be achieved when selecting different apertures, results subject to changes of the source condition at the time of the experiment.

Aperture Size (μm)	Beam current (pA, measured)
120	5800
60	1000
30	297
20	112
10	35
7.5	18

Table 3.1: The typical value of beam currents achieved in the NVision 40 SEM measured by the Faraday cup using various common apertures.

The build-in pattern generator in the Elphy Quantum (Raith) lithography system is used for pattern file (.gds) generation. The SEM in NVision is not a specialised lithographic tool, so there is no proximity effect correction, allowing for fair comparison with HIBL results. However, the conventional complicated fractions on curved elements would cause over-exposure and pattern distortion. The Elphy Quantum not only generates simple patterns, i.e. patterns with no curve, arc or circle elements and partitioned into rectangles of various sizes, but also curved elements using a smart single-pass spiral outwards exposure strategy, which minimises the exposure time and optimise the exposure outcome. This exposure strategy matches to that used in the HIBL experiments.

The doses to be applied to the pattern is normally predetermined and the step-size, i.e. the pixel spacing of the beam, is normally set as close to the resolution limit as possible, especially when it is a high-resolution exposure. With the help of the exposure time calculator in the software, the area/line/dot dwell time and most importantly the overall exposure time can be computed based on the dose, estimated step-size and a beam current chosen from Table 3.1. If the overall exposure time is suitable, the corresponding aperture can then be selected in the SEM system and an accurate current in that instance can be measured for use.

When multiple features are to be exposed at the same dose, they are placed in the same layer in the design file and share an identical GDS II number. When features require different doses, they are assigned different GDS II numbers and they are placed on distinct layers, so that they can be addressed separately. In addition, a base dose (smaller or equal to the smallest dose in the series) is adopted in the exposure time calculator, and a dose parameter, the multiplier between the actual dose

and the base dose is given to each feature. For example, if the doses to be applied are 10, 20, 30, 40 and 50 μC/cm^2. The base dose can be set as 10 μC/cm^2 (or any value smaller than 10 μC/cm^2), whilst the corresponding dose parameter for each feature is 1, 2, 3, 4 and 5. It is worth noting that for all features, the only variant is the dwell time which leads to different doses. Thus, it is appropriate to have a relatively short exposure time for the feature exposed with the base dose, since the exposure time will be multiple times longer for the other patterns. If the calculated exposure time is too long (e.g. over 10-15 mins), it is sensible to choose a larger beam aperture for a greater current.

The stage is navigated to place the Chessy calibration sample beneath the electron beam. The focus, alignment and stigmation of the beam are tuned in several iterations at increasing magnification to optimise the beam, a SEM image is shown in Figure 3.7. This process is very similar to that in HIM. With the electron column selected on the control box and the external scan control enabled in the SmartSEM, the Elphy Quantum pattern generator is given control of the beam.

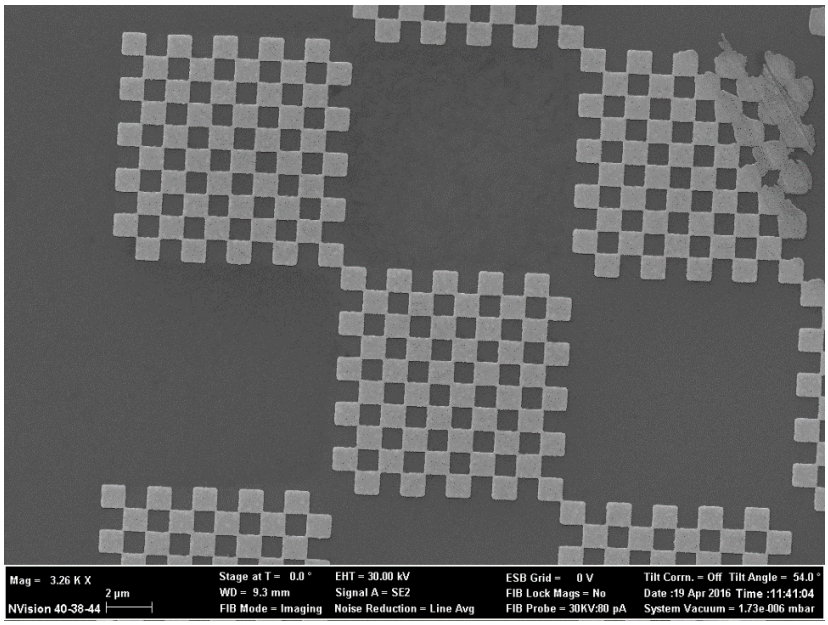

Figure 3.7: SEM image of the Chessy calibration sample showing good contrast between the gold squares and the silicon substrate with the imaging conditions of 30-keV beam energy with a 30 μm aperture and a working distance of 9.3 mm.

For lithography experiments conducted in this PhD, the following setups are followed. After the writefield is set to be 100 μm with a ×400 magnification, it is calibrated against the Chessy sample. The stage is moved so that the beam can be refocused onto the end of the scratch on the resist sample, where the origin, u-v coordinates and angle corrections are modified prior to the exposure. Pattern files (.gds) are imported into a new position list, and they will be exposed in order with automatic

stage navigation to the predetermined u-v coordinates for each pattern. For all exposures, a beam energy of 30 keV is used. Since there is no beam blanker in the EBL system, the beam remains on during the idle state (when the beam is not tracing a pattern) and it rests ~55 µm northwest from the writefield of the pattern. Therefore, the stage is quickly navigated away from the area upon the completion of the exposure. If more than one patterns are to be exposed, at least 150 - 200 µm space is allocated between each pattern to avoid the idle beam landing on the exposed pattern accidently.

3.5 Development Process

The patterned sample is unloaded from the HIM and taken directly to the yellow room for the post-exposure development process. Since all resists used in this PhD were non-chemically amplified, no post-exposure bake was needed. After checking that the extraction system of the aqueous developer bench is functioning, non-metal contaminated glassware, such as measuring cylinders and beakers, are used to measure and hold the developer, stopper and/or DI water needed during the resist development process. The sample is gripped on the edge using a pair of clean tweezers and carefully lowered into the solution until fully submerged. Light agitation was given to the sample to displace any air bubbles on the sample surface. The process is carried out at room temperature and timed to achieve the desired pattern formation. After the process, the sample is gently blown dry by the nitrogen gun, whilst the glassware was rinsed and cleaned by acetone and IPA, and blown dry before being returned to the glassware oven. Each sample is then characterised using at least one of the following techniques: ellipsometer, optical microscope, atomic force microscopy (AFM), SEM and HIM. More details regarding to the methodology used in the characterisation are described in the following section.

3.6 Characterisation

A series of characterisation tools were deployed in this PhD to extract experimental data from the fabricated samples for analysis. This section introduces the techniques as well as the methodology adopted in regarding measurements and characterisation apart from HIM and SEM mentioned previously.

3.6.1 Ellipsometer

Figure 3.8: The ellipsometer (M-2000™, J. A. Woollam Co.) at SNC.

To measure a resist layer thickness spun on silicon, an M-2000™ Spectroscopic Ellipsometer (J. A. Woollam Co.) as shown in Figure 3.8 was used. It uses polarised light to characterise thin films on bulk materials, and it is controlled via the CompleteEASE software for data acquisition and analysis. When the incident light beam undergoes a change in polarisation as it interacts with the sample structure, Psi (Ψ) and Delta (Δ) verses wavelength of the light are measured by the ellipsometer. These two parameters reflect the amplitude and phase change in the outgoing polarisation respectively, and they are analysed for determination of material properties, such as the film thickness, refractive index and roughness. When light hits a film, there is an increasing separation between the light reflected from the surface and the light that travels through the film as the film thickness increases, as shown in Figure 3.9. This phase delay caused is related to both the physical thickness and the refraction index. When the reflected light signals are accurately recorded, the film thickness and the refractive index can be calculated. When an approximate refractive index is known or measured from a thick film, a thin layer down to a nanometer can be determined by the ellipsometer because of its high sensitivity.

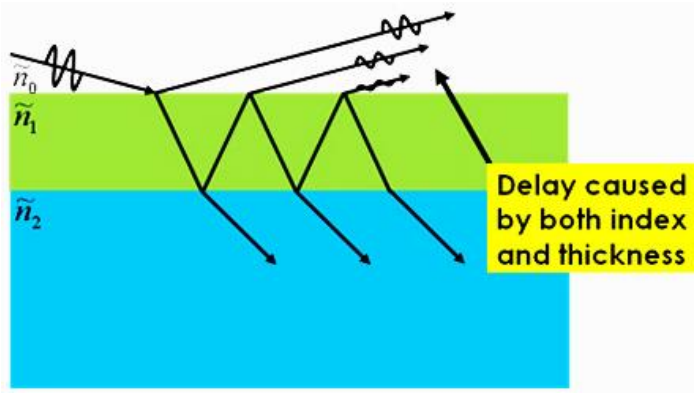

Figure 3.9: An interface of two mediums (a thin layer on top of a bulk substrate) with refractive indices as n_1 and n_2.

To measure the thickness of a resist layer, the sample is placed on the stage and held by a vacuum. The stage is moved so that the sample is underneath the incident beam. Mappings containing multiple measurement points that evenly spread across a wafer of up to 8 inches in size are available. However, it is more viable to repeat a single measurement at a single point at multiple locations for a small chip. Layers of materials such as PMMA and Al_2O_3 were measured using this technique, since their refractive indices are available in the database (PMMA: 1.4905 and Al_2O_3: 1.7682) and verified on thick films. To start the measurement, a simple two-layer model is created with a thin layer of interest placed on top of a silicon substrate. The acquisition time was set to be 2s and the angle of the incident beam was set to be 75 degrees. The thickness of the thin layer is set to be the fitting parameters whilst others are imported from the database. The accurate layer thickness can then be determined by fitting the experimentally measured data to the model and equations.

3.6.2 Atomic Force Microscopy

AFM is a high-resolution scanning probe microscope and it is used as an alternative method to measure or confirm the thickness of a resist layer, especially when there is no established or reliable data for the material in terms of its physical properties. AFM has also been used to characterise various patterned resist samples for extracting depth and surface information.

An AFM measures the force between the probe and the sample surface. The probe, which is normally a 3-6 μm tall pyramid sharp tip with a 10-40 nm end radius, is attached to the end of a cantilever. A laser beam hits the flat top of the cantilever at an angle and its reflected light strikes the origin of a position-sensitive photo detector. As the probe tip approaches the surface, an attractive force between the surface and the tip causes the cantilever to deflect towards the surface. When the cantilever is brought even closer and finally touches the sample surface, a repulsive force instead occurs and deflects the cantilever away from the surface. Any deflection of the cantilever will change the

direction of the reflected beam, which results in a beam position shift on the photo detector. This displacement represents the force between the sample and the tip at each instant. The tapping mode of the AFM is used for imaging samples during this PhD, where the cantilever is excited to oscillate up and down at or near its natural frequency, whilst its driving signal remains the same. When the probe comes very closely to the sample surface, the force between the sample and the tip interferes and changes the amplitude of the cantilever's oscillation. This change is then fed back to the electronic control loop and the height of the probe is adjusted so that a constant amplitude of oscillation is maintained as the probe scans across the sample. The height of the probe is then recorded, and the data is plotted in a pseudocolor image, in which each pixel represents a position on a sample and the colour represents the recorded signal. Hence, an accurate topographic map of the surface features is generated.

Figure 3.10: AFM (Multimode™ V, Veeco) in the Measurement Lab on a suspended workbench.

A Multimode™ V AFM system (Veeco), with a vertical resolution down to sub-nanometer, is used for various surface characteristics measurements, as shown in Figure 3.10. If it is a freshly coated resist layer for thickness determination, a clean pointed object with a hardness greater than that of the resist material, but smaller than that of the silicon substrate, e.g. a tip from a pair of stainless steel tweezers, was used to scrape off resist in long strips from the sample surface to expose the silicon substrate underneath. The scratch is scanned across so that the depth of the trench, i.e. the resist layer thickness can be measured. For capturing the topography of a patterned sample, no extra preparation steps are needed. To navigate the AFM tip above the area that needs measuring, the pattern has to be

visible via the ×25 optical microscope that is part of the system. Hence, it is recommended to firstly confirm that the patterns can be found at a similar magnification via the microscope after the development. During the pattern designing stage, multiple measures can be taken to enhance the visibility of a pattern. For instance, bulk edges with lengths and widths of 5-10 μm and ~2 μm are often exposed at resist critical dose around small features or features of low contrasts when AFM characterisation is required.

After checking the workbench on which the AFM is placed is well suspended, the scanner that allows a maximum vertical scanning range of 5 μm and a horizontal scanning area of 120 μm × 120 μm is installed. This wide range allows searching and navigation of patterns on a sample surface. The sample is mounted on the stage with the patterned area placed relatively in the centre. The AFM is fully assembled and set up, and the laser beam is directed on top of the cantilever which is above the pattern of interest. All is in view with good focus on the PC screen via the optical microscope. The values shown in the display on the base represent laser position readouts from the photo detector, and they are carefully set to the default values before initiating the scanning. The AFM tip is driven to oscillate at or near its natural frequency whilst its amplitude and phase response are measured after the tuning for the tapping mode.

To start a measurement, the integral gain that controls the shift between the trace and retrace of the signal is normally set to be 1, whilst the proportional gain that controls the correlation between trace and retrace is set to be 2 for the tapping mode. Initially, high values are given to the scan size and rate (e.g. 80 μm and 2 Hz for a 50-μm pattern) for a quick preview. The values are then refined to zoom in onto a more specific area at a much lower frequency (e.g. 0.6 Hz), the offset function can also be used to centre the area of interest. Meanwhile, a low resolution (128 or 256) is set at the beginning and then increased to a higher value (512 or 1024) for better image quality. The direction of the scan can also be defined. The image is formed in a raster scan style, and it can be analysed using the Gwyddion software. The data can be displayed in various colour gradients and in 3D effects. The orientation, step, tilt and other artefacts of the image can also be corrected. AFM has been used for obtaining various experimental results presented in the result chapters, where the specific recipe used for each sample will be described.

3.6.3 High Resolution HIM Imaging

The general HIM imaging procedure has been introduced in the previous Section 3.2. In this section, the techniques and recipes developed for the high-resolution HIM imaging especially on small features such as arrays of lines will be described. This is vital since it enables surface characterisation of the fabricated sample, and information such as pitch, linewidth and LER can be extracted and

analysed from these images. During this PhD, several imaging tasks on characterising samples from SNM project partners were carried out and some results were shown here as example.

Locating micrometre-sized features is usually a quick and straight forward process. The beam is scanned across the sample with a fast scanning recipe in a relatively large field of view, i.e. at low magnification, and low resolution. Recipe such as "Navigation" is often used during this process, please refer to Appendix 8.2 for details of parameters in each imaging recipe. The short dwell time along with small number of averages result in minimal amount of helium ions on the sample surface. However, this is not applicable when finding features of sub-20 nm in size, which are not as visible in low resolution. When switched to a slow scanning recipe with a higher imaging resolution at higher magnification, it takes much longer to navigate across the sample and the scanning beam can cause unnecessary accumulation of helium ions and damage the feature. The following procedure was developed and practiced as an efficient way of finding small features whilst introducing minimal beam exposure.

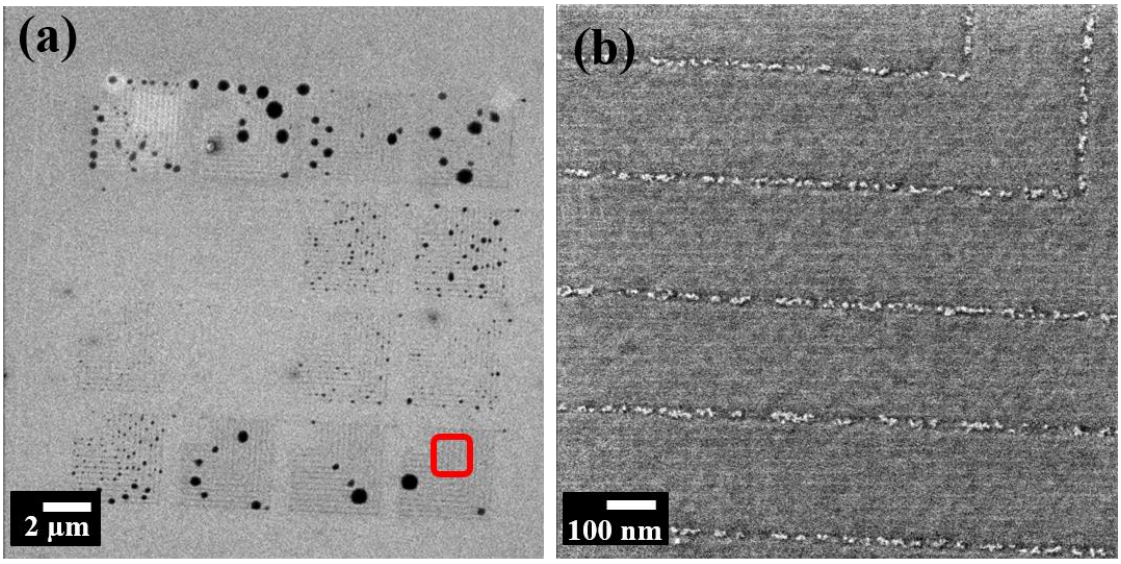

Figure 3.11: HIM images of the SPL-patterned corner-structures in calixarene resist (sample courtesy of M. Kästner, TUIL) with a FOV of (a) 25 µm and (b) 1 µm. (b) is a magnified image of the area circled in red in (a), and the magnifications are ×8k and ×167k, respectively.

The HIM is first set up as described in Section 3.2. Once the beam (30 keV, 10 µm aperture, 0.5 pA, WD = 7 mm) is optimised on a feature away from the area of interest, the beam is blanked and the FOV is adjusted to a value that is greater than the overall size of the pattern. For example, the sample has a patterned overall area of 18 µm, the FOV can be set to 25 – 40 µm, so that the chance of capturing the pattern is good and if captured, the patterns are not too small in the image. The stage is then moved from the current location in one stepped motion to the feature of interest with the beam

blanked. An image is taken with a medium-resolution recipe, such as “Medium scan” as shown in Figure 3.11, where the 16 SPL-patterned corner structures formed in positive tone calixarene resist are clearly visible and well within the 25-µm FOV.

Once the patterned area is located, to zoom in onto a section can be done using the following technique. First, double click the centre of the area of interest (for example, the area circled in red in Figure 3.11a) on the HIM image. This sets it as the new centre point (with the beam blanked), and the field of view is adjusted to a suitable value, 1 µm in this case. Then, an image can be captured using a high-resolution scanning recipe such as “Slow scan” or “High-res scan”. Figure 3.11b shows the captured magnified image where the lines and the residual particles are clearly resolvable. It is also recommended to refocus and adjust the stigmation of the beam next to the pattern prior to the imaging.

It is worth noting that the unpatterned positive-tone calixarene resist has a high resist sensitivity to the helium ion beam, hence prone to modification on exposure. Extremely fine horizontal lines with a 25-nm pitch are visible in Figure 3.11b. which caused by the previous helium ion beam scanning at low magnification when capturing the 25-µm FOV image. This is confirmed by the line pitch matching to the pixel spacing of the raster scan. These lines are very faint and therefore do not appear to have significantly changed the patterned corner structure, however, it can be avoided in the future by using a recipe with lower number of averages. On the other hand, this unintended fine scale patterning demonstrates the extremely small spot size of the HIM.

The effect of the same area being consecutively imaged three times by HIM with a decreasing magnification (with an increasing FOV) is shown in Figure 3.12. The darker areas in Figure 3.12c indicates that some hydrocarbon contamination was built up on the sample surface after the first two scans at higher magnifications (Figure 3.12a and b). This effect can be improved by cleaning the chamber thoroughly before imaging, and running a plasma clean on the samples at the start of the loading procedure. For this sample, the plasma clean was not carried out because it is known to modify thin film polymer samples [103]. The fine scale features including CD of lines, LER and the particles within the patterned lines, however, appear virtually unchanged amongst the three images. This indicates that no significant sputtering or damage has occurred during the beam scan used to form the images.

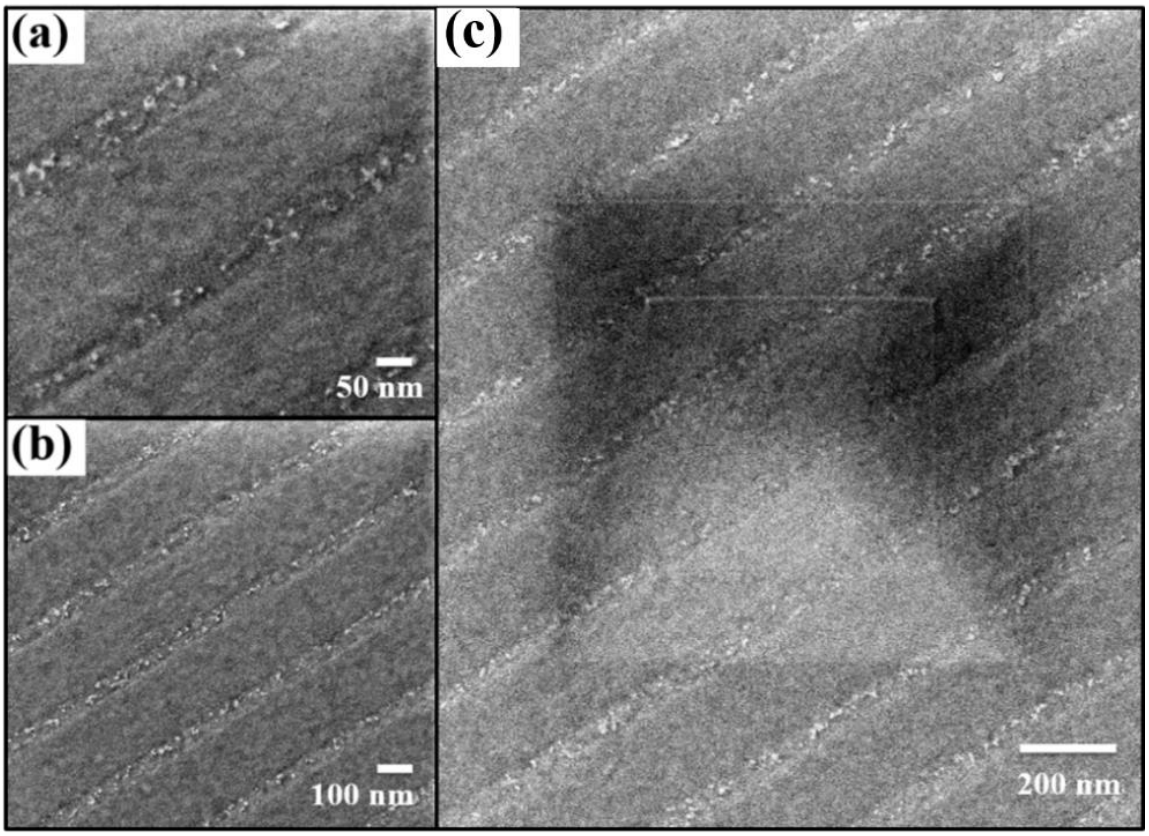

Figure 3.12: HIM images of the same SPL patterned line features in calixarene resist with an imaging FOV of (a) 600 nm, (b) 1 µm and (c) 1.8 µm. The magnifications are ×334k, ×167k and ×111k, respectively.

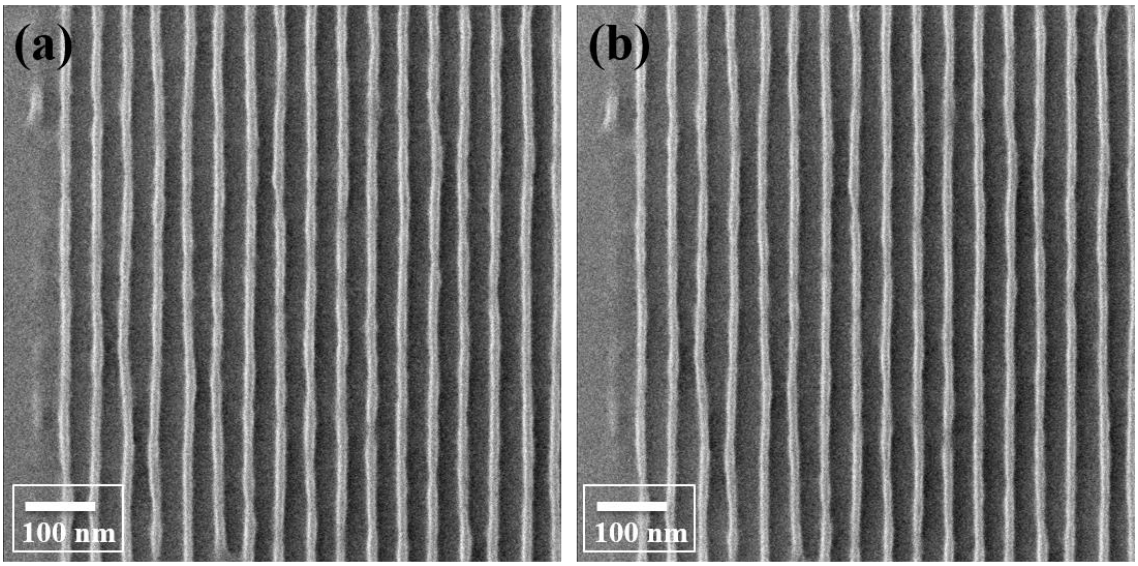

Figure 3.13: High resolution HIM images of 22-nm lines at 44-nm pitch in an EUV resist (sample courtesy of P. Schepper, Imec) with a FOV of 800 nm. (b) was taken after (a) with the same imaging recipe.

To investigate the impact of high-resolution imaging using helium ion beam has on a sample, 22-nm line features patterned in an EUV resist were imaged twice with the same FOV of 800 nm and magnification of ×251k. The “High-res scan” recipe was used, and the beam conditions were kept identical. No significant changes in features (line width, shape of the feature, etc.) are observable in the two images, hence, the sputtering/modification caused by the helium beam imaging proves to be negligible. So far, the techniques of obtaining high resolution images whilst causing minimal alteration to the sample have been reviewed and the advantage of using HIM as a metrology tool has been demonstrated.

High resolution HIM images can then imported into imaging processing software such as Gwyddion for linewidth and pitch measurements, and more details can be found in Appendix 8.4. SuMMIT (EUV Technology Corp.), an analysis package for line-edge/width roughness and CD uniformity, was also used in the fullerene related studies on LER analysis through the collaboration with University of Birmingham. It processes various types of images such as SEM, HIM, AFM images, etc. It is also capable of performing large batch of images, allowing large volumes of data to be analysed quickly, making it especially useful in the industry.

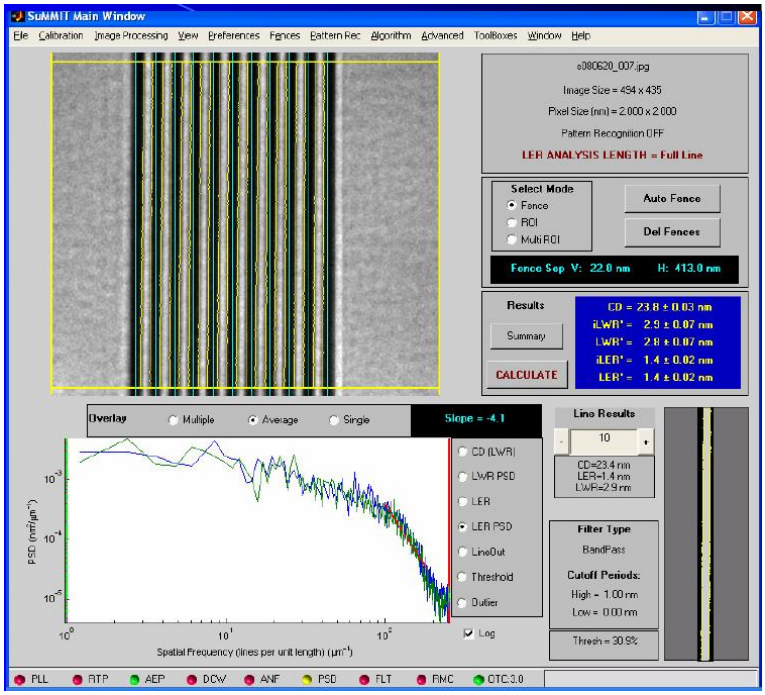

Figure 3.14: Screenshot of the SuMMIT software UI showing an imported SE graph of a line arrays lines and calculated CD, LER and LWR are presented on the right.

HIM image is firstly loaded into SuMMIT, the software comes with image processing tools for adjusting rotation, cropping, zoom of the image. Once the region of interest is positioned within the

window, Auto Fence function allows line-space recognition and the computation of CD and LER. The analysis threshold for line/edge detection and line-edge roughness algorithms can be tuned by the user for better and more accurate results.

So far, the methodology involving sample preparation, patterning and characterisation for the investigation of helium ion beam lithography has been described. In the following chapters, various experiments carried out using HIBL will be presented.

3.7 Brief Helium Ion Beam Simulation

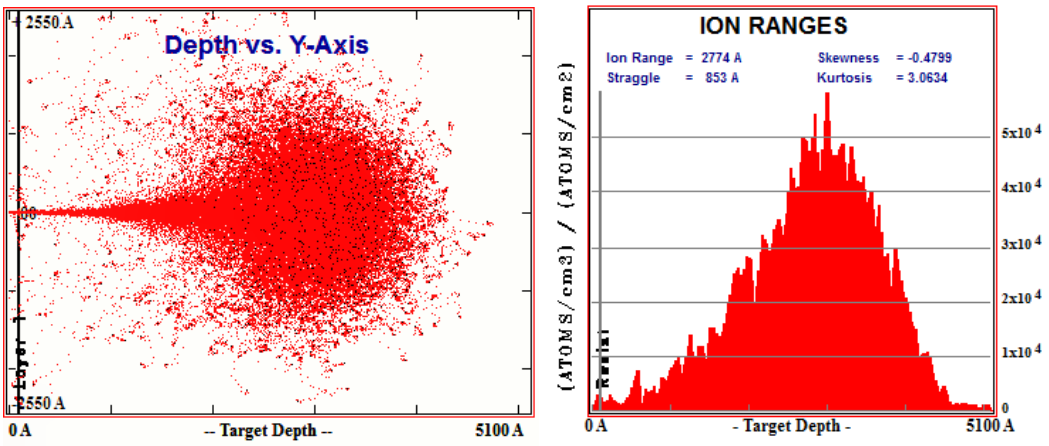

Figure 3.15: (a) He^+ ion trajectories through a 10-nm-thick carbon-based resist on a bulk Si substrate with 30-keV beam energy (b) The resulting ion ranges generated from the simulation. Both were calculated using SRIM [104].

The ion tracks and the mean ion implantation ranges for He^+ ions in different materials have been calculated using the SRIM code from Ziegler [104]. The resist-on-silicon system has been modelled using a 10-nm layer of carbon on a silicon wafer. This target is impacted with He^+ ions at the optimum beam energy of 30 keV. The results, plotted in Figure 3.15b, show the He^+ ions implanted deep in the silicon with a mean projected range and straggle calculated as R_p = 277 nm ± 43 nm. It is important to note that there is minimal backscattering of ions at 0.125% of the incident beam, which indicates that proximity effect will be negligible - a prediction confirmed by experiments in Chapter 5.

CHAPTER 4

HELIUM ION BEAM LITHOGRAPHY ON PMMA

4.1 Introduction

PMMA is a common organic polymeric positive tone resist with high resolution and excellent adhesion to most substrates, and it comes at relatively low cost. It has played a key role in the development of both EBL and ion beam lithography. Upon the exposure, the scission of the polymer backbone and subsequent development process removes the exposed lower molecular-weighted PMMA resist and forms structures. It was used in baseline experiments at the beginning of this PhD for the development of HIBL processes, where resist sensitivity measurements and high-resolution patterning evaluations were carried out. In the following sections, the detailed experimental procedures along with results and discussions are presented.

4.2 Exposure Pattern Design

The first experiment was to determine the resist sensitivity of HIBL in PMMA and to obtain the dose response curve across the full dose spectrum. Figure 4.1 shows the pattern designed for the large area exposure. The pattern has a 50 μm × 50 μm field and it consists of three elements: the rectangle dose areas in the centre, the edge markers in long thin rectangles around the edges and the identification marker on the top left corner of the pattern. The complete coding for both .pat and .ctl files in ECP to generate the exposure pattern in Figure 4.1 can be found in Appendix 8.1.

There are fifteen rectangles with the same dimension of 5 μm × 10 μm in the centre of the pattern and they are evenly spaced 3 μm from each other. The beam dwell time and the pixel spacing of the helium ion beam are set to vary for each rectangle to achieve fifteen different doses, results of which can be obtained at once for every pattern exposed. Compared to the results obtained from the method of exposing only one dose square and moving the stage for the next, these results tend to be more reliable due to fewer variations between dose exposures and more controlled experimental conditions. The dose areas are designed to be big enough to provide sufficient data when scanned by an AFM, whist to be small enough to avoid a long beam writing time, which can potentially lead to stage drift

and beam instability during the exposure and cause unreliable results. The pattern also allows a set of results to be collected from a single AFM measurement which is productive and efficient.

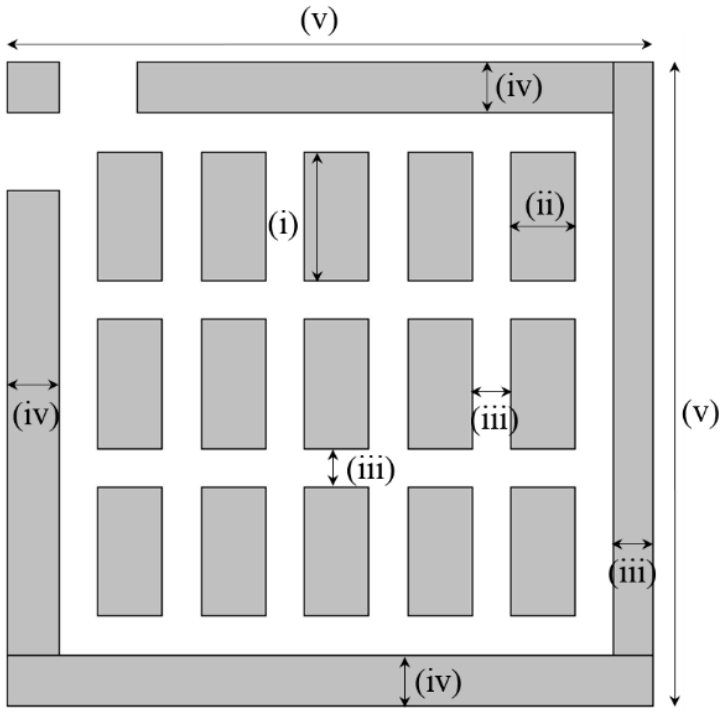

No.	(μm)
(i)	10
(ii)	5
(iii)	3
(iv)	4
(v)	50

Figure 4.1: Dose test pattern generated in ECP consisting of three elements: exposure areas, edge markers and identification marker. All dimensions are listed in the table on the right.

The edge markers are 4 μm wide and stretch along the border of the 50 μm pattern field. Since PMMA is a positive tone resist, the height of resists from the areas exposed with extremely low doses and the unexposed areas are almost the same after the development, resulting in very low visual contrasts. This makes it extremely difficult to locate the patterned area under an optical microscope or an AFM. To tackle this problem, the edge markers were designed in a way so that the pattern can be found more easily during the characterisation: they are large in size enclosing all the dose areas, and exposed with a fixed large dose for improved contrast and visibility when the sample is developed.

Nine designed identification markers, located in the top left corner of each pattern, are shown in Figure 4.2. Same dose is applied to the identification markers as the edge markers. When multiple patterns are exposed onto one sample, the identification marker not only differentiates but also reveals the orientation of the patterns. Both edge and identification markers were used in almost every pattern developed during this PhD for same purposes regardless of the resists used.

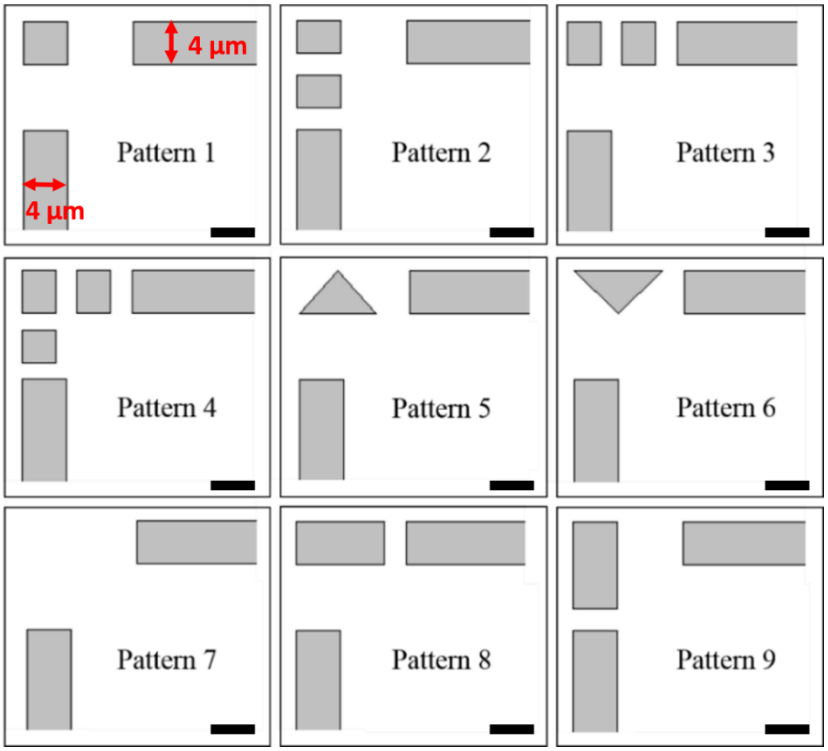

Figure 4.2: Nine identification markers designed and generated in ECP for pattern differentiation in multiple exposures. Scale bar: 4 µm.

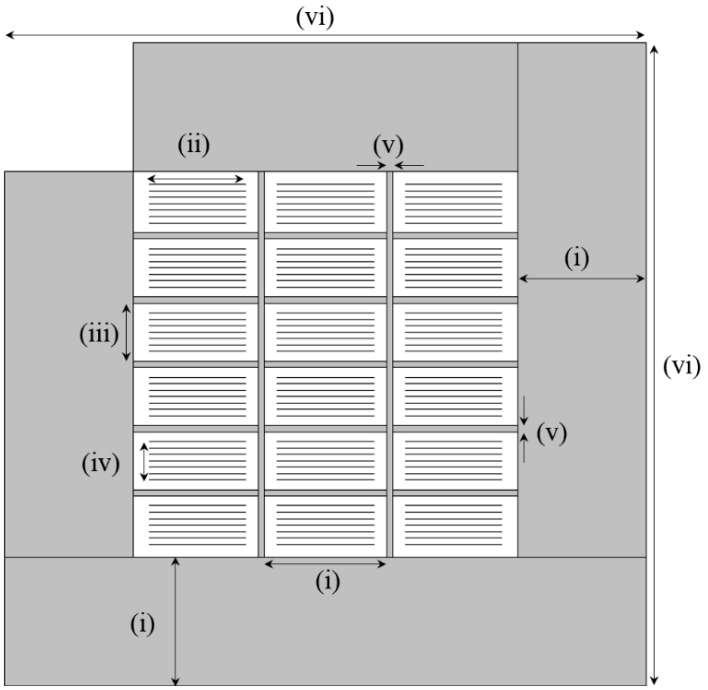

No.	(µm)
(i)	2
(ii)	1.5
(iii)	0.9
(iv)	0.6
(v)	0.1
(vi)	10
pitch	0.1

Figure 4.3: The designed ECP pattern with a FOV of 10 µm × 10 µm containing 3 × 6 single-pixel sparse line arrays. All dimensions are listed in the table on the right.

The second experiment was to evaluate high resolution sparse feature patterning using HIBL in thin layer of PMMA resist. Figure 4.3 shows the designed pattern of single-pixel line arrays in ECP. It has an overall area of 10 µm × 10 µm, containing 2-µm-thick edge markers that enclose 18 arrays of sparse single-pixel lines. Thus, 18 variations of line dose can be tested at a time from one exposure. There is good separation between each array and from the edge markers to avoid any impacts from the proximity effect. There are 7 sparse lines of 1.5 µm long in each array that are exposed to a specific line dose in unit of nC/cm. The increment was set to be 1 for all line exposures and hence the pixel spacing works out to be 0.2 nm to avoid any discontinuity in the fabricated pattern.

4.3 Experimental

Standard PMMA products are formulated with resins of molecular weight of either 495,000 or 950,000 in anisole solvent, and they are available as PMMA495 and PMMA950. PMMA495 was chosen in all PMMA related experiments for its smaller molecular size, which allows finer features to be formed with reduced LER. Spun at maximum speed of 8000 rpm, the thinnest possible layer formed by 4% PMMA495 (MICROCHEM) was measured to be ~105 nm, which exceeds the ideal resist thickness for HIBL experiments. Therefore, an EBL resist thinner, ZEP-A (ZEON), composed of anisole, was used to dilute and thin down the resist. Different amounts of ZEP-A were measured and mixed into the original PMMA solution to produce resist solutions of lower concentrations (3%, 2% PMMA solutions, 1:2 and 1:3 PMMA/ZEP-A). All diluted resists were left at room temperature for stabilisation and used after 24 hours.

The sample cleaning was carried out as described in Section 3.1 in the Methodology Chapter. 0.1-0.2 ml of the PMMA resist was dispensed for each silicon chip and EMS Photo Resist Spinner Model 6000 was used. Initially, a short spreading step with low rotational velocity spreads the dispensed resist across the whole sample for 5 s, followed by a ramping-up step to reach the full speed at a maximum acceleration of 9000 rpm/s. Silicon samples were spun for 45 s at speeds ranging from 3000 rpm to 7000 rpm and coated with PMMA films from various concentrations. A 70-second pre-exposure bake at 180 ^{o}C on a hot plate was carried out to dehydrate the resist whilst promoting the adhesion between the resist and the substrate. After the initial characterisation using an ellipsometer, more resist spinning was performed to produce 20, 50 and 70-nm-thick layers for use in experiments.

Following the methodology detailed in Section 3.2, a HIM (Orion^{TM} Plus, Zeiss) was used to expose the PMMA resist with doses ranging from 0.1 µC/cm^2 up to 500 µC/cm^2 with a focus on the full-clearance dose range of 2 – 40 µC/cm^2. An accelerating voltage of 30 keV and a working distance of 6.8 mm were used in all cases, whilst the helium pressure was maintained at 5×10^{-6} Torr. For dose area exposures, the 20-µm beam-limiting aperture was selected to allow a greater current and 5 pA

was used in the resist sensitivity evaluation. For patterning high resolution single pixel lines, a smaller 10-μm aperture was used with a much lower current of 0.5 pA to achieve high resolution.

After the beam exposure, the samples were then developed in methyl isobutyl ketone (MIBK)/IPA (1:3) solution, a high resolution and low sensitivity developer, at room temperature for 60 s. The sample was then rinsed in DI water for 10 seconds to terminate the development process and prevent scumming and at last blow-dried by nitrogen. The fabricated structures were then characterised and analysed using the following techniques: the unexposed resist film thickness was measured using an ellipsomter (M-2000 ™, J. A. Woollam) with 75 degrees beam angle for an acquisition time of 2 s. The tapping mode of an AFM (Multimode™ V, Veeco) was used to extract depth and surface information from the large fabricated features with a scanning frequency of 0.723 Hz and sample/line resolution of 512. HIM was used to obtain high-resolution top-down SE images with the following imaging conditions: 30-keV beam energy, 0.5-pA beam current with a working distance of 7 mm.

AFM data were captured for large area scans (FOV of 50 μm) with the following conditions: scanning frequency of 0.723Hz with resolution of 512 samples/line and lines. Scanning frequency of 0.6 Hz with resolution of 640 samples/line and lines was applied for smaller scanning areas (FOV of ~10 μm). The integral gain was between 3 and 6 and the proportional gain was around 2 to match trace and retrace of the signal.

4.4 Results and Discussion

4.4.1 Resist Film Spinning

The spin speed versus film thickness curves displayed in Figure 4.4 provide approximate information required to select the appropriate diluted PMMA solutions and spin conditions needed to obtain the desired film thickness. It is found from the spin curves that 1:3 PMMA-ZEP-A solution shows promises for high resolution lithography due to its resulting sub-20 nm film thicknesses, whilst other solutions can be used to produce thicker resist films for the dose test experiments. Samples with resist thicknesses of 20, 30, 50 and 70 nm were used in the HIBL experiments reported in the following sections. The corresponding spin speeds used to obtain each thickness are listed in Table 4.1.

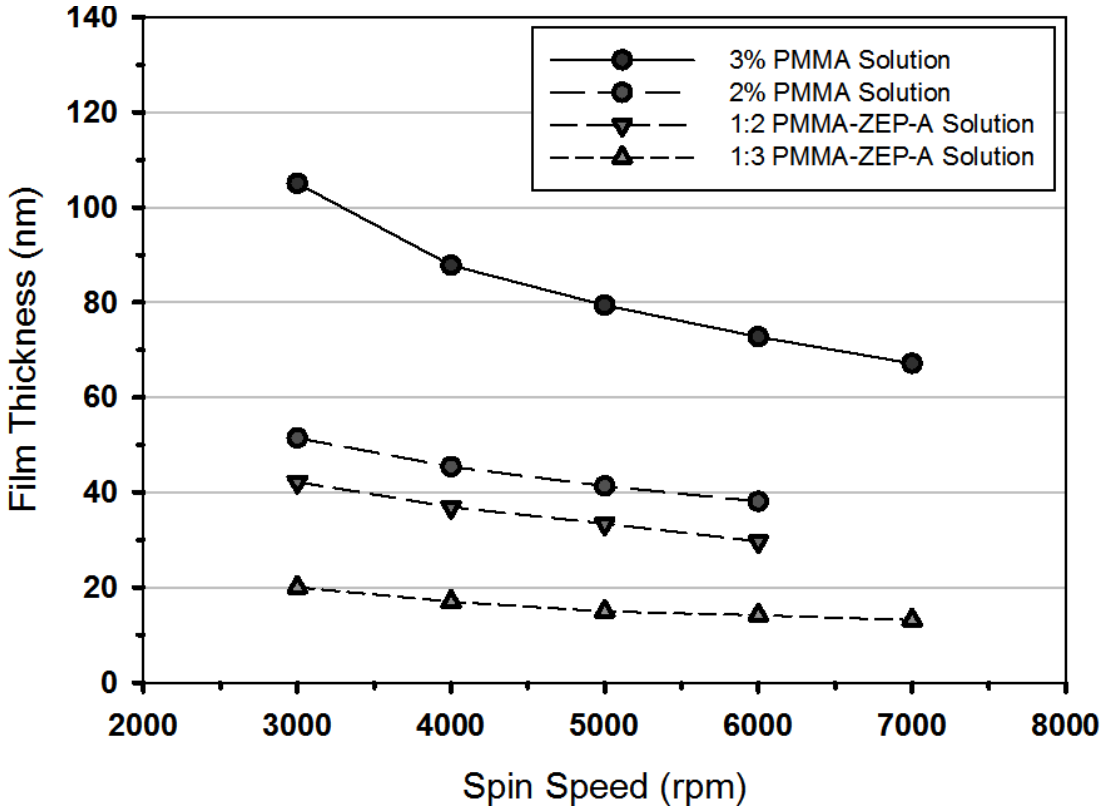

Figure 4.4: Spin curves of four diluted resist solutions from 4% 495PMMA.

PMMA layer thickness	20 nm	30 nm	50 nm	70 nm
Solution used	1:3 PMMA-ZEP-A	1:2 PMMA-ZEP-A	2% PMMA Solution	3% PMMA Solution
Spin Speed (rpm)	3000	6000	3000	6000

Table 4.1: Resist solutions and spin speeds used for 20, 30, 50 and 70-nm-thick PMMA layer.

4.4.2 Resist Thickness Evaluation

The aim of this experiment was to develop a complete working process for HIBL, whilst investigating the effect that resist thicknesses have on the imaging contrast of the fabricated features in PMMA resist.

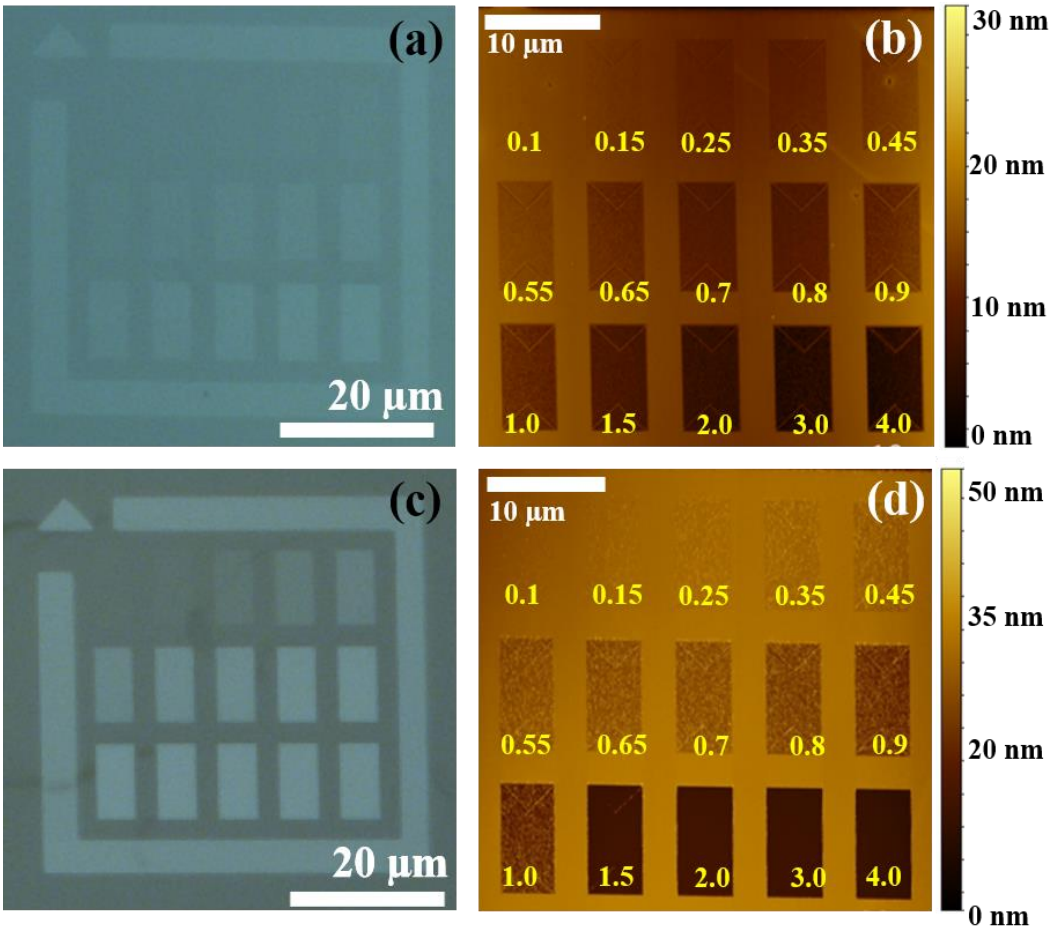

Figure 4.5: Optical micrograph of an exposed and developed patterns on (a) 30-nm and (c) 50-nm-thick PMMA on silicon. Each pattern consists of 15 rectangular areas (5 µm × 10 µm) exposed to various He ion doses. Top-down 2D AFM images of the same developed patterns on (b) 30-nm and (d) 50-nm PMMA on silicon. The dose (unit: µC/cm^2) applied to each area is labelled on the AFM graphs in (b-d).

Optical micrographs (e.g. Figure 4.5 (a) and (c)) show an example of fabricated dose test patterns using HIBL in 30 and 50 nm PMMA resists. Initial measurements reveal that the dimensions of the developed features match to those in the designed ECP pattern (Figure 4.1), confirming the precise transfer of the pattern from the pattern generating software to the physical sample. Contrast variations display amongst dose squares within each pattern, this is due to the thickness differences of the resist residuals from the areas that received different doses. Although the same set of doses were applied, and identical standard optical microscope settings were used, patterns formed in the 30-nm-thick PMMA resist appear less visible compared to those formed in 50 nm resist. The low contrast is due to the thinner resist layer and the subsequent small differences between the unexposed and the exposed areas. Being able to locate the patterned areas under the optical microscope means that AFM measurement of the sample is feasible.

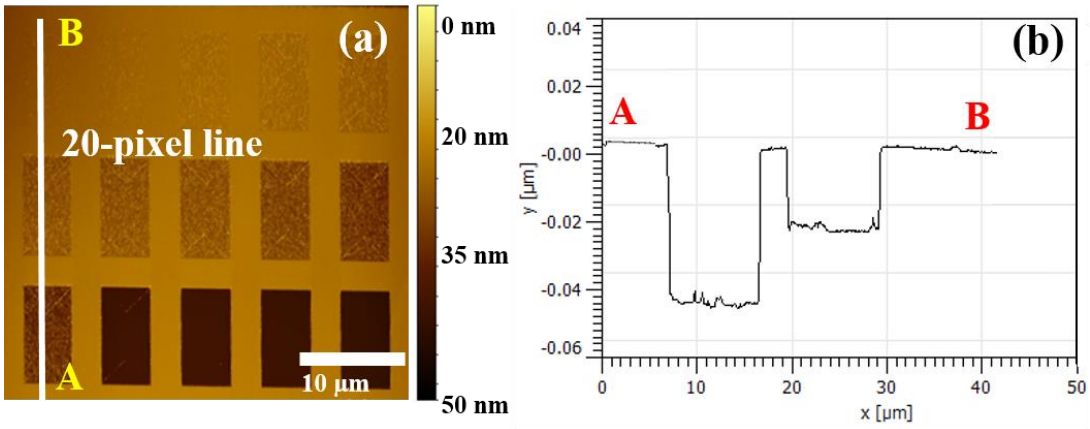

Figure 4.6: Line profile function in Gwyddion used for the extraction of the cross-section information from the AFM measurements. The line profile in (b) shows the cross-sectional information over the 20-pixel line marked in (a).

In order to generate exposure response curves for the different initial thicknesses of resist, the residual layer thickness was measured in AFM. Top-down 2D AFM images of the patterned 30 and 50 nm PMMA samples are shown in Figure 4.5 (b) and (d). Good consistency is demonstrated between the optical micrograph and the AFM results for the same patterned area. Gwyddion, an Open Source modular program for imaging analysis, was used to extract the height of features, surface roughness, etc. The line profile function was used to characterise the cross-sections of the patterned areas. After levelling the data by plane, a 20-pixel-thick line was dragged across the dose squares for extraction of data, such as depth, dimension and roughness. Figure 4.6 (b) shows the profile of the cross-section given by the line in Figure 4.6 (a). This technique was used to measure and characterise the residual thickness of PMMA and surface roughness on exposed/unexposed areas of the fabricated patterns.

4.4.3 Resist Sensitivity Investigation

Dose response curves (e.g. Figure 4.7) plot the normalized thickness of PMMA resist film (exposed and developed) as a function of received helium ion dose. The normalization is to the initial thickness prior to development, i.e. 20, 50 and 70 nm. Three regions of the dose exposure curves are identified in Figure 4.7: region A where low doses result in partial exposure and incomplete removal of the PMMA resist; region B where the resist is completely exposed and removed after the development revealing the silicon substrate and region C where high doses triggers the negative tone behaviour because of cross-linking of the PMMA molecules.

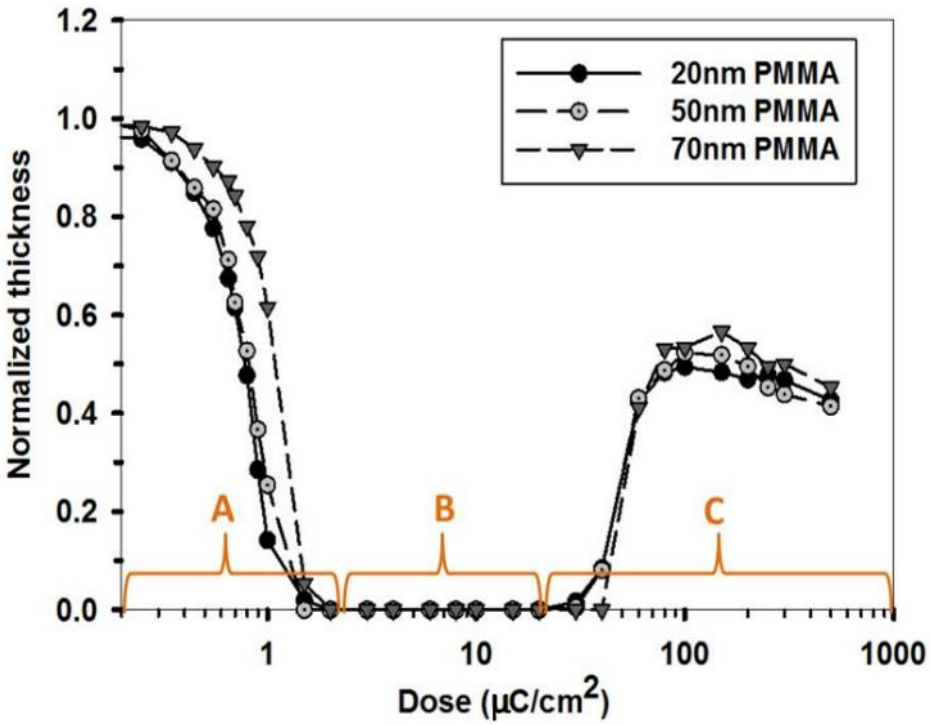

Figure 4.7: Exposure response curves showing the normalized thickness of residual resist layer as a function of dose for 20, 50 and 70 nm-thick PMMA upon helium ion beam exposure at 30 keV. The normalization is to the thickness prior to the development.

High sensitivity is confirmed where the He^+ ion dose required to expose and fully clear the positive tone PMMA with no resist remaining is ~2 μC/cm^2 for all three thicknesses. This is more than two orders of magnitude lower than the dose typically required for EBL exposure of PMMA based on literature [54]. It also matches the reported sensitivity improvement factor of 100-300 for HIBL compared to EBL in PMMA [5]. The high sensitivity of HIBL partly results from the high yield of SEs from helium ion beams [33]. Moreover, the generated SEs are mainly of low energy (<20eV [42]), to which the resists are particularly sensitive. At high exposure dose of ~40 μC/cm^2 or above, PMMA starts to exhibit negative tone behaviour as a result of cross-linking of the resist molecules. This threshold value is also 100 times less than that of the dose applied in electron beam as reported in [58]. The results in Figure 4.7 also show that, within the limits of experimental error, the sensitivity of PMMA in HIBL is independent of resist thickness for values of 20, 50, 70 nm. This is consistent with the ion mean range data in Figure 3.15: the ion energy is deposited below the resist layer for values in this range so that the dependence of sensitivity on resist thickness is weak.

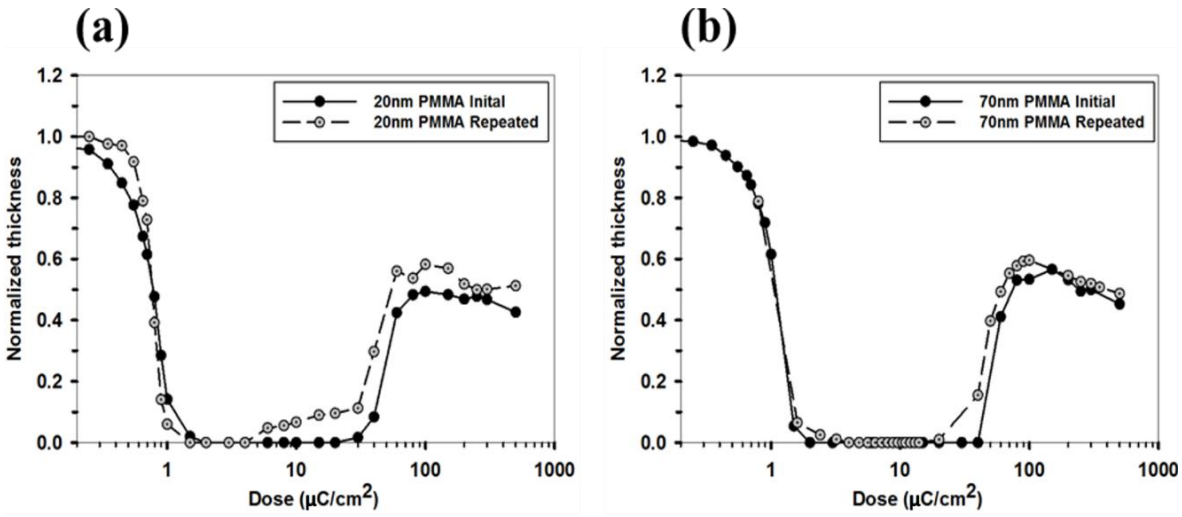

Figure 4.8: Exposure response curves show the normalized thickness of residual layer as a function of dose for (a) repeated 20-nm-thick PMMA and (b) repeated 70-nm-thick PMMA samples upon helium ion beam exposure at 30 keV. Normalization is to thickness prior to development.

To verify the reliability of the results, the experiment was repeated in 20 and 70 nm PMMA samples. All the processes including the coating of the resist, HIBL exposure and sample development were carried out within the same day and kept identical as the initial experiment. The exposure response curves were plotted for both the initial and repeated experiment in Figure 4.8, and they show good consistency and exhibit good repeatability. Due to the surface roughness, averaged values were used when measuring from the AFM result to obtain the residual thicknesses. Any defects on the surface such as small dust particles, or any noise during the measurement were included in the measurements and hence contribute to the averaged value. This error exists in both 20 and 70 nm sample measurements; however, the same amount of difference has bigger impact on the 20-nm sample when calculating the normalized value. This explains the larger variations in 20 nm sample compared to that in 70 nm.

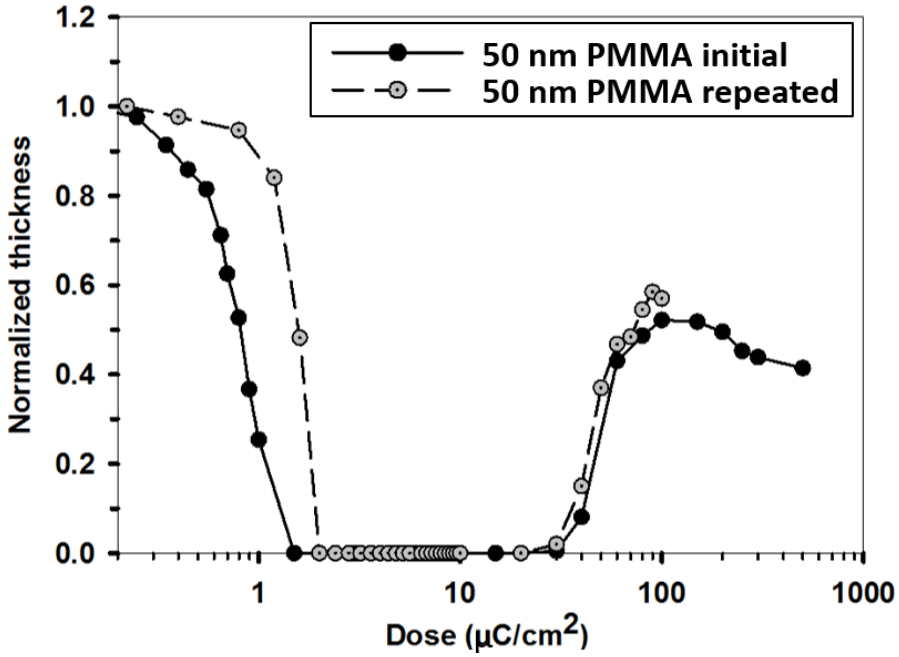

Figure 4.9: Exposure response curves of HIBL on 50-nm-thick PMMA resists freshly prepared before the exposure (line with black dots) and 24 hrs prior to the exposure (line with grey dots), revealing that the sensitivity was affected by the aging of the resist.

To evaluate whether time variation in processes can affect HIBL, the exposure and development processes were conducted 24 hours after coating the resist, as opposed to the standard process where all process slips are done sequentially without any gaps within one day. A significant shift to higher doses in the partially exposed area (Region A) on the dose response curve (line with grey dots in Figure 4.9) is observed, whilst other parts remain roughly unchanged. The dose required for a full exposure is 1.5 times more than that achieved in the standard processing condition and this may be partly due to the resist aging. Some preliminary investigation suggests that resist aging of PMMA can cause low PMMA contrast, shallower and widened features [105]. However, the exact reasons are unclear.

4.4.4 Surface Roughness Evaluation

Roughness values are extracted from the AFM data for the developed HIBL-exposed 20 nm PMMA sample in all three dose regions (Figure 4.10). The results reveal that the under-exposed material (region A) exhibits an average roughness of 0.3 nm (0.38 nm RMS) whereas the cross-linked material remaining after high dose exposures (region C) is as smooth as the polished bare silicon substrate surface from which all resist has been removed (region B). The average roughness in regions B and C is as low as 0.1 nm (0.11 nm RMS).

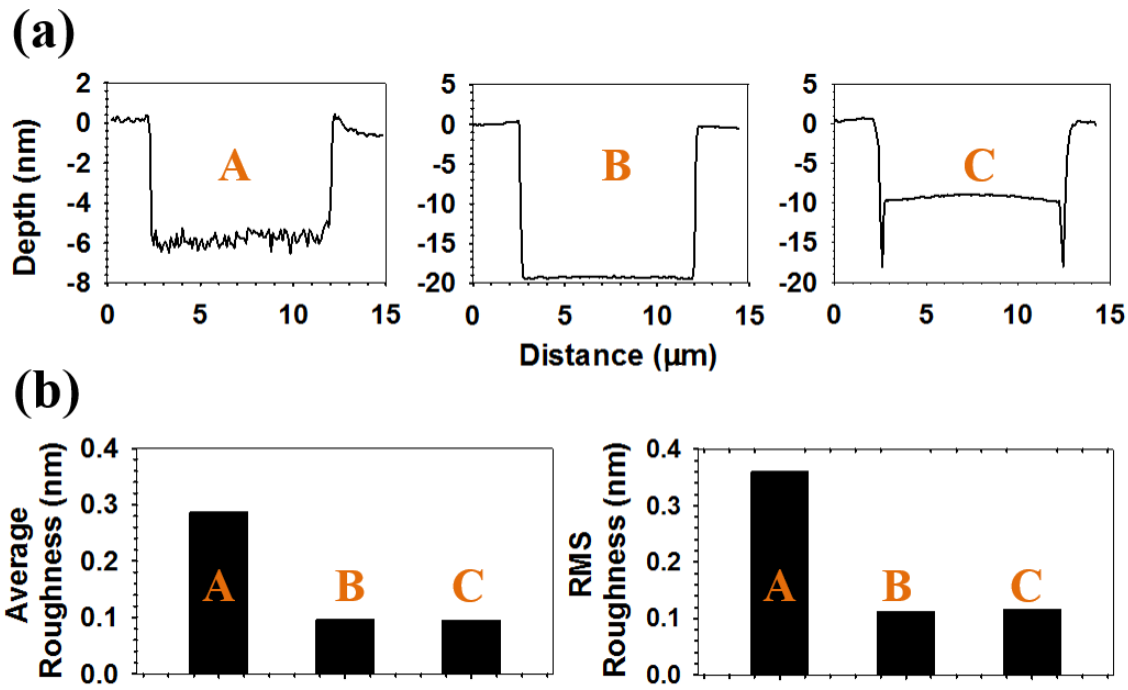

Figure 4.10: (a) Sample surface profiles obtained from 20-pixel-thick line across 3 dose regions of the patterned 20 nm PMMA sample; (b) Average and RMS roughness values for three dose regions extracted from the AFM data.

To find out whether a similar trend is exhibited in the 50 and 70 nm samples, roughness values in each dose region amongst all three thicknesses of PMMA samples are extracted and presented in Figure 4.11. The results reveal that compared to the 50 and 70 nm-thick PMMA films, the underexposed region (Region A) surface of the 20-nm-thick sample is smoother by approximately a factor of 3. The average roughness for 50 and 70 nm-thick samples are comparable and valued at 0.98 and 0.85 nm (1.25 and 1.03 nm RMS), respectively. Despite the considerable roughness difference in region A between thicker (50 and 70 nm) and thinner (20 nm) samples, in region C (high dose exposure region), all three thicknesses demonstrate low surface roughness valued between 0.05 to 0.14 nm for average surface roughness (0.072-0.18 nm RMS). This is a promising result for the use of high He^+ doses for negative tone resist patterning, a technique that with EBL is limited in resolution by proximity effect [106].

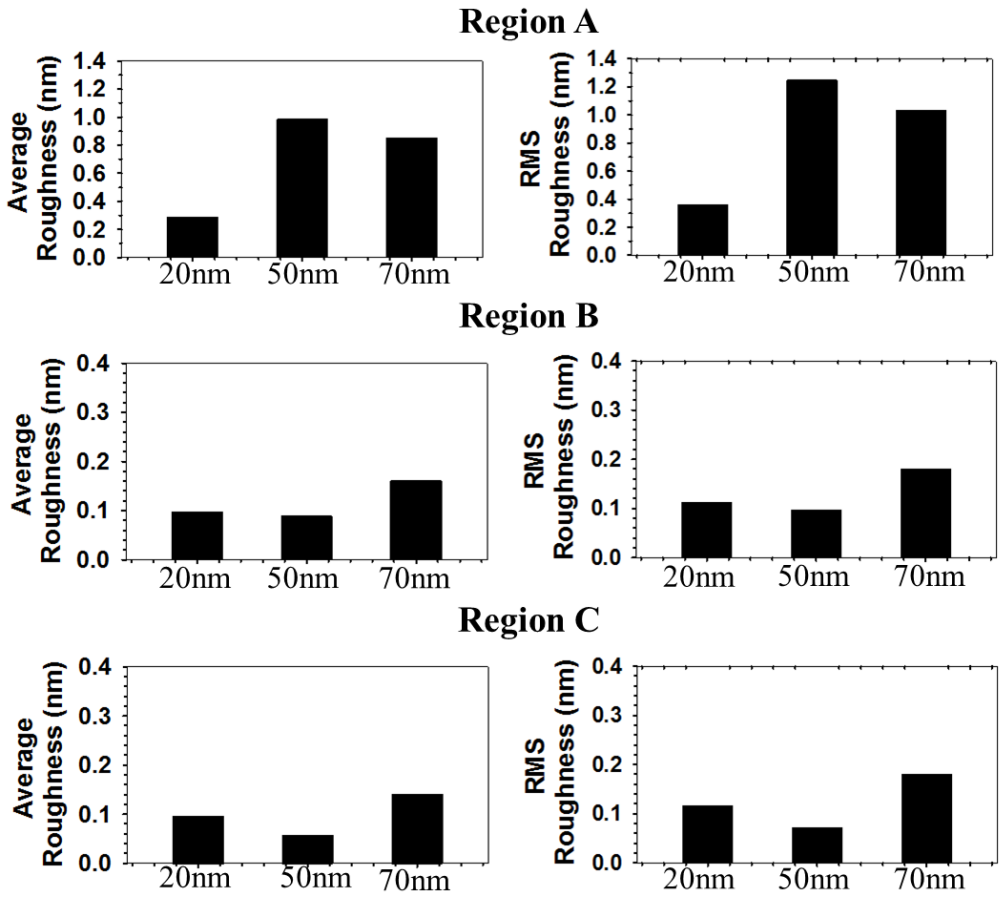

Figure 4.11: Average and RMS roughness values for patterned 20, 50 and 70 nm-thick PMMA samples in each dose region extracted from AFM data.

4.4.5 Pre-exposure Bake Investigation

Low resist surface roughness is key to achieving optimal line width and low LER in sub-10 nm features. Pre-exposure bake or soft bake allows solvent in the resist to evaporate prior to the exposure, hence increases the density of the resist. The bake has a direct impact on the resist surface, hence a recipe that produces a smoother resist surface is preferred. It is reported that low surface roughness was achieved by applying a 1-hour prebake at 170 ˚C and an average line width of 14.5 ± 2 nm was achieved on a 20 nm PMMA layer [54]. In previous experiments, all samples were pre-baked in the hotplate at 180 ˚C for 70s. To compare the different pre-bake recipes and study their effects on the sample surface roughness, the dose test experiment was conducted on a 20-nm PMMA with a 30-min pre-bake at 170 ˚C.

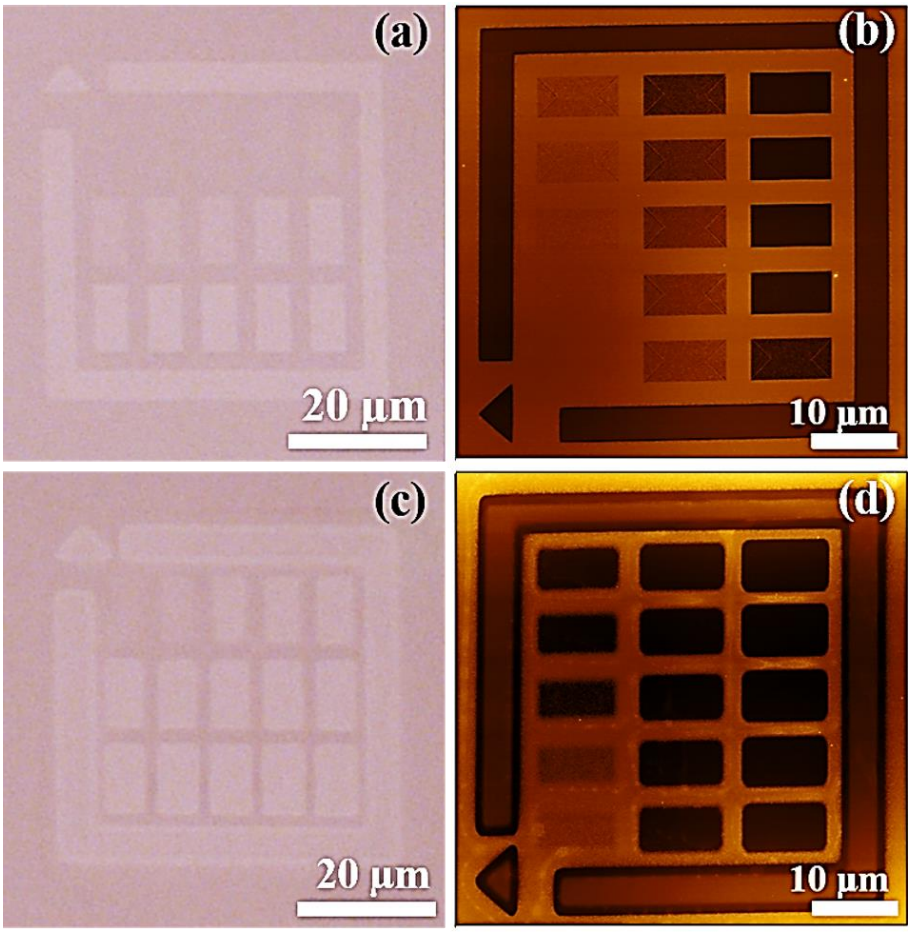

Figure 4.12: Optical micrographs of the patterned 20-nm-thick PMMA resist samples with (a) 70s and (c) 30 mins pre-bake respectively; (b),(d) Corresponding top-down 2D AFM images of the developed 20-nm-thick PMMA samples.

From the optical micrographs, the features in Figure 4.12b appear less sharp and clear compared to the previous results (Figure 4.12a). The same set of doses were applied to the dose areas in the experiments, however, greater contrasts are exhibited in Figure 4.12c. Higher sensitivity was confirmed via the dose response curve (Figure 4.13) extracted from the AFM measurements (Figure 4.12d) and this explains the higher contrasts. The full exposure was achieved at only 0.5 µC/cm^2, which is 4 times more sensitive than previous results. Except for a significant shift to the lower doses in region A, the overall behaviour is not considerably different from the previous sets of results in region B and C.

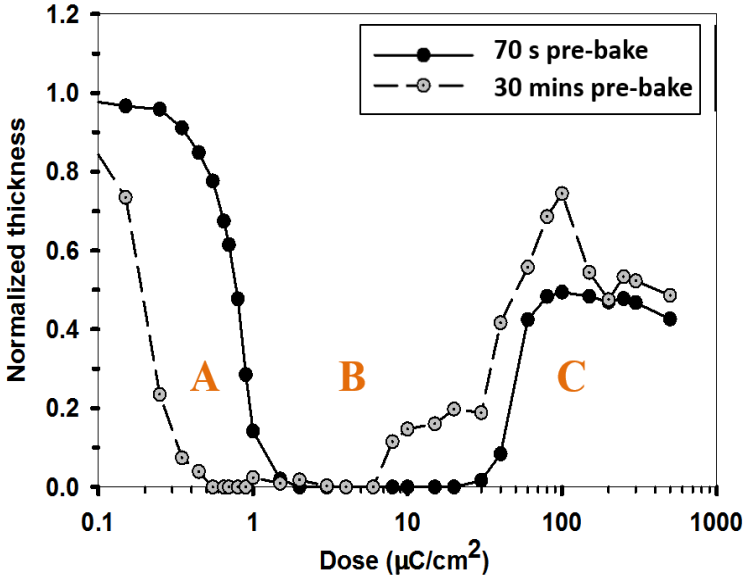

Figure 4.13: Exposure response curves of HIBL on 20-nm-thick PMMA resists with 70 s and 30 min pre-exposure bake in the hotplate prior to the helium ion beam exposure at 30 keV and the development process.

The surface roughness of the 30-min pre-baked sample was measured and presented in Figure 4.14. Compared to the previous results obtained from a 70-s pre-bake recipe, although a slightly smoother surface is demonstrated in Region A with 0.04 nm less in average roughness value (0.05-nm decrease in RMS), no obvious overall improvements were observed. Further study on reducing surface roughness of the fabricated sample surface can be carried out by testing different resist solvents, varying pre-bake temperature and time, however, based on the current results, 70s pre-bake recipe is used for all following experiments including resolution tests and proximity effect investigation.

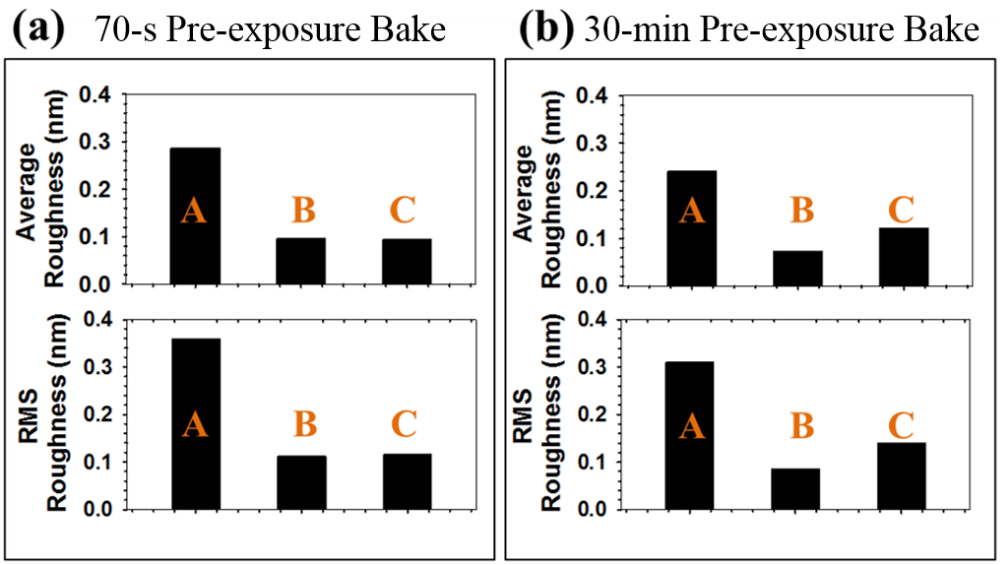

Figure 4.14: Average and RMS roughness values for patterned 20-nm-thick PMMA resists with (a) 70 s pre-bake and (b) 30 min pre-bake in the three dose regions extracted from AFM data.

Overall, good consistency and repeatability was demonstrated in HIBL on PMMA when the experimental conditions are controlled. It is found that the behaviour of the partially exposed area (Region A) could be changed by varying process timings, hence affecting the resulting dose response curve. However, with more understanding and experiments, this property could be employed in the future when the dose required to form a specific pattern needs to be adjusted into a certain range that is higher or lower than its default value.

4.4.6 High Resolution Sparse Feature Patterning

As explained in Section 2.2.2, the HIM is capable of generating a subnanometer probe size owing to the extremely high brightness GFIS and the use of helium gas. Furthermore, the highly localised ion-solid interactions make it theoretically possible to fabricate features of comparable size to the beam spot. Modelling work described in the previous section suggests that HIBL is expected to achieve higher resolution patterning than EBL. An experiment to characterise minimum feature size for HIBL on PMMA was conducted using the ECP pattern in Figure 4.3 with line doses ranging from 2 to 37 pC/cm. Figure 4.15 shows HIM images of 1.5 µm long, high-resolution single-pixel sparse line features on the 20-nm-thick PMMA resist layer after development process. It is observed that the linewidth increases from Figure 4.15a through Figure 4.15e with an increased applied dose.

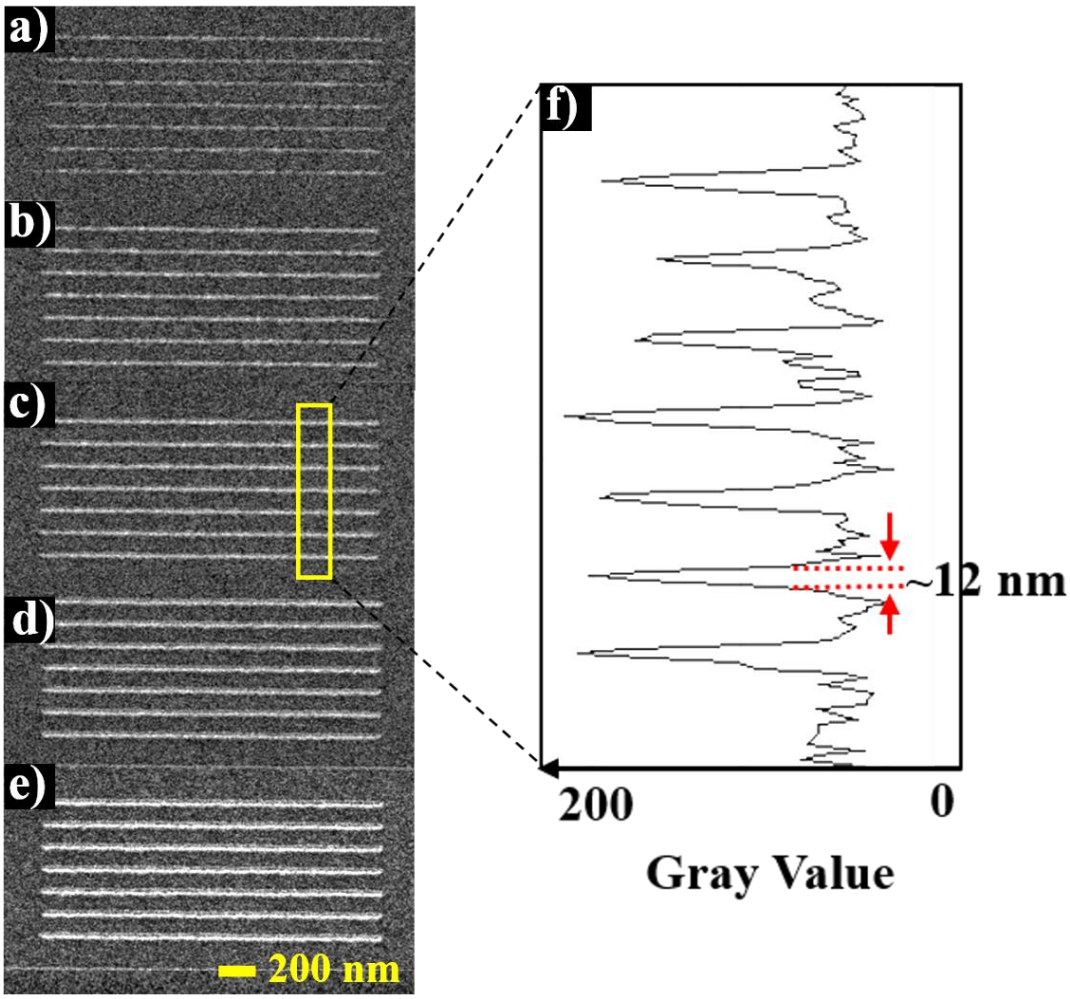

Figure 4.15: HIM image of sparsely-spaced single-pixel lines on 20-nm PMMA with line doses of (a) 2 pC/cm, (b) 3 pC/cm, (c) 4 pC/cm, (d) 12 pC/cm amd (e) 30 pC/cm. Line widths of approximately 12 nm were confirmed from the SE contrast line profile (c).

Conventionally, trenches appear darker whilst hills appear brighter than the surrounding area on SE images. However, the lines formed by the removal of PMMA molecules after scission process appear brighter in Figure 4.15. This reversed contrast can be explained by the edge effect. There are more secondary electrons emitted from the edges due to a larger surface area, resulting in a higher signal intensity. However, some of the emitted electrons from the trenches become trapped and get absorbed by the side walls, resulting in a lower intensity, and so appear darker. Hence, the bright lines show the effect of the two edges merged together at this ×25k imaging magnification, suggesting the trenches formed are extremely narrow. To verify this, AFM measurements were performed to confirm the topographical properties of the fabricated line. High resolution AFM scans (see Figure 4.16) show good correspondence with the HIM images and verify positive tone exposure of narrow lines, i.e. fabricated lines are trenches rather than hills.

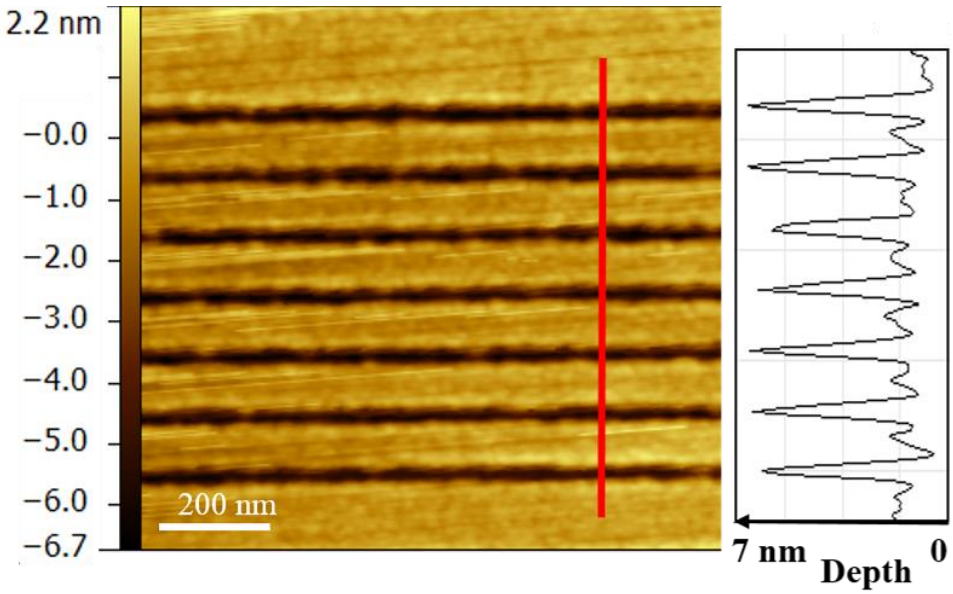

Figure 4.16: AFM image and line profile of pattern in Figure 4.15e demonstrating positive tone exposure as the bright lines in the HIM image correspond to the trenches in AFM scan.

Very thin lines were fabricated using the line dose of 2 pC/cm as shown in Figure 4.17a, however, the lines appear very shallow with a low contrast from the unpatterned PMMA. There is also a greater linewidth variation compared to the lines formed with higher doses, suggesting that resist was not fully cleared due to the underexposure. Lines exposed at 5 pC/cm or above appear straighter (see Figure 4.17c); the line widths however were broadened suggesting overexposure has occurred. The optimum line dose was identified to be 4 pC/cm (Figure 4.17b), where clearly resolved and well-defined lines with widths of approximately 12-nm-wide lines in a 20-nm-thick PMMA layer on silicon was achieved. The linewidths were measured at various locations by the SE contrast line profile from the HIM images with 20-pixel line averaging and the averaged value taken as the critical dimension as shown in Figure 4.15f.

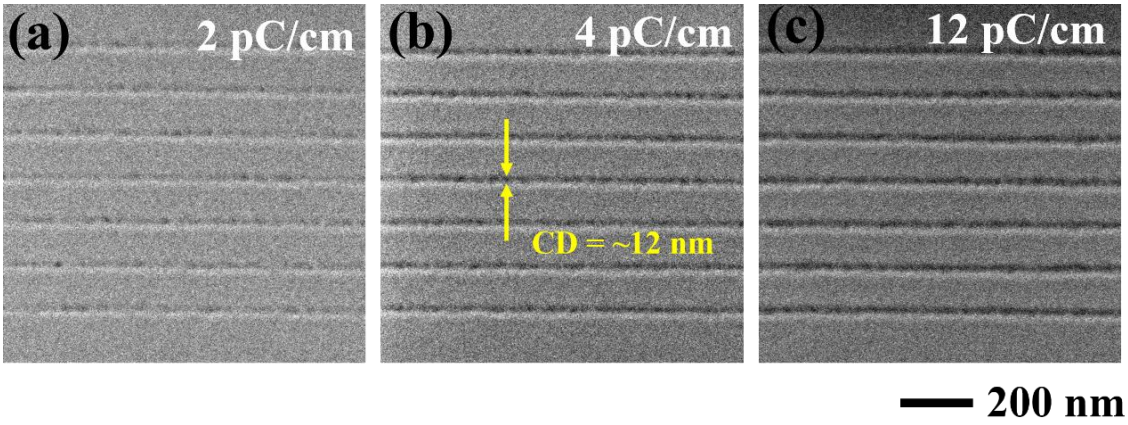

Figure 4.17: HIM images show the single-pixel sparsely-spaced line patterns exposed on 20-nm-thick PMMA resist. The line doses are (a) 2 pC/cm, (b) 4 pC/cm and (c) 12 pC/cm.

4.5 Conclusions

In summary, results so far collectively demonstrate the potential of the HIM as a high-resolution patterning tool for nanofabrication, in addition to its state-of-the-art imaging capabilities. The high sensitivity enables HIBL for the rapid prototyping of nanoscale designs. However, the demonstrated line widths of 12 nm in PMMA are well in excess of the resolution limits of the helium ion probe, indicating that resolution is being limited by other factors rather than the HIBL technique itself. Contributing factors include the properties of the PMMA resist such as molecular size, and the development method used which is known to play a key part in minimum pattern definition in PMMA [70], [107].

CHAPTER 5

PROXIMITY EFFECT COMPARISON IN HELIUM ION AND ELECTRON BEAM LITHOGRAPHY*

5.1 Introduction

Proximity effect is an effect where an area adjacent to the primary exposed area is exposed unintentionally. This effect is pronounced in EBL due to beam broadening from the backscattered/deflected primary electrons and their resulting secondary electrons. Helium ions have limited backscattering and ion deflection [27], [53], and this leads to a much-reduced proximity effect in lithography, enabling patterns with higher density and resolution to be fabricated. The quantification of the proximity effect will allow for better understanding of the resolution limits and the patterning capabilities in HIBL in comparison to EBL. However, there is yet to be a direct comparison of these two techniques on thin layer resists. Here, we present a quantitative and direct comparison study on EBL and HIBL with respect to sensitivity and proximity effects in PMMA, leading to a demonstration of high resolution HIBL patterning of line arrays.

---

* Based on conference submissions entitled “Proximity effect quantification and dose optimization for high resolution helium ion beam lithography (2015)” and “A quantitative comparison between helium ion and electron beam lithography on PMMA resist (2016)” presented in Micro and Nano Engineering (MNE).

5.2 Quantification of Proximity Effect

The proximity effect can lead to pattern broadening, edge blurriness and pattern distortion, limiting the highest achievable resolution at high densities. Previously, the proximity effect has been observed in the AFM micrograph of the large areas patterned using HIBL (shown in Figure 5.1), where doses ranging from 8 to 100 μC/cm^2 (top left to bottom right) were exposed on a 50-nm-thick PMMA layer. Areas with dark colour on the AFM image correspond to trenches on the sample, whereas areas with light colour show the unexposed resist. The areas with darkest colour represent the silicon substrate where PMMA was fully exposed and removed (first 6 rectangles counting from the top left corner). The other nine dose squares are of brighter colour, representing shallower trenches where PMMA behaves as a negative tone resist due to the overexposure and the cross-linked materials remained on the silicon.

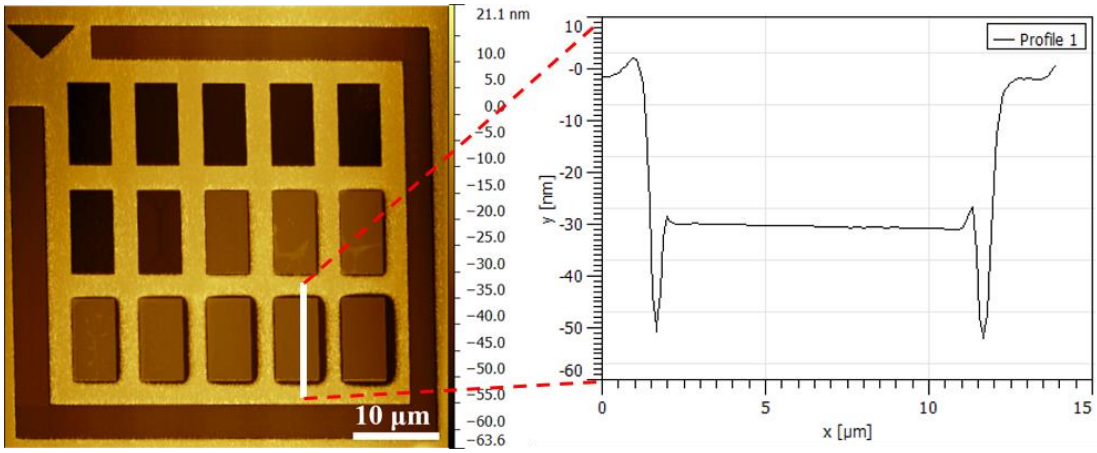

Figure 5.1: (a) AFM image of a developed dose test pattern on a 50-nm-thick PMMA resist layer using HIBL from Chapter 4; (b) Line profile shows the depth information across an overexposed dose area revealing proximity effect.

It was observed that around the overexposed areas were thin strips with darker colour that is comparable to that of silicon substrate, suggesting deeper trenches are around the patterned areas. While no apparent distortion is exhibited in the primary exposure areas, the widths of the darker strips widens as the dose increases amongst the overexposed squares. Both facts suggest that full clearance dose (between 2 and 30 μC/cm^2) were received just outside the edges of the pattern due to the proximity effect and this was confirmed by the line profile (Figure 5.1) obtained from the AFM. In this case, the proximity effect was pronounced due to the opposite resist tone that PMMA adopts under different doses. In other cases, proximity effect can be identified by comparing the actual shape/dimensions of a pattern fabricated by a calibrated instrument against the original pattern design.

A large beam current of 5 pA as well as a long dwell time were used to deliver the dose efficiently across the large patterning area. However, the resulting bigger probe size decreases the pattern resolution and worsens the proximity effect. During the exposure, the long dwell time could lead to the occurrence of stage drift, which can also contribute to the formation of the fully exposed strips around the edges. Hence, these results may not accurately represent the typical proximity effect in HIBL.

Previously, several approaches have been developed by others to determine the proximity parameters in EBL [60], [61], [63]. Here, a "doughnut" method described by Stevens et al. [108] was adapted for use to quantify the proximity effect in HIBL on the positive-tone benchmark resist PMMA coated silicon.

An array of doughnut structures with variable inner radius (R_1) and a fixed outer radius (R_2) were exposed at various doses Q (see Figure 5.2).

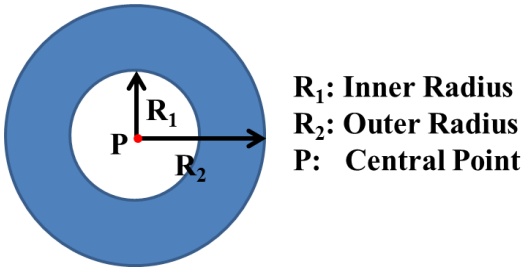

Figure 5.2: Doughnut structure with inner radius R_1 and outer radius R_2 were used for proximity effect investigation. The ring coloured in blue is to be exposed by primary helium ions.

When the outer radius (R_2) is set to be much greater (2 times or more) than the backscattering range of the primary particles (β) and the inner circle has just been fully cleared due to the proximity effect, the effective dose received at the centre of the inner circle (Q_p) can be expressed in the following expression [108]:

$$Q_p = D_0 = \frac{Q}{(1+\eta)}\left[e^{-\left(\frac{R_1}{\alpha}\right)^2} + \eta\, e^{-\left(\frac{R_1}{\beta}\right)^2} \right] \qquad (5.1)$$

where Q is the exposure dose and D_0 is the critical dose that just leads to a full clearance of the positive-tone resist. This formula is greatly simplified from the original Double Gaussian function (see *Section 2.4.2*) due to the radial symmetry of the pattern. When the feature sizes are much bigger

than the forward scattering range α (for helium ions α is typically less than 5 nm [5], [27]), the forward scattering component can be eliminated [109]. The function is further simplified to:

$$\ln Q = \frac{1}{\beta^2} R_1{}^2 + \ln\left[\frac{Q_p(1+\eta)}{\eta}\right] \qquad (5.2)$$

, where lnQ is linearly proportional to R_1^2. The inner circle of the doughnut is not directly exposed to the primary beam and so if the material here is cleared then it has been exposed through proximity effects. The critical dose, Q_p, at which this happens is such that Q_p is equal to the sensitivity of PMMA. Hence, the experiment relies upon identification of the value of the set inner radius of the doughnut for which the resist is fully cleared right to the centre, and the doughnut annulus becomes a full circle.

In the following sections, the proximity effect quantification using HIBL and EBL on the 20-nm-thick benchmark resist PMMA coated silicon will be presented, where the design of patterns, experimental procedures, results and discussion are described.

5.3 Exposure Pattern Design

Before carrying out the proximity effect comparison in HIBL and EBL, the resist sensitivity of 30-keV EBL in PMMA was first investigated. Figure 5.3 shows the pattern designed for the large area exposure using Elphy Quantum. The pattern has an overall writing field of 100 μm by 100 μm, comprising an eight-by-four array of rectangles with a dimension of 5 μm × 10 μm. This dimension has been used in the HIBL resist sensitivity experiment (Figure 4.1) which allowed for easy navigation and data extraction under the AFM. However, the spacing between two rectangles in the EBL pattern was designed to be either 7.5 horizontally or 15 μm vertically, which is much greater than that in HIBL pattern. Spacing out the exposures in such a way has two purposes, the first is to avoid primary exposure areas receiving any extra dose from the adjacent exposures via the proximity effect; and the second is to test for an optimal spacing to use in the following doughnut structures. Different GDSII number was given to each dose square, and the dose variation was achieved by varying electron beam dwell times, whilst the beam current and step size remained unchanged. Up to 32 doses can be experimented using this pattern.

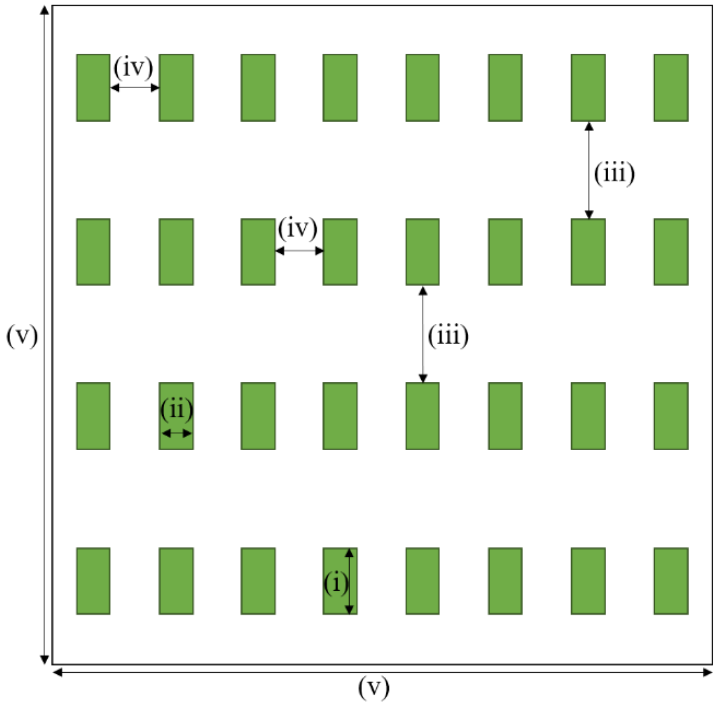

No.	(μm)
(i)	10
(ii)	5
(iii)	15
(iv)	7.5
(v)	100

Figure 5.3: Schematic of the pattern generated in Elphy Quantum for large area dose test to determine the dose response curve for fullerene resist using EBL.

The pattern for the investigation of the proximity effect in HIBL was designed in ECP (see Figure 5.4). It has a 10 μm × 10 μm field size in which there are 50,000 by 50,000 addressable pixels. Hence, the minimum pixel spacing is 0.2 nm which is much smaller than the estimated HIM probe size to avoid any discontinuity in the exposed pattern, especially when the ion beam is extremely focused. The design consists of two main parts: the edge markers and the 7 × 7 doughnut array. The asymmetrical, 2-μm-thick edge markers were designed not only for the orientation definition, but also for locating the pattern after the development during the optical/helium ion microscope characterisations. The doughnut array lies within the 6 μm by 6 μm field surrounded by the edge markers.

The doughnuts are 400 nm away from the edge marker and they are also evenly spaced at 400 nm from each other. This distance is far greater than the reported helium ion backscattering range [42], ensuring that all prime exposure areas will be unaffected by the nearby exposures. All doughnuts have a fixed outer radius of 200 nm whilst the inner radii vary. Doughnuts in the same column are exposed to a same dose, but the inner radii of the doughnuts decrease from top to bottom. The inner radii of the doughnuts in the same row are kept the same, however, the doses applied increase from left to right. Thus, up to seven doses can be investigated for each pattern exposure. For this study, doughnuts with inner radii ranging from 125 nm down to 2.5 nm were fabricated in HIBL. The ECP coding to generate the exposure pattern in Figure 5.4 can be found in Appendix 8.1.

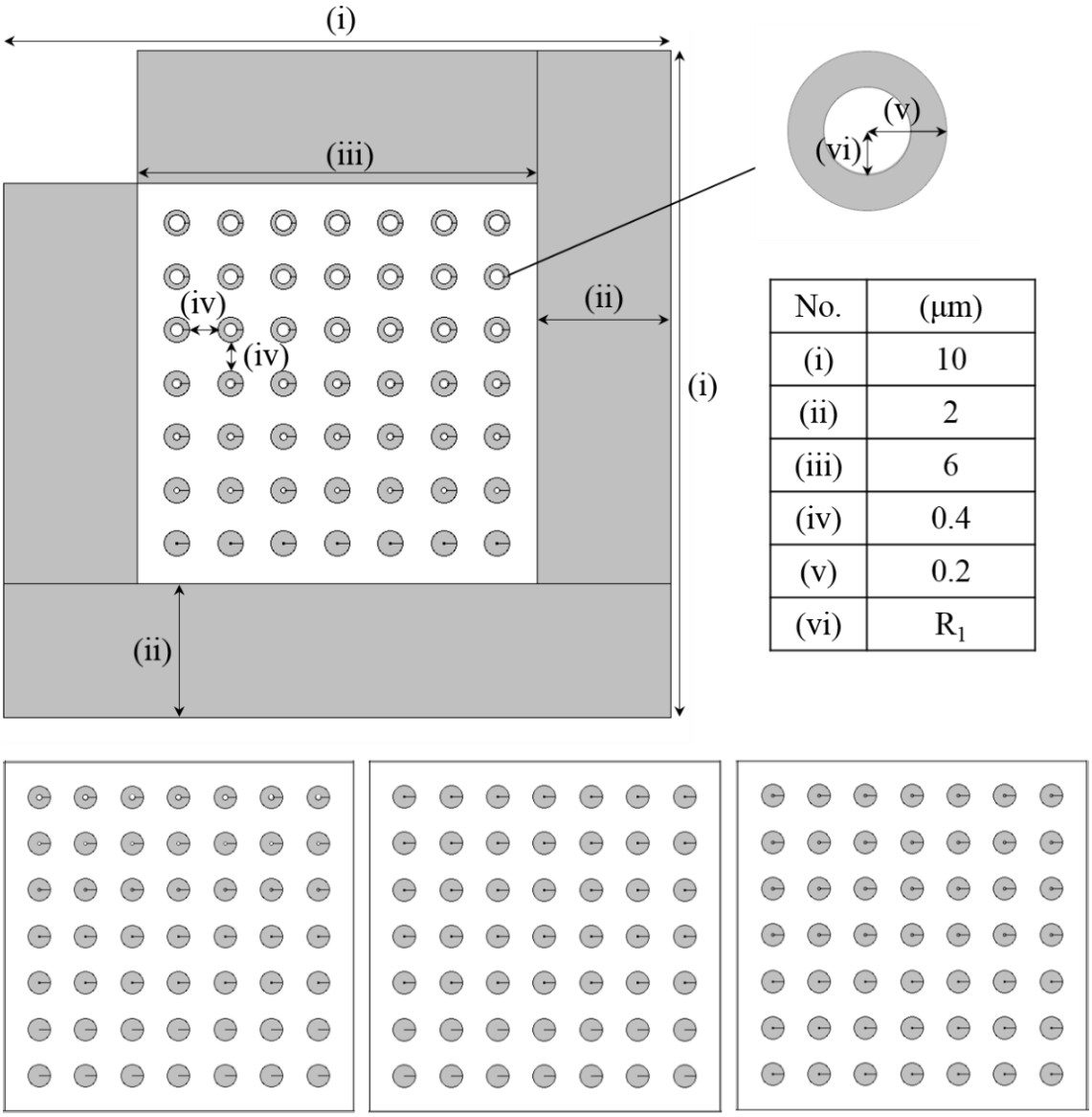

No.	(μm)
(i)	10
(ii)	2
(iii)	6
(iv)	0.4
(v)	0.2
(vi)	R_1

Figure 5.4: The doughnut arrays designed in ECP for 30-keV HIBL proximity effect investigation has a FOV of 10 μm × 10 μm, consisting of 7 × 7 doughnuts with a fixed outer radius of 200 nm and varied inner radii.

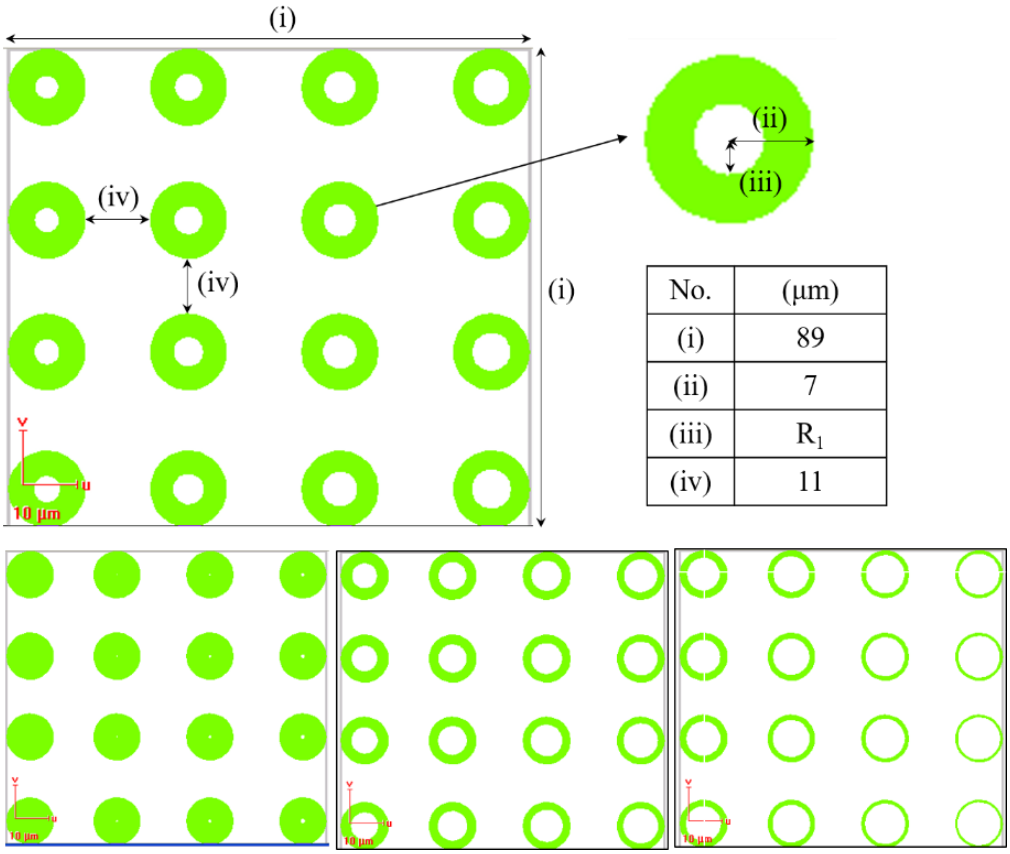

No.	(µm)
(i)	89
(ii)	7
(iii)	R_1
(iv)	11

Figure 5.5: The doughnut arrays designed in Elphy Quantum for 30-keV EBL proximity effect investigation has a FOV of 89 µm × 89 µm, consisting of 4 × 4 doughnuts with a fixed outer radius of 7 µm and varied inner radii.

The doughnut arrays designed in Elphy Quanum for the investigation of proximity effect in EBL is shown in Figure 5.5. The pattern occupies an area of 89 µm × 89 µm, but it will be exposed with a 100 µm × 100-µm write field, creating an 11-µm space between the doughnuts and the edge of the write field. The 4 × 4 doughnut array enables 16 inner radii variation per pattern and exposed to one electron dose. The dose variation is achieved across patterns that are exposed with different electron beam dwell times. This design is greatly simplified compared to that with varied doses within the pattern, and time is saved by having all doughnuts on a single layer without setting different dose parameters. It is also easier to identify the critical doughnuts during the characterisation stage. The outer radius is fixed at 7 µm, which is much greater than the reported electron backscattering range [62], and the inner radius ranges from 0.04 µm to 6.5 µm.

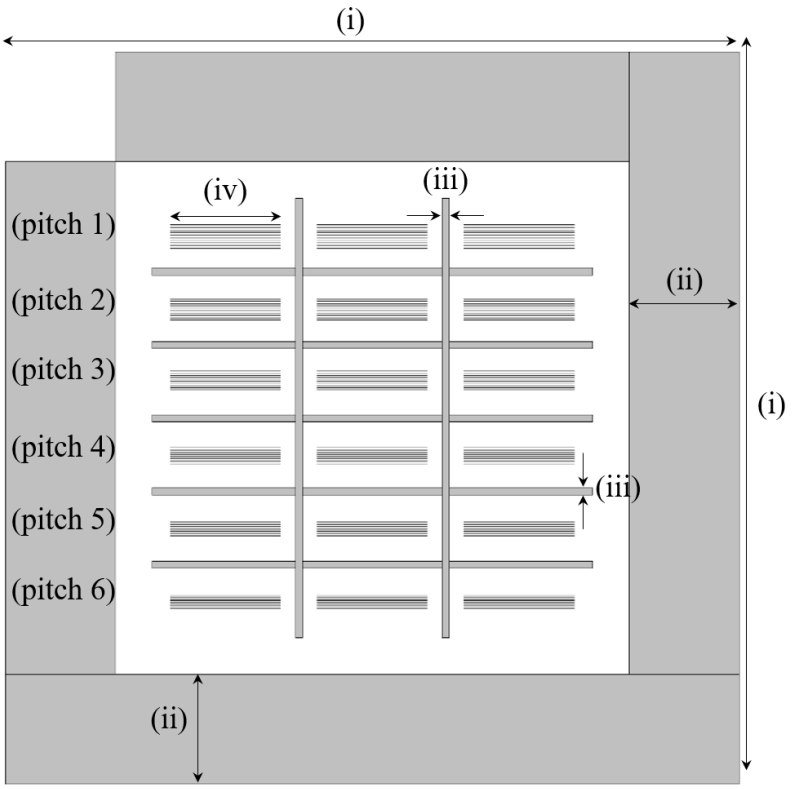

No.	(μm)
(i)	10
(ii)	1.5
(iii)	0.1
(iv)	1.5
Pitch 1	0.38
Pitch 2	0.34
Pitch 3	0.30
Pitch 4	0.28
Pitch 5	0.26
Pitch 6	0.24

Figure 5.6: Schematic of dense single-pixel line arrays with pitches ranging from 38 nm to 24 nm designed in ECP to determine the highest pattern density achievable on 20-nm-thick PMMA resist.

To find out the minimum pitch achievable in 20-nm-thick PMMA using 30-keV HIBL exposure, high-density single-pixel line arrays were designed in ECP as shown in Figure 5.6. The 3 × 6 single-pixel line arrays were surrounded by the 1.5-μm-thick edge marker. The line pitches decrease from top to bottom covering a range of 38 nm – 24 nm, whilst the line arrays in the same row having a same pitch. The line doses increase from left to right and the dose is the same for line arrays in one column. The range of the dose can be easily expanded by exposing the pattern with different sets of doses. The ECP coding to generate this pattern can be found in Appendix 8.1.

5.4 Experimental

Silicon chips were spin coated with 20-nm-thick PMMA layers and baked in the hotplate at 180 ^{o}C for 70s, following the working procedure described in Chapter 4. Doughnut structures were exposed using a 30-keV helium ion beam with a 10-μm aperture and a working distance of 7 mm. The beam current was 0.5 pA, and doses ranging from 0.5 μC/cm^2 up to 500 μC/cm^2 were experimented with a focus on the full-clearance dose range of 2 - 40 μC/cm^2 for PMMA (as shown in region B of Figure

4.7). For the high-resolution high-density line arrays, a beam current of 0.4 pA was used and the line doses ranging from 3-5 pA were investigated based on the results obtained in Section 4.4.6.

To find out the resist sensitivity in EBL, the PMMA samples were exposed in the Gemini FEG-SEM (NVision 40 FIB SEM) to a 30-keV focused electron beam generated from a Schottky source at a working distance of 7.6 mm. A current of 112 pA was used with a beam limiting aperture of 20 µm covering a dose range of 0-30,800 µC/cm. The base dose was set to be 10 µC/cm^2 with a step size of 0.022 µm and the dwell time was 0.000432 ms. The dose factor is calculated as the desired dose divided by the base dose. For instance, if the doses to be applied are 10 µC/cm^2, 20 µC/cm^2 and 35 µC/cm^2, the dose factors of 1, 2 and 3.5 are assigned to each of the feature, respectively.

For the doughnut structures fabricated using 30-keV EBL on 20-nm-thick PMMA, a beam current of 289.1 pA was used with a 30-µm aperture. Five dose ranges were recognised from the full dose range of 80-4000 µC/cm^2, for the exposure of pattern with different inner radii ranges, as demonstrated in Table 5.1. The smallest dose in each range was set to be the base dose, the step size, i.e. pixel spacing, and the beam dwell time were varied to achieve 27 exposure doses. This is identical to the way of varying dose in HIBL exposures using ECP, making the two methods comparable.

EBL dose range (µC/cm^2)	Inner radii (µm)	Aperture (µm)	Current (pA)	Step size (µm)	Dwell time (ms)	Base dose (µC/cm^2)
80 – 140	0.04 – 0.8	30	289.1	0.014	0.000542	80
150 – 225	1.4 – 2.8	30	289.1	0.010	0.000519	150
250 – 400	2.2 – 3.8	30	289.1	0.008	0.000553	250
400 – 1600	3.8 – 5.5	30	289.1	0.006	0.000498	400
2000 – 4000	5 – 6.5	30	289.1	0.004	0.001107	2000

Table 5.1: Five EBL dose ranges (column 1) and their respective doughnut-array patterns designed in the Elphy Quantum with varied inner radii (column 2) for the proximity effect investigation. Column 3-7 show experimental parameters such as electron beam current, aperture size, step size and dwell time used in EBL exposure for each doughnut pattern.

All samples were developed in MIBK/IPA (1:3) solution at room temperature for 60s and rinsed in the stopper DI water before being blow-dried by nitrogen. It is worth noting that apart from the exposure method, identical procedures were carried out in the same lab environment to minimise the uncertainness in the results.

The produced structures were then characterised and analysed using the following techniques: The tapping mode of Multimode AFM (Veeco) was used to extract depth information from the large

features as well as the doughnuts with a scanning rate of 0.723 Hz and sample/line resolution of 512. HIM was used to obtain high-resolution images for HIBL doughnuts with the following conditions: 30-keV beam energy, 0.5-pA current with a 10-µm aperture and a working distance of 6.9 mm. The top-down images of the fabricated EBL samples were captured using SEM with a 2-keV electron beam energy. 30-µm aperture was selected, and the beam current was 289.1 pA with a working distance of 7.6 mm. The brightness value was 49.5% and a contrast of 27%. Scan speed of 6 and line averaging of 5 (for noise reduction) were adopted to generate images in 1024 ×768 resolution.

5.5 Results and Discussion

5.5.1 Resist Sensitivity Comparison in HIBL and EBL

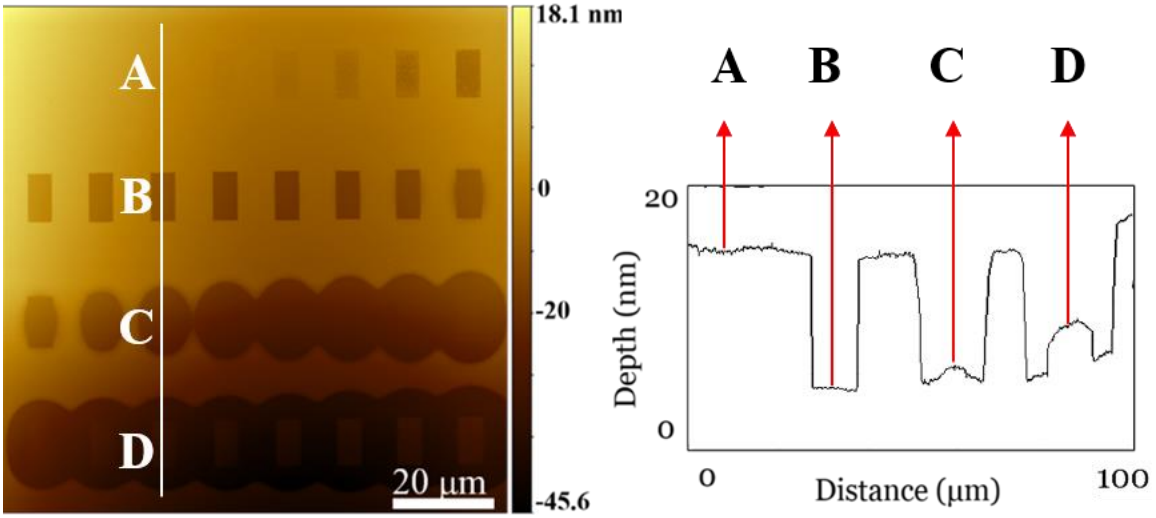

Figure 5.7: Top-down 2D AFM images of exposed and developed patterns on 20-nm-thick PMMA on silicon using a 30-keV electron beam. The pattern consists of 32 rectangular areas of 5 µm × 10 µm exposed to various electron doses.

Top-down 2D AFM image (e.g. Figure 5.7) shows the fabricated large area exposure for resist sensitivity characterisation using 30-keV EBL on 20-nm PMMA resist. Contrast variations display amongst the dose squares due to the thickness differences of the resist residuals after development. The high brightness background in AFM image corresponds to the unexposed resist, the dark areas correspond to the positive pattern resulting from the removal of exposed PMMA after development (i.e. the darker the colour, the deeper the trenches). The negative pattern has a reduced layer thickness compared to the unpatterned resist, hence, it has an intermediate brightness. Different from the HIBL results in 20-nm PMMA resist shown in Figure 4.6, where the dimensions of the fabricated dose squares are identical to that in the designed pattern irrespective to the dose applied, significant pattern broadening due to the proximity effect was observed in the EBL-fabricated dose areas exposed to

high doses. The line profile in Figure 5.7 demonstrates how the length of the fabricated pattern increases with increase of dose in the negative region of the resist (D > C > B = A). The horizontal spacing of 7.5 µm has proven to be insufficient in length, since patterns exposed to a high dose were merged together due to the long range of the backscattered electrons.

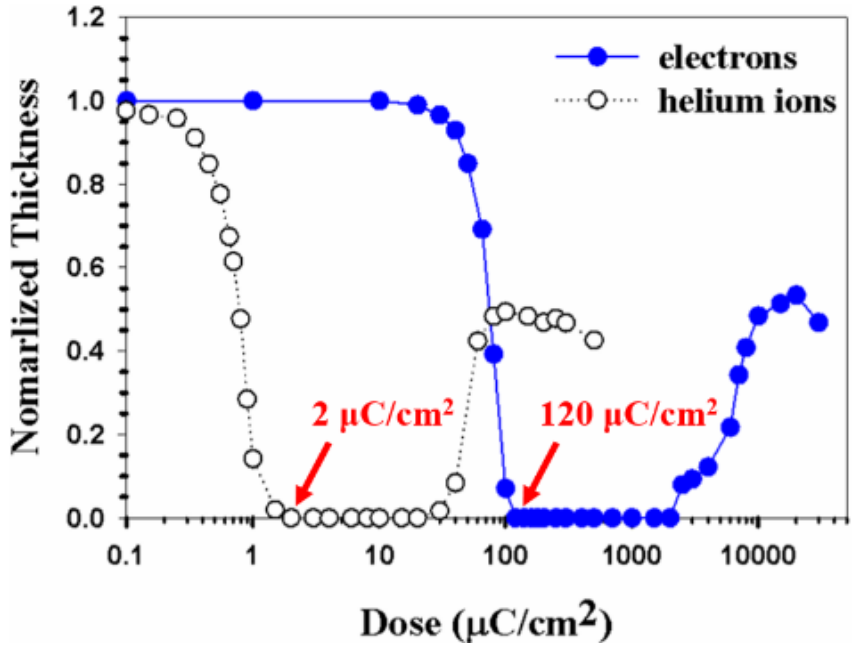

Figure 5.8: Dose response curves of 20-nm PMMA on silicon substrate using He^+ and electron beam exposures at 30 keV, revealing two orders of magnitude sensitivity enhancement in HIBL compared to EBL, respectively.

To generate the dose response curve for 30-keV EBL, the residual layer thickness was measured in AFM. The results plotted for comparison with HIBL results for exposure of 20-nm PMMA on silicon substrate (previously in Figure 4.7) are shown in Figure 5.8. For both beams, PMMA behaves as a positive tone resist for low dose range and exhibits negative tone behaviour when it is exposed to a high dose. A reduced layer thickness is observed in the negative region and the trend of decreasing thickness continues with increasing dose. This may be caused by shrinkage of the resist under heavy bombardment by energetic particles. The PMMA sensitivity values are 2 and 120 µC/cm^2 in HIBL and EBL respectively, after identical resist preparation and development processes, negative tone resist behaviour begins at 60 and 2500 µC/cm^2, respectively. The sensitivity enhancement of HIBL compared to EBL is therefore confirmed, with a gain of 60 in the positive tone region and a gain of 42 in the negative none region, while maintaining similar contrast values of ~1.

5.5.2 Proximity Effect in HIBL and EBL

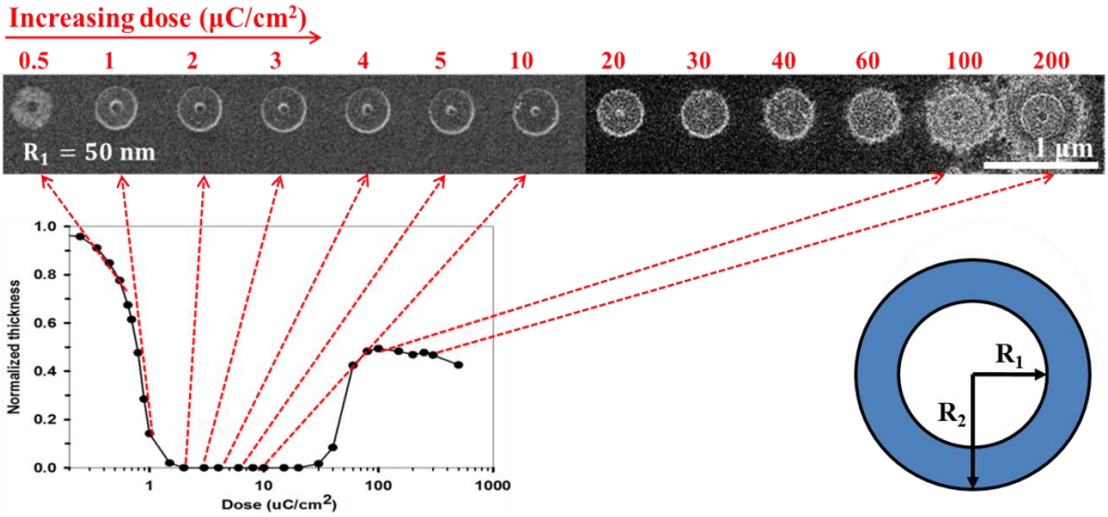

Figure 5.9: HIM images show examples of fabricated doughnut structures using 30-keV HIBL on 20-nm-thick PMMA on silicon after development. The doughnuts have fixed outer radius (R_2) of 200 nm and inner radius (R_1) of 50 nm across a dose range from 0.5 to 200 μC/cm². The dose used for each doughnut was marked on the dose response curve of the HIBL on PMMA.

Figure 5.9 shows an example of HIM images of the fabricated doughnut structures with outer radius of 200 nm and inner radius of 50 nm using 30-keV HIBL on 20-nm-thick PMMA on silicon after development. The exposure doses used to expose the doughnuts were marked on the PMMA dose response curve correspondingly. It is observed that with an increase of the exposure dose (from 0.5 μC/cm² – 40 μC/cm²), the diameter of the central remaining core of the resists reduces. The exposure of the inner circle is caused by the proximity effect and when the dose is further increased to 60 μC/cm², the entire 50-nm-radius inner circle received exactly enough dose to reach full clearance and disappeared after development. For the doughnuts overexposed with doses of 100 μC/cm² and 200 μC/cm², both the unexposed inner circle and the area outside of the ring received sufficient dose by proximity effect to achieve full resist clearance. Results so far demonstrate that the doughnut method is a promising technique for indicating the proximity effect in HIBL and the design has been proved feasible.

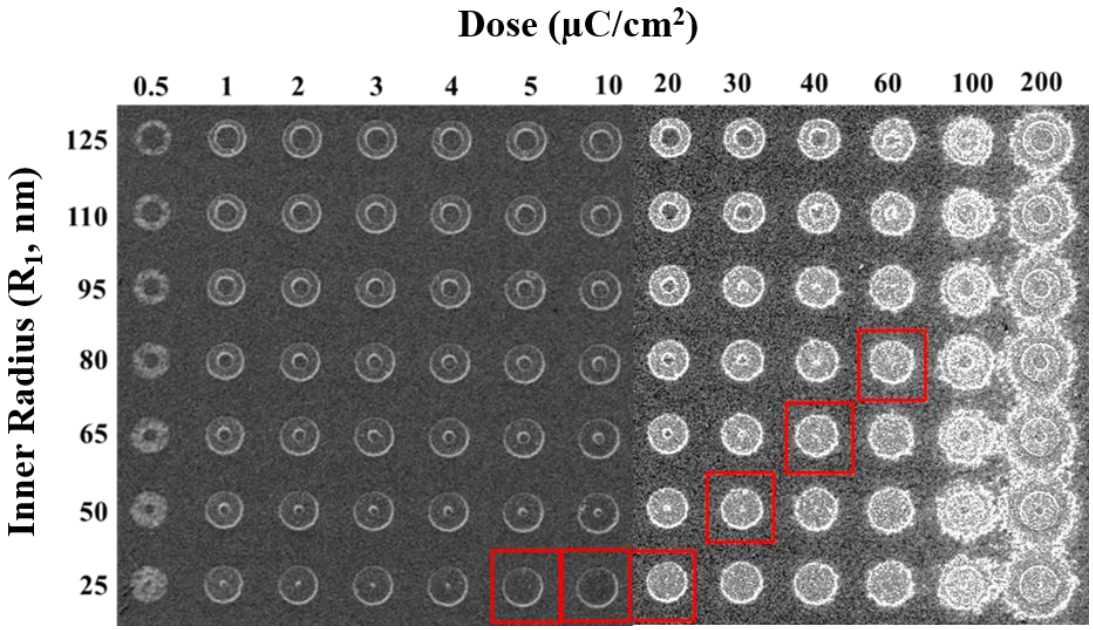

Figure 5.10: HIM images of fabricated doughnut structures of a fixed outer radius of 200 nm using 30-keV HIBL and enclosed in red squares are the critical doughnuts when the inner circles are fully exposed by the proximity effect. The applied doses range from 0.5 to 200 μC/cm^2 and the inner radii range from 125 down to 25 nm.

A series of doughnut patterns with various inner radius were fabricated for the investigation of the proximity effect in 30 keV HIBL. Seven inner radii were initially chosen between 25-125 nm and they were exposed by thirteen doses within the 0.5 - 200 μC/cm^2 range. Figure 5.10 show the exposed doughnut arrays on 20-nm-thick PMMA after development using 30-keV HIBL. The exposure dose applied to each doughnut is indicated above the HIM image, whist the inner radii of the inner circles are indicated on the left-hand side of the HIM images. It is worth noting that for each row of doughnuts, the radii of the inner circles are designed to be identical. However, the fabricated doughnuts show a decrease in size from left to right with an increase of dose. This pattern transfer difference is caused by the fact that the dose applied to the ring area has also exposed areas just outside the ring, i.e. proximity effect, resulting in wider developed patterns than designed patterns.

Enclosed in the red boxes are the identified "critical doughnuts", their entire inner circles were fully exposed and cleared due to the proximity effect. This means that the dose received at the centre point of these doughnuts can be described by the proximity function (see Equation 5.1). As the applied dose increases from the left to the right colomn, the inner radius (R_1) of the critical doughnut increases, hence the doughnut with a fully-cleared inner circle also shifts upwards by row. At this stage, however, these results cannot be fitted into the proximity effect equation due to its sparse data range which can introduce significant errors. However, these results are extremely useful as they not only illustrate the conditions under which the critical doughnuts occurred, but also serve as a guideline in choosing reasonable parameter range and increments for the subsequent refining

experiments. For example, doughnuts with inner radius of 25 nm were fully exposed by doses between 10 to 30 μC/cm^2, to find out more accurate information, an extra doughnut array was fabricated as shown in Figure 5.11 with much refined dose and inner radii variations. Additional seven doses between 9-32.8 μC/cm^2 and seven inner radii were set between 15-37.5 nm were investigated. The critical doughnuts in this array are identified (enclosed by red boxes) and the corresponding dose (Q) and inner radius (R_1) are therefore suitable for curve fitting to extract the proximity effect parameter. Thus, further HIBL experiments with more refined parameter variations were conducted covering the full dose and inner radii ranges.

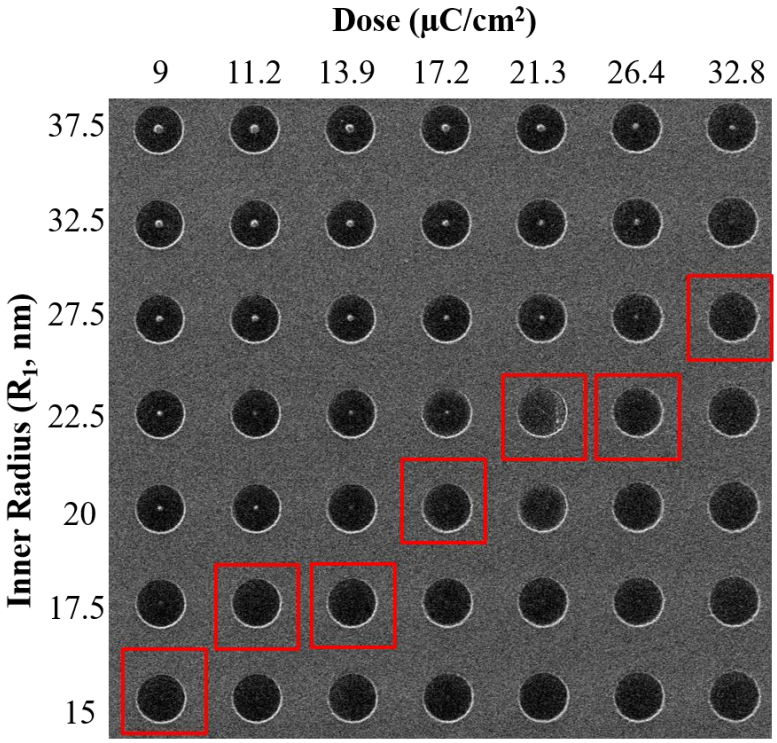

Figure 5.11: HIM images of the fabricated doughnut structures of a fixed outer radius of 200 nm using 30-keV HIBL with a refined range of parameters: the applied doses range from 9 to 32.7 μC/cm^2 and the inner radii range from 15 to 37.5 nm. Enclosed in red squares are the critical doughnuts when the inner circles are fully exposed by the proximity effect.

Similar procedures were applied to investigate and identify the critical doughnuts using 30-keV EBL. Figure 5.12 shows examples of SEM images of the fabricated doughnut structures with a fixed outer radius of 7 μm and decreasing inner radii in y-meander fashion starting from the top-right corner (the inner radius of the doughnut in the top-right corner is the biggest, whilst the inner radius is smallest for the doughnut in the top-left corner). Figure 5.12a and Figure 5.12b show the effect of the same pattern exposed with different doses of 120 μC/cm^2 and 164 μC/cm^2, respectively. The inner radius of the critical doughnut increases with an increase of the applied dose. Across the patterns, it can be

observed that the size of the inner circle is smaller in Figure 5.12b compared to that in Figure 5.12a at the same location due to the proximity effect.

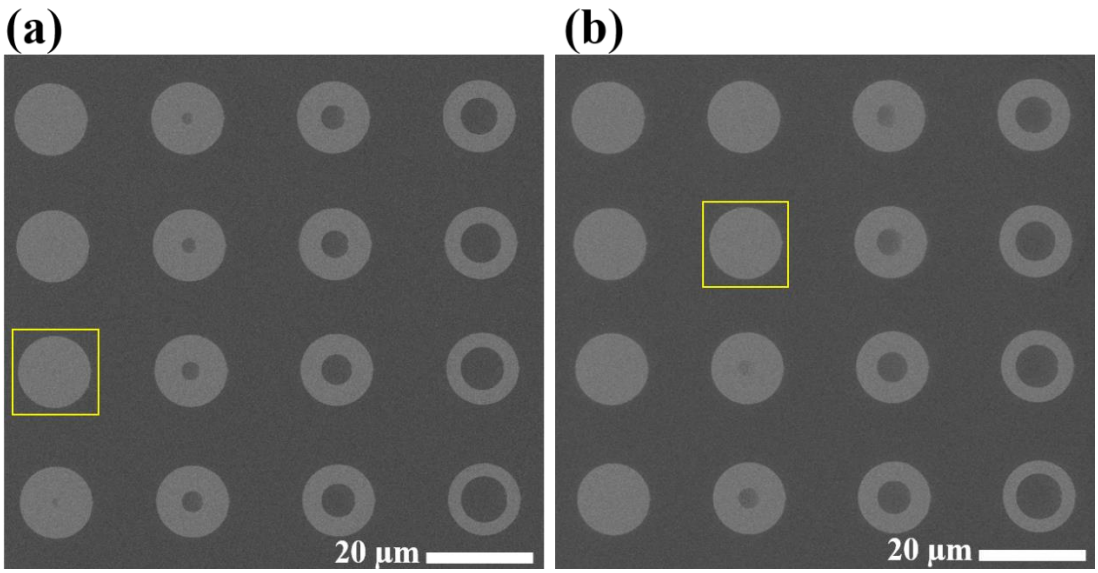

Figure 5.12: SEM images show the fabricated doughnut structures based on a same pattern but with a dose of (a) 120 µC/cm^2 and (b) 165 µC/cm^2 using 30-keV EBL. The pattern consists of doughnuts with a fixed outer radius of 7 µm and varied inner radii. Enclosed in yellow squares are the critical doughnuts when the inner circles are fully exposed by the proximity effect.

AFM results containing the surface depth information were obtained to verify the interpretation of the top-down 2D HIM and SEM images. HIM/SEM and corresponding AFM images of the fabricated doughnuts structures are shown in Figure 5.13, where doughnuts with/without resist material remaining in the centre were imaged. It can be seen from the SE contrast curves obtained from HIM/SEM images that good contrast difference was exhibited. It also matches well to the depth profile obtained from the AFM measurement. The high brightness in HIM image corresponds to a hill in the AFM line profile whilst the low brightness in HIM image corresponds to a trench in the AFM line profile. Whereas, the high brightness in SEM image corresponds to a trench in the AFM line profile, whilst the low brightness corresponds to a hill. Overall, the obtained results match the expected proximity behaviour and a good consistency between HIM/SEM and AFM characterisation was confirmed.

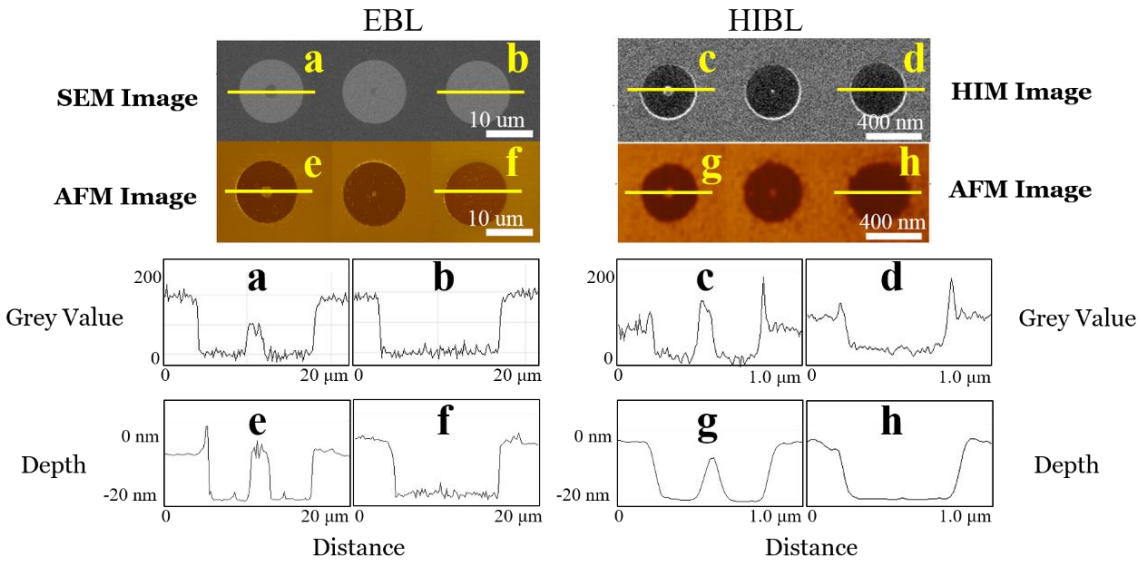

Figure 5.13: HIM/SEM images and corresponding AFM measurement of doughnuts fabricated using HIBL and EBL with fixed outer radii (R_2) of 200 nm and 7 µm, respectively, and varied inner radii (R_1) after development. The SE contrast curves in HIM/SEM images match well to the depth profiles in AFM.

5.5.3 Determination of Proximity Effect Parameters

To determine the proximity parameters in the 20-nm-thick PMMA using HIBL and EBL, the exposed doughnuts of which the inner circle was fully exposed and cleared by the proximity effect after the development process were identified from the high-resolution images such as HIM/SEM and AFM micrographs. The inner radii and corresponding applied doses of these critical doughnuts were recorded for all exposed doughnuts using HIBL and EBL, listed in Table 5.2. The simplified proximity function (Equation 5.2) has been fitted to the experimental results as shown in Figure 5.14.

HIBL Data		**EBL Data**	
Q (µC/cm^2)	**R_1 (nm)**	**Q (µC/cm^2)**	**R_1 (µm)**
1.7	5	80	0.3
1.9	5	100	0.3
2	5	120	0.3
2.5	10	140	0.34
2.7	10	150	1.6
2.9	10	165	1.64
3.1	10	180	2.04
3.8	12.5	195	2.04
4.7	12.5	250	2.9

5.9	15	275	3
7.3	15	300	3.2
9.0	15	325	3.3
11.2	17.5	350	3.5
13.8	17.5	375	3.6
17.2	20	400	3.9
21.3	22.5	600	4.3
26.4	22.5	800	4.6
32.8	32.5	1000	4.9
37.5	37.5	1200	5
40	40	1400	5.1
45	50	1600	5.2
50	52.5	2000	5.6
55	55	2500	5.8
60	62.5	3000	5.9
65	65	4000	6

Table 5.2: The inner radius (R_1) and corresponding applied dose Q of the critical doughnuts whose inner circle is fully cleared by the proximity effect shown in the HIM/SEM images of HIBL/EBL fabricated doughnut arrays.

The backscattered electrons/ions range (β) were determined to be ~3.26 μm in EBL and ~0.067 μm in HIBL. Significant reduction in proximity effect, i.e. 2 orders of magnitude, has been revealed by directly comparing the results using HIBL to that in EBL. The value of the backscattering coefficient β in EBL match well to the typical value reported in literature [61], [63], [110]. The value of β for HIBL is ~4.8 times greater compared to the results obtained by Winston [27] where 31-nm-thick HSQ resist layer was used. Since the proximity parameters are affected by parameters such as the resist compositions, film thickness and development method, it seems the effect from the smaller molecular sizes of HSQ outweighed the impact of using a thicker resist layer, causing a reduced proximity effect. Despite the difference, the calculated values are comparable and consistent to the results.

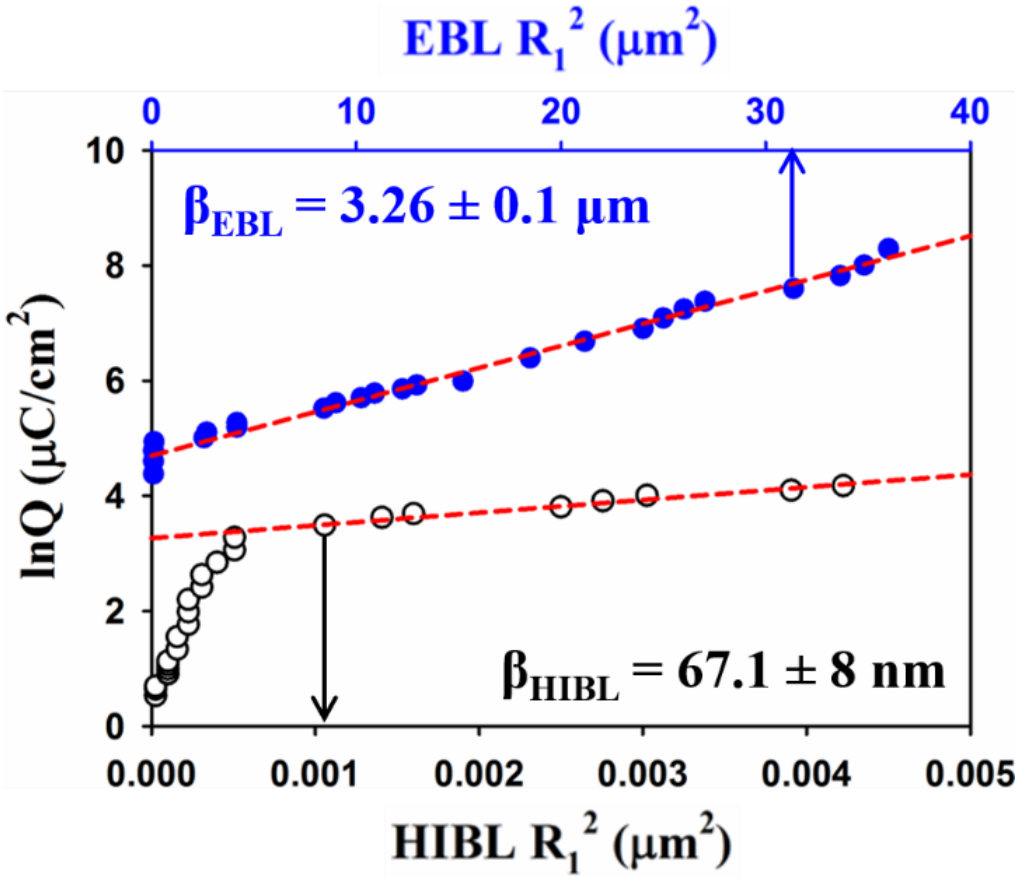

Figure 5.14: Comparison of the proximity effect for HIBL and EBL on 20-nm-thick PMMA. The ranges of the backscattered ions/electrons are calculated to be 67.1 nm and 3.26 μm for HIBL and EBL, respectively, revealing an almost 50 times proximity reduction in HIBL.

In conclusion, while there is some residual proximity effect in the case of HIBL due to the light weight of the He^+ ions, these effects are negligible when compared to those due to electron backscattering in EBL. It is clear from the SRIM modelling results that the back scattering of He^+ ions from the resist-on-silicon target is too low (0.13% of incident ion flux as shown in Section 3.7) to be responsible for the small proximity effect in HIBL. Instead, this is almost certainly due to ion induced secondary electrons.

5.5.4 High Resolution Dense Feature Patterning

To demonstrate the benefit of the reduced proximity effect, dense single-pixel line arrays were exposed on 20-nm-thick PMMA using HIBL. With the optimum line dose of 4 pA/cm, well-defined line arrays with pitches down to 30 nm were demonstrated. As shown in Figure 5.15, the measured average critical dimensions remain the same at around 11.7 nm regardless of the pitch. This result is consistent but better than that achieved in the previous study where line widths of 14.5 ± 2 nm were

demonstrated on 20-nm PMMA [54], , indicating a very high resolution and small proximity effect associated with HIBL.

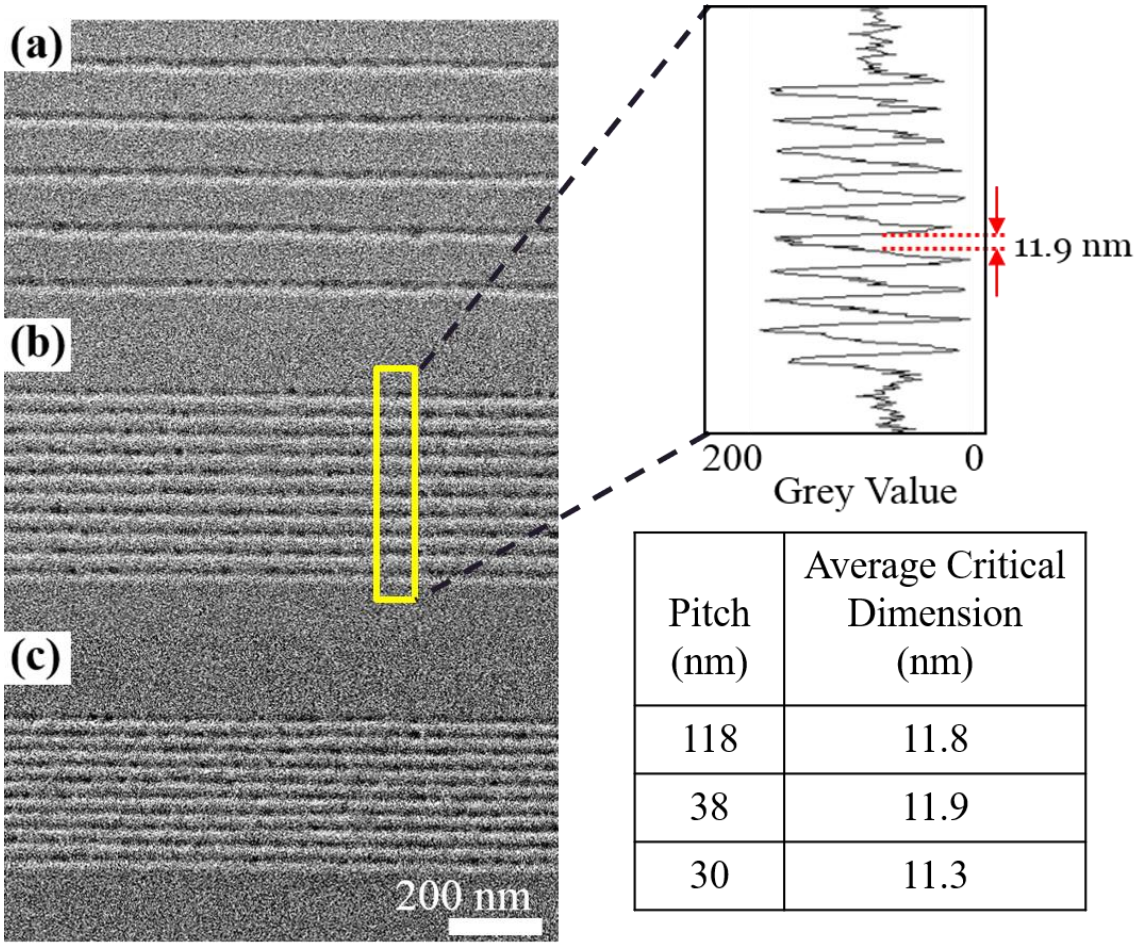

Pitch (nm)	Average Critical Dimension (nm)
118	11.8
38	11.9
30	11.3

Figure 5.15: HIM images of single pixel lines fabricated using HIBL with a line dose of 4 pC/cm at pitches of (a) 118, (b) 38.5 and (c) 30 nm on 20-nm-thick PMMA. Critical dimension of approximately 11.5 nm remains the same for all pitches as shown in the table above.

5.6 Conclusions

In summary, a direct quantitative comparison of the proximity effect in HIBL and EBL using the doughnut method has been demonstrated. Results indicate 2 orders of magnitude reduction of the backscattered ion range in HIBL compared to that in EBL. This reduced proximity effect suggests that HIBL can produce high-resolution patterns with a higher density owing to its almost 50 times smaller proximity effect without applying complex and costly PEC. Unfortunately, despite its high sensitivity and tone flexibility under 30-keV He^+ ion irradiation, PMMA has poor durability in plasma etch making it unsuitable for the pattern transfer processes. For this reason, a novel fullerene resist promising to create high-resolution features of low LER will be reported in Chapter 6.

CHAPTER 6

HIBL ON FULLERENE MOLECULAR RESISTS*

6.1 Introduction

As nanoelectronic device design pushes towards ever smaller feature sizes, there is an increasing need for novel resist materials and lithographic patterning techniques. From the previous review of literature, patterns of the highest resolution have been formed in resist layers with thicknesses less than 10 nm. This is because the beam broadening through scattering increases with depth from the surface, so smaller feature sizes can be defined as the thickness of the resist decreases. However, such thin layers of resist can cause significant issues due to the insufficient protection of the substrate underneath during subsequent pattern transfer processes. Hence, resists that exhibit high etch resistance, as well as high resolution, are needed in nanolithographic applications.

Figure 6.1: Molecular diagram of generic mono-adduct methanofullerene derivative resists. R represents the attached side chains to the C_{60} molecule.

* Based on paper entitled "Heium ion beam lithography on fullerene molecular resists for sub-10 nm patterning" published in Micoelectronic Engineering (2016).

A new class of fullerene-based molecular resists are being developed to meet this need, taking advantage of a smaller molecular size to achieve higher resolution pattern definition for EBL than the traditional polymeric resists such as PMMA allow [111]. Recent EBL investigations with fullerene resists have demonstrated high resolution patterning, with a high sensitivity and low LER [90]. In this chapter, our latest results from an investigation into HIBL with a novel fullerene-derivative molecular resist are presented, with a focus on spin-coating solvent choice effects, resist sensitivity and high-resolution patterning of isolated and high-density lines.

For the development of an ultra-thin film and ultra-high-resolution resist for HIBL, an easily synthesised methanofullerene derivative which has not previously been reported as a lithographic material was identified and used as the basis of the proprietary resist HM-01 (Irresistible Materials Ltd.) as shown in Figure 6.1. It was examined specifically for the HIBL project on the basis of its size, film formation and solubility properties. The carbon content of the material was found to be ~95 wt% (percentage by weight); the Ohnishi number was calculated to be ~1.26 and the ring parameter was ~0.87 (see Section 2.5), both indicating that the resist has excellent etching resistance. The resist was formulated at 5 g/l in anisole, the typical solvents utilised for organic resist formulations such as PMMA, and in chlorobenzene. The solutions were filtered with a 200 nm teflon syringe filter prior to spin coating to filter out any fine particulate sediment and ensure the consistency of resulting resist films.

6.2 Exposure Pattern Design

The large area exposure pattern designed in ECP for studying resist sensitivity and contrast of the fullerene resist using HIBL is shown in Figure 6.2, which is identical to that used in Chapter 4.2 for PMMA. The 50 µm × 50 µm field allows for 15 different dose levels in the array of 5 µm × 10 µm rectangles from each exposure. Figure 6.3 shows the pattern designed in Elphy Quantum for the dose test in EBL, which is identical to that used in Chapter 5.3 for PMMA. The 100 µm by 100 µm writing field comprises an eight-by-four array of rectangles with a dimension of 5 µm × 10 µm, and 32 doses can be tested using this pattern.

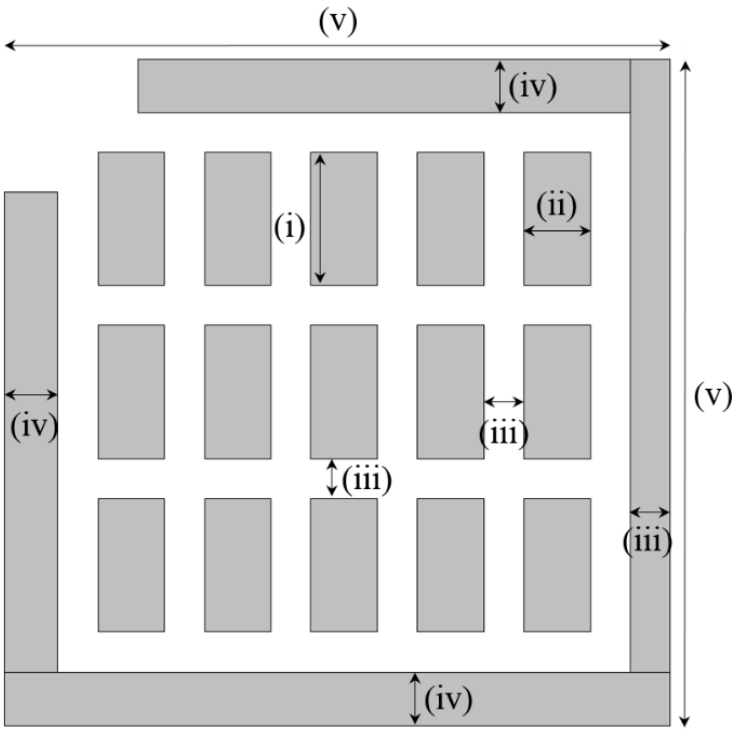

No.	(μm)
(i)	10
(ii)	5
(iii)	3
(iv)	4
(v)	50

Figure 6.2: Schematic of pattern generated in ECP for large area dose test to determine the dose response curve for fullerene resist using HIBL.

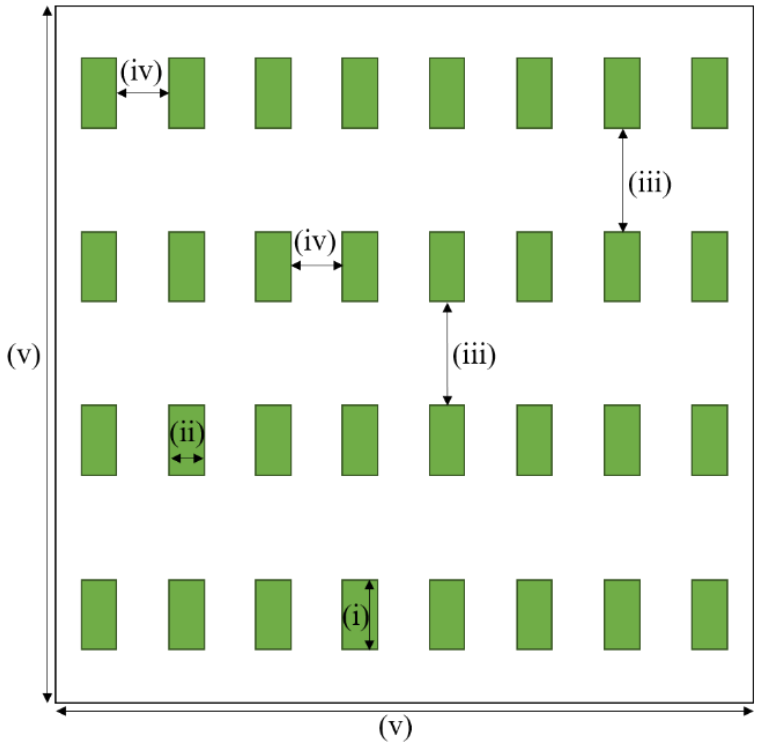

No.	(μm)
(i)	10
(ii)	5
(iii)	15
(iv)	7.5
(v)	100

Figure 6.3: Schematic of pattern generated in Elphy Quantum for large area dose test to determine the dose response curve for fullerene resist using EBL.

Sparsely-spaced single-pixel line arrays were designed in ECP for the systematic study on optimal line doses and achievable minimum linewidth (see Figure 6.4). The pattern has a 10 µm × 10 µm FOV and consists of a 2-µm edge marker and 18 line-arrays pitched at 100 nm. There are seven lines of 1.5 µm in length in each array and exposed to a line dose. Up to 18 line dose variations can be investigated with this pattern.

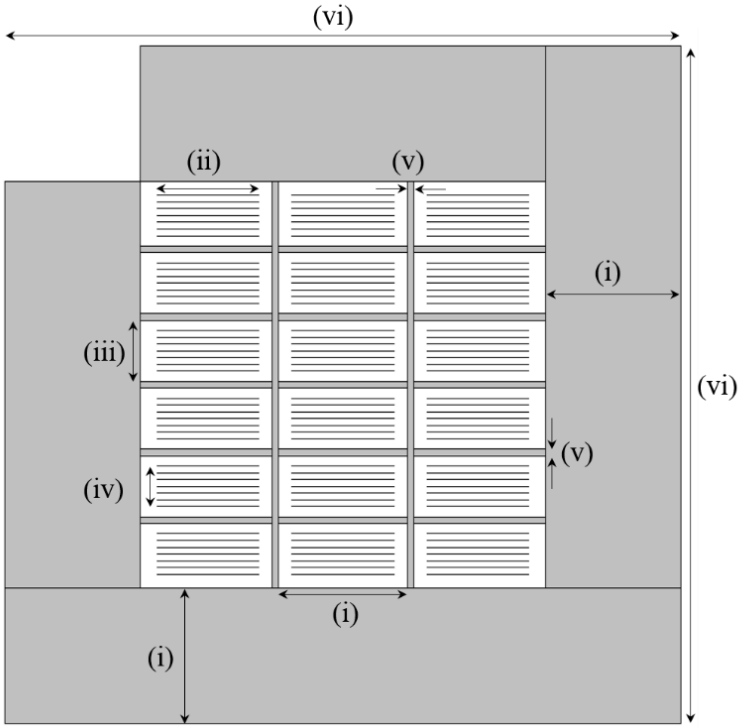

No.	(µm)
(i)	2
(ii)	1.5
(iii)	0.9
(iv)	0.6
(v)	0.1
(vi)	10
pitch	0.1

Figure 6.4: Schematic of the sparse single-pixel line arrays with a constant line pitch designed in ECP for the determination of the resolution limit on 10-nm fullerene resist.

High-density single-pixel line arrays were designed in ECP for the identification of the highest density that fullerene resist allows as shown in Figure 6.5 and Figure 6.6. For both patterns, the pitch decreases from the top to bottom and the line arrays in a same row share the same pitch; the dose increases from left to right and the dose is the same for line arrays in one column. The line arrays are sparser in the first pattern, with a pitch ranging from 34 nm down to 18 nm, whilst the pitch ranges from 17 nm down to 12 nm in the second pattern with a higher pattern density. The ECP coding to generate these patterns can be found in Appendix 8.1.

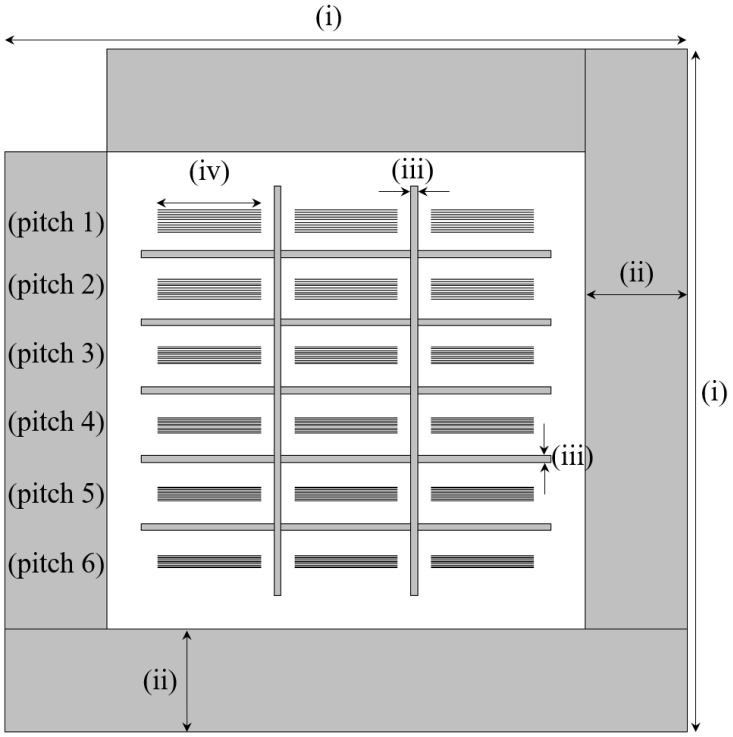

No.	(μm)
(i)	10
(ii)	1.5
(iii)	0.1
(iv)	1.5
Pitch 1	0.034
Pitch 2	0.030
Pitch 3	0.026
Pitch 4	0.022
Pitch 5	0.020
Pitch 6	0.018

Figure 6.5: Schematic of the dense single-pixel line arrays with pitches ranging from 34 nm to 18 nm designed in ECP for the determination of the highest pattern density achievable on 10-nm fullerene resist.

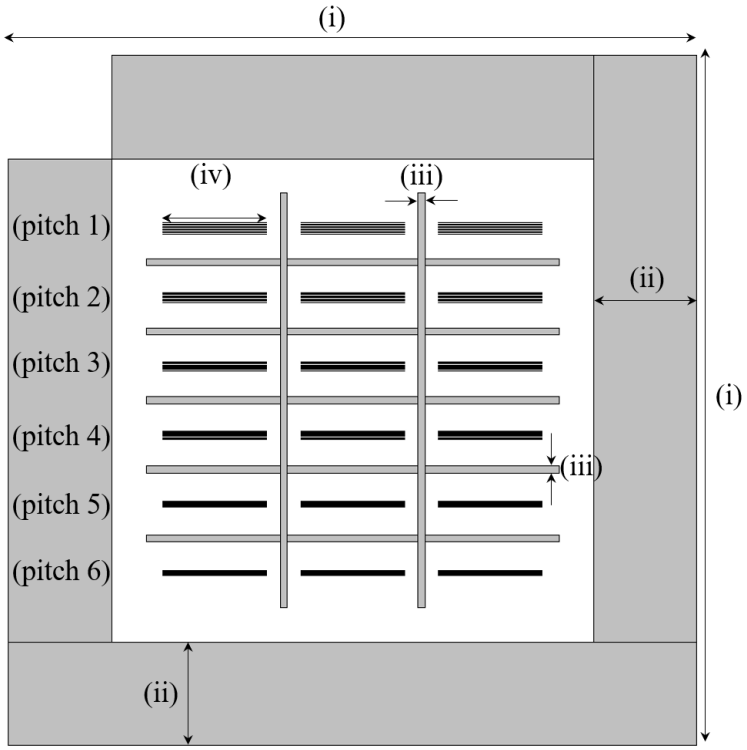

No.	(μm)
(i)	10
(ii)	1.5
(iii)	0.1
(iv)	1.5
Pitch 1	0.017
Pitch 2	0.016
Pitch 3	0.015
Pitch 4	0.014
Pitch 5	0.013
Pitch 6	0.012

Figure 6.6: Schematic of the dense single-pixel line arrays with pitches ranging from 17 nm to 12 nm designed in ECP for the determination of the highest pattern density achievable on 10-nm fullerene resist.

6.3 Experimental

The samples were prepared and cleaned as described in Section 3.1. For small samples, a dispense of 100 - 200 µl resist per chip was used, whilst 1 – 2 ml was dispensed for 100 mm wafer coating. No spreading step was utilised, and the spin coater was set to ramp to 4000 rpm with maximum acceleration of 9000 rpm/sec. Chips were spun for 60 s, before receiving a pre-exposure bake on a hotplate at 70 °C for 5 minutes.

An Orion^{TM} Plus HIM with Xenos pattern generator and beam blanker unit was used for HIBL on fullerene derivative resists. A beam voltage of 30 keV and a working distance of 7 mm were used in all cases. Helium pressure was maintained at 5×10^{-6} Torr during the exposure and a 10-µm beam limiting aperture was selected. The beam current was set to 5 pA to expose the large areas efficiently in the resist sensitivity evaluation, using a single-pass, centre to edge writing strategy. For the high-resolution patterning, a small beam current of 0.5 pA was applied to optimise the beam spot size and achieve the highest resolution, and the beam followed single-pass lines.

For a direct comparison of resist sensitivities in HIBL and EBL, the HM-01 samples were also exposed in the Gemini FEG-SEM (NVision 40 FIB SEM) to a 30-keV focused electron beam generated from a Schottky source at a working distance of 10 mm. A current of 1 nA was used during the exposure with a beam limiting aperture of 60 µm. The base dose was set to be 1000 µC/cm^2, and a dose ranging from 0 to 205,000 µC/cm^2 were applied. The sample preparation and the subsequent development process were identical to that in the HIBL processes.

The exposed samples were then developed in cyclohexanone, an organic developer, for 20 seconds and rinsed in IPA for 10 seconds, followed by being blow-dried in nitrogen to produce various negative tone patterns. No post exposure bake was applied prior to development.

The film thickness remaining after the HIBL and EBL large area exposure and post development was measured using an AFM (Multimode^{TM} V, Veeco). An intermittent-contact (tapping) mode in AFM with a scanning frequency of 0.723 Hz with 640-line resolution was used to obtain the surface depth information. HIM was used to image the high-resolution HIBL samples with the following imaging conditions: a beam energy of 30 keV, beam current of 0.5 pA with a working distance of 7 mm.

6.4 Results and Discussion

6.4.1 Film Spinning in Solvents

Films of the resist were coated onto cleaned silicon chips by spin coating. The resist formulation concentration and spinning time were held constant whilst the spin speed was varied between 1000 and 7000 rpm. The spin curves for HM-01A (fullerene derivative resist formulated in anisole) and HM-01C (chlorobenzene was used as the solvent for the fullerene resist) were determined by measuring the resulting thicknesses of the film. These are presented in *Figure 6.7*. Due to the lack of a precise ellipsometry model for the fullerene resist, the thicknesses of resist layers were measured in a profilometer assisted by the stick-on tape technique, where a small piece of tape was applied in the centre of the substrate before the coating of resist and removed after the coating. Ideally, the substrate covered by the tape is free from the resist; hence, the resist layer can be measured against the substrate. However, this method can lead to some degree of inaccuracy: extra material maybe accumulated around the edges of the tape, and the original material distribution may be altered when the tape is removed. Smooth and uniform films were obtained for all spin speeds and film thicknesses ranging from 40 nm down to sub-10 nm were achieved.

Figure 6.7(b) shows the spin curve for HM-01 formulated in chlorobenzene (HM-01C). In this case, smooth films were seen for spin speeds up to 5000 rpm. Films were apparent in the range 6000–8000 rpm but were insufficiently smooth to make an accurate thickness measurement. Films spun from anisole were on average ~15% thinner than those spun from chlorobenzene, making anisole a more suitable solvent to generate thinner resist films for high resolution patterning. Thus, HM-01A was used in all the following investigations. Higher formulation concentrations in both solvents have been used to prepare thicker films of up to 120 nm.

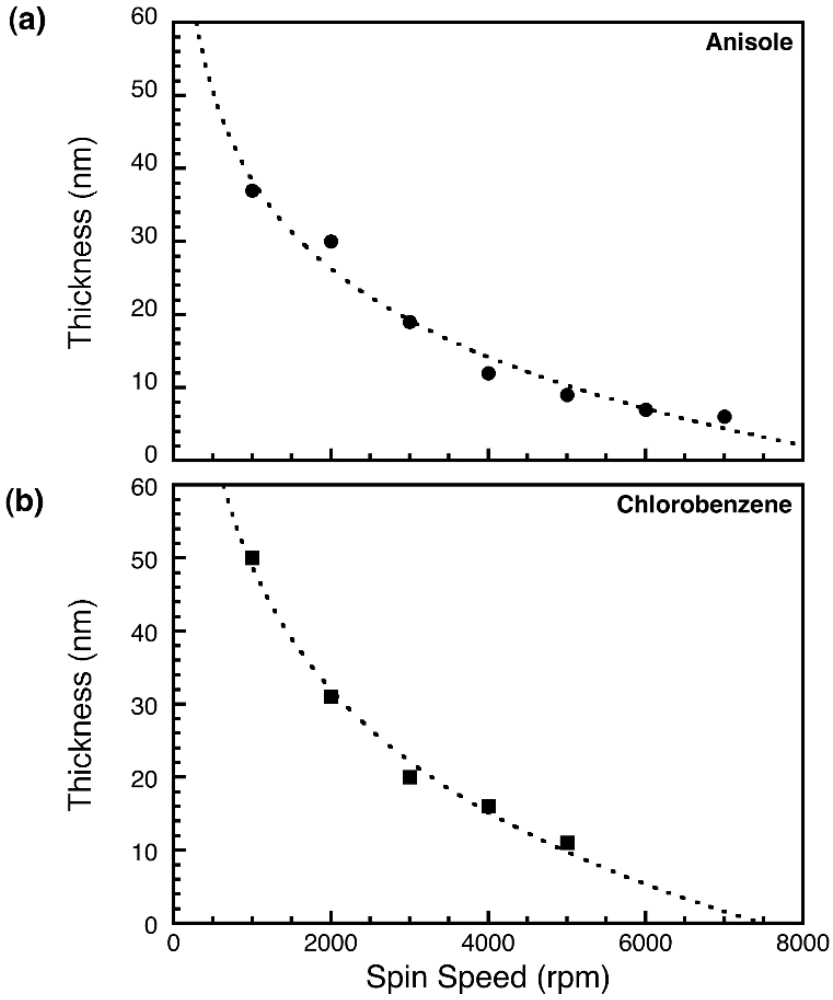

Figure 6.7: Thickness versus spin speed using (a) anisole and (b) chlorobenzene casting solvents.

6.4.2 Evaluation of Resist Sensitivity

Based on the designed pattern in Figure 6.2 and Figure 6.3, large area exposures using 30-keV HIBL and EBL were performed on the ~10 nm-thick HM-01A resist, achieved by spin coating at 4000 rpm. The applied dose ranged from 0 – 288 μC/cm^2 for HIBL and 0 – 205 mC/cm^2 for EBL, followed by cyclohexanone development process. The residual film thickness after development was measured using AFM to determine the dose response curve. An optical micrograph of five of the exposed areas with the applied dose of 38, 56, 85, 128 and 192 μC/cm^2 (from left to right) is shown in Figure 6.8 (a) along with the corresponding AFM data in Figure 6.8 (b). The first dose area appears shallower with a lower contrast compared to the other four. The surface line profile obtained from the AFM (Figure 6.8 (c)) confirms a thinner resist remaining for the first area due to the underexposure, whilst thicker resist layers remain for other areas that were fully exposed.

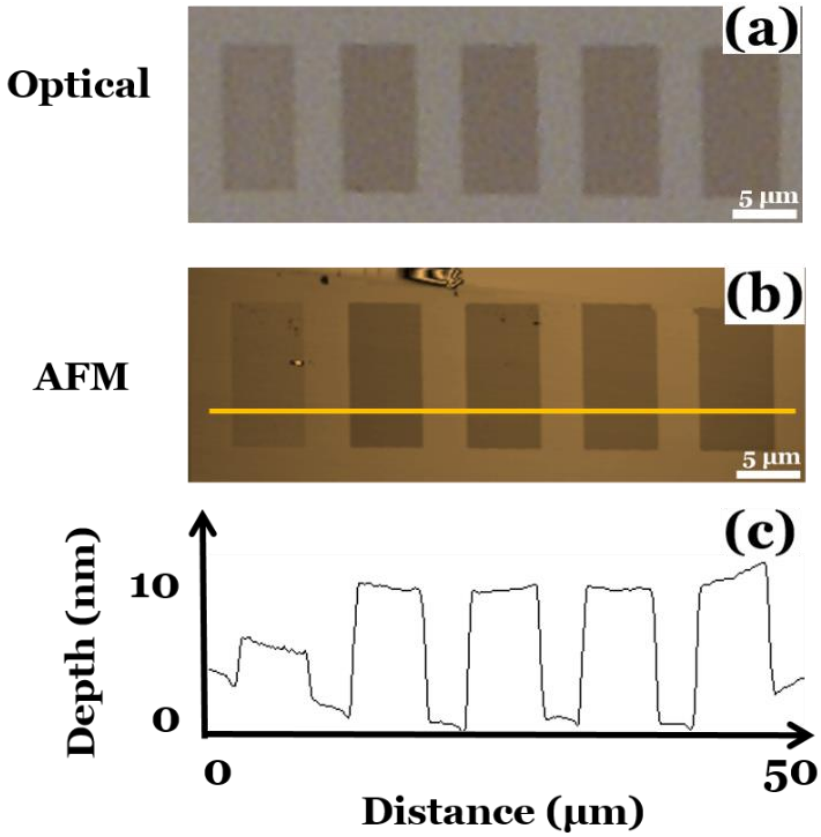

Figure 6.8: (a) Optical micrograph, (b) AFM image and (c) line profile (values plotted were averaged from a 20-pixel range) of the same dose test areas on the ~10 nm fullerene derivative resist (IM-HM-01A) patterned using HIBL after development. The applied doses are 37.9, 56.5, 85.0, 128.0 and 192.0 µC/cm^2 from left to right.

The dose response curves for HM-01A in EBL and HIBL are presented in Figure 6.9, where the normalized resist thickness after development was plotted against the logarithm of applied dose. The resist exhibits negative tone behaviour under both beams. The resist sensitivity (taken for a negative tone resist as the dose at which 50% of the film is retained after the development) is measured to be 40 µC/cm^2 using HIBL. This sensitivity is around 20 times lower than that in positive tone PMMA, however, it is very similar to the dose required for negative tone exposure of PMMA as shown in the previous chapter. Furthermore, the exposure dose used in HIBL can be converted to an ion density of 2.5×10^{14} ions/cm^2, which is considered sufficiently low to limit physical damage by ion implantation to the underlying substrate in these regions [50]. This means that HIBL patterning would cause little sub-surface modification, such as bubble formation and swelling, which can limit the highest achievable resolution and prevent subsequent pattern transfer. The contrast, defined as the gradient of the linear rising portion of the curve, was also calculated to be approximately 3.

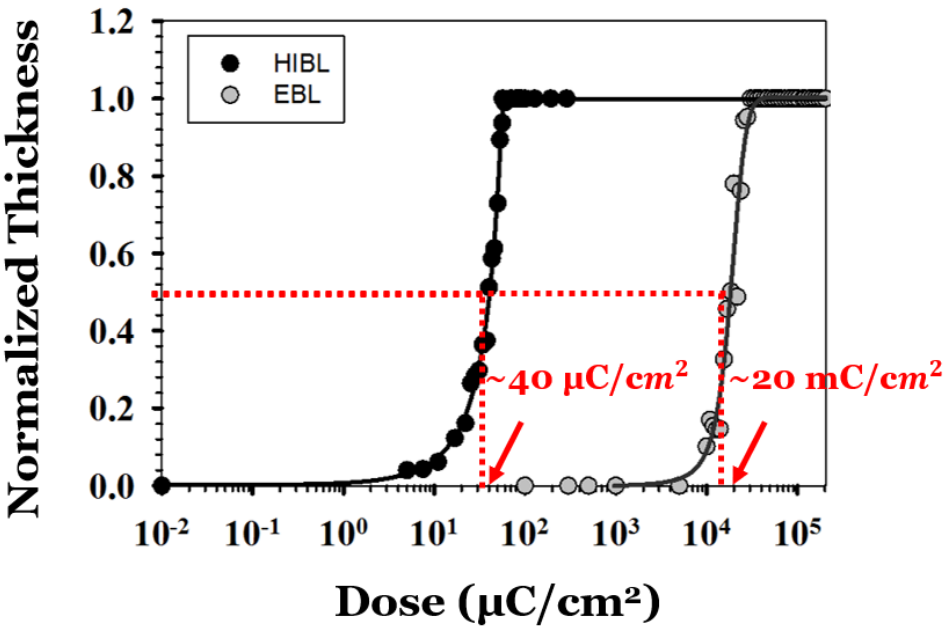

Figure 6.9: Comparison of the dose response curves for HM-01A in HIBL and EBL. The sensitivities are measured to be 40 µC/cm^2 and 20 mC/cm^2, respectively, revealing a 500 times sensitivity improvement in HIBL.

In EBL, a significantly higher dose of ~20 mC/cm^2 is required for 50% retention of the film and the contrast value was measured to be approximately 2.5. Therefore, there is a 500 times improvement in sensitivity when exposed with He^+, when compared with e-beam exposure for this resist. These results indicate there is a significantly reduced required current and exposure time, and an improved efficiency in HIBL. The higher contrast value with a 20% improvement from EBL allows for better vertical resist profile and better resolution to be achieved in HIBL, whilst the high sensitivity makes HIBL feasible for rapid prototyping applications.

6.4.3 High Resolution Sparse Feature Patterning

To find out the minimum linewidth, i.e. CD, achievable, arrays of 1.5 µm long, single-pixel lines at a pitch of 100 nm as shown in Figure 6.4 were patterned by HIBL in 10-nm-thick resists. The line dose was varied from 5 pC/cm to 510 pC/cm with an increment of 5 pC/cm. Figure 6.10 shows HIM images of 40-nm-pitch sparse lines formed in ~10 nm-thick HM-01A after the development process. The lines are well defined, with high contrast from the silicon substrate. The linewidths were measured at various locations by the SE contrast from the HIM images with 20-pixel line averaging and the averaged value is taken as the CD. The CDs for the single pixel lines vary from 7.3 to 8.3 nm with different doses. There is discontinuity and evident roughness in line features exposed to 0.045 and 0.06 nC/cm, indicating under-exposure has occurred. Measurements further reveal that

some parts of the lines in Figure 6.10 b are significantly wider, at around 9 nm, which is close to the thickness of the resist layer. This suggests that very thin lines were fabricated by the low dose, however some of these lines collapsed onto the substrate during the subsequent development process due to the high aspect ratio. An illustration (Figure 8.3) explaining this effect can be found in the Appendix 8.3. This results in a greater value of CD in the underexposed pattern compared to that exposed by an optimal dose. The lines with a dose of 0.09 nC/cm appear thicker due to over-exposure. The optimal line dose, judged as the lowest dose for which continuous lines with smallest CD were patterned, was identified to be 0.075 nC/cm.

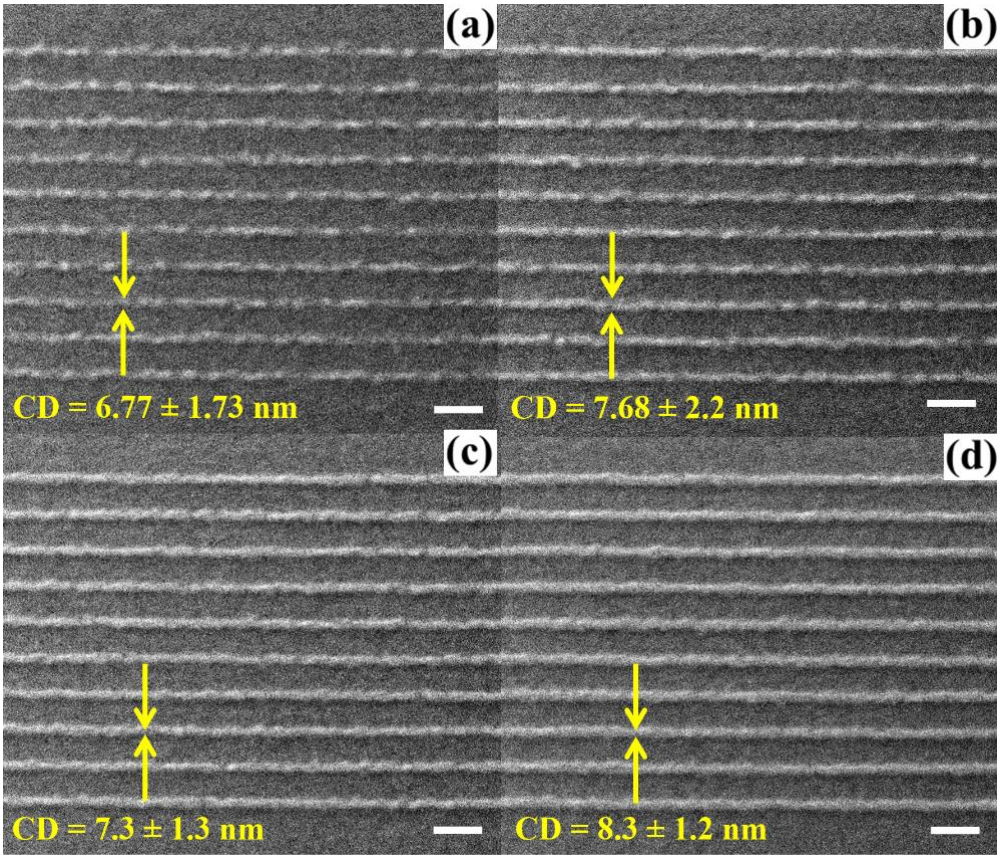

Figure 6.10: HIM images showing the single pixel sparsely-spaced line patterns exposed on ~10 nm-thick HM-01A resist (line doses are (a) 0.045, (b) 0.06, (c) 0.075 and (d) 0.09 nC/cm). Scale bar: 50 nm.

To understand the relationship between the line dose and the LER in the fabricated line features, the SuMMIT software package (EUV Technology Corp.) was used to extract LER values as shown in Table 6.1. The results are heavily dependent on the imaging processing methods, hence are not absolute values, but they provide an indication of trend within this study. The greater values of LER in the underexposed patterns were due to the discontinuity in lines. This effect weakens as the dose

level rises, hence producing lower LER values. Overall, results show a decrease in resolution when the dose is not optimum, LER decreases when the dose is increased and a low LER was achieved with the optimal dose.

Line Dose (nC/cm)	0.045	0.06	0.075	0.09
CD (nm)	6.77 ± 1.73	7.68 ± 2.2	7.3 ± 1.3	8.3 ± 1.2
LER (nm)	4.82 ± 0.22	3.66 ± 0.12	2.95 ± 0.06	2.65 ± 0.08

Table 6.1:Critical dimensions measured by the SE contrast and the line edge roughness values extracted for line doses of 0.045, 0.06, 0.075 and 0.09 nC/cm in Figure 6.10.

6.4.4 High Resolution Dense Feature Patterning

To determine the highest pattern density of HIBL on 10-nm-thick HM-01A, arrays of densely-packed single-pixel lines with a pitch ranging from 34 nm down to 12 nm (see Figure 6.5 and Figure 6.6) were exposed over a range of dose from 0.005 to 0.1 nC/cm. Examples of HIM secondary electron images of the resulting patterns are presented in Figure 6.11. Figure 6.11 (a)-(c) show the effect of decreasing the pitch at a fixed line dose of 0.075 nC/cm. The three pitches are 30, 22 and 14.5 nm respectively. The results show that the linewidths of all three pitches remain consistent to that of the sparse line features which is ~7.3 nm, indicating a very small proximity effect in HIBL. Figure 6.11 (d)-(e) show the effect of increasing the line dose at a fixed pitch of 14.5 nm; the three doses are 0.045, 0.075 and 0.09 nC/cm respectively. The measured CDs are ~6.8, ~7.3 and ~8.3 nm respectively, which match to those in the sparse line features (Figure 6.10). The correlation of the dose level and the resulting linewidths is also consistent between the dense and sparse features which has further demonstrated the small proximity effect in HIBL patterning at high density.

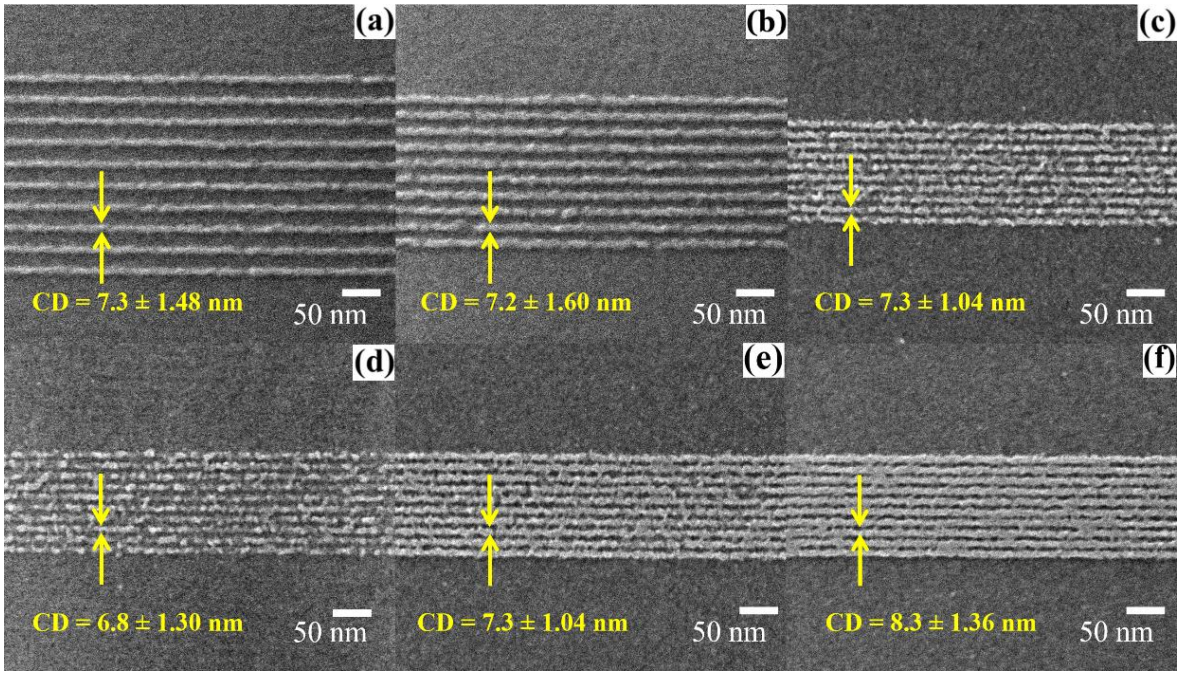

Figure 6.11: (a)-(c) HIM images show the effect of decreasing the pitch at a fixed line dose of 0.075 nC/cm (pitches are (a) 30; (b) 22 and (c) 14.5 nm); (d) – (f) HIM images show the effect of increasing the line dose at a fixed 14.5 nm-pitch (line doses are (d) 0.045; (e) 0.075 and (f) 0.09 nC/cm).

The best results to date are the continuous and well-defined lines with a pitch of 17 nm and a 0.5 mark-space ratio (line width of ~ 8.5 nm), produced with line dose of 0.09 nC/cm as shown in the HIM image and corresponding contrast line profile in Figure 6.12. This is comparable to the best achievable with state-of-the-art EBL, despite being carried out using a tool not optimised for lithography with standard processing conditions. Figure 6.13 shows resolvable but broken densely-packed lines with a pitch of 12 nm and a 0.5 line-space ratio (line width of ~ 6 nm) achieved with a line dose of 0.04 nC/cm. The discrete charges of the helium ion beam current lead to shot noise which exhibits as a spatial random fluctuation of the helium ion dose received by the resist. Shot noise of the incident beam is considered to affect the CD uniformity and LER and is a fundamental limit to lithography.

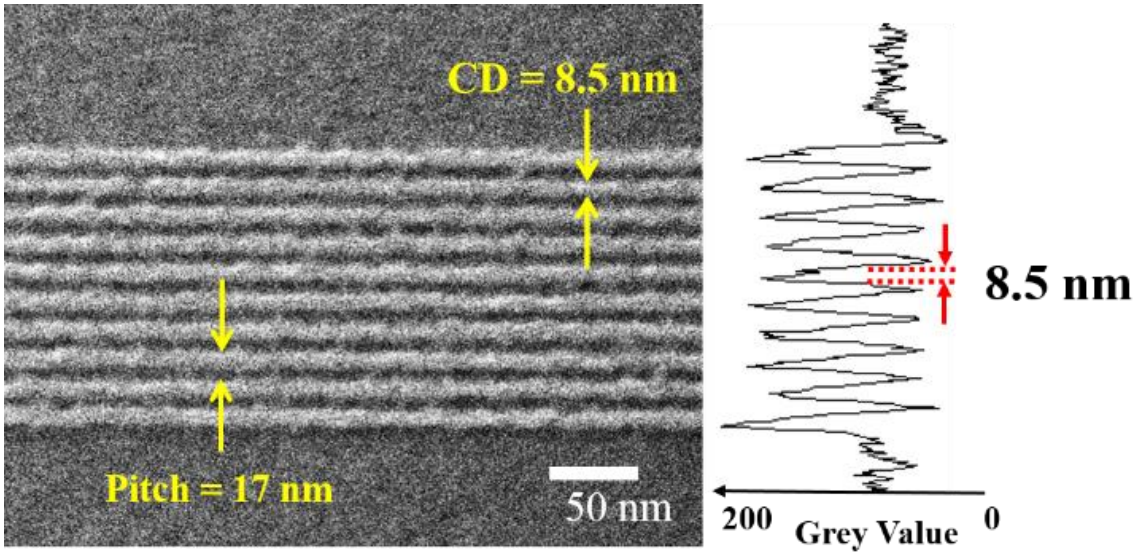

Figure 6.12: Left: HIM image of dense single pixel features exposed at 0.09 nC/cm on ~10 nm-thick HM-01A resist using helium ion beam lithography. Right: SE contrast profile reveals that 17-nm pitch and 8.5-nm line width were achieved in the well-defined, continuous lines.

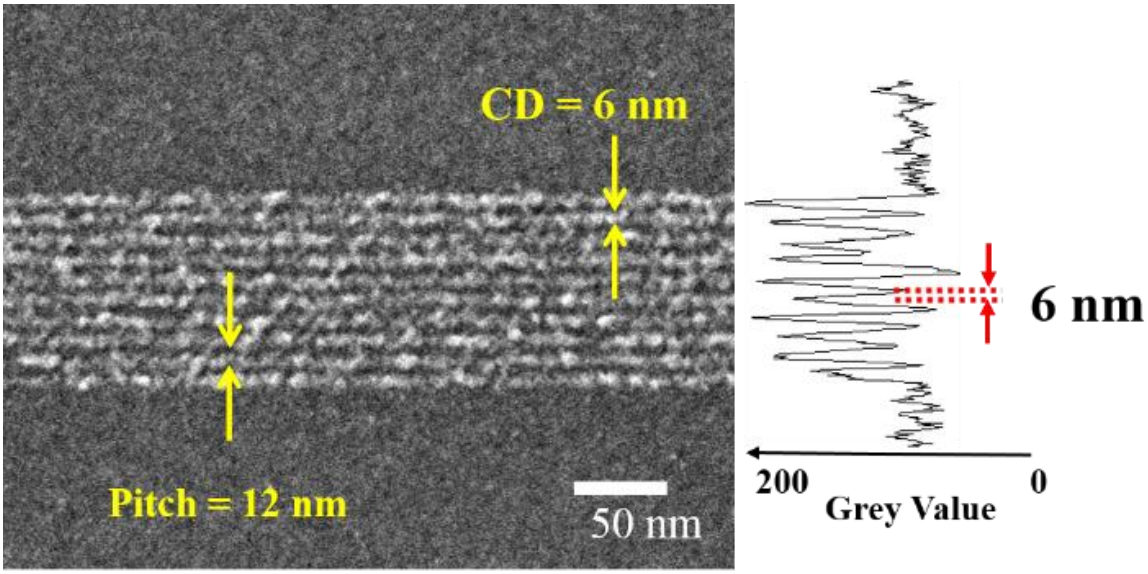

Figure 6.13: Left: HIM image of dense single pixel features exposed at 0.04 nC/cm on ~10 nm-thick HM-01A resist using helium ion beam lithography. Right: SE contrast profile reveals 12-nm pitch and 6-nm line width were achieved in the resolvable but broken lines.

In Figure 6.13, the applied line dose of 0.04 nC/cm is equivalent to 25 ions/nm, giving a SNR of 5:1. The subsequent shot noise manifests itself in line discontinuity caused by shot noise dependent missing pixels. The way in which line dose determines this effect is clear in Figure 6.11 (d)- (f) showing fewer missing pixels and more well-defined lines with increasing dose. This is entirely due

to the decrease in shot noise with increasing dose. It can be mitigated by adjusting the scan strategy to reduce pixel to pixel spacing or by partial overlap of adjacent pixels. As the features in Figure 6.13 approach an aspect ratio of 2:1 it is likely that pattern collapse on development is occurring, hence for pitches below 18 nm a thinner resist film should be explored. Further improvements could include using a smoother silicon substrate, applying point-of-use resist nanofiltration (with less than 5 nm pore sizes), varying post exposure bake parameters and developer/development recipe optimisation, with the aim of further improving fidelity of features in the sub 10 nm regime.

6.5 Conclusions

A high-resolution, high-sensitivity resist famulated by a soluble derivative of the fullerene molecule was demonstrated using helium ion beam lithography. A negative tone behaviour with a sensitivity of ~40 μC/cm^2, almost three orders of magnitude more sensitive than that in EBL, was achieved. Sparse line features with line widths of 7.3 nm were achieved on the 10-nm-thick resist. The fabrication of 8.5 nm half-pitched lines with good feature separation and 6 nm half-pitched lines with inferior but still resolvable separation is also shown in this study. To the best of our knowledge, we have demonstrated the best resolution data in a fullerene derivative molecular resist to date using HIBL with standard processing conditions, achieving high-density sub-10 nm patterning. This provides an excellent combination of nanoscale patterning capability with low LER and extraordinarily high durability in plasma etch demonstrated elsewhere [112]. Fullerene resists do not suffer from post exposure delay line broadening and are thus suitable for serial patterning process such as EBL and HIBL. This also establishes potential for HIBL as an alternative to EBL for rapid prototyping of beyond CMOS devices.

CHAPTER 7

CONCLUSIONS AND OUTLOOK

For this PhD, helium ion beam lithography (HIBL), an emerging technique that uses a sub-nanometer focused beam of helium ions generated in the helium ion microscope (HIM) to expose resist was extensively investigated in terms of resist sensitivity, proximity effect and high-resolution patterning. The aim was to extend beyond the current limits of conventional electron beam lithography (EBL). Both the benchmark EBL resist PMMA and a novel fullerene-based molecular resist (HM-01) with a much smaller molecular size were examined.

The dose response curves obtained from large area exposures reveal that PMMA behaves similarly in EBL and HIBL, exhibiting positive first then negative tone with an increase in dose; whilst HM-01 behaves as a negative tone resist. A sensitivity of ~2 μC/cm^2 and ~40 μC/cm^2 using 30-keV helium ion beam were achieved on PMMA and HM-01 respectively, which are 60 times and 500 times higher than those achieved with 30-keV electron beam for the same resists. This substantial increase in sensitivity is mainly due to the significantly larger low-energy SE yield from the energetic helium ions compared to an electron beam on the same energy. Proximity effect, caused by the backscattered primary particles and their subsequent secondary electrons, significantly limit the performance of the established EBL. However, due to low ion backscattering and deflection, HIBL is expected to have a reduced proximity effect. To quantify the proximity effect in HIBL and directly compare it with that in EBL, a "doughnut" method was adapted for application on 20-nm-thick PMMA resist on silicon. By fitting the lithographic data to a Gaussian approximation of the proximity function, the ranges of the backscattered electrons/ions were determined to be ~3.26 μm and 0.067 μm for EBL and HIBL, respectively, suggesting that HIBL can produce patterns with a higher density owing to its almost 50 times smaller proximity effect whilst avoiding the inadvertent exposure of surrounding material. The advantage of the sub-nanometer beam spot and the reduced proximity effect was demonstrated in the high-resolution sparse single-pixel line arrays, where line dose optimisation was conducted for both resists. The optimum line doses were identified to be 4 pC/cm and 75 pC/cm for 20-nm-thick PMMA and 10-nm-thick HM-01, followed by high-density single-pixel line array patterning. A consistent linewidth of ~11.7 nm was achieved on 20-nm-thick PMMA for line pitches ranging from 118 nm down to 30 nm, indicating a high resolution and small proximity effect associated with HIBL. However, the demonstrated linewidths are well in excess of the resolution

limits of the helium ion probe, indicating that resolution is being limited by factors such as the resist property and development process. High-resolution patterning on fullerene derivative resist was then investigated with the aim of bringing pattern resolutions closer to the fundamental limit of the HIM sub-nanometer probe size. Sparse line features with line widths of 7.3 nm with low line-edge roughness were achieved on the 10-nm-thick resist. The fabrication of 8.5 half-pitched lines with good feature separation and 6 nm half-pitched lines with inferior but still resolvable separation were also demonstrated, suggesting HIBL in combination with molecular resists is a promising candidate for rapid prototyping technique for "beyond Moore" and "beyond CMOS" devices.

In summary, we have demonstrated for the first time a direct comparison of resist sensitivity and proximity effect quantification using HIBL and EBL on thin layer resists. With standard processing conditions, the high-resolution patterning on PMMA using HIBL show feature sizes and densities comparable to that of the state-of-the-art EBL; whilst to the best of our knowledge, we have demonstrated the best resolution data in a fullerene derivative molecular resist to date using HIBL. These results collectively demonstrate the high resist sensitivity, i.e. high exposure efficiency, high resolution and low proximity effect in HIBL and its potential to become an important rapid prototyping tool for nanofabrication of nanodevices. Other applications include the rapid characterisation and prescreening of new resists such as EUV resists and inorganic resists (oxides and metal halides), fabrication and repair of nanoimprint templates which also conquer the drawback of slow-writing speed in the direct write method and lead to a potential route to larger volume manufacture with increased throughput.

Several challenges remain that could hinder progress with the technique. Although high sensitivities have been demonstrated, it is important to note that this does not immediately translate to higher throughput. The beam currents generated in the HIM are generally lower (<5 pA) than that generated in an EBL system if a sub-nm probe size is to be maintained, which could negate any writing speed gain from an increased sensitivity. Compared to other ion beam species, such as Ga^+, light helium ions cause less damage and contamination to the sample. However, substrate damage through defect generation as a result of collision cascades caused by the impinging ion beam is still a concern. Whilst required exposure doses are generally less than those that result in observable damage (amorphisation, bubble formation etc.) it remains to be seen whether defect creation in the underlying substrate during HIBL has a detrimental effect on the electrical properties of devices fabricated using this approach. The nanoimprint pattern transfer route may provide a way to circumvent these problems by allowing HIBL to define the feature size whilst avoiding direct ion beam exposure of the active material from which the device will be made.

A number of future work directions are suggested. So far, standard resist processing recipes from EBL have been used in the HIBL experiments, and there is likely to be scope for further improvement

in pattern fidelity through process optimisation, such as the exposure dose and the resist development procedure. Due to its carbon rich nature, HM-01 shows great promises to have high etch resistance in plasma etch, which is desirable for subsequent pattern transfer. Negative-tone PMMA has exhibited superb low surface roughness which is a promising feature for the ultra-high resolution patterning. Its etch durability and subsequent pattern transfer can be investigated. Also, the systems used for HIBL to date are primarily microscopes designed for imaging. A dedicated lithography tool using GFIS technology and accurate stage movement mechanisms would lead to further improvements in terms of throughput, alignment accuracy, and stitching of write-fields. For example, the current HIM tool stage movement introduces a stitching error of ~3.28 μm for adjacent write fields (see Appendix 8.3). Furthermore, helium is just one of many ion species compatible with the GFIS approach. Neon FIBs are now available in commercial ion microscopes, which are also capable of exposing sub-10-nm features in HSQ resist [29]. Other GFIS tools with alternative ion species are being developed which may also have an impact in the field of FIB lithography in the near future.

CHAPTER 8

APPENDICES

8.1 Example of ECP Coding

In this section, the complete ECP coding of patterns including the large area exposure for resist sensitivity study, the sparse/dense single-pixel line arrays for high resolution patterning and the doughnut arrays for proximity effect investigation are presented. For each pattern, the pattern file (.pat) to generate patterns is listed on the left, whilst the control file (.ctl) to communicate with the pattern file and run command of exposing patterns is on the right.

In the pattern file, the following text command can be found in assembling the pattern structure:

D *name of the pattern*
I *increment, i.e. pixel spacing*
C *dwell time of the beam at each pixel in ns, minimum dwell time is 100 ns*
FSIZE *size of the overall writing field*
RECT/LINE/DOT/CIRCLE *coordinates of the shape*
…
END

D next *name of the pattern*
…..
End

In the control file, the following text command can be found that controls the helium ion beam:

current = *actual beam current* of the system *set for the exposure (it is not capable of changing the beam current)*
origin = coordinates of the overall pattern to be exposed on the sample
sfile = .pat file name
fsize = FOV of the overall pattern

draw (name of the pattern in .pat file)

draw (….)

; the exposure is in order of the pattern called in this list.

DoseTest1.pat	**DoseTest1.ctl**
D edgemark I 1 C 160 FSIZE 50 um ;The Pattern Edge ;---------- RECT 0, 0, 50000, 4000 RECT 47000, 4000, 50000, 50000 RECT 0, 4000, 4000, 40000 RECT 10000, 46000, 47000, 50000 ;---------- #dose=80.0 END D dosesquare11 I 4 C 160 FSIZE 50 um RECT 7000, 33000, 12000, 43000 #dose=5.0 END D dosesquare12 I 3 C 135 FSIZE 50 um RECT 15000, 33000, 20000, 43000 #dose=7.5 END D dosesquare13 I 3 C 202 FSIZE 50 um RECT 23000, 33000, 28000, 43000 #dose=11.222 END D dosesquare14 I 2 C 135 FSIZE 50 um RECT 31000, 33000, 36000, 43000	current = 5 origin= 0,0 sfile = DoseTest1 fsize= 50 draw (edgemark) draw (dosesquare11) draw (dosesquare12) draw (dosesquare13) draw (dosesquare14) draw (dosesquare15) draw (dosesquare21) draw (dosesquare22) draw (dosesquare23) draw (dosesquare24) draw (dosesquare25) draw (dosesquare31) draw (dosesquare32) draw (dosesquare33) draw (dosesquare34) draw (dosesquare35)

```
#dose=16.875
END

D dosesquare15
I 2
C 202
FSIZE 50 um
RECT 39000, 33000, 44000, 43000
#dose=25.25
END

D dosesquare21
I 2
C 303
FSIZE 50 um
RECT 7000, 20000, 12000, 30000
#dose=37.875
END

D dosesquare22
I 1
C 113
FSIZE 50 um
RECT 15000, 20000, 20000, 30000
#dose=56.5
END

D dosesquare23
I 1
C 170
FSIZE 50 um
RECT 23000, 20000, 28000, 30000
#dose=85.0
END

D dosesquare24
I 1
C 256
FSIZE 50 um
RECT 31000, 20000, 36000, 30000
#dose=128.0
END

D dosesquare25
I 1
C 384
FSIZE 50 um
RECT 39000, 20000, 44000, 30000
#dose=192.0
END
```

D dosesquare31 I 1 C 576 FSIZE 50 um RECT 7000, 7000, 12000, 17000 #dose=288.0 END D dosesquare32 I 2 C 224 FSIZE 50 um RECT 15000, 7000, 20000, 17000 #dose=28.0 END D dosesquare33 I 2 C 248 FSIZE 50 um RECT 23000, 7000, 28000, 17000 #dose=31.0 END D dosesquare34 I 2 C 272 FSIZE 50 um RECT 31000, 7000, 36000, 17000 #dose=34.0 END D dosesquare35 I 2 C 176 FSIZE 50 um RECT 39000, 7000, 44000, 17000 #dose=22.0 END	

SparseLines.pat	**SparseLines.ctl**
;current=0.5pA, FOV=10um D edgemark I 5 C 120 FSIZE 10 um	current = 0.5 origin= 0,0 sfile = SparseLines fsize= 10

```
;The Pattern Edge
;----------------------------
RECT 0, 0, 50000, 10000
RECT 40000, 10000, 50000, 50000
RECT 0, 10000, 10000, 40000
RECT 10000, 40000, 40000, 50000
;----------------------------
#dose=6.0
END

D seperators
I 6
C 115
FSIZE 10 um
;Vertical seperators
;----------------------------
RECT 19750, 10000, 20250, 40000
RECT 29750, 10000, 30250, 40000
;----------------------------
;Horizontal seperator
;----------------------------
;The horizontal seperators:B1
RECT 10000, 14750, 19750, 15250
RECT 20250, 14750, 29750, 15250
RECT 30250, 14750, 40000, 15250
;The horizontal seperators:B2
RECT 10000, 19750, 19750, 20250
RECT 20250, 19750, 29750, 20250
RECT 30250, 19750, 40000, 20250
;The horizontal seperators:B3
RECT 10000, 24750, 19750, 25250
RECT 20250, 24750, 29750, 25250
RECT 30250, 24750, 40000, 25250
;The horizontal seperators:B4
RECT 10000, 29750, 19750, 30250
RECT 20250, 29750, 29750, 30250
RECT 30250, 29750, 40000, 30250
;The horizontal seperators:B5
RECT 10000, 34750, 19750, 35250
RECT 20250, 34750, 29750, 35250
RECT 30250, 34750, 40000, 35250
;----------------------------
;----------------------------
#dose=3.993
END

D Dose1
I 2
C 176
FSIZE 10 um
```

```
draw (Dose1)
draw (Dose2)
draw (Dose3)
draw (Dose4)
draw (Dose5)
draw (Dose6)
draw (Dose7)
draw (Dose8)
draw (Dose9)
draw (Dose10)
draw (Dose11)
draw (Dose12)
draw (Dose13)
draw (Dose14)
draw (Dose15)
draw (Dose16)
draw (Dose17)
draw (Dose18)
draw (seperators)
draw (edgemark)
```

```
;Linedose1
;----------------------------
LINE 11250, 39000, 18750, 39000
LINE 11250, 38500, 18750, 38500
LINE 11250, 38000, 18750, 38000
LINE 11250, 37500, 18750, 37500
LINE 11250, 37000, 18750, 37000
LINE 11250, 36500, 18750, 36500
LINE 11250, 36000, 18750, 36000
;----------------------------
#line dose=0.0022nc/cm
END

D Dose2
I 2
C 192
FSIZE 10 um
;Linedose2
;----------------------------
LINE 21250, 39000, 28750, 39000
LINE 21250, 38500, 28750, 38500
LINE 21250, 38000, 28750, 38000
LINE 21250, 37500, 28750, 37500
LINE 21250, 37000, 28750, 37000
LINE 21250, 36500, 28750, 36500
LINE 21250, 36000, 28750, 36000
;----------------------------
#line dose=0.0024nc/cm
END

D Dose3
I 1
C 104
FSIZE 10 um
;Linedose3
;----------------------------
LINE 31250, 39000, 38750, 39000
LINE 31250, 38500, 38750, 38500
LINE 31250, 38000, 38750, 38000
LINE 31250, 37500, 38750, 37500
LINE 31250, 37000, 38750, 37000
LINE 31250, 36500, 38750, 36500
LINE 31250, 36000, 38750, 36000
;----------------------------
#line dose=0.0026 nC/cm
END

D Dose4
I 1
C 112
```

```
FSIZE 10 um
;Linedose4
;-----------------------------
LINE 11250, 34000, 18750, 34000
LINE 11250, 33500, 18750, 33500
LINE 11250, 33000, 18750, 33000
LINE 11250, 32500, 18750, 32500
LINE 11250, 32000, 18750, 32000
LINE 11250, 31500, 18750, 31500
LINE 11250, 31000, 18750, 31000
;-----------------------------
#line dose=0.0028nC/cm
END

D Dose5
I 1
C 120
FSIZE 10 um
;Linedose5
;-----------------------------
LINE 21250, 34000, 28750, 34000
LINE 21250, 33500, 28750, 33500
LINE 21250, 33000, 28750, 33000
LINE 21250, 32500, 28750, 32500
LINE 21250, 32000, 28750, 32000
LINE 21250, 31500, 28750, 31500
LINE 21250, 31000, 28750, 31000
;-----------------------------
#line dose=0.003nC/cm
END

D Dose6
I 1
C 128
FSIZE 10 um
;Linedose6
;-----------------------------
LINE 31250, 34000, 38750, 34000
LINE 31250, 33500, 38750, 33500
LINE 31250, 33000, 38750, 33000
LINE 31250, 32500, 38750, 32500
LINE 31250, 32000, 38750, 32000
LINE 31250, 31500, 38750, 31500
LINE 31250, 31000, 38750, 31000
;-----------------------------
#line dose=0.0032nC/cm
END

D Dose7
I 1
```

```
C 136
FSIZE 10 um
;Linedose7
;----------------------------
LINE 11250, 29000, 18750, 29000
LINE 11250, 28500, 18750, 28500
LINE 11250, 28000, 18750, 28000
LINE 11250, 27500, 18750, 27500
LINE 11250, 27000, 18750, 27000
LINE 11250, 26500, 18750, 26500
LINE 11250, 26000, 18750, 26000
;----------------------------
#line dose=0.0034nC/cm
END

D Dose8
I 1
C 144
FSIZE 10 um
;Linedose8
;----------------------------
LINE 21250, 29000, 28750, 29000
LINE 21250, 28500, 28750, 28500
LINE 21250, 28000, 28750, 28000
LINE 21250, 27500, 28750, 27500
LINE 21250, 27000, 28750, 27000
LINE 21250, 26500, 28750, 26500
LINE 21250, 26000, 28750, 26000
;----------------------------
#line dose=0.0036nC/cm
END

D Dose9
I 1
C 152
FSIZE 10 um
;Linedose9
;----------------------------
LINE 31250, 29000, 38750, 29000
LINE 31250, 28500, 38750, 28500
LINE 31250, 28000, 38750, 28000
LINE 31250, 27500, 38750, 27500
LINE 31250, 27000, 38750, 27000
LINE 31250, 26500, 38750, 26500
LINE 31250, 26000, 38750, 26000
;----------------------------
#line dose=0.0038nC/cm
END

D Dose10
```

```
I 1
C 160
FSIZE 10 um
;Linedose10
;----------------------------
LINE 11250, 24000, 18750, 24000
LINE 11250, 23500, 18750, 23500
LINE 11250, 23000, 18750, 23000
LINE 11250, 22500, 18750, 22500
LINE 11250, 22000, 18750, 22000
LINE 11250, 21500, 18750, 21500
LINE 11250, 21000, 18750, 21000
;----------------------------
#line dose=0.004nC/cm
END

D Dose11
I 1
C 168
FSIZE 10 um
;Linedose11
;----------------------------
LINE 21250, 24000, 28750, 24000
LINE 21250, 23500, 28750, 23500
LINE 21250, 23000, 28750, 23000
LINE 21250, 22500, 28750, 22500
LINE 21250, 22000, 28750, 22000
LINE 21250, 21500, 28750, 21500
LINE 21250, 21000, 28750, 21000
;----------------------------
#line dose=0.0042nC/cm
END

D Dose12
I 1
C 176
FSIZE 10 um
;Linedose12
;----------------------------
LINE 31250, 24000, 38750, 24000
LINE 31250, 23500, 38750, 23500
LINE 31250, 23000, 38750, 23000
LINE 31250, 22500, 38750, 22500
LINE 31250, 22000, 38750, 22000
LINE 31250, 21500, 38750, 21500
LINE 31250, 21000, 38750, 21000
;----------------------------
#line dose=0.0044nC/cm
END
```

```
D Dose13
I 1
C 184
FSIZE 10 um
;Linedose13
;----------------------------
LINE 11250, 19000, 18750, 19000
LINE 11250, 18500, 18750, 18500
LINE 11250, 18000, 18750, 18000
LINE 11250, 17500, 18750, 17500
LINE 11250, 17000, 18750, 17000
LINE 11250, 16500, 18750, 16500
LINE 11250, 16000, 18750, 16000
;----------------------------
#line dose=0.0046nC/cm
END

D Dose14
I 1
C 192
FSIZE 10 um
;Linedose14
;----------------------------
LINE 21250, 19000, 28750, 19000
LINE 21250, 18500, 28750, 18500
LINE 21250, 18000, 28750, 18000
LINE 21250, 17500, 28750, 17500
LINE 21250, 17000, 28750, 17000
LINE 21250, 16500, 28750, 16500
LINE 21250, 16000, 28750, 16000
;----------------------------
#line dose=0.0048nC/cm
END

D Dose15
I 1
C 200
FSIZE 10 um
;Linedose15
;----------------------------
LINE 31250, 19000, 38750, 19000
LINE 31250, 18500, 38750, 18500
LINE 31250, 18000, 38750, 18000
LINE 31250, 17500, 38750, 17500
LINE 31250, 17000, 38750, 17000
LINE 31250, 16500, 38750, 16500
LINE 31250, 16000, 38750, 16000
;----------------------------
#line dose=0.005nC/cm
END
```

```
D Dose16
I 1
C 208
FSIZE 10 um
;Linedose16
;----------------------------
LINE 11250, 14000, 18750, 14000
LINE 11250, 13500, 18750, 13500
LINE 11250, 13000, 18750, 13000
LINE 11250, 12500, 18750, 12500
LINE 11250, 12000, 18750, 12000
LINE 11250, 11500, 18750, 11500
LINE 11250, 11000, 18750, 11000
;----------------------------
#line dose=0.0052nC/cm
END

D Dose17
I 1
C 216
FSIZE 10 um
;Linedose17
;----------------------------
LINE 21250, 14000, 28750, 14000
LINE 21250, 13500, 28750, 13500
LINE 21250, 13000, 28750, 13000
LINE 21250, 12500, 28750, 12500
LINE 21250, 12000, 28750, 12000
LINE 21250, 11500, 28750, 11500
LINE 21250, 11000, 28750, 11000
;----------------------------
#line dose=0.0054nC/cm
END

D Dose18
I 1
C 224
FSIZE 10 um
;Linedose18
;----------------------------
LINE 31250, 14000, 38750, 14000
LINE 31250, 13500, 38750, 13500
LINE 31250, 13000, 38750, 13000
LINE 31250, 12500, 38750, 12500
LINE 31250, 12000, 38750, 12000
LINE 31250, 11500, 38750, 11500
LINE 31250, 11000, 38750, 11000
;----------------------------
#line dose=0.0056nC/cm
```

END	

DenseLines.pat	**DenseLines.ctl**
D edgemark I 5 C 120 FSIZE 10 um ;The Pattern Edge ;The Pattern Edge ;---------- RECT 0, 0, 50000, 7500 RECT 42500, 7500, 50000, 50000 RECT 0, 7500, 7500, 42500 RECT 7500, 42500, 42500, 50000 ;---------- #dose=6.0 END D seperators I 6 C 115 FSIZE 10 um ;Vertical seperators ;---------- RECT 19750, 10000, 20250, 40000 RECT 29750, 10000, 30250, 40000 ;---------- ;Horizontal seperator ;---------- ;The horizontal seperators:B1 RECT 10000, 14750, 19750, 15250 RECT 20250, 14750, 29750, 15250 RECT 30250, 14750, 40000, 15250 ;The horizontal seperators:B2 RECT 10000, 19750, 19750, 20250 RECT 20250, 19750, 29750, 20250 RECT 30250, 19750, 40000, 20250 ;The horizontal seperators:B3 RECT 10000, 24750, 19750, 25250 RECT 20250, 24750, 29750, 25250 RECT 30250, 24750, 40000, 25250 ;The horizontal seperators:B4 RECT 10000, 29750, 19750, 30250 RECT 20250, 29750, 29750, 30250 RECT 30250, 29750, 40000, 30250 ;The horizontal seperators:B5 RECT 10000, 34750, 19750, 35250	current = 0.5 origin= 0,0 sfile = DenseLines fsize= 10 draw (Dose1) draw (Dose2) draw (Dose3) draw (seperators) draw (edgemark)

```
RECT 20250, 34750, 29750, 35250
RECT 30250, 34750, 40000, 35250
;----------------------------
;----------------------------
#dose=3.993
END

D Dose1
I 1
C 120
FSIZE 10 um
;Linedose1
;----------------------------
LINE 11250, 37860, 18750, 37860
LINE 11250, 37770, 18750, 37770
LINE 11250, 37680, 18750, 37680
LINE 11250, 37590, 18750, 37590
LINE 11250, 37500, 18750, 37500
LINE 11250, 37410, 18750, 37410
LINE 11250, 37320, 18750, 37320
LINE 11250, 37230, 18750, 37230
LINE 11250, 37140, 18750, 37140
LINE 11250, 37050, 18750, 37050
;----------------------------
LINE 11250, 32820, 18750, 32820
LINE 11250, 32740, 18750, 32740
LINE 11250, 32660, 18750, 32660
LINE 11250, 32580, 18750, 32580
LINE 11250, 32500, 18750, 32500
LINE 11250, 32420, 18750, 32420
LINE 11250, 32340, 18750, 32340
LINE 11250, 32260, 18750, 32260
LINE 11250, 32180, 18750, 32180
LINE 11250, 32100, 18750, 32100
;----------------------------
LINE 11250, 27780, 18750, 27780
LINE 11250, 27710, 18750, 27710
LINE 11250, 27640, 18750, 27640
LINE 11250, 27570, 18750, 27570
LINE 11250, 27500, 18750, 27500
LINE 11250, 27430, 18750, 27430
LINE 11250, 27360, 18750, 27360
LINE 11250, 27290, 18750, 27290
LINE 11250, 27220, 18750, 27220
LINE 11250, 27150, 18750, 27150
;----------------------------
LINE 11250, 22740, 18750, 22740
LINE 11250, 22680, 18750, 22680
LINE 11250, 22620, 18750, 22620
LINE 11250, 22560, 18750, 22560
```

```
LINE 11250, 22500, 18750, 22500
LINE 11250, 22440, 18750, 22440
LINE 11250, 22380, 18750, 22380
LINE 11250, 22320, 18750, 22320
LINE 11250, 22260, 18750, 22260
LINE 11250, 22200, 18750, 22200
;----------------------------
LINE 11250, 17700, 18750, 17700
LINE 11250, 17650, 18750, 17650
LINE 11250, 17600, 18750, 17600
LINE 11250, 17550, 18750, 17550
LINE 11250, 17500, 18750, 17500
LINE 11250, 17450, 18750, 17450
LINE 11250, 17400, 18750, 17400
LINE 11250, 17350, 18750, 17350
LINE 11250, 17300, 18750, 17300
LINE 11250, 17250, 18750, 17250
;----------------------------
LINE 11250, 12660, 18750, 12660
LINE 11250, 12620, 18750, 12620
LINE 11250, 12580, 18750, 12580
LINE 11250, 12540, 18750, 12540
LINE 11250, 12500, 18750, 12500
LINE 11250, 12460, 18750, 12460
LINE 11250, 12420, 18750, 12420
LINE 11250, 12380, 18750, 12380
LINE 11250, 12340, 18750, 12340
LINE 11250, 12300, 18750, 12300
;----------------------------
#line dose=0.003 nC/cm
END

D Dose2
I 1
C 140
FSIZE 10 um
;Linedose2
;----------------------------
LINE 21250, 37860, 28750, 37860
LINE 21250, 37770, 28750, 37770
LINE 21250, 37680, 28750, 37680
LINE 21250, 37590, 28750, 37590
LINE 21250, 37500, 28750, 37500
LINE 21250, 37410, 28750, 37410
LINE 21250, 37320, 28750, 37320
LINE 21250, 37230, 28750, 37230
LINE 21250, 37140, 28750, 37140
LINE 21250, 37050, 28750, 37050
;----------------------------
LINE 21250, 32820, 28750, 32820
```

LINE 21250, 32740, 28750, 32740 LINE 21250, 32660, 28750, 32660 LINE 21250, 32580, 28750, 32580 LINE 21250, 32500, 28750, 32500 LINE 21250, 32420, 28750, 32420 LINE 21250, 32340, 28750, 32340 LINE 21250, 32260, 28750, 32260 LINE 21250, 32180, 28750, 32180 LINE 21250, 32100, 28750, 32100 ;---------- LINE 21250, 27780, 28750, 27780 LINE 21250, 27710, 28750, 27710 LINE 21250, 27640, 28750, 27640 LINE 21250, 27570, 28750, 27570 LINE 21250, 27500, 28750, 27500 LINE 21250, 27430, 28750, 27430 LINE 21250, 27360, 28750, 27360 LINE 21250, 27290, 28750, 27290 LINE 21250, 27220, 28750, 27220 LINE 21250, 27150, 28750, 27150 ;---------- LINE 21250, 22740, 28750, 22740 LINE 21250, 22680, 28750, 22680 LINE 21250, 22620, 28750, 22620 LINE 21250, 22560, 28750, 22560 LINE 21250, 22500, 28750, 22500 LINE 21250, 22440, 28750, 22440 LINE 21250, 22380, 28750, 22380 LINE 21250, 22320, 28750, 22320 LINE 21250, 22260, 28750, 22260 LINE 21250, 22200, 28750, 22200 ;---------- LINE 21250, 17700, 28750, 17700 LINE 21250, 17650, 28750, 17650 LINE 21250, 17600, 28750, 17600 LINE 21250, 17550, 28750, 17550 LINE 21250, 17500, 28750, 17500 LINE 21250, 17450, 28750, 17450 LINE 21250, 17400, 28750, 17400 LINE 21250, 17350, 28750, 17350 LINE 21250, 17300, 28750, 17300 LINE 21250, 17250, 28750, 17250 ;---------- LINE 21250, 12660, 28750, 12660 LINE 21250, 12620, 28750, 12620 LINE 21250, 12580, 28750, 12580 LINE 21250, 12540, 28750, 12540 LINE 21250, 12500, 28750, 12500 LINE 21250, 12460, 28750, 12460 LINE 21250, 12420, 28750, 12420	

```
LINE 21250, 12380, 28750, 12380
LINE 21250, 12340, 28750, 12340
LINE 21250, 12300, 28750, 12300
;----------------------------
#dose=0.0035
END

D Dose3
I 1
C 160
FSIZE 10 um
;Linedose3
;----------------------------
LINE 31250, 37860, 38750, 37860
LINE 31250, 37770, 38750, 37770
LINE 31250, 37680, 38750, 37680
LINE 31250, 37590, 38750, 37590
LINE 31250, 37500, 38750, 37500
LINE 31250, 37410, 38750, 37410
LINE 31250, 37320, 38750, 37320
LINE 31250, 37230, 38750, 37230
LINE 31250, 37140, 38750, 37140
LINE 31250, 37050, 38750, 37050
;----------------------------
LINE 31250, 32820, 38750, 32820
LINE 31250, 32740, 38750, 32740
LINE 31250, 32660, 38750, 32660
LINE 31250, 32580, 38750, 32580
LINE 31250, 32500, 38750, 32500
LINE 31250, 32420, 38750, 32420
LINE 31250, 32340, 38750, 32340
LINE 31250, 32260, 38750, 32260
LINE 31250, 32180, 38750, 32180
LINE 31250, 32100, 38750, 32100
;----------------------------
LINE 31250, 27780, 38750, 27780
LINE 31250, 27710, 38750, 27710
LINE 31250, 27640, 38750, 27640
LINE 31250, 27570, 38750, 27570
LINE 31250, 27500, 38750, 27500
LINE 31250, 27430, 38750, 27430
LINE 31250, 27360, 38750, 27360
LINE 31250, 27290, 38750, 27290
LINE 31250, 27220, 38750, 27220
LINE 31250, 27150, 38750, 27150
;----------------------------
LINE 31250, 22740, 38750, 22740
LINE 31250, 22680, 38750, 22680
LINE 31250, 22620, 38750, 22620
LINE 31250, 22560, 38750, 22560
```

```
LINE 31250, 22500, 38750, 22500
LINE 31250, 22440, 38750, 22440
LINE 31250, 22380, 38750, 22380
LINE 31250, 22320, 38750, 22320
LINE 31250, 22260, 38750, 22260
LINE 31250, 22200, 38750, 22200
;----------------------------
LINE 31250, 17700, 38750, 17700
LINE 31250, 17650, 38750, 17650
LINE 31250, 17600, 38750, 17600
LINE 31250, 17550, 38750, 17550
LINE 31250, 17500, 38750, 17500
LINE 31250, 17450, 38750, 17450
LINE 31250, 17400, 38750, 17400
LINE 31250, 17350, 38750, 17350
LINE 31250, 17300, 38750, 17300
LINE 31250, 17250, 38750, 17250
;----------------------------
LINE 31250, 12660, 38750, 12660
LINE 31250, 12620, 38750, 12620
LINE 31250, 12580, 38750, 12580
LINE 31250, 12540, 38750, 12540
LINE 31250, 12500, 38750, 12500
LINE 31250, 12460, 38750, 12460
LINE 31250, 12420, 38750, 12420
LINE 31250, 12380, 38750, 12380
LINE 31250, 12340, 38750, 12340
LINE 31250, 12300, 38750, 12300
;----------------------------
#line dose=0.004
END
```

Doughnut_1.pat

```
;0.5pA 10um Field
D edgemark
I 5
C 120
FSIZE 10 um
;The Pattern Edge
;----------------------------
RECT 0, 0, 50000, 10000
RECT 40000, 10000, 50000, 50000
RECT 0, 10000, 10000, 40000
RECT 10000, 40000, 40000, 50000
;----------------------------
#dose=6.0
```

Doughnut_1.ctl

```
current = 0.5
origin= 0,0
sfile = Doughnut_1
fsize= 10

draw (Dose1)
draw (Dose2)
draw (Dose3)
draw (Dose4)
draw (Dose5)
draw (Dose6)
draw (Dose7)
draw (edgemark)
```

```
END
;Outer radius: 200nm
;Inner radius:
;Row 1: 100nm, Row 2: 97.5nm, Row 3:
95nm
;Row 4: 92.5nm, Row 5: 90nm, Row 6:
87.5nm, Row 7: 85nm

D Dose1
I 2
C 120
FSIZE 10 um
;----------------------------
RING 13000, 37000, 1000, 500
RING 13000, 33000, 1000, 512.5
RING 13000, 29000, 1000, 525
RING 13000, 25000, 1000, 537.5
RING 13000, 21000, 1000, 550
RING 13000, 17000, 1000, 562.5
RING 13000, 13000, 1000, 575
;----------------------------
#dose=37.5
END

D Dose2
I 2
C 128
FSIZE 10 um
;----------------------------
RING 17000, 37000, 1000, 500
RING 17000, 33000, 1000, 512.5
RING 17000, 29000, 1000, 525
RING 17000, 25000, 1000, 537.5
RING 17000, 21000, 1000, 550
RING 17000, 17000, 1000, 562.5
RING 17000, 13000, 1000, 575
;----------------------------
#dose=40
END

D Dose3
I 2
C 144
FSIZE 10 um
;----------------------------
RING 21000, 37000, 1000, 500
RING 21000, 33000, 1000, 512.5
RING 21000, 29000, 1000, 525
RING 21000, 25000, 1000, 537.5
RING 21000, 21000, 1000, 550
```

```
RING 21000, 17000, 1000, 562.5
RING 21000, 13000, 1000, 575
;-----------------------------
#dose=45
END

D Dose4
I 2
C 160
FSIZE 10 um
;-----------------------------
RING 25000, 37000, 1000, 500
RING 25000, 33000, 1000, 512.5
RING 25000, 29000, 1000, 525
RING 25000, 25000, 1000, 537.5
RING 25000, 21000, 1000, 550
RING 25000, 17000, 1000, 562.5
RING 25000, 13000, 1000, 575
;-----------------------------
#dose=50.0
END

D Dose5
I 2
C 176
FSIZE 10 um
;-----------------------------
RING 29000, 37000, 1000, 500
RING 29000, 33000, 1000, 512.5
RING 29000, 29000, 1000, 525
RING 29000, 25000, 1000, 537.5
RING 29000, 21000, 1000, 550
RING 29000, 17000, 1000, 562.5
RING 29000, 13000, 1000, 575
;-----------------------------
#dose=55
END

D Dose6
I 2
C 192
FSIZE 10 um
;-----------------------------
RING 33000, 37000, 1000, 500
RING 33000, 33000, 1000, 512.5
RING 33000, 29000, 1000, 525
RING 33000, 25000, 1000, 537.5
RING 33000, 21000, 1000, 550
RING 33000, 17000, 1000, 562.5
RING 33000, 13000, 1000, 575
```

;---------- #dose=60 END D Dose7 I 2 C 208 FSIZE 10 um ;---------- RING 37000, 37000, 1000, 500 RING 37000, 33000, 1000, 512.5 RING 37000, 29000, 1000, 525 RING 37000, 25000, 1000, 537.5 RING 37000, 21000, 1000, 550 RING 37000, 17000, 1000, 562.5 RING 37000, 13000, 1000, 575 ;---------- #dose=65.0 END	

8.2 HIM Imaging Recipes

Various recipes were developed during this PhD: for navigation and locating the patterned features whilst inducing minimal amount of helium ion exposure on to the sample, quick capturing of the overall pattern at low magnification and taking high-resolution images for sub-10 nm fine features. The key parameters are listed in the following table.

Recipe	**Dwell time (µsec)**	**ET brightness**	**ET contrast**	**Number of average**	**Scan mode**	**Scan size**
Navigation	3	N/A	N/A	2	off	512 × 512
Medium scan	2	N/A	N/A	8	Line	512 × 512
Slow scan	2	44.75	47.71	32	Line	1024 × 1024
High-res scan	0.5	50.83	70.69	128	Line	1024 × 1024

8.3 Stitching Error in HIM

When the size of an exposure pattern exceeds the maximum writing field of a lithography system, the pattern is divided into smaller writing fields, which are then stitched together by stage movement to generate the large area pattern. Inter-field stitching error is the unintended discontinuities which occur at the boundaries between adjacent fields. Precise stage movement is the key in minimizing the stitching error. In many lithography systems, this is achieved by using a laser interferometer-controlled stage, the beam deflection is adjusted to match the stage movement and a writing field alignment is performed before the exposure.

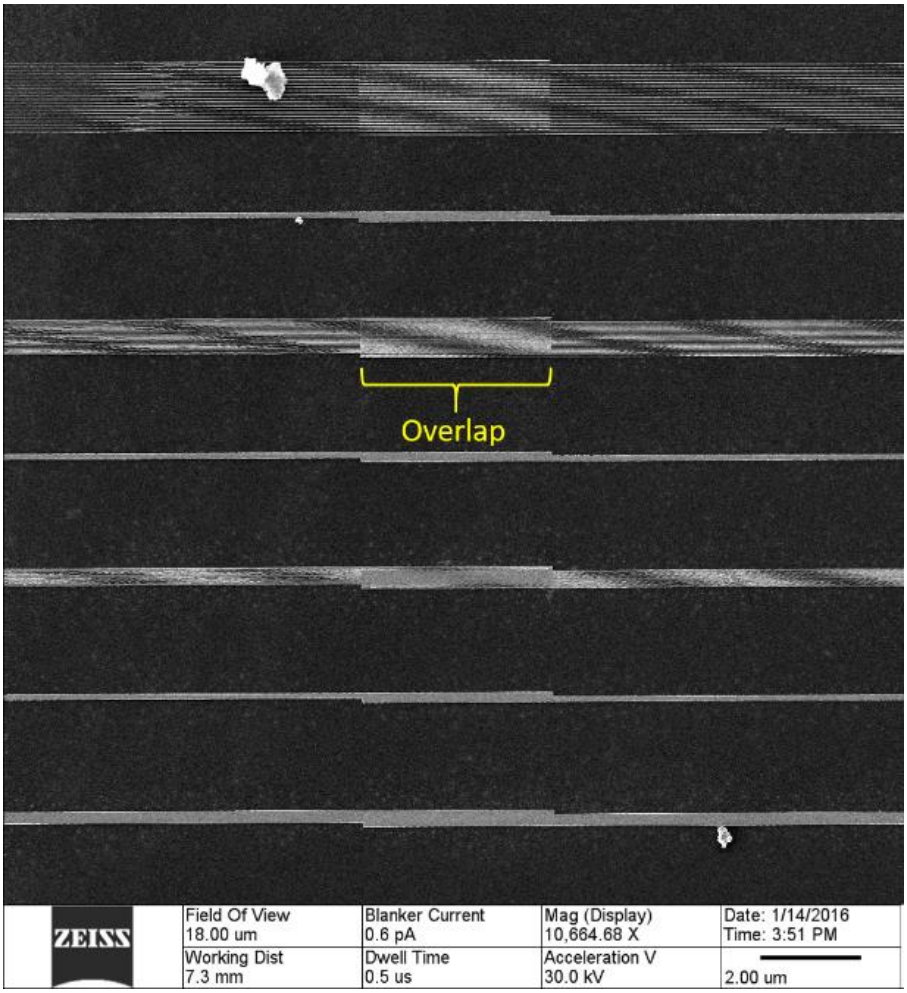

Figure 8.1:HIM image show the boundary of two adjacent exposures of 20 µm long, single-pixel lines arrays exposed by HIBL via a 20 µm stage movement.

HIM is not a specialised lithographic tool, hence it is not equipped with the laser interferometer and prone to stitching errors. To demonstrate and measure the stitching errors in HIM, arrays of single-

pixel lines of 20 µm long in various pitches were exposed on 50-nm-thick HM-01A using HIBL for multiple times consecutively with a 20 µm horizontal stage movement between every two exposures, to form an adjoining pattern. A beam current of 0.5 pA was applied to achieve line dose of 90 pC/cm. The developed pattern was imaged using HIM and the imaging conditions are a beam energy of 30 keV, beam current of 0.6 pA with a working distance of 7.3 mm. A boundary between two adjacent fields is shown in Figure 8.1. It can be observed that some overlapping of the pattern has occurred with a significant lateral stitching error and a minor longitudinal stitching error. This effect is consistent along the patterns.

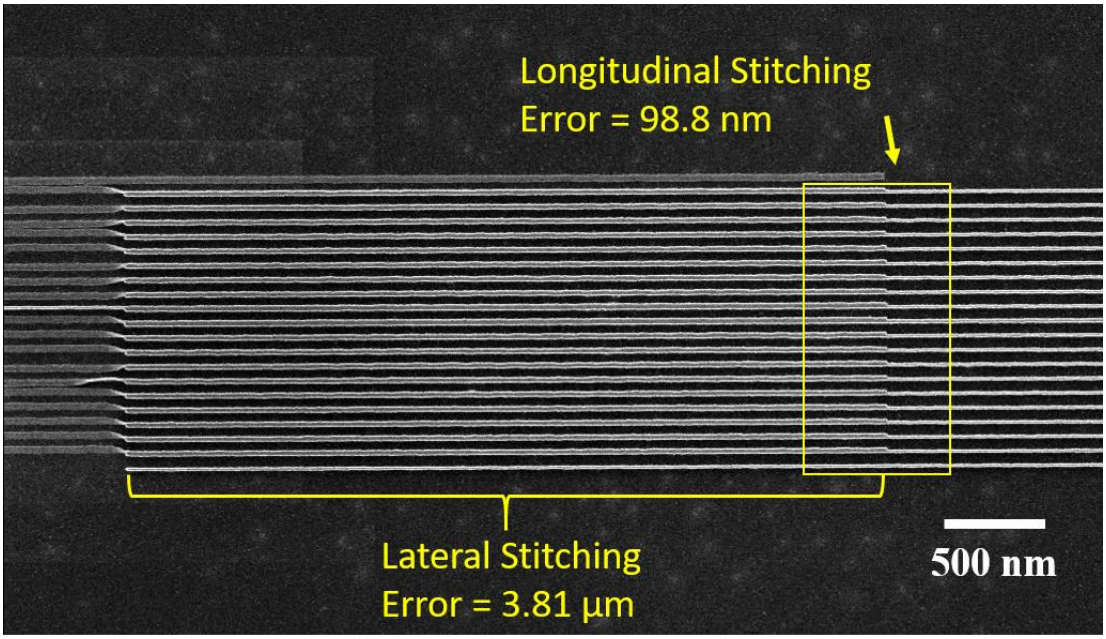

Figure 8.2: HIM image show the boundary of two adjacent exposures of 20 µm long, single-pixel lines arrays exposed by HIBL via a 20 µm stage movement, revealing stitching errors of 3.81 µm and 98.8 nm laterally and longitudinally.

Figure 8.2 shows a magnified HIM image of the boundary between two exposures, where three regions are identified. The first region shows upright line arrays on the right (as illustrated in Figure 8.3a) and the average linewidth was measured to be ~26 nm; the second region shows collapsed line arrays on the left (as illustrated in Figure 8.3b), which may be caused by the wet process and the nitrogen flow during the development, and the average linewidth in region 2 (apart from the 10^{th} line from the top which measures 26 nm) was measured to be ~50 nm, which is identical to that of the resist thickness; and finally the third region shows the overlapping of the two exposures where two lines are merged into one.

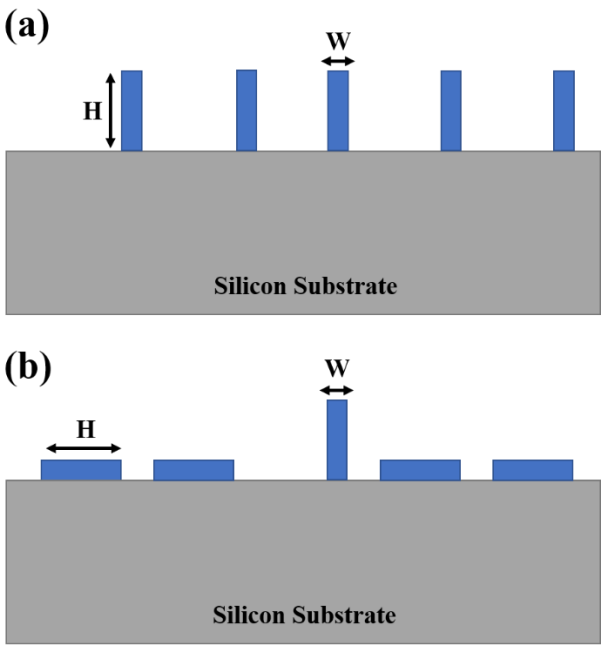

Figure 8.3:Ilustration of fabricated sparse arrays of lines with height of H and linewidth of W on silicon substrate. When pattern collapse happens, the measured linewidth from top-down 2D image can be the height, i.e. the resist thickness of the fabricated feature.

To determine the stitching errors in both axes, Gwyddion software was used to extract the line profile from the HIM image shown in Figure 8.2. The horizontal length of the third region was measured to be ~3.81 µm which is the lateral stitching error when the stage is moved for 20 µm horizontally. The distance from the top of a line in region 3 (identical to that in region 1) to the top of a line underneath in region 2 was measured, revealing a longitudinal stitching error of ~98.8 nm when the stage is moved for 20 µm horizontally.

Experiments were repeated, and consistent stitching errors were obtained in both axes. The stitching error in HIM has not affected the results achieved in this PhD due to the small nature of the patterns used. This effect can be mitigated superficially by manually setting the stage movement to be 23.8 µm instead when a 20 µm movement is required.

8.4 Pitch and Linewidth Measurement using Gwyddion

In this PhD, Gwyddion software package was mainly used for the visualisation and analysis of height fields from the fabricated resist samples measured by AFM. It was also utilised to measure the pitch and critical dimension of lines from the greyscale high-resolution images captured by HIM. The methods are briefly described in the following table. The high-resolution HIM images show Si lines, capped with Si_3N_4, with a pitch of approximately 0.05 µm (sample courtesy of Imec). The images were captured using HIM with the beam conditions of 30 keV beam energy, 10 µm aperture, 0.5 pA beam current and a working distance of 6.8 mm.

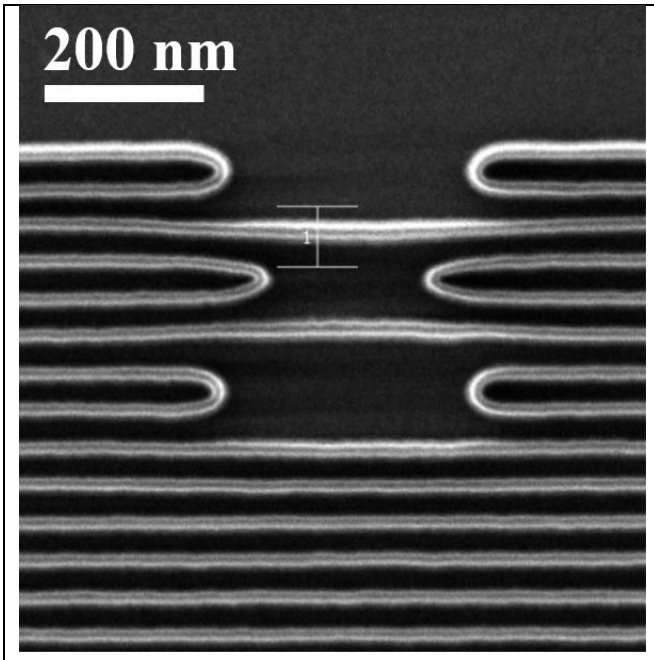

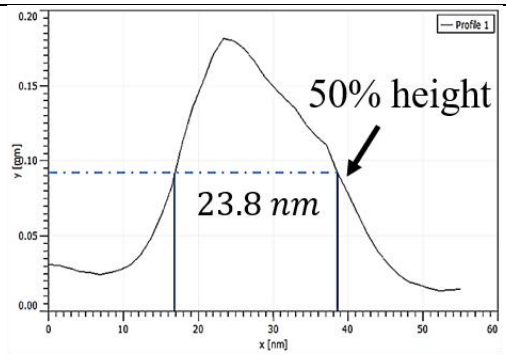

Position 1	23.8 nm
Position 2	24.3 nm
Position 3	24.5 nm
Position 4	24.5 nm

Average CD: **24.3 nm**

The linewidth can be determined by measuring the distance between the two points, that are on the SE contrast line profile of the line, representing 50% of the maximum intensity. The SE contrast profile can then be generated at multiple locations along the line of interest, and the linewidth is the average value from all measurements. For example, the distance is measured to be 23.8 nm at position 1 between the 2 points at 50% of maximum height on the SE contrast curve of the line. This procedure was repeated at three other locations along the line and the average value of 24.3 nm is taken as the CD of the line.

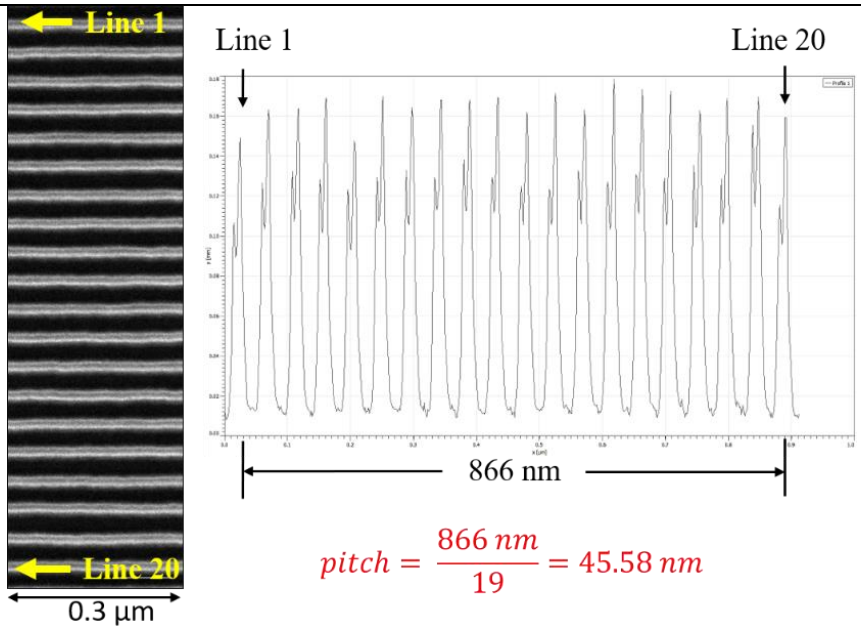

The pitch can be determined by first measuring the distance between two peaks on the SE contrast profile across the line array. The pitch is then calculated by dividing the measured distance by the number of gaps between the two lines. It is recommended to choose two peaks as far apart from each other as possible, so that any measurement errors are kept minimal to the calculated pitch. For example, the distance between Line 1 and Line 20 is measured to be 866 nm from the SE contrast profile. There are 19 spaces between the chosen lines, hence, the pitch is calculated to be 45.58 nm.

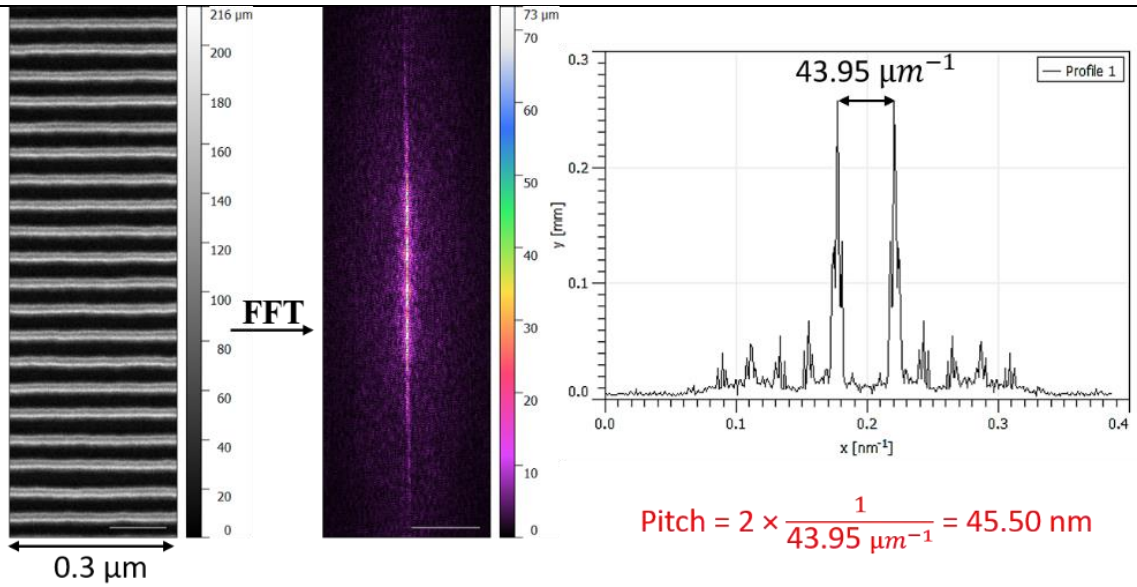

Another way of measuring the pitch of a line array when there is a good contrast difference between lines and spaces is to perform integral transformation of 2D fast Fourier transform (2D FFT) on the HIM image. The peaks in the line profile of the transform give us the frequencies of the seperation of the lines in HIM image. The inverse of the difference between the two peaks is the seperation, and the pitch is twice of the value.

BIBLIOGRAPHY

[1] T. Song, W. Rim, S. Park, Y. Kim, G. Yang, H. Kim, S. Baek, J. Jung, B. Kwon, S. Cho, H. Jung, Y. Choo, and J. Choi, "A 10 nm FinFET 128 Mb SRAM With Assist Adjustment System for Power, Performance, and Area Optimization," *IEEE J. Solid-State Circuits*, vol. 52, no. 1, pp. 240–249, 2017.

[2] R. Xie, P. Montanini, K. Akarvardar, N. Tripathi, B. Haran, S. Johnson, T. Hook, B. Hamieh, D. Corliss, J. Wang, X. Miao, J. Sporre, J. Fronheiser, N. Loubet, M. Sung, S. Sieg, S. Mochizuki, C. Prindle, S. Seo, A. Greene, J. Shearer, A. Labonte, S. Fan, L. Liebmann, R. Chao, A. Arceo, K. Chung, K. Cheon, P. Adusumilli, H. P. Amanapu, Z. Bi, J. Cha, H. Chen, R. Conti, R. Galatage, O. Gluschenkov, V. Kamineni, K. Kim, C. Lee, F. Lie, Z. Liu, S. Mehta, E. Miller, H. Niimi, C. Niu, C. Park, D. Park, M. Raymond, B. Sahu, M. Sankarapandian, S. Siddiqui, R. Southwick, L. Sun, C. Surisetty, S. Tsai, S. Whang, P. Xu, Y. Xu, C. Yeh, P. Zeitzoff, J. Zhang, J. Li, J. Demarest, J. Arnold, D. Canaperi, D. Dunn, N. Felix, D. Gupta, H. Jagannathan, S. Kanakasabapathy, W. Kleemeier, C. Labelle, M. Mottura, P. Oldiges, S. Skordas, T. Standaert, T. Yamashita, M. Colburn, M. Na, V. Paruchuri, S. Lian, R. Divakaruni, T. Gow, S. Lee, A. Knorr, H. Bu, and M. Khare, "A 7nm FinFET Technology Featuring EUV Patterning and Dual Strained High Mobility Channels," *IEEE Int. Electron Devices Meet.*, vol. 12, no. c, pp. 47–50, 2016.

[3] E. P. Office, "European Commission: CORDIS: Single Nanometer Manufacturing for Beyond CMOS Devices." [Online]. Available: http://cordis.europa.eu/project/rcn/104931_en.html. [Accessed: 11-Sep-2017].

[4] T. U. Ilmenau, "SNM Project - Single Nanometer Manufacturing for beyond CMOS devices." [Online]. Available: https://www.tu-ilmenau.de/snm-project/. [Accessed: 11-Sep-2017].

[5] M. Stepanova and S. Dew, *Nanofabrication: techniques and principles*. 2011.

[6] M. HATZAKIS, "Electron resists for microcircuit and mask production," *Electrochem Soc-J*, vol. 116, no. 7, pp. 1033–1037, 1969.

[7] D. L. Olynick, B. Cord, A. Schipotinin, D. F. Ogletree, and P. J. Schuck, "Electron beam exposure mechanisms in hydrogen silsesquioxane investigated by vibrational spectroscopy and in-situ electron beam induced desorption," *J. Vac. Sci. Technol. B*, 2010.

[8] Harriott L.R., Hull R. (2004) Nanolithography. In: Di Ventra M., Evoy S., Heflin J.R. (eds)

Introduction to Nanoscale Science and Technology. Nanostructure Science and Technology. Springer, Boston, MA

[9] H. Y. Liu and X. X. Zhu, “Lower critical solution temperatures of N-substituted acrylamide,” *Polymer (Guildf).*, vol. 40, p. 6985, 1999.

[10] M. A. Mohammad, T. Fito, J. Chen, S. Buswell, M. Aktary, M. Stepanova, and S. K. Dew, “Systematic study of the interdependence of exposure and development conditions and kinetic modelling for optimizing low-energy electron beam nanolithography,” *Microelectron. Eng.*, vol. 87, no. 5–8, pp. 1104–1107, 2010.

[11] H. J. Cho, H. S. Oh, K. J. Nam, Y. H. Kim, K. H. Yeo, W. D. Kim, Y. S. Chung, Y. S. Nam, S. M. Kim, W. H. Kwon, M. J. Kang, I. R. Kim, H. Fukutome, C. W. Jeong, H. J. Shin, Y. S. Kim, D. W. Kim, S. H. Park, H. S. Oh, J. H. Jeong, S. B. Kim, D. W. Ha, J. H. Park, H. S. Rhee, S. J. Hyun, D. S. Shin, D. H. Kim, H. Y. Kim, S. Maeda, K. H. Lee, Y. H. Kim, M. C. Kim, Y. S. Koh, B. Yoon, K. Shin, N. I. Lee, S. B. Kangh, K. H. Hwang, J. H. Lee, J. H. Ku, S. W. Nam, S. M. Jung, H. K. Kang, J. S. Yoon, and E. S. Jung, “Si FinFET based 10nm technology with multi Vt gate stack for low power and high performance applications,” in *Digest of Technical Papers - Symposium on VLSI Technology*, 2016, vol. 2016–Septe.

[12] J. K. W. Yang, B. Cord, H. Duan, K. K. Berggren, J. Klingfus, S. Nam, K.-B. Kim, and M. J. Rooks, “Understanding of hydrogen silsesquioxane electron resist for sub-5-nm-half-pitch lithography,” *J. Vac. Sci. Technol. B Microelectron. Nanom. Struct.*, vol. 27, pp. 2622–27, 2009.

[13] B. Cord, J. Yang, H. Duan, D. C. Joy, J. Klingfus, and K. K. Berggren, “Limiting factors in sub-10 nm scanning-electron-beam lithography,” *J. Vac. Sci. Technol. B Microelectron. Nanom. Struct.*, vol. 27, no. 6, p. 2616, 2009.

[14] V. R. Manfrinato, L. L. Cheong, H. Duan, D. Winston, H. I. Smith, and K. K. Berggren, “Sub-5keV electron-beam lithography in hydrogen silsesquioxane resist,” *Microelectron. Eng.*, vol. 88, no. 10, pp. 3070–3074, 2011.

[15] A. Olkhovets and H. G. Craighead, “Low voltage electron beam lithography in PMMA,” *J. Vac. Sci. Technol. B Microelectron. Nanom. Struct.*, vol. 17, no. 4, p. 1366, 1999.

[16] J. M. Pavkovich, “Proximity effect correction calculations by the integral equation approximate solution method,” *J. Vac. Sci. Technol. B Microelectron. Nanom. Struct.*, vol. 4, no. 1986, p. 159, 1986.

[17] H. Eisenmann, “PROXECCO—Proximity effect correction by convolution,” *J. Vac. Sci. Technol. B Microelectron. Nanom. Struct.*, vol. 11, no. 6, p. 2741, 1993.

[18] F. Murai, “Fast proximity effect correction method using a pattern area density map,” *J. Vac. Sci. Technol. B Microelectron. Nanom. Struct.*, vol. 10, no. 6, p. 3072, 1992.

[19] M. Parikh, “Corrections to proximity effects in electron beam lithograhy. I. Theory,” *J. Appl. Phys.*, vol. 50, no. 6, p. 4383, 1979.

[20] R. Wüest, P. Strasser, M. Jungo, F. Robin, D. Erni, and H. Jäckel, “An efficient proximity-effect correction method for electron-beam patterning of photonic-crystal devices,” *Microelectron. Eng.*, vol. 67–68, pp. 182–188, 2003.

[21] S. Tan, R. Livengood, Y. Greenzweig, Y. Drezner, and D. Shima, “Probe current distribution characterization technique for focused ion beam,” *J. Vac. Sci. Technol. B Microelectron. Nanom. Struct.*, vol. 30, no. 6, p. 06F606, 2012.

[22] K. Horiuchi, T. Itakura, and H. Ishikawa, “Fine pattern lithography using a helium field ion source,” *J. Vac. Sci. Technol. B*, vol. 6, no. 1, p. 241, 1988.

[23] J. Notte, B. Ward, N. Economou, R. Hill, R. Percival, L. Farkas, and S. McVey, “An introduction to the helium ion microscope,” *AIP Conf. Proc.*, vol. 931, pp. 489–496, 2007.

[24] D. Winston, “Sub-10nm lithography of resist on silicon with helium and neon gas field ionization sources,” no. November, pp. 13–16, 2012.

[25] A. Pimpin and W. Srituravanich, “Reviews on micro- and nanolithography techniques and their applications,” *Eng. J.*, vol. 16, no. 1, pp. 37–55, 2012.

[26] B. W. Ward, J. A. Notte, and N. P. Economou, “Helium ion microscope: A new tool for nanoscale microscopy and metrology,” *J. Vac. Sci. Technol. B Microelectron. Nanom. Struct.*, vol. 24, no. 6, p. 2871, 2006.

[27] D. Winston, B. M. Cord, B. Ming, D. C. Bell, W. F. DiNatale, L. A. Stern, A. E. Vladar, M. T. Postek, M. K. Mondol, J. K. W. Yang, and K. K. Berggren, “Scanning-helium-ion-beam lithography with hydrogen silsesquioxane resist,” *J. Vac. Sci. Technol. B Microelectron. Nanom. Struct.*, vol. 27, no. 6, p. 2702, 2009.

[28] F. H. M. Rahman, S. McVey, L. Farkas, J. A. Notte, S. Tan, and R. H. Livengood, “The prospects of a subnanometer focused neon ion beam,” *Scanning*, vol. 34, pp. 129–134, 2012.

[29] D. Winston, V. R. Manfrinato, S. M. Nicaise, L. L. Cheong, H. Duan, D. Ferranti, J. Marshman, S. McVey, L. Stern, J. Notte, and K. K. Berggren, “Neon ion beam lithography (NIBL),” *Nano Lett.*, vol. 11, no. 10, pp. 4343–4347, 2011.

[30] X. Shi and S. A. Boden, “Scanning helium ion beam lithography,” in *Frontiers of Nanoscience*, vol. 11, 2016, pp. 563–594.

[31] V. N. Tondare, “Quest for high brightness, monochromatic noble gas ion sources,” *J. Vac. Sci. Technol. A Vacuum, Surfaces, Film.*, vol. 23, no. 6, p. 1498, 2005.

[32] L. E. Ocola, C. Rue, and D. Maas, “High-resolution direct-write patterning using focused ion beams,” *MRS Bull.*, vol. 39, no. 04, pp. 336–341, 2014.

[33] J. Morgan, J. Notte, R. Hill, and B. Ward, “An Introduction to the Helium Ion Microscope,” 2006.

[34] R. Hill and F. H. M. Faridur Rahman, “Advances in helium ion microscopy,” *Nucl. Instrum. Methods Phys. Res., Sect. A*, vol. 645, no. 1, pp. 96–101, 2011.

[35] G. Hlawacek, V. Veligura, R. van Gastel, and B. Poelsema, “Helium ion microscopy,” *J. Vac. Sci. Technol. B Microelectron. Nanom. Struct.*, vol. 32, no. 2, p. 020801, 2014.

[36] R. Hill, J. A. Notte, and L. Scipioni, *Chapter 2 – Scanning helium ion microscopy*, vol. 170. 2012.

[37] E. H. Lee, G. R. Rao, M. B. Lewis, and L. K. Mansur, “Effects of electronic and recoil processes in polymers during ion implantation,” *J. Mater. Res.*, vol. 9, no. 04, pp. 1043–1050, 1994.

[38] E. H. Lee, “Ion-beam modification of polymeric materials - fundamental principles and applications,” *Nucl. Instruments Methods Phys. Res. Sect. B Beam Interact. with Mater. Atoms*, vol. 151, no. 1–4, pp. 29–41, 1999.

[39] S. Sijbrandij, B. Thompson, J. Notte, B. W. Ward, and N. P. Economou, “Elemental analysis with the helium ion microscope,” *J. Vac. Sci. Technol. B Microelectron. Nanom. Struct.*, vol. 26, no. 6, pp. 2103–2106, 2008.

[40] L. Scipioni, C. A. Sanford, J. Notte, B. Thompson, and S. McVey, “Understanding imaging modes in the helium ion microscope,” *J. Vac. Sci. Technol. B Microelectron. Nanom. Struct.*, vol. 27, no. 6, p. 3250, 2009.

[41] P. F. A. Alkemade, E. M. Koster, E. Van Veldhoven, and D. J. Maas, “Imaging and

nanofabrication with the helium ion microscope of the van leeuwenhoek laboratory in Delft," *Scanning*, vol. 34, no. 2, pp. 90–100, 2012.

[42] R. Ramachandra, B. Griffin, and D. Joy, "A model of secondary electron imaging in the helium ion scanning microscope.," *Ultramicroscopy*, vol. 109, no. 6, pp. 748–57, 2009.

[43] Y. Petrov and O. Vyvenko, "Secondary electron emission spectra and energy selective imaging in helium ion microscope," in *Proc. SPIE*, 2011, vol. 8036.

[44] K. Inai, K. Ohya, and T. Ishitani, "Simulation study on image contrast and spatial resolution in helium ion microscope," *J. Electron Microsc. (Tokyo).*, vol. 56, no. 5, pp. 163–169, 2007.

[45] D. Cohen-Tanugi and N. Yao, "Superior imaging resolution in scanning helium-ion microscopy: A look at beam-sample interactions," *J. Appl. Phys.*, vol. 104, no. 6, p. 063504, 2008.

[46] M. T. Postek and A. E. Vladár, "Helium ion microscopy and its application to nanotechnology and nanometrology," *Scanning*, vol. 30, no. November, pp. 457–462, 2008.

[47] Y. V. Petrov, O. F. Vyvenko, and A. S. Bondarenko, "Scanning helium ion microscope: Distribution of secondary electrons and ion channeling," *J. Surf. Investig. X-ray, Synchrotron Neutron Tech.*, vol. 4, no. 5, pp. 792–795, 2010.

[48] D. C. Joy, M. S. Prasad, and H. M. Meyer, "Experimental secondary electron spectra under SEM conditions," *J. Microsc.*, vol. 215, no. 1, pp. 77–85, 2004.

[49] M. P. Seah and W. A. Dench, "Quantitative electron spectroscopy of surfaces: A standard data base for electron inelastic mean free paths in solids," *Surf. Interface Anal.*, vol. 1, no. 1, pp. 2–11, 1979.

[50] R. Livengood, S. Tan, Y. Greenzweig, J. Notte, and S. McVey, "Subsurface damage from helium ions as a function of dose, beam energy, and dose rate," *J. Vac. Sci. Technol. B Microelectron. Nanom. Struct.*, vol. 27, no. 6, p. 3244, 2009.

[51] R. H. Livengood, M. Grumski, Y. Greenzweig, T. Liang, R. Jamison, and Q. Xie, "Helium ion microscope invasiveness study and novel imaging analysis for semiconductor applications," *Phys. Procedia*, vol. 1, no. 1, pp. 143–148, 2008.

[52] S. M. Sze and K. K. Ng, "Physics of Semiconductor Devices, 3rd Edition - Simon M. Sze, Kwok K. Ng," *Phys. Semicond. Devices, 3rd Ed. John Wiley Sons, Inc.; NJ*, pp. 164, 682, 2007.

[53] V. Sidorkin, E. van Veldhoven, E. van der Drift, P. Alkemade, H. Salemink, and D. Maas, "Sub-10-nm nanolithography with a scanning helium beam," *J. Vac. Sci. Technol. B Microelectron. Nanom. Struct.*, vol. 27, p. 18, 2009.

[54] V. A. Sidorkin, "Resist and exposure processes for sub-10-nm electron and ion beam lithography," Delft University of Technology, 2010.

[55] W. Li, W. Wu, and R. Stanley Williams, "Combined helium ion beam and nanoimprint lithography attains 4 nm half-pitch dense patterns," *J. Vac. Sci. Technol. B Microelectron. Nanom. Struct.*, vol. 30, no. 6, p. 06F304, 2012.

[56] D. Maas, E. van Veldhoven, A. van Langen–Suurling, P. F. A. Alkemade, S. Wuister, R. Hoefnagels, C. Verspaget, J. Meessen, and T. Fliervoet, "Evaluation of EUV resist performance below 20nm CD using helium ion lithography," *SPIE Adv. Lithogr.*, vol. 9048, p. 90482Z, 2014.

[57] A. N. Broers, J. M. E. Harper, and W. W. Molzen, "250-Å linewidths with PMMA electron resist," *Appl. Phys. Lett.*, vol. 33, no. 5, pp. 392–394, 1978.

[58] H. Duan, D. Winston, J. K. W. Yang, B. M. Cord, V. R. Manfrinato, and K. K. Berggren, "Sub-10-nm half-pitch electron-beam lithography by using poly(methyl methacrylate) as a negative resist," *J. Vac. Sci. Technol. B Microelectron. Nanom. Struct.*, vol. 28, no. 6, p. C6C58, 2010.

[59] T. H. P. Chang, "Proximity effect in electron-beam lithography," *J. Vac. Sci. Technol.*, vol. 12, no. 6, pp. 1271–1275, 1975.

[60] S. V. Dubonos, B. N. Gaifullin, H. F. Raith, A. A. Svintsov, and S. I. Zaitsev, "Evaluation, verification and error determination of proximity parameters α, β and ν in electron beam lithography," *Microelectron. Eng.*, vol. 21, no. 1–4, pp. 293–296, Apr. 1993.

[61] A. Misaka, K. Harafuji, and N. Nomura, "Determination of proximity effect parameters in electron-beam lithography," *J. Appl. Phys.*, vol. 68, pp. 6472–6479, 1990.

[62] M. G. Rosenfield, S. J. Wind, W. W. Molzen, and P. D. Gerber, "Determination of proximity effect correction parameters for 0.1 μm electron-beam lithography," *Microelectron. Eng.*, vol. 11, no. 1–4, pp. 617–623, 1990.

[63] E. Soe, B. K. Choi, and O. Kim, "Determination of proximity effect parameters and the shape bias parameter in electron beam lithography," *Microelectron. Eng.*, vol. 53, no. 1, pp. 305–308, 2000.

[64] E. van der Drift and D. J. Maas, “Helium ion lithography principles and performance,” Jan. 2012.

[65] A. E. Grigorescu, M. C. van der Krogt, C. W. Hagen, and P. Kruit, “10nm lines and spaces written in HSQ, using electron beam lithography,” *Microelectron. Eng.*, vol. 84, no. 5–8, pp. 822–824, 2007.

[66] L. D. Bozano, P. J. Brock, H. D. Truong, M. I. Sanchez, G. M. Wallraff, W. D. Hinsberg, R. D. Allen, M. Fujiwara, K. Maeda, and M. H. Somervell, “Bound PAG Resists: An EUV and electron beam lithography performance comparison of fluoropolymers,” *Adv. Resist Mater. Process. Technol. Xxviii*, vol. 7972, 2011.

[67] W. M. Arden, “The International Technology Roadmap for Semiconductors--Perspectives and challenges for the next 15 years,” *Curr. Opin. Solid State Mater. Sci.*, vol. 6, no. 5, pp. 371–377, 2002.

[68] C. C. Welch, A. L. Goodyear, T. Wahlbrink, M. C. Lemme, and T. Mollenhauer, “Silicon etch process options for micro- and nanotechnology using inductively coupled plasmas,” *Microelectron. Eng.*, vol. 83, no. 4–9 SPEC. ISS., pp. 1170–1173, 2006.

[69] D. Olynick, A. Schwartzberg, and D. Keszler, “Mainstreaming inorganic metal-oxide resists for high-resolution lithography,” in *Materials and Processes for Next Generation Lithography*, A. Robinson and R. Lawson, Eds. Oxford, UK: Elsevier, 2016, pp. 349–75.

[70] W. (Walter) Hu, K. Sarveswaran, M. Lieberman, and G. H. Bernstein, “Sub-10 nm electron beam lithography using cold development of poly(methylmethacrylate),” *J. Vac. Sci. Technol. B Microelectron. Nanom. Struct.*, vol. 22, no. 4, p. 1711, 2004.

[71] E. Gogolides, P. Argitis, E. A. Couladouros, V. P. Vidali, M. Vasilopoulou, G. Cordoyiannis, C. D. Diakoumakos, and A. Tserepi, “Photoresist etch resistance enhancement using novel polycarbocyclic derivatives as additives,” *J. Vac. Sci. Technol. B Microelectron. Nanom. Struct.*, vol. 21, no. 1, p. 141, 2003.

[72] S. Hien, G. Rich, G. Molina, H. B. Cao, P. F. Nealey, I. Technologies, and I. Sematech, “Collapse behavior of single layer 193 and 157 nm resists : Use of surfactants in the rinse to realize the sub 130 nm nodes,” vol. 4690, pp. 254–261, 2002.

[73] K. Yoshimoto, C. Higgins, A. Raghunathan, J. G. Hartley, D. L. Goldfarb, H. Kato, K. Petrillo, M. E. Colburn, J. Schefske, O. Wood, and T. I. Wallow, “Revisit pattern collapse for 14nm node and beyond,” vol. 7972, p. 79720K–79720K–12, 2011.

[74] C. M. Stafford, B. D. Vogt, C. Harrison, R. V April, V. Re, M. Recei, and V. June, “Elastic Moduli of Ultrathin Amorphous Polymer Films,” pp. 5095–5099, 2006.

[75] M. Carcasi, D. Bassett, W. Printz, S. Kawakami, and Y. Miyata, “Line-pattern collapse mitigation status for EUV at 32nm HP and below,” *SPIE Adv. …*, vol. 8325, p. 83250K, 2012.

[76] P. Naulleau, “EUV lithography patterning challenges,” in *Materials and Processes for Next Generation Lithography*, A. Robinson and R. Lawson, Eds. Oxford, UK: Elsevier, 2016, pp. 177–192.

[77] M. D. Shumway, P. Naulleau, K. A. Goldberg, and J. Bokor, “Measuring line roughness through aerial image contrast variation using coherent extreme ultraviolet spatial filtering techniques,” *J. Vac. Sci. Technol. B Microelectron. Nanom. Struct.*, vol. 23, no. 6, p. 2844, 2005.

[78] Y. Ekinci, M. Vockenhuber, B. Terhalle, M. Hojeij, L. Wang, and T. R. Younkin, “Evaluation of resist performance with EUV interference lithography for sub-22 nm patterning,” *Proc. SPIE Vol. 8322*, vol. 8322, p. 83220W–83220W–11, 2012.

[79] B. Cardineau, W. Early, T. Fujisawa, K. Maruyama, M. Shimizu, S. Sharma, K. Petrillo, and R. Brainard, “LER Limitations of Resist Thin Films,” *J. Photopolym. Sci. Technol.*, vol. 25, no. 5, pp. 633–640, 2012.

[80] D. Drygiannakis, G. P. Patsis, I. Raptis, D. Niakoula, V. Vidali, E. Couladouros, P. Argitis, and E. Gogolides, “Stochastic simulation studies of molecular resists,” *Microelectron. Eng.*, vol. 84, no. 5–8, pp. 1062–1065, 2007.

[81] H. Gokan, S. Esho, and Y. Ohnishi, “Dry Etch Resistance of Organic Materials,” *J. Electrochem. Soc.*, vol. 130, no. 1, pp. 143–146, 1983.

[82] R. R. Kunz, S. C. Palmateer, A. R. Forte, R. D. Allen, G. M. Wallraff, R. A. Di Pietro, and D. C. Hofer, “Limits to etch resistance for 193-nm single-layer resists,” *Soc. Photogr. Instrum. Eng.*, vol. 2724, p. 365, 1996.

[83] G. S. Oehrlein, R. J. Phaneuf, and D. B. Graves, “Plasma-polymer interactions: A review of progress in understanding polymer resist mask durability during plasma etching for nanoscale fabrication,” *J. Vac. Sci. Technol. B, Nanotechnol. Microelectron. Mater. Process. Meas. Phenom.*, vol. 29, no. 1, p. 010801, 2011.

[84] M. Yoshiiwa, H. Kageyama, Y. Shirota, F. Wakaya, K. Gamo, and M. Takai, “Novel class

of low molecular-weight organic resists for nanometer lithography," *Appl. Phys. Lett.*, vol. 69, no. 17, p. 2605, 1996.

[85] T. Kadota, H. Kageyama, F. Wakaya, K. Gamo, and Y. Shirota, "Novel electron-beam molecular resists with high resolution and high sensitivity for nanometer lithography," *Chem. Lett.*, vol. 33, no. 6, pp. 706–707, 2004.

[86] H. M. Zaid, A. P. G. Robinson, R. E. Palmer, M. Manickam, and J. A. Preece, "Chemical amplification of a triphenylene molecular electron beam resist," *Adv. Funct. Mater.*, vol. 17, no. 14, pp. 2522–2527, 2007.

[87] A. M. Rao, P. Zhou, K. Wang, G. T. Hager, J. M. Holden, Y. Wang, W. Lee, X. Bi, P. C. Eklund, D. S. Cornett, M. A. Duncan, and J. Amster, "Photoinduced polymerization of solid C60 films," *Science (80-.).*, vol. 1011, no. February, pp. 10–12, 1992.

[88] T. Tada and T. Kanayama, "Nanolithography using fullerene films as an electron beam resist," *Japanese J. Appl. Physics, Part 2 Lett.*, vol. 35, no. 1 A, 1996.

[89] A. Robinson, R. Palmer, and T. Tada, "Exposure mechanism of fullerene derivative electron beam resists," *Chem. Phys. Lett.*, vol. 312, no. October, pp. 469–474, 1999.

[90] D. X. Yang, A. Frommhold, X. Xue, R. E. Palmer, and a. P. G. Robinson, "Chemically amplified phenolic fullerene electron beam resist," *J. Mater. Chem. C*, vol. 2, no. 8, p. 1505, 2014.

[91] J. Manyam, F. P. Gibbons, S. Diegoli, M. Manickam, J. A. Preece, R. E. Palmer, and A. P. G. Robinson, "Chemically amplified fullerene resists for e-beam lithography," *Proc. SPIE*, vol. 6923, no. 0, p. 69230M–69230M–8, 2008.

[92] A. P. G. Robinson, R. E. Palmer, T. Tada, T. Kanayama, E. J. Shelley, and J. A. Preece, "Fullerene derivatives as novel resist materials for fabrication of MEMS devices by electron beam lithography," *Proc. Mater. Res. Soc.*, vol. 546, pp. 219–224, 1999.

[93] X. Chen, R. E. Palmer, and A. P. G. Robinson, "A high resolution water soluble fullerene molecular resist for electron beam lithography.," *Nanotechnology*, vol. 19, no. 27, p. 275308, 2008.

[94] J. Manyam, M. Manickam, J. A. Preece, R. E. Palmer, and A. P. G. Robinson, "Plasma etching of high-resolution features in a fullerene molecular resist," *Proc. SPIE*, vol. 7972, p. 79722N–79722N–12, 2011.

[95] A. P. G. Robinson, R. E. Palmer, T. Tada, T. Kanayama, M. T. Allen, J. A. Preece, and K.

D. M. Harris, “10 nm scale electron beam lithography using a triphenylene derivative as a negative/positive tone resist,” *J. Phys. D. Appl. Phys.*, vol. 32, no. 16, pp. L75–L78, 1999.

[96] D. J. Maas and R. van Gastel, “Helium ion microscopy,” *Surf. Sci. Tech.*, pp. 461–497, 2013.

[97] T. Levesque, “Application of Plasma Cleaning Technology in Microscopy,” 2014.

[98] R. Garcia, A. D. Batchelor, C. B. Mooney, A. D. Garetto, R. Vane, and D. P. Griffis, “Effect of Cleaning Parameters on Cleaning Effectiveness in an SEM Equipped with an Oxygen Plasma Etching Device,” *Microsc. Microanal.*, vol. 13, no. Suppl 2, pp. 1–2, 2007.

[99] A. J. Pearson, S. A. Boden, D. M. Bagnall, D. G. Lidzey, and C. Rodenburg, “Imaging the bulk nanoscale morphology of organic solar cell blends using helium ion microscopy,” *Nano Lett.*, vol. 11, no. 10, pp. 4275–4281, 2011.

[100] K. Ohya, T. Yamanaka, K. Inai, and T. Ishitani, “Comparison of secondary electron emission in helium ion microscope with gallium ion and electron microscopes,” *Nucl. Instruments Methods Phys. Res. Sect. B Beam Interact. with Mater. Atoms*, vol. 267, no. 4, pp. 584–589, 2009.

[101] W. B. Thompson, J. Notte, L. Scipioni, and L. Stern, “The helium ion microscope for high resolution imaging, materials analysis and FA applications,” in *2008 15th International Symposium on the Physical and Failure Analysis of Integrated Circuits*, 2008, pp. 1–6.

[102] D. Pickard and L. Scipioni, “Graphene nano-ribbon patterning in the Orion Plus,” 2009.

[103] A. J. Pearson, S. A. Boden, D. M. Bagnall, D. G. Lidzey, and C. Rodenburg, “Imaging the bulk nanoscale morphology of organic solar cell blends using helium ion microscopy,” *Nano Lett.*, vol. 11, no. 10, pp. 4275–4281, 2011.

[104] J. F. Ziegler, M. D. Ziegler, and J. P. Biersack, “SRIM – The stopping and range of ions in matter (2010),” *Nucl. Instruments Methods Phys. Res. Sect. B Beam Interact. with Mater. Atoms*, vol. 268, no. 11–12, pp. 1818–1823, 2010.

[105] W. (Walter) Hu, “Ultrahigh resolution electron beam lithography for molecular electronics,” 2004.

[106] W. H. Teh, C. Te Liang, M. Graham, and C. G. Smith, “Cross-linked PMMA as a low-dimensional dielectric sacrificial layer,” *J. Microelectromechanical Syst.*, vol. 12, no. 5, pp. 641–648, 2003.

[107] C. Vieu, F. Carcenac, A. Pepin, Y. Chen, M. Mejias, A. Lebib, L. Manin-Ferlazzo, L. Couraud, and H. Launois, “Electron beam lithography - Resolution limits and applications,” *Appl. Surf. Sci.*, vol. 164, pp. 111–117, 2000.

[108] L. Stevens, R. Jonckheere, E. Froyen, S. Decoutere, and D. Lanneer, “Determination of the proximity parameters in electron beam lithography using doughnut-structures,” *Microelectron. Eng.*, vol. 5, no. 1–4, pp. 141–150, 1986.

[109] E. Boere, E. van der Drift, J. Romijn, and B. Rousseeuw, “Experimental study on proximity effects in high voltage e-beam lithography,” *Microelectron. Eng.*, vol. 11, no. 1–4, pp. 351–354, 1990.

[110] C. Shaw, “Proximity parameters determination for electron beam lithography using a novel technique,” *J. Vac. Sci. Technol.*, vol. 19, no. 1981, p. 1286, 1981.

[111] A. P. G. Robinson, R. E. Palmer, T. Tada, T. Kanayama, and J. A. Preece, “A fullerene derivative as an electron beam resist for nanolithography,” *Appl. Phys. Lett.*, vol. 72, no. 1998, pp. 1302–1304, 1998.

[112] A. Frommhold, D. Yang, A. McClelland, X. Xue, Y. Ekinci, R. E. Palmer, and A. P. G. Robinson, “Performance of negative tone chemically amplified fullerene resists in extreme ultraviolet lithography,” *J. Micro/Nanolithography, MEMS, MOEMS*, vol. 12, no. 3, p. 033010, 2013.